

広島大学学位請求論文

First measurement of ω and ϕ mesons

via di-electron decay channels

in proton+proton collisions at $\sqrt{s} = 200$ GeV

(重心系衝突エネルギー 200GeV の陽子 + 陽子衝突における
電子・陽電子崩壊過程を用いた ω 、 ϕ 中間子の最初の測定)

2012年1月

広島大学大学院理学研究科
物理科学専攻

来島 孝太郎

目次

1. 主論文

First measurement of ω and ϕ mesons via di-electron decay channels
in proton+proton collisions at $\sqrt{s} = 200$ GeV

(重心系衝突エネルギー 200GeV の陽子 + 陽子衝突における電子・陽電子崩壊
過程を用いた ω 、 ϕ 中間子の最初の測定)

来島 孝太郎

2. 公表論文

- (1) Measurement of neutral mesons in $p+p$ collisions at $\sqrt{s} = 200$ GeV and
scaling properties of hadron production
A.Adare, K.M.Kijima *et al.*, (別紙、共著者リスト 1 参照)
Physical Review C83, 052004 (2011).

3. 参考論文

- (1) Nuclear modification factors of ϕ mesons in $d+\text{Au}$, $\text{Cu}+\text{Cu}$ and
 $\text{Au}+\text{Au}$ collisions at $\sqrt{s_{NN}} = 200\text{GeV}$

A.Adare, K.M.Kijima *et al.*, (別紙、共著者リスト 2 参照)
Physical Review C83, 024909 (2011).

- (2) Identified charged hadron production in $p+p$ collisions at $\sqrt{s} = 200$
and 62.4GeV

A.Adare, K.M.Kijima *et al.*, (別紙、共著者リスト 3 参照)
Physical Review C83, 064903 (2011).

共著者リスト 1

A.Adare, S.Afanasiev, C.Aidala, N.N.Ajitanand, Y.Akiba, H.Al-Bataineh, J.Alexander, K.Aoki, L.Aphecetche, R.Armendariz, S.H.Aronson, J.Asai, E.TAtomssa, R.Averbeck, T.C.Awes, B.Azmoun, V.Babintsev, M.Bai, G.Baksay, L.Baksay, A.Baldisseri, K.N.Barish, P.D.Barnes, B.Bassalleck, A.T.Basye, S.Bathe, S.Batsouli, V.Baublis, C.Baumann, A.Bazilevsky, S.Belikov, R.Bennett, A.Berdnikov, Y.Berdnikov, A.A.Bickley, J.G.Boissevain, H.Borel, K.Boyle, M.L.Brooks, H.Buesching, V.Bumazhnov, G.Bunce, S.Butsyk, C.M.Camacho, S.Campbell, B.S.Chang, W.C.Chang, J.-L.Charvet, S.Chernichenko, J.Chiba, C.Y.Chi, M.Chiu, I.J.Chi, R.K.Choudhury, T.Chujo, P.Chung, A.Churyn, V.Cianciolo, Z.Citron, C.R.Cleven, B.A.Cole, M.P.Comets, P.Constantin, M.Csanad, T.Csorgo, T.Dahms, S.Dairaku, K.Das, G.David, M.B.Deaton, K.Dehmelt, H.Delagrange, A.Denisov, D.d'Enterria, A.Deshpande, E.J.Desmond, O.Dietzsch, A.Dion, M.Donadelli, O.Drapier, A.Drees, K.A.Drees, A.K.Dubey, A.Durum, D.Dutta, V.Dzhordzhadze, Y.V.Efremenko, J.Egdemir, F.Ellinghaus, W.S.Emam, T.Engelmore, A.Enokizono, H.En'yo, S.Esumi, K.O.Eyser, B.Fadem, D.E.Fields, M.Finger, Jr., M.Finger, F.Fleuret, S.L.Fokin, Z.Fraenkel, J.E.Frantz, A.Franz, A.D.Frawley, K.Fujiwara, Y.Fukao, T.Fusayasu, S.Gadrat, I.Garishvili, A.Glenn, H.Gong, M.Gonin, J.Gosset, Y.Goto, R.Granie.d.Cassagnac, N.Grau, S.V.Greene, M.Gross.Perdekamp, T.Gunji, H.-A.Gustafsson, T.Hachiya, A.Had.Henni, C.Haegemann, J.S.Haggerty, H.Hamagaki, R.Han, H.Harada, E.P.Hartouni, K.Haruna, E.Haslum, R.Hayano, M.Heffner, T.K.Hemmick, T.Hester, X.He, H.Hiejima, J.C.Hill, R.Hobbs, M.Hohlmann, W.Holzmann, K.Homma, B.Hong, T.Horaguchi, D.Hornback, S.Huang, T.Ichihara, R.Ichimiya, H.Iinuma, Y.Ikeda, K.Imai, J.Imrek, M.Inaba, Y.Inoue, D.Isenhower, L.Isenhower, M.Ishihara, T.Isobe, M.Issah, A.Isupov, D.Ivanischev, B.V.Jacak, J.Jia, J.Jin, O.Jinnouchi, B.M.Johnson, K.S.Joo, D.Jouan, F.Kajihara, S.Kametani, N.Kamihara, J.Kamin, M.Kaneta, J.H.Kang, H.Kanou, J.Kapustinsky, D.Kawall, A.V.Kazantsev, T.Kempel, A.Khanzadeev, K.M.Kijima, J.Kikuchi, B.I.Kim, D.H.Kim, D.J.Kim, E.Kim, S.H.Kim, E.Kinney, K.Kiriluk, A.Kiss, E.Kistenev, A.Kiyomichi, J.Klay, C.Klein-Boesing, L.Kochenda, V.Kochetkov, B.Komkov, M.Konno, J.Koster, D.Kotchetkov, A.Kozlov, A.Kral, A.Kravitz, J.Kubart, G.J.Kunde, N.Kurihara, K.Kurita, M.Kurosawa, M.J.Kweon, Y.Kwon, G.S.Kyle, R.Lacey, Y.S.Lai, J.G.Lajoie, D.Layton, A.Lebedev, D.M.Lee, K.B.Lee, M.K.Lee, T.Lee, M.J.Leitch, M.A.L.Leite, B.Lenzi, P.Liebing, T.Liska, A.Litvinenko, H.Liu, M.X.Liu, X.Li, B.Love, D.Lynch, C.F.Maguire, Y.I.Makdisi, A.Malakhov, M.D.Malik, V.I.Manko, E.Mannel, Y.Mao, L.Masek, H.Masui, F.Matathias, M.McCumber, P.L.McGaughey, N.Means, B.Meredith, Y.Miake, P.Mikes, K.Miki, T.E.Miller, A.Milov, S.Mioduszewski, M.Mishra, J.T.Mitchell, M.Mitrovski, A.K.Mohanty, Y.Morino, A.Morreale, D.P.Morrison, T.V.Moukhanova, D.Mukhopadhyay, J.Murata, S.Nagamiya, Y.Nagata, J.L.Nagle, M.Naglis, M.I.Nagy, I.Nakagawa, Y.Nakamiya, T.Nakamura, K.Nakano, J.Newby, M.Nguyen, T.Niita, B.E.Norman, R.Nouicer, A.S.Nyanin, E.O'Brien, S.X.Oda, C.A.Ogilvie, H.Ohnishi, K.Okada, M.Oka, O.O.Omiwade, Y.Onuki, A.Oskarsson, M.Ouchida, K.Ozawa, R.Pak, D.Pal, A.P.T.Palounek, V.Pantuev, V.Papavassiliou, J.Park, W.J.Park, S.F.Pate, H.Pe, J.-C.Peng, H.Pereira, V.Peresedov, D.Yu.Peressounko, C.Pinkenburg, M.L.Purschke, A.K.Purwar, H.Qu, J.Rak, A.Rakotozafindrabe, I.Ravinovich, K.F.Read, S.Rembeczki, M.Reuter, K.Reygers, V.Riabov, Y.Riabov, D.Roach, G.Roche, S.D.Rolnick, A.Romana, M.Rosati, S.S.E.Rosendahl, P.Rosnet, P.Rukoyatkin, P.Ruzicka, V.L.Rykov, B.Sahmueller, N.Saito, T.Sakaguchi, S.Sakai, K.Sakashita, H.Sakata, V.Samsonov, S.Sato, T.Sato, S.Sawada, K.Sedgwick, J.Seele, R.Seidl, A.Yu.Semenov, V.Semenov, R.Seto, D.Sharma, I.Shein, A.Shevvel, T.-A.Shibata, K.Shigaki, M.Shimomura, K.Shoji, P.Shukla, A.Sickles, C.L.Silva, D.Silvermyr, C.Silvestre, K.S.Sim, B.K.Singh, C.P.Singh, V.Singh, S.Skutnik, M.Slunecka, A.Soldatov, R.A.Soltz, W.E.Sondheim, S.P.Sorensen, I.V.Sourikova, F.Staley, P.W.Stankus, E.Stenlund, M.Stepanov, A.Ster, S.P.Stoll, T.Sugitate, C.Suire, A.Sukhanov, J.Sziklai, T.Tabaru, S.Takagi, E.M.Takagui, A.Taketani, R.Tanabe, Y.Tanaka, K.Tanida, M.J.Tannenbaum, A.Taranenko, P.Tarjan, H.Themann, T.L.Thomas, M.Togawa, A.Toia, J.Tojo, L.Tomasek, Y.Tomita, H.Torii, R.S.Towell, V-N.Tram, I.Tserruya, Y.Tsuchimoto, C.Vale, H.Valle, H.W.va.Hecke, A.Veicht, J.Velkovska, R.Vertesi, A.A.Vinogradov, M.Virius, V.Vrba, E.Vznuzdaev, M.Wagner, D.Walker, X.R.Wang, Y.Watanabe, F.Wei, J.Wessels, S.N.White, D.Winter, C.L.Woody, M.Wysocki, W.Xie, Y.L.Yamaguchi, K.Yamaura, R.Yang, A.Yanovich, Z.Yasin, J.Ying, S.Yokkaichi, G.R.Young, I.Younus, I.E.Yushmanov, W.A.Zajc, O.Zaudtke, C.Zhang, S.Zhou, J.Zimanyi, L.Zolin

共著者リスト 2

A.Adare, S.Afanasiev, C.Aidala, N.N.Ajitanand, Y.Akiba, H.Al-Bataineh, J.Alexander, A.Al-Jamel, A.Angerami, K.Aoki, N.Apadula, L.Aphecetche, Y.Aramaki, R.Armendariz, S.H.Aronson, J.Asai, E.TAtomssa, R.Averbeck, T.C.Awes, B.Azmoun, V.Babintsev, M.Bai, G.Baksay, L.Baksay, A.Baldisseri, K.N.Barish, P.D.Barnes, B.Bassalleck, A.T.Basye, S.Bathe, S.Batsouli, V.Baublis, F.Bauer, C.Baumann, A.Bazilevsky, S.Belikov, R.Belmont, R.Bennett, A.Berdnikov, Y.Berdnikov, J.H.Bhom, A.A.Bickley, M.T.Bjorndal, D.S.Blau, J.G.Boissevain, J.S.Bok, H.Borel, N.Borggren, K.Boyle, M.L.Brooks, D.S.Brown, D.Bucher, H.Buesching, V.Bumazhnov, G.Bunce, J.M.Burward-Hoy, S.Butsyk, S.Campbell, A.Caringi, J.-S.Chai, B.S.Chang, J.L.Charvet, C.H.Chen, S.Chernichenko, J.Chiba, C.Y.Chi, M.Chiu, I.J.Chi, J.B.Chi, R.K.Choudhury, P.Christiansen, T.Chujo, P.Chung, A.Churyn, O.Chvala, V.Cianciolo, Z.Citron, C.R.Cleven, Y.Cobigo, B.A.Cole, M.P.Comets, Z.Cones.de.Valle, M.Connors, P.Constantin, M.Csanad, T.Csorgo, T.Dahms, S.Dairaku, I.Danchev, K.Das, A.Datta, G.David, M.K.Dayananda, M.B.Deaton, K.Dehmelt, H.Delagrange, A.Denisov, D.d'Enterria, A.Deshpande, E.J.Desmond, K.V.Dharmawardane, O.Dietzsch, A.Dion, M.Donadelli, L.D'Orazio, J.L.Drachenberg, O.Drapier, A.Drees, K.A.Drees, A.K.Dubey, J.M.Durham, A.Durum, D.Dutta, V.Dzhordzhadze, S.Edwards, Y.V.Efremenko, J.Egdemir, F.Ellinghaus, W.S.Emam, T.Engelmore, A.Enokizono, H.En'yo, B.Espagnon, S.Esumi, K.O.Eyser, B.Fadem, D.E.Fields, M.Finge.Jr., M.Finger, F.Fleuret, S.L.Fokin, B.Forestier, Z.Fraenkel, J.E.Frantz, A.Franz, A.D.Frawley, K.Fujiwara, Y.Fukao, S.Y.Fung, T.Fusayasu, S.Gadrat, I.Garishvili, F.Gastineau, M.Germain, A.Glenn, H.Gong, M.Gonin, J.Gosset, Y.Goto, R.Granier.de.Cassagnac, N.Grau, S.V.Greene, G.Grim, M.Gross.Perdekamp, T.Gunji, H.-A.Gustafsson, T.Hachiya, A.Had.Henni, C.Haegemann, J.S.Haggerty, M.N.Hagiwara, K.I.Hahn, H.Hamagaki, J.Hamble, J.Hanks, R.Han, H.Harada, E.P.Hartouni, K.Haruna, M.Harvey, E.Haslum, K.Hasuko, R.Hayano, M.Heffner, T.K.Hemmick, T.Hester, J.M.Heuser, X.He, H.Hiejima, J.C.Hill, R.Hobbs, M.Hohlmann, M.Holmes, W.Holzmann, K.Homma, B.Hong, T.Horaguchi, D.Hornback, S.Huang, M.G.Hur, T.Ichihara, R.Ichimiya, H.Iinuma, Y.Ikeda, K.Imai, M.Inaba, Y.Inoue, D.Isenhower, L.Isenhower, M.Ishihara, T.Isobe, M.Issah, A.Isupov, D.Ivanischev, Y.Iwanaga, B.V.Jacak, J.Jia, X.Jiang, J.Jin, O.Jinnouchi, B.M.Johnson, T.Jones, K.S.Joo, D.Jouan, D.S.Jumper, F.Kajihara, S.Kametani, N.Kamihara, J.Kamin, M.Kaneta, J.H.Kang, H.Kanou, J.Kapustinsky, K.Karatsu, M.Kasai, T.Kawagishi, D.Kawall, M.Kawashima, A.V.Kazantsev, S.Kelly, T.Kempel, A.Khanzadeev, K.M.Kijima, J.Kikuchi, A.Kim, B.I.Kim, D.H.Kim, D.J.Kim, E.Kim, Y.-J.Kim, Y.-S.Kim, E.Kinney, A.Kiss, E.Kistenev, A.Kiyomichi, J.Klay, C.Klein-Boesing, L.Kochenda, V.Kochetkov, B.Komkov, M.Konno, J.Koster, D.Kotchetkov, D.Kotov, A.Kozlov, A.Kral, A.Kravitz, P.J.Kroon, J.Kubart, G.J.Kunde, N.Kurihara, K.Kurita, M.Kurosawa, M.J.Kweon, Y.Kwon, G.S.Kyle, R.Lacey, Y.S.Lai, J.G.Lajoie, A.Lebedev, Y.L.Borne, S.Leckey, D.M.Lee, J.Lee, K.B.Lee, K.S.Lee, M.K.Lee, T.Lee, M.J.Leitch, M.A.L.Leite, B.Lenzi, P.Lichtenwalner, P.Liebing, H.Lim, L.A.Linde.Levy, T.Liska, A.Litvinenko, H.Liu, M.X.Liu, X.Li, X.H.Li, B.Love, D.Lynch, C.F.Maguire, Y.I.Makdisi, A.Malakhov, M.D.Malik, V.I.Manko, E.Mannel, Y.Mao, L.Masek, H.Masui, F.Matathias, M.C.McCain, M.McCumber, P.L.McGaughey, N.Means, B.Meredith, Y.Miake, T.Mibe, A.C.Mignerey, P.Mikes, K.Miki, T.E.Miller, A.Milov, S.Mioduszewski, G.C.Mishra, M.Mishra, J.T.Mitchell, M.Mitrovski, A.K.Mohanty, H.J.Moon, Y.Morino, A.Morreale, D.P.Morrison, J.M.Moss, T.V.Moukhanova, D.Mukhopadhyay, T.Murakami, J.Murata, S.Nagamiya, Y.Nagata, J.L.Nagle, M.Naglis, M.I.Nagy, I.Nakagawa, Y.Nakamiya, K.R.Nakamura, T.Nakamura, K.Nakano, S.Nam, J.Newby, M.Nguyen, M.Nihashi, B.E.Norman, R.Nouicer, A.S.Nyanin, J.Nystrand, C.Oakley, E.O'Brien, S.X.Oda, C.A.Ogilvie, H.Ohnishi, I.D.Ojha, K.Okada, M.Oka, O.O.Omiwade, Y.Onuki, A.Oskarsson, I.Otterlund, M.Ouchida, K.Ozawa, R.Pak, D.Pal, A.P.T.Palounek, V.Pantuev, V.Papavassiliou, I.H.Park, J.Park, S.K.Park, W.J.Park, S.F.Pate, H.Pe, J.-C.Peng, H.Pereira, V.Peresedov, D.Yu.Peressounko, R.Petti, C.Pinkenburg, R.P.Pisani, M.Proissl, M.L.Purschke, A.K.Purwar, H.Qu, J.Rak, A.Rakotozafindrabe, I.Ravinovich, K.F.Read, S.Rembeczki, M.Reuter, K.Reygers, V.Riabov, Y.Riabov, E.Richardson, D.Roach, G.Roche, S.D.Rolnick, A.Romana, M.Rosati, C.A.Rosen, S.S.E.Rosendahl, P.Rosnet, P.Rukoyatkin, P.Ruzicka, V.L.Rykov, S.S.Ryu, B.Sahlmueller, N.Saito, T.Sakaguchi, S.Sakai, K.Sakashita, H.Sakata, V.Samsonov, S.Sano, H.D.Sato, S.Sato, T.Sato, S.Sawada, K.Sedgwick, J.Seele, R.Seidl, V.Semenov, R.Seto, D.Sharma, T.K.Shea, I.Shein, A.Shevvel, T.-A.Shibata, K.Shigaki, M.Shimomura, T.Shohjoh, K.Shoji, P.Shukla,

A.Sickles, C.L.Silva, D.Silvermyr, C.Silvestre, K.S.Sim, B.K.Singh, C.P.Singh, V.Singh, S.Skutnik, M.Slunecka, W.C.Smith, A.Soldatov, R.A.Soltz, W.E.Sondheim, S.P.Sorensen, I.V.Sourikova, F.Staley, P.W.Stankus, E.Stenlund, M.Stepanov, A.Ster, S.P.Stoll, T.Sugitate, C.Suire, A.Sukhanov, J.P.Sullivan, J.Sziklai, T.Tabaru, S.Takagi, E.M.Takagui, A.Taketani, R.Tanabe, K.H.Tanaka, Y.Tanaka, S.Taneja, K.Tanida, M.J.Tannenbaum, S.Tarafdar, A.Taranenko, P.Tarjan, H.Themann, D.Thomas, T.L.Thomas, M.Togawa, A.Toia, J.Tojo, L.Tomasek, H.Torii, R.S.Towell, V.-N.Tram, I.Tserruya, Y.Tsuchimoto, S.K.Tuli, H.Tydesjo, N.Tyurin, C.Vale, H.Valle, H.W.va.Hecke, E.Vazquez-Zambrano, A.Veicht, J.Velkovska, R.Vertesi, A.A.Vinogradov, M.Virius, V.Vrba, E.Vznuzdaev, M.Wagner, D.Walker, X.R.Wang, D.Watanabe, K.Watanabe, Y.Watanabe, F.Wei, J.Wessels, S.N.White, N.Willis, D.Winter, C.L.Woody, R.M.Wright, M.Wysocki, W.Xie, Y.L.Yamaguchi, K.Yamaura, R.Yang, A.Yanovich, Z.Yasin, J.Ying, S.Yokkaichi, G.R.Young, I.Younus, Z.You, I.E.Yushmanov, W.A.Zajc, O.Zaudtke, C.Zhang, S.Zhou, J.Zimanyi, L.Zolin

共著者リスト 3

A.Adare, S.Afanasiev, C.Aidala, N.N.Ajitanand, Y.Akiba, H.Al-Bataineh, J.Alexander, K.Aoki, L.Aphecetche, R.Armendariz, S.H.Aronson, J.Asai, E.TAtomssa, R.Averbeck, T.C.Awes, B.Azmoun, V.Babintsev, M.Bai, G.Baksay, L.Baksay, A.Baldisseri, K.N.Barish, P.D.Barnes, B.Bassalleck, A.T. Basye, S.Bathe, S.Batsouli, V.Baublis, C.Baumann, A.Bazilevsky, S.Belikov, R.Bennett, A.Berdnikov, Y.Berdnikov, A.A.Bickley, J.G.Boissevain, H.Borel, K.Boyle, M.L.Brooks, H.Buesching, V.Bumazhnov, G.Bunce, S.Butsyk, C.M.Camacho, S.Campbell, B.S.Chang, W.C.Chang, J.-L.Charvet, S.Chernichenko, J.Chiba, C.Y.Chi, M.Chiu, I.J.Chi, R.K.Choudhury, T.Chujo, P.Chung, A.Churyn, V.Cianciolo, Z.Citron, C.R.Cleven, B.A.Cole, M.P.Comets, P.Constantin, M.Csanad, T.Csorgo, T.Dahms, S.Dairaku, K.Das, G.David, M.B.Deaton, K.Dehmelt, H.Delagrange, A.Denisov, D.d'Enterria, A.Deshpande, E.J.Desmond, O.Dietzsch, A.Dion, M.Donadelli, O.Drapier, A.Drees, K.A.Drees, A.K.Dubey, A.Durum, D.Dutta, V.Dzhordzhadze, Y.V.Efremenko, J.Egdemir, F.Ellinghaus, W.S.Emam, T.Engelmore, A.Enokizono, H.En'yo, S.Esumi, K.O.Eyser, B.Fadem, D.E.Fields, M.Finge.Jr., M.Finger, F.Fleuret, S.L.Fokin, Z.Fraenkel, J.E.Frantz, A.Franz, A.D.Frawley, K.Fujiwara, Y.Fukao, T.Fusayasu, S.Gadrat, I.Garishvili, A.Glenn, H.Gong, M.Gonin, J.Gosset, Y.Goto, R.Granie.d.Cassagnac, N.Grau, S.V.Greene, M.Gross.Perdekamp, T.Gunji, H.-A.Gustafsson, T.Hachiya, A.Had.Henni, C.Haegemann, J.S.Haggerty, H.Hamagaki, R.Han, H.Harada, E.P. Hartouni, K.Haruna, E.Haslum, R.Hayano, M.Heffner, T.K.Hemmick, T.Hester, X.He, H.Hiejima, J.C. Hill, R.Hobbs, M.Hohlmann, W.Holzmann, K.Homma, B.Hong, T.Horaguchi, D.Hornback, S.Huang, T.Ichihara, R.Ichimiya, H.Iinuma, Y.Ikeda, K.Imai, J.Imrek, M.Inaba, Y.Inoue, D.Isenhower, L.Isenhower, M.Ishihara, T.Isobe, M.Issah, A.Isupov, D.Ivanischev, B.V.Jacak, J.Jia, J.Jin, O.Jinnouchi, B.M.Johnson, K.S.Joo, D.Jouan, F.Kajihara, S.Kametani, N.Kamihara, J.Kamin, M.Kaneta, J.H.Kang, H.Kanou, J.Kapustinsky, D.Kawall, A.V.Kazantsev, T.Kempel, A.Khanzadeev, K.M.Kijima, J.Kikuchi, B.I.Kim, D.H.Kim, D.J.Kim, E.Kim, S.H.Kim, E.Kinney, K.Kiriluk, A.Kiss, E.Kistenev, A.Kiyomichi, J.Klay, C.Klein-Boesing, L.Kochenda, V.Kochetkov, B.Komkov, M.Konno, J.Koster, D.Kotchetkov, A.Kozlov, A.Kral, A.Kravitz, J.Kubart, G.J.Kunde, N.Kurihara, K.Kurita, M.Kurosawa, M.J.Kweon, Y.Kwon, G.S.Kyle, R.Lacey, Y.S.Lai, J.G.Lajoie, D.Layton, A.Lebedev, D.M.Lee, K.B.Lee, M.K.Lee, T.Lee, M.J.Leitch, M.A.L.Leite, B.Lenzi, P.Liebing, T.Liska, A.Litvinenko, H.Liu, M.X.Liu, X.Li, B.Love, D.Lynch, C.F.Maguire, Y.I.Makdisi, A.Malakhov, M.D.Malik, V.I.Manko, E.Mannel, Y.Mao, L.Masek, H.Masui, F.Matathias, M.McCumber, P.L. McGaughey, N.Means, B.Meredith, Y.Miake, P.Mikes, K.Miki, T.E.Miller, A.Milov, S.Mioduszewski, M.Mishra, J.T.Mitchell, M.Mitrovski, A.K.Mohanty, Y.Morino, A.Morreale, D.P.Morrison, T.V.Moukhanova, D.Mukhopadhyay, J.Murata, S.Nagamiya, Y.Nagata, J.L.Nagle, M.Naglis, M.I.Nagy, I.Nakagawa, Y.Nakamiya, T.Nakamura, K.Nakano, J.Newby, M.Nguyen, T.Niita, B.E.Norman, R.Nouicer, A.S. Nyanin, E.O'Brien, S.X.Oda, C.A.Ogilvie, H.Ohnishi, K.Okada, M.Oka, O.O.Omiwade, Y.Onuki, A.Oskarsson, M.Ouchida, K.Ozawa, R.Pak, D.Pal, A.P.T.Palounek, V.Pantuev, V.Papavassiliou, J.Park, W.J.Park, S.F.Pate, H.Pei, J.-C.Peng, H.Pereira, V.Peresedov, D.Yu.Peressounko, C.Pinkenburg, M.L. Purschke, A.K.Purwar, H.Qu, J.Rak, A.Rakotozafindrabe, I.Ravinovich, K.F.Read, S.Rembeczki, M.Reuter, K.Reygers, V.Riabov, Y.Riabov, D.Roach, G.Roche, S.D.Rolnick, A.Romana, M.Rosati, S.S. E.Rosendahl, P.Rosnet, P.Rukoyatkin, P.Ruzicka, V.L.Rykov, B.Sahlueller, N.Saito, T.Sakaguchi, S.Sakai, K.Sakashita, H.Sakata, V.Samsonov, S.Sato, T.Sato, S.Sawada, K.Sedgwick, J.Seele, R.Seidl, A.Yu.Semenov, V.Semenov, R.Seto, D.Sharma, I.Shein, A.Shevle, T.-A.Shibata, K.Shigaki, M.Shimomura, K.Shoji, P.Shukla, A.Sickles, C.L.Silva, D.Silvermyr, C.Silvestre, K.S.Sim, B.K. Singh, C.P.Singh, V.Singh, S.Skutnik, M.Slunecka, A.Soldatov, R.A.Soltz, W.E.Sondheim, S.P.Sorensen, I.V.Sourikova, F.Staley, P.W.Stankus, E.Stenlund, M.Stepanov, A.Ster, S.P.Stoll, T.Sugitate, C.Suire, A.Sukhanov, J.Sziklai, T.Tabaru, S.Takagi, E.M.Takagui, A.Taketani, R.Tanabe, Y.Tanaka, K.Tanida, M.J.Tannenbaum, A.Taranenko, P.Tarjan, H.Themann, T.L.Thomas, M.Togawa, A.Toia, J.Tojo, L.Tomasek, Y.Tomita, H.Torii, R.S.Towell, V-N.Tram, I.Tserruya, Y.Tsuchimoto, C.Vale, H.Valle, H.W.va.Hecke, A.Veicht, J.Velkovska, R.Vertesi, A.A.Vinogradov, M.Virius, V.Vrba, E. Vznuzdaev, M.Wagner, D.Walker, X.R.Wang, Y.Watanabe, F.Wei, J.Wessels, S.N.White, D.Winter, C.L.Woody, M.Wysocki, W.Xie, Y.L.Yamaguchi, K.Yamaura, R.Yang, A.Yanovich, Z.Yasin, J.Ying, S.Yokkaichi, G.R.Young, I.Younus, I.E.Yushmanov, W.A.Zajc, O.Zaudtke, C.Zhang, S.Zhou, J.Zimanyi, L.Zolin

主論文

First measurement of ω and ϕ mesons
via di-electron decay channels
in proton+proton collisions at $\sqrt{s} = 200$ GeV

Kotaro M. Kijima

Department of Physical Science, Graduate School of Science
Hiroshima University
Kagamiyama 1-3-1, Higashi-Hiroshima, 739-8526, Japan

January 2012

Abstract

The work in this thesis is to study ω and ϕ meson production in $p+p$ collisions at $\sqrt{s} = 200$ GeV measured via di-electron decay channels using the PHENIX detector at RHIC in Year 2004/2005.

We have measured spectra of differential cross sections of ω and ϕ mesons as a function of transverse momentum in the range of $0 < p_T < 4$ GeV/ c . The ω and ϕ were identified from invariant mass spectra reconstructed by electron and positron pairs extracted from large background of hadrons. The yield of ω and ϕ were statistically subtracted from large amount of background which comes from combinatorial pairs mainly due to π^0 Dalitz decay, photon conversion and other hadron decays. After applying corrections for the PHENIX detector acceptance, electron identification efficiency, trigger efficiency obtained by simulation studies based on GEANT, the cross sections of ω and ϕ meson were obtained.

First measurements of ω and ϕ meson obtained by di-electron decay channel in $p+p$ collisions at $\sqrt{s} = 200$ GeV extend the p_T coverage to zero and allows direct calculation of the total cross sections $d\sigma^\omega/dy = 4.19 \pm 0.33^{stat.} \pm 0.33^{sys.}$ mb and $d\sigma^\phi/dy = 0.431 \pm 0.031^{stat.} \pm 0.028^{sys.}$ mb in the mid-rapidity. The spectra of differential cross sections of ω and ϕ mesons consists an exponential function at low p_T and a power function at high p_T . The Tsallis distribution including both of exponential and power law described the spectra over the wide p_T range obtained by both of di-electron decay channel and hadronic decay channels. The measured spectra of ω and ϕ mesons were in a good agreement with result of an event generator PYTHIA based on perturbative Quantum ChromoDynamics(pQCD) calculation. The various meson spectra ($\pi^+ + \pi^-$)/2, π^0 , ($K^+ + K^-$)/2, K_s^0 , η , ω , ϕ and J/ψ in $p+p$ collisions at $\sqrt{s} = 200$ GeV measured by PHENIX described by Tsallis distribution. The global picture of m_T scaling worked also for these various mesons even quite wide m_T ranges in $p+p$ collisions at $\sqrt{s} = 200$ GeV as well as at previous experiment in $p+p$ and $p+\bar{p}$. Thesis scaling results suggested a similar production mechanism of mesons in $p+p$ collisions at $\sqrt{s} = 200$ GeV.

Due to the chiral symmetry restoration in the hot matter created by the

high energy heavy ions collisions at RHIC, the observation of mass modification of ω and ϕ mesons are expected. On the other hand, the mass modification is not expected in case of $p+p$ collisions, since the matter created by $p+p$ collisions should be much smaller than the life time of these mesons. It is essentially needed to quantitatively evaluate the mass spectra of ω and ϕ mesons in $p+p$ collisions as solid the baseline since attempting observation of mass modification in heavy ion collisions is challenging due to the huge background. By using the model of this analysis for evaluating mass modification in $p+p$ collisions, two parameters corresponding to the ratio of mass shift Δ and the fraction of modified meson yield R were estimated, and the best value were $\Delta = -3.3^{+2.4}_{-3.8}\%$, $R = 7.5^{+4.9}_{-4.9}\%$ for ω meson and $\Delta = -1.2^{+0.9}_{-0.8}\%$, $R = 9.7^{+8.0}_{-8.0}\%$ for ϕ meson. The results for ω and ϕ mesons are consistent with assumption that no mass shift was observed in $p+p$ collisions within 1.4σ , respectively.

Our results for ω and ϕ meson production in $p+p$ collisions provided a crucial data as a solid baseline to understand physics of heavy ion interactions.

Contents

1	Introduction	15
1.1	Quantum ChromoDynamics	15
1.2	pQCD in Hadron Collision	18
1.3	QCD phase transition	22
1.3.1	Quark Gluon Plasma	22
1.3.2	Chiral Symmetry breaking and restoration	25
1.3.3	Low mass vector meson	27
1.4	Motivation and scopes of this thesis	29
2	Experimental Setup	31
2.1	Relativistic Heavy Ion Collider (RHIC)	31
2.2	the PHENIX Detector	34
2.2.1	Beam Beam Counters (BBC)	34
2.2.2	Zero Degree Counters (ZDC)	37
2.2.3	PHENIX tracking system	37
2.2.4	Ring Image Cherenkov Counters (RICH)	44
2.2.5	Electro Magnetic Calorimeter (EMC)	44
2.3	Data Acquisition system (DAQ)	47
2.4	Event trigger	49
3	Analysis	53
3.1	Outline of Analysis	53
3.2	Run and Trigger Selection	53
3.3	Track Selection and electron identification (eID)	56
3.3.1	Number of Hit PMT (n0)	56
3.3.2	RHIC match	56
3.3.3	EMC match	57
3.3.4	deposition energy over momentum ratio (dep)	58
3.4	Fiducial cut	59
3.5	Pair reconstruction	62
3.6	Background subtraction	62

3.6.1	Fake electron pairs	63
3.6.2	Photon conversion	64
3.6.3	Combinatorial background	66
3.6.4	continuum contribution	69
3.7	Signal Extraction	71
3.7.1	Spectral Shape of Resonances	71
3.7.2	Signal extraction	73
3.8	Monte Carlo simulation	77
3.8.1	Reconstruction efficiency	77
3.8.2	ERT trigger efficiency	82
3.9	Invariant differential cross section	84
3.10	Systematic Uncertainty	87
3.10.1	Total systematic error	87
4	Results and Discussions	89
4.1	Spectra of the invariant cross sections	89
4.2	Integrated cross sections	91
4.3	particle ratio of ω and ϕ to π	98
4.4	Scaling properties	98
4.5	Mass line shape analysis	105
5	Summary and Conclusions	111

List of Figures

1.1	Summary of the value of α_s as a function of the respective energy scale Q [48].	17
1.2	Parton Distribution Function as a function of x at $Q = 5\text{GeV}$ [3].	20
1.3	The fragmentation function for all charged particles as a function of x for different \sqrt{s} in e^+e^- collisions [48].	21
1.4	The phase diagram of QCD in Temperature T and baryon-chemical potential μ_B plane [34].	22
1.5	Nuclear modification factor R_{AA} for π^0 as a function of p_T for minimum bias and five centrality classes in Au + Au collisions in $\sqrt{s_{NN}} = 200$ GeV [36]. Error bars are statistical and p_T uncorrelated errors, boxes around the points indicate p_T correlated errors. Single box around $R_{AA} = 1$ on the left is the error due to N_{coll} , whereas the single box on the right is the overall normalization error of the $p + p$ reference spectrum.	24
1.6	Potential of a) QCD vacuum in $T > T_c$. b) QCD vacuum in $T < T_c$	26
1.7	Temperature and density dependence of quark condensate $\langle \bar{q}q \rangle$ [52]	27
2.1	Overview of Brookhaven National Laboratory accelerator complex, consisting of LINAC, booster, AGS and RHIC [70]	32
2.2	The PHENIX Detector configuration [88] The upper panel shows the beam view. Two central arms and central magnet can be seen. The bottom panel shows side view. Two muon arms and muon magnet can be seen.	35
2.3	the PHENIX global coordinate system.	36
2.4	Left) BBC arrays consisting 64 elements. Right) One of the BBC elements consisting quartz Čherenkov radiator and mesh-dynode type PMT.	36
2.5	schematic view of the ZDC location including deflection of protons and charged fragments [74]	38

2.6	Left) overview of the PHENIX Magnets. The line shows the contour of the magnetic. Right) total magnetic field strength as a function of R at the $\theta=0$ symmetry plane of the Central Magnet for +(outer), ++(Outer+Inner), and +- (Outer-Inner) configuration	39
2.7	The layout of wire position of DC. The X1 and X2 wire cells runs in parallel to the beam to perform precise track measurements in $r\phi$. U1, V1, U2, V2 wires have stereo angle of about 6° relative to the X wires and measure the z coordination of track [78].	40
2.8	the pad and pixel geometry(left), A cell defined by three pixels is at the center of the right picture [78].	41
2.9	Illustration of the track reconstruction in the PHENIX up to PC1 on $x-y$ plane and $r-z$ plane.	42
2.10	A cut through view of RICH detector	45
2.11	Interior view of a lead-scintillator calorimeter module	46
2.12	Exploded view of a lead-glass detector supermodule	46
2.13	block diagram of DAQ [88]	48
2.14	Integrated luminosity as a function of date for 200GeV $p+p$ collisions collected by PHENIX in year2004/2005.	50
2.15	schematic view of EMCAL RICH level1 Trigger: Both the super-Module of EMCAL and RICH are fired for e^+, e^- . Only the EMCAL is fired for photon, while only the RICH is fired for high p_T pion. We are able to effectively collect the events including e^+e^- pair.	51
3.1	Collision vertex distribution. The events in yellow band range are selected for this analysis.	54
3.2	number of electrons per events as a function of collision vertex.	54
3.3	Number of electron in $0.3 < p_T < 4.0 \text{ GeV}/c$ per sampled Minimum Bias triggered event as a function of run number.	55
3.4	Number of electron detected in EAST (top) and WEST (bottom) arms per sampled Minimum Bias triggered event.	55
3.5	$N_{ERT\&\&MB}^{ERT} / N_{ERT\&\&MB}^{MB}$ as a function of run number. This ratio should be unity when there is no file segment lost at data reconstruction.	56
3.6	Schematic description of the definitions of variable which characterized the RICH ring. The five fit PMTs are shown as an example.	57
3.7	Track quality distribution.	58
3.8	(distribution of n_0 (left) and <i>RICH matching</i> (right)).	58

3.9	distribution of <i>EMCal matching</i> for σ_ϕ (left) and σ_z (right)	59
3.10	(left) E/p distribution in minimum bias event for all charged tracks, for electron candidates and for randomly associated hadrons .(right) dep distribution applying $n0 > 0$	59
3.11	Alpha vs board distribution for both sides of the DC East and West after applying the fiducial cuts	60
3.12	Occupancy of EMCal sectors after applying the fiducial cuts	61
3.13	$\Delta\phi$ and Δz distribution for pairs of the tracks in DC. The box represents the cut for removed fake pairs in DC.	63
3.14	The distribution for $PFOA$ and $\Delta RICH$. The detail is in the sentence. The box represents the cut for removed fake pairs for ring sharing tracks.	64
3.15	Φ_V distribution in the mass range $30 < m_{ee} < 90 MeV/c^2$. blue line show the Φ_V distribution reconstructed in event mixing which normalized arbitrary range. Vertical red line on $0.035\pi[rad]$ indicates cut value in this mass region	65
3.16	Schematic view of conversion pair. The electrons produced at $R > 0$ are reconstructed with incorrect momentum.	65
3.17	Invariant mass distribution for all e^+e^- pairs. The filled yellow histogram shows the ghost pairs. The filled blue histogram shows the pairs removed by the phiV angle cut.	66
3.18	like-sign pairs distribution as a function of mass and pair p_T after subtraction of mixed event background. The background is normalized in the normalization area A shown as the dashed area.	68
3.19	invariant e^+e^- mass spectrum. The blue line indicate combinatorial background evaluated by the event mixing method.	69
3.20	Invariant mass spectra divided by pT bins. The blue line indicate combinatorial background evaluated by the event mixing method.	70
3.21	Diagrams for final state radiation [90]. The decay into $e^+e^-\gamma$ is described by (a). The infrared divergence in the decay is canceled by interference with the diagrams in (b).	72
3.22	e^+e^- mass spectrum in the radiative decay $\phi \rightarrow e^+e^-\gamma$ for $E_{min} = 10 MeV$ (orange) smeared with $10 MeV$ (red).	73
3.23	Invariant mass spectra divided by pT bins after background subtraction. The black line are the fitting result, which is sum of the known decays, ω (left magenta line), ϕ (right magenta line), ρ (light blue line), radiative decay of ω and ϕ (orange line) and BG(blue line).	75

3.24 Raw counts in counting range for ω (left) and ϕ (right) mesons as a function of p_T . The black lines show all contributions, the magenta points show ω (left) and ϕ (right) mesons including statistical errors, green line lines show combinatorial background, the light blue lines show ρ mesons, and blue lines show exponential+polynomial as contribution of other hadron continuum.	76
3.25 The PHENIX central arm detectors represented in GEANT simulation	77
3.26 Left panel) RICH n0. Right panel) RICH displacement.	78
3.27 Left panel) EMC match for ϕ direction. Middle panel) EMC match for z direction. Right panel) Energy over momentum ratio normalized that width : dep direction.	78
3.28 Comparison of Drift Chamber hit distribution for ϕ direction in the real data(red) and simulation data(blue). The p_T range of the electron is $0.3 < p_T < 4.0 \text{GeV}/c$ for both real and simulation data.	79
3.29 Comparison of PC1 hit distribution for z direction in the real data(red) and simulation data(blue). The p_T range of the electron is $0.3 < p_T < 4.0 \text{GeV}/c$ for both real and simulation data.	80
3.30 Left panel) The invariant mass spectra for ω meson reconstructed e^+e^- in simulation for the $1.0 \leq p_T < 1.25 \text{ GeV}/c$. The solid line shows Gaussian convoluted relativistic Breit-Winger function. Right panel) p_T dependent detector mass resolution.	81
3.31 Left panel) The invariant mass spectra for ϕ meson reconstructed e^+e^- in simulation for the $1.0 \leq p_T < 1.25 \text{ GeV}/c$. The solid line shows Gaussian convoluted relativistic Breit-Winger function. Right panel) p_T dependent detector mass resolution.	81
3.32 Reconstruction efficiency for ω and ϕ mesons ϵ_{pair}^{reco} as a function of p_T	82
3.33 (left) The p_T distribution for single electron in MB(black) and fired ERT(red). (right) Trigger efficiency for single electrons ϵ_{single}^{ERT} as a function of p_T	83
3.34 Trigger efficiency for ω (blue) and ϕ (red) mesons ϵ_{pair}^{ERT} as a function of p_T	84
3.35 Bin shift correction for ω . Blue point and line shows before correction, and red point shows after correction.	86

3.36 Bin shift correction for ϕ . Blue point and line shows before correction, and red point shows after correction.	86
4.1 Invariant cross section of ω and ϕ production in $p + p$ collision at $\sqrt{s} = 200\text{GeV}$ measured in $\omega \rightarrow e^+e^-$ and $\phi \rightarrow e^+e^-$ decay channels as a function of p_T . Bars and boxes represent statistical and systematic errors, respectively.	90
4.2 (Top)The invariant cross section of ω production in $p + p$ collision at $\sqrt{s} = 200\text{GeV}$ measured in $\omega \rightarrow e^+e^-$, $\pi^0\pi^+\pi^-$ and $\pi^0\gamma$ decay channels. The curves show Levy(red), modified Power-law(Green) and Exponential(black) fit to the data measured in both dilepton and hadronic decay modes. (Bottom)Ratio of the data and Levy fit.	92
4.3 Invariant cross section of ϕ production in $p + p$ collision at $\sqrt{s} = 200\text{GeV}$ measured in $\phi \rightarrow e^+e^-$, K^+K^- decay channels. The curves show Levy(red), modified Power-law(Green) and Exponential(black) fit to the data measured in both dilepton and hadronic decay modes. (Bottom)Ratio of the data and Levy fit.	93
4.4 The invariant cross section of ω production in $p + p$ collision at $\sqrt{s} = 200\text{GeV}$ compared with PYTHIA version 6.421 with Tune A.	94
4.5 Invariant cross section of ϕ production in $p + p$ collision at $\sqrt{s} = 200\text{GeV}$ compare with PYTHIA version 6.421 with Tune A.	95
4.6 Ratio of cross section, σ_ω/σ_π (square) and σ_ϕ/σ_π (circle), measured for $p + p$ data as a function of center-of-mass energy.	96
4.7 Measured ω/π^0 as a function of p_T in $p+p$ collisions at $\sqrt{s} = 200\text{GeV}$. Straight lines show fits to a constant for $2 < p_T < 3\text{GeV}/c$	100
4.8 Measured ϕ/π^0 as a function of p_T in $p+p$ collisions at $\sqrt{s} = 200\text{GeV}$. Straight lines show fits to a constant for $3 < p_T < 7\text{GeV}/c$	100
4.9 Spectra of invariant differential cross section as a function of p_T for $(\pi^+ + \pi^-)/2$, π^0 , $(K^+ + K^-)/2$, K_s^0 , η , ω , ϕ and J/ψ in $p + p$ collision at $\sqrt{s} = 200\text{GeV}$ at mid-rapidity.	101
4.10 Scaled spectra of invariant differential cross section as a function of p_T for $(\pi^+ + \pi^-)/2$, π^0 , $(K^+ + K^-)/2$, K_s^0 , η , ω , ϕ and J/ψ in $p+p$ collision at $\sqrt{s} = 200\text{GeV}$ at mid-rapidity. Solid line expressed pure power law function fitted in $5.0 < p_T < 20\text{GeV}/c$	102

4.11 (top) m_T spectra for $(\pi^+ + \pi^-)/2, \pi^0, (K^+ + K^-)/2, K_s^0, \eta, \omega, \phi$ and J/ψ in $p + p$ collision at $\sqrt{s} = 200\text{GeV}$ at mid-rapidity.	103
(Bottom) The ratio of the spectra to Levy fit to π . Bars show uncertainties combined with statistical and systematic errors.	
4.12 Scaled m_T spectra for $(\pi^+ + \pi^-)/2, \pi^0, (K^+ + K^-)/2, K_s^0, \eta, \omega, \phi$ and J/ψ in $p + p$ collision at $\sqrt{s} = 200\text{GeV}$ at mid-rapidity.	104
4.13 Schematic representation of the model to evaluate mass spectra with mass shift. The shapes of $f(m_{ee})$ and $f'(m_{ee})$ represent the measured spectra of vector meson decaying outside and inside medium, respectively.	106
4.14 Invariant mass distribution with fitting results for ω mesons for three p_T bins corresponding to the weighted average of $\langle\beta\gamma\rangle = 1.01, 2.04, 4.85$. Blue line shows $F(m_{ee})$, magenta and light blue line correspond to f and f' , respectively. The dash line shows the fit result with $\Delta = 0$ and $R = 0$. The green line shows ρ meson contribution.	107
4.15 a) and b) show χ^2 distribution as a function of $(1+\Delta)$ and R for ω meson, respectively. The red points are best fit value.	108
4.16 χ^2 distribution in 2-dimensional space for $(1 + \Delta)$ and R for ω meson. The red point is best fit value and the bars are statistical errors corresponding to $\Delta\chi^2 = +1$	108
4.17 Invariant mass distribution with fitting results for ω mesons for three p_T bins corresponding to weighted average of $\langle\beta\gamma\rangle = 0.74, 1.82, 3.68$. Blue line shows $F(m_{ee})$, magenta and light blue line correspond to f and f' , respectively. The dash line shows the fit result with $\Delta = 0$ and $R = 0$. The green line shows ρ meson contribution.	109
4.18 a) and b) show χ^2 distribution as a function of $(1 + \Delta)$ and R for ϕ meson, respectively. The red points are best fit value.	110
4.19 χ^2 distribution in 2-dimensional space for $(1 + \Delta)$ and R for ϕ meson. The red point is best fit value and the bars are statistical errors corresponding to $\Delta\chi^2 = +1$	110

List of Tables

1.1	Summary of up, down, strange quarks. [48]	16
1.2	Summary of charm, bottom, top [48]	16
1.3	Summary of gauge bosons [48]	16
1.4	Suggested qq quark-model assignment for some of the observed light mesons. [48]	18
2.1	summary of the RHIC operation. The integrated luminosity is recorded in PHENIX.	33
2.2	Summary of the track quality	44
2.3	Summary of parameters of two type of PHENIX EMCal . . .	45
3.1	Electron ID cuts used in this analysis.	60
3.2	The pole masses and natural decay widths of the vector mesons taken from the PDG [48]	71
3.3	Total systematic error for ω meson	88
3.4	Total systematic error for ϕ meson	88
4.1	Summary of fitting parameters	97

Chapter 1

Introduction

1.1 Quantum ChromoDynamics

Quantum Chromodynamics (QCD) is the gage field theory which describes the strong interaction of colored quarks and gluons. A quark have a specific flavor as shown Table.1.1 and Table.1.2 and one color of three, red, green and blue. The gluon have a color of the eight. The hadons are color-singlet combinations of quarks and anti-quarks, and gluons. The classical QCD Lagrangian describing the interaction of quarks and gluons is

$$L_{QCD} = -\frac{1}{4}F_{\mu\nu}^a F_a^{\mu\nu} + \bar{q}(i\gamma^\mu D_\mu - \mathbf{M})q \quad (1.1)$$

The D_μ is a covariant derivative defined as

$$D_\mu \equiv \partial_\mu + ig_s t^a A_\mu^a \quad (1.2)$$

The $F_{\mu\nu}^a$ is the field tensors of the gluon given by

$$F_{\mu\nu}^a = \partial_\mu A_\nu^a - \partial_\nu A_\mu^a - g_s f_{abc} A_\mu^b A_\nu^c \quad (1.3)$$

where Ψ_q corresponds the field of the each quarks of colors and flavors, the A_μ^a corresponds the gluon gauge field, g_s is the QCD coupling constant, γ^μ are Dirac matrices defined as, $\gamma^\mu \gamma^\nu + \gamma^\nu \gamma^\mu = 2g^{\mu\nu}$, and f_{abc} is the structure constant of the SU(3). The \mathbf{M} represents the diagonal matrix of “ current quark masses” as shown Table.1.1.

Asymptotic freedom and confinement

The QCD successfully describes the strong interaction, which is characterized by the two specific feature. One is the asymptotic freedom and the other is the the confinement.

	u	d	s
Q -electric charge	$+\frac{2}{3}$	$-\frac{1}{3}$	$-\frac{1}{3}$
J -spin	$\frac{1}{2}$	$\frac{1}{2}$	$\frac{1}{2}$
I_z -isospin	$+\frac{1}{2}$	$-\frac{1}{2}$	0
S -strangeness	0	0	-1
C -charm	0	0	0
B -bottomness	0	0	0
T -topness	0	0	0
mass [MeV/ c^2]	1.5-3.0	3.0-7.0	95±25

Table 1.1: Summary of up, down, strange quarks. [48]

	c	b	t
Q -electric charge	$+\frac{2}{3}$	$-\frac{1}{3}$	$+\frac{2}{3}$
J -spin	$\frac{1}{2}$	$\frac{1}{2}$	$\frac{1}{2}$
I_z -isospin	0	0	0
S -strangeness	0	0	0
C -charm	+1	0	0
B -bottomness	0	-1	0
T -topness	0	0	+1
mass [GeV/ c^2]	1.25±0.09	4.20±0.07	174.2±3.3

Table 1.2: Summary of charm, bottom, top [48]

	γ	W^+	W^-	Z	g
Q -electric charge	0	+1	-1	0	0
J -spin	1	1	1	1	1
mass [GeV/ c^2]	0	80.39	80.29	91.18	0
relative strength	10^{-2}		10^{-13}		1

Table 1.3: Summary of gauge bosons [48]

The running coupling constant $g(\mu)$ is defined as an effective coupling strength among quarks and gluons at the energy scale μ . The effective cou-

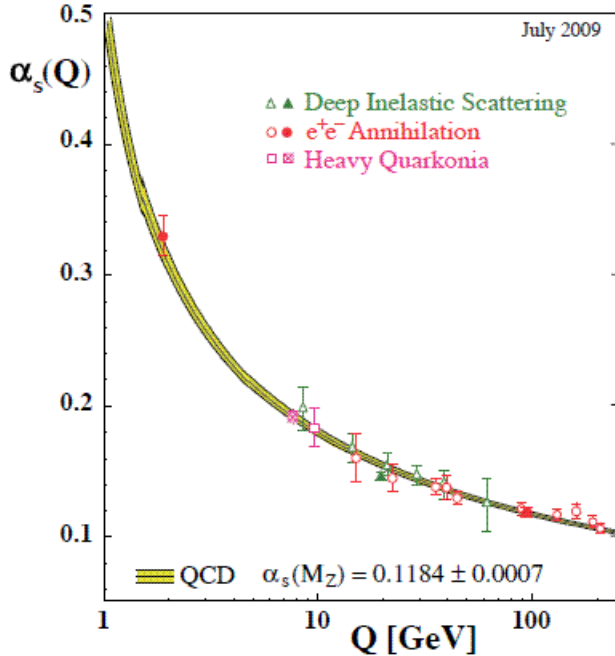


Figure 1.1: Summary of the value of α_s as a function of the respective energy scale Q [48].

pling constant $\alpha_s(\mu)$ is expressed as follows

$$\alpha_s(\mu) \equiv \frac{g(\mu)^2}{4\pi} \quad (1.4)$$

$$\simeq \frac{1}{4\pi\beta_0 \ln(\mu/\Lambda_{QCD}^2)} \left(1 - \frac{\beta_1}{\beta_0^2} \frac{\ln[\ln(\mu^2/\Lambda_{QCD}^2)]}{\ln(\mu^2/\Lambda_{QCD}^2)} \right) \quad (1.5)$$

where $\beta_0 = (11 - \frac{2}{3}N_f)/(4\pi)^2$, $\beta_1 = (102 - \frac{38}{3}N_f)/(4\pi)^4$, N_f is the number of flavors, and Λ_{QCD} is called the QCD scale parameter. The running coupling constant α_s determined by data from several experiments is shown in Fig.1.1.

Fig.1.1 and Eq.1.5 tell us that the running coupling constant α_s decreases logarithmically as μ increase. This means that for short distance the strength of strong interaction is relatively weak unlike Quantum Electro-Dynamics(QED). This property of the interaction at short distance is called "asymptotic freedom". Due to the small α_s at large mu , perturbative Quantum ChiromoDynamics(pQCD) calculation are possible and it can describe the hadron-hadron interaction as shown Section 1.2.

On the other hand, Fig.1.1 and Eq.1.5 indicate that the running coupling constant increase and become strong at low energy, $\mu \sim \Lambda_{QCD} \sim 200\text{MeV}$. This is the typical energy scale as confinement of quarks and gluons and the dynamical symmetry breaking as shown in Section 1.3.2. Then, the perturbative approach is not applicable. As a consequence of confinement, isolated color has never been observed experimentally, which indicates that the quarks and gluons are always bound together to form color-white as hadrons. For example, the suggested $q\bar{q}$ quark-model assignments for some of the observed light mesons are shown in Table.1.4. If the orbital angular momentum of the $q\bar{q}$ state is l , then the parity P is $(-1)^{l+1}$. The meson spin J is given by the relation $|l - s| < J < |l + s|$ where s is 0 or 1 corresponding to antiparallel quark spin or parallel quark spin, respectively. The charge conjugation C is $(-1)^{l+s}$.

J^{PC}	I=1 $u\bar{d}, \bar{u}d, \frac{1}{\sqrt{2}}(d\bar{d} - u\bar{u})$	I=1/2 $u\bar{s}, d\bar{s}; \bar{d}s, -\bar{u}s$	I=0 f'	I=0 f
0^{-+}	π	K	η	$\eta'(958)$
1^{--}	$\rho(770)$	$K^*(892)$	$\phi(1020)$	$\omega(782)$
0^{++}	$a_0(1450)$	$K_0^*(1430)$	$f_0(1710)$	$f_0(1370)$
1^{++}	$a_1(1260)$	K_{1A}^*	$f_1(1420)$	$f_1(1285)$

Table 1.4: Suggested qq quark-model assignment for some of the observed light mesons. [48]

1.2 pQCD in Hadron Collision

Many experimental data of hadron production in $p+p$ and $p+\bar{p}$ collisions are existing [4–15]. In the parton model, the hard scattering process of the two hadrons at high energy is represented as the interaction of the quarks and gluons which are the constituents of intial hadrons. For example, the cross section of the hadron production for a hard scattering process in $p+p$ collision can be expressed as follows,

$$\begin{aligned} \sigma^{pp \rightarrow hX} = & \sum_{f_1, f_2, f} \int dx_1 dx_2 dz \cdot f_1^p(x_1, \mu^2) \cdot f_2^p(x_2, \mu^2) \\ & \times \sigma^{f_1 f_2 \rightarrow fX}(x_1 p_1, x_2 p_2, p_h, \mu) \times D_f^h(z, \mu^2) \end{aligned} \quad (1.6)$$

where μ is the factorization scale, f_1, f_2, f represent parton, $f_1^p(x_1, \mu)$ is parton distribution function(PDF) of parton in incoming 1st proton, $f_2^p(x_2, \mu)$ is parton distribution function(PDF) of parton in incoming 2nd proton, $D_f^h(z_h, \mu^2)$ is fragmentation function (FF) from parton f to final state hadron h , p_1 and p_2 are the momentum of initial protons, x is the momentum fraction of the initial parton in initial proton, z is the momentum fraction of the final state hadron in the final parton.

The picture of the parton model as shown in Eq.1.6 is represented by the convolution of the tree parts; one is a parton distribution function f_i^p which represents probability for finding a type of parton in the proton, another is a parton-parton scattering cross section $\sigma^{f_1 f_2 \rightarrow f X}$, the other is a fragmentation function D_f^h which represents the hadronization mechanism. It is difficult to calculate the parton distribution function and the fragmentation function by the first principles in QCD at present. On the other hand, the parton-parton scattering cross section $\sigma^{f_1 f_2 \rightarrow f X}$ can be calculated by pQCD.

The cross section is required to satisfy in the following condition,

$$\mu \frac{\partial \sigma^{pp \rightarrow hX}}{\partial \mu} = 0 \quad (1.7)$$

because the cross section must be independent of the arbitrary scale μ . Although the optimization of the scale is discussed in several theoretical groups [56].

Parton Distribution Function(PDF)

The parton distribution function is the probability density for finding a type of parton in the proton. The proton structure function $F_2(x, Q^2)$ is measured by lepton deep inelastic scattering (DIS) in many experiments: using electron-proton scattering at DESY, SLAC, and muon-proton scattering at FNAL. The ratio of \bar{d}/\bar{u} is extract from the ratio of lepton pair Drell-Yan production in $p + p$ and $p + d$ collisions measured by NA51 [53] and E866 [54]. The ratio of d/u is extracted from the asymmetry between $W \rightarrow l^\pm \nu$ measured by CDF. The gluon density is given by the inclusive jet production and direct photon production.

The parton distribution function is tried to extract from experimental data by several theoretical groups. An example of the global analysis based on the next-to-leading-order(NLO) pQCD calculation is shown in Fig.1.2.

Fragmentation Function(FF)

The fragmentation function, $D_h^k(z, Q^2)$, is the probability density for finding a hadron h with the fraction of momentum z in the final parton k . The

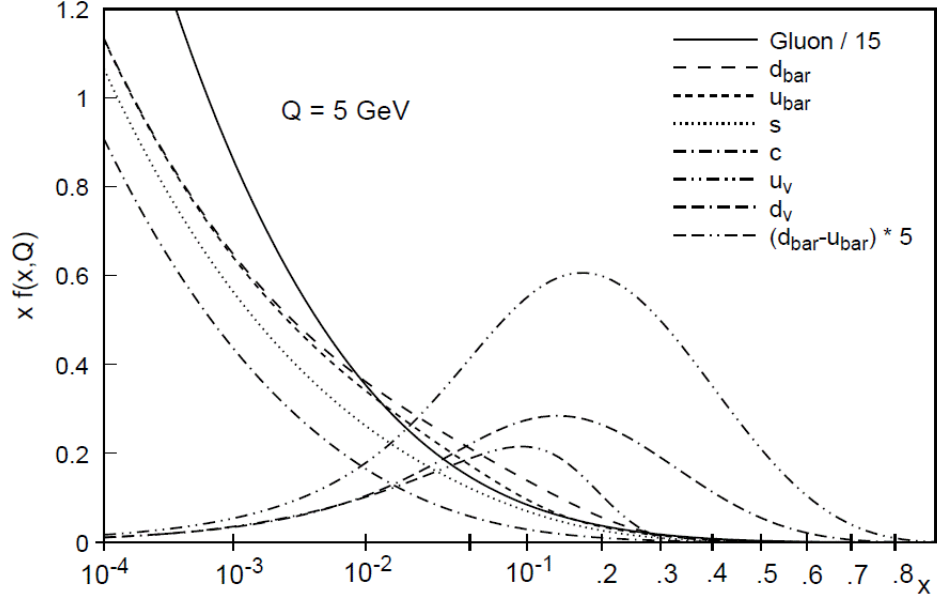


Figure 1.2: Parton Distribution Function as a function of x at $Q = 5\text{GeV}$ [3].

fragmentation function satisfies the sum rule as follows:

$$\sum_h \int z D_k^h(z, Q^2) dz = 1 \quad (1.8)$$

The fragmentation function is measured by ALEPH [17, 18], OPAL [19–22], DELPHI [23] and L3 [24] at CERN, HRS [25], MARKII [26, 27] and TPC [28] at SLAC, TASSO [29, 30] at DESY, AMY [31] at KEK in $e^+ + e^-$ collisions using the $e^+ + e^- \rightarrow \gamma$ or $Z \rightarrow h + X$. The fragmentation function for all charged particles in e^+e^- collisions is shown in Fig.1.3 [48].

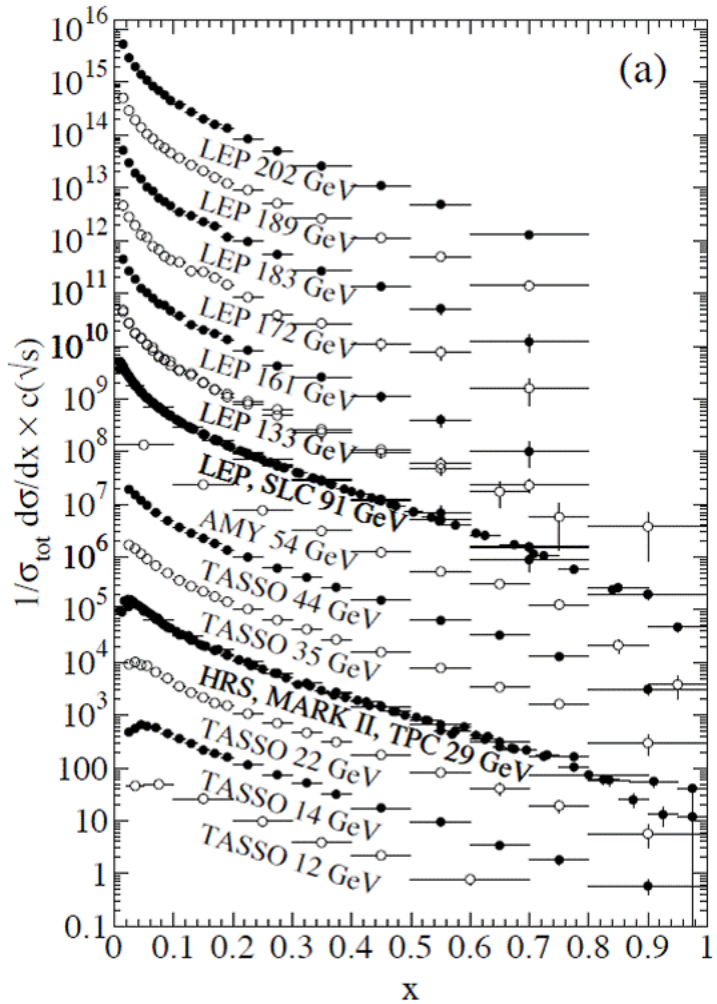


Figure 1.3: The fragmentation function for all charged particles as a function of x for different \sqrt{s} in e^+e^- collisions [48].

1.3 QCD phase transition

1.3.1 Quark Gluon Plasma

The ordinary matter consists of proton and neutrons in which quarks and gluons are confined. In the extreme condition as high temperature and/or dense density, QCD suggests that the quarks and gluons do not any more confined normal hadrons. The state of matter consisting of many-body system of deconfined quarks and gluons is called as "Quark Gluon Plasma" (QGP) [32]. The lattice QCD calculation based on the first principle QCD is most powerful tool to predict the transition temperature from hadronic matter to QGP. Fig.1.4 shows the QCD phase diagram for two massless quarks as a function of temperature T and baryon chemical potential μ_B [34]. The normal nuclear matter at zero temperature indicates 1 GeV since the μ_B corresponds to the energy of the system per baryon number. The model calculation suggest that for finite baryon chemical potential $\mu_B > 0$ and small value of temperature the transition hadronic matter to QGP is a first order phase transition. On the other hand, lattice calculation at vanishing μ_B suggest that for the transition to the high temperature phase of QCD is crossover. The critical temperature at $\mu_B = 0$ from lattice calculations is 172 \pm 11 MeV [35]

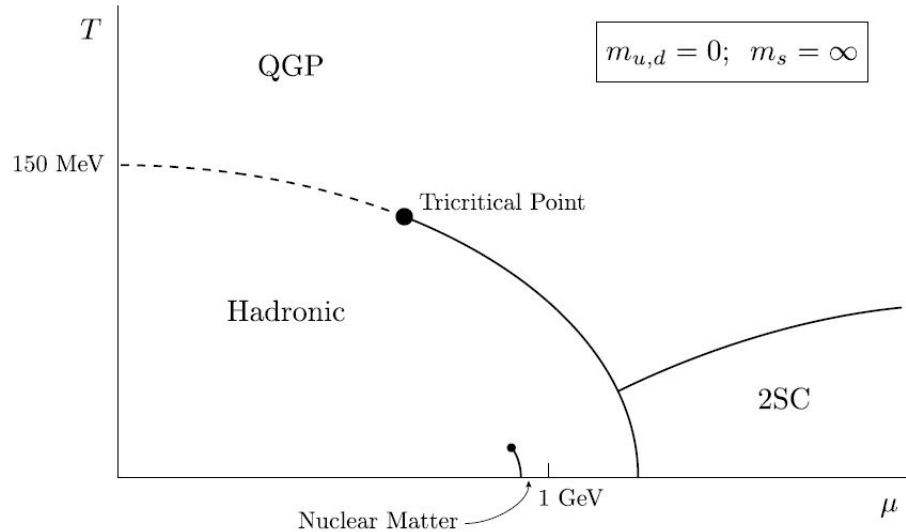


Figure 1.4: The phase diagram of QCD in Temperature T and baryon-chemical potential μ_B plane [34].

The large experimental observation for signature of QGP implies the formation of QGP in heavy ion collisions at Relativistic Heavy Ion Collider (RHIC) in Brookhaven National Laboratory (BNL). We briefly review the most important experimental signature of QGP, high transverse momentum particle suppression and strong elliptic flow.

High p_T suppression

The point-like hard scattering with large momentum exchange between partons in the incoming nucleon is well described by perturbative QCD as introducing in Sec. 1.2. The scattered partons emerge back-to-back direction and fragment into a pair of hadron jets. In such process, the high transverse momentum particles produced. If the hot and dense matter is created in nucleus-nucleus collisions ($A + A$), the scattered partons pass through the matter created in the $A + A$ collisions. Therefore, the these high transverse momentum particles may suppressed due to an energy loss by parton-matter interaction in the matter. In contrast, the particle production in $A + A$ collisions is described by the superposition of the particle production in $p + p$ collisions when no such effects present.

To quantify the high p_T particle production in $A + A$ collisions comparing with $p + p$ collisions, the nuclear modification factor R_{AA} is defined as

$$R_{AA} = \frac{d^2N^{AA}/dydp_T}{\langle N_{coll} \rangle \times d^2N^{pp}/dydp_T} \quad (1.9)$$

where p_T is the transverse momentum, y is the rapidity, $d^2N^{AA}/dydp_T$ and $d^2N^{pp}/dydp_T$ is the differential yield per event in $A + A$ collisions and $p + p$ collisions, respectively. $\langle N_{coll} \rangle$ is the number of inelastic binary nucleon-nucleon collisions. $\langle N_{coll} \rangle$ depends on impact parameter of collision event and calculated by Glauber Monte-Carlo simulation. If $R_{AA} = 1$, this indicates that the particle production in $A + A$ collisions is described by the superposition of the particle production in $p + p$ collisions.

The PHENIX experiment reported the nuclear modification factor R_{AA} and large suppression of high p_T various neutral and charged hadron yield in central Au + Au collisions with respect to the result in $p + p$ collisions scaled by number of nucleus-nucleus binary collisions [36–43]. The nuclear modification factor R_{AA} for neutral pions in central to peripheral Au + Au collisions at $\sqrt{s_{NN}} = 200$ GeV shown in Fig. 1.5 [36]. In the central Au + Au collisions, R_{AA} indicate the yield is strongly suppressed by the factor of ~ 5 at $p_T > 5\text{GeV}/c$ compared to the binary scaled $p + p$ reference. While as becoming the central to peripheral collisions, R_{AA} approaches unity $R_{AA} = 1$ as it is interpreted that the size of the medium should be smaller.

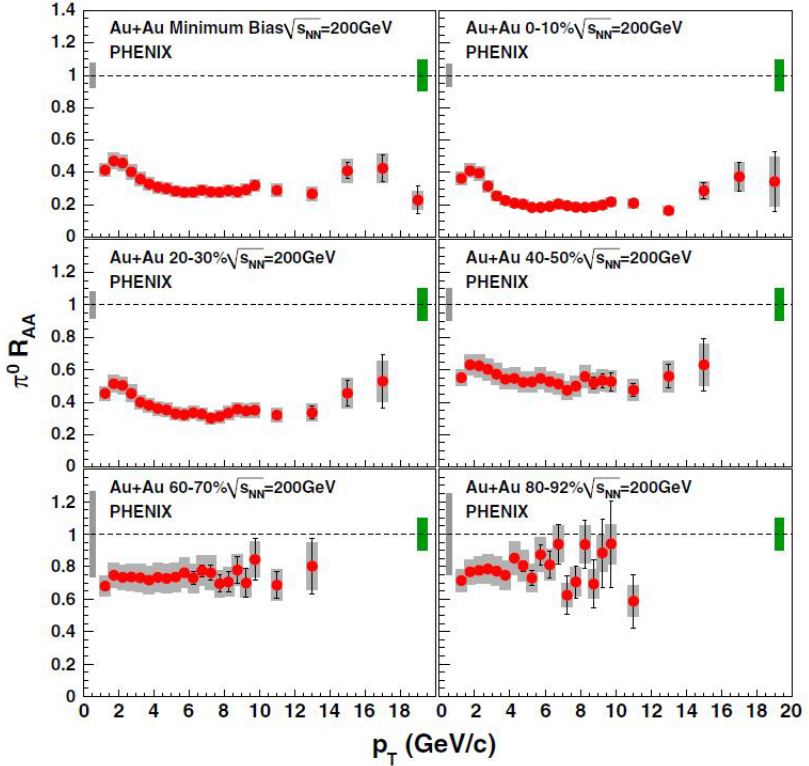


Figure 1.5: Nuclear modification factor R_{AA} for π^0 as a function of p_T for minimum bias and five centrality classes in Au + Au collisions in $\sqrt{s_{NN}} = 200$ GeV [36]. Error bars are statistical and p_T uncorrelated errors, boxes around the points indicate p_T correlated errors. Single box around $R_{AA} = 1$ on the left is the error due to N_{coll} , whereas the single box on the right is the overall normalization error of the $p + p$ reference spectrum.

The modification factor in $d + \text{Au}$ collisions, R_{dAu} reflects the contributions of initial state normal nuclear effect such as Cronin effect [44], the nuclear modified parton distribution functions (nPDFs) [46] and gluon saturation [45]. As a consequence of observation of R_{AA} and R_{dA} , The data suggest that the suppression at high p_T particles in Au + Au collisions is due to final state interactions in the extremely dense medium produced by the collisions.

1.3.2 Chiral Symmetry breaking and restoration

The left-handed and right-handed quarks as two eigenstates of chirality operator, γ^5 with the eigenvalues ± 1 can be described as follows

$$q_L = \frac{1 - \gamma^5}{2} q, \quad q_R = \frac{1 + \gamma^5}{2} q. \quad (1.10)$$

For the massless quarks, the chirality is equivalent to the helicity $\mathbf{s} \cdot \mathbf{p}/|\mathbf{s} \cdot \mathbf{p}|$. Then the quark mass, M , becomes an $N_f \times N_f$ matrix, the QCD Lagrangian Eq.1.1 may be decomposed as follows

$$L_{QCD} = -\frac{1}{4} F_{\mu\nu}^a F_a^{\mu\nu} + \bar{q}_L i\gamma^\mu D_\mu q_L + \bar{q}_R i\gamma^\mu D_\mu q_R - (\bar{q}_L \mathbf{M} q_R + \bar{q}_R \mathbf{M} q_L). \quad (1.11)$$

It is clear from this expression that, in the limiting case where $m = 0$, the QCD Lagrangian Eq.1.1 are invariant under the global transformation (chiral transformation):

$$q_L \rightarrow e^{-i\lambda^j \theta_L^j} q_L \quad (1.12)$$

$$q_R \rightarrow e^{-i\lambda^j \theta_R^j} q_R \quad (1.13)$$

where the $\theta_{R,L}^i$ ($j = 0, 1, \dots, N_f - 1$) are space time independent parameters and $\lambda^0 = \sqrt{2/N_f}, \lambda^j = 2t^j$ ($j = 1, \dots, N_f^2 - 1$). This is called chiral symmetry.

In the real world where quarks have a finite current mass, chiral symmetry is explicitly broken by the mass term, $-(\bar{q}_L \mathbf{M} q_R + \bar{q}_R \mathbf{M} q_L)$, in the Lagrangian. However, the current masses of u and d quarks is quite small comparing with $\Lambda_{QCD} \sim 200\text{MeV}$. Therefore, the chiral symmetry is expected to be an approximate symmetric in the light quark sector of QCD Lagrangian.

The symmetry is broken due to a non-vanishing ground state expectation value of the QCD vacuum for the quark condensate $\langle \bar{q}q \rangle$. The QCD vacuum $|0\rangle$ at zero temperature and density is considered. According to recent lattice QCD calculation, the order parameter $\langle 0|\bar{q}q|0 \rangle = \langle 0|\bar{q}_R q_L + \bar{q}_L q_R|0 \rangle$ is non-zero, $\langle 0|\bar{q}q|0 \rangle = \sim -[251\text{MeV}]^3$ [55]. This result implies that QCD vacuum is the Bose-Einstein condensate of quark-antiquark pairs $\langle \bar{q}q \rangle$ and has a power to change left-handed quarks to right-handed quarks as well as right-handed quarks to left-handed quarks. Namely, the chiral symmetry is spontaneously broken and the condensate induces a dynamical quark mass.

Y.Nambu and G.Jona-Lasinio (NJL) introduced a model of dynamical mechanism of the chiral phase transition inspired by the phase transition of the superconductivity, in which the chiral condensate $\langle \bar{q}q \rangle$ corresponds to pair of the electron $\langle e^\dagger e^\downarrow \rangle$ [49–51]. The QCD Lagrangian is expressed by NJL model as

$$L_{QCD} = \bar{q}i\gamma^\mu \partial_\mu q + \frac{1}{2}g((q\bar{q})^2 + (\bar{q}i\gamma^5 \tau q)^2) \quad (1.14)$$

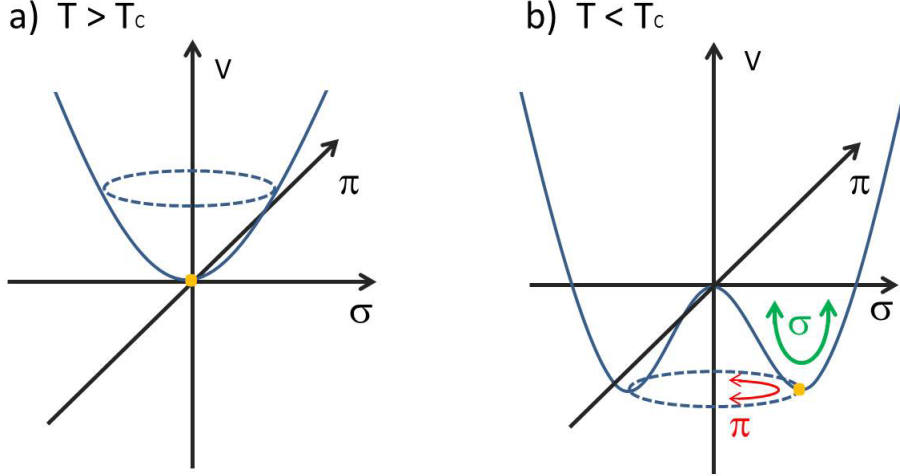


Figure 1.6: Potential of a) QCD vacuum in $T > T_c$. b) QCD vacuum in $T < T_c$.

This Lagrangian can be re-written by the linear sigma model as

$$L_{QCD} = \frac{1}{2}[(\partial_\mu \sigma)^2 + (\partial_\mu \pi)^2] + V(\sigma^2 + \pi^2) \quad (1.15)$$

where σ and π meson field are defined as

$$\sigma = \bar{q}q \quad (1.16)$$

$$\pi = \bar{q}i\gamma^5\tau q \quad (1.17)$$

Then, The π meson is created with zero mass as Nambu-Goldstone boson as result of chiral symmetry breaking. It is supported by the small mass of π meson as compared to other hadrons.

In the chiral symmetric phase, all states of hadrons have a chiral partner with opposite parity and same mass as doublet of parity. But experimental results indicate the chiral partners does not exist at the same masses. For instance, the mass of ρ meson ($J^{PC} = 1^{--}$: vector meson) is $770 MeV/c^2$, while the mass of the chiral partner A_1 meson ($J^{PC} = 1^{++}$: axial-vector meson), is $1250 MeV/c^2$. This is also direct evidence of dynamical breaking of chiral symmetry.

As the temperature and/or density increase, the $\langle q\bar{q} \rangle$ pair is dissociated and eventually the transition to chiral symmetric phase will take place [52]. The experimental observation of the effect of chiral symmetry restoration

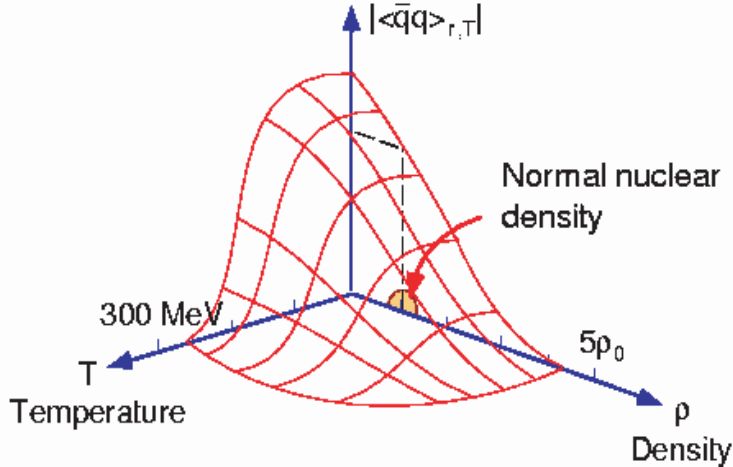


Figure 1.7: Temperature and density dependence of quark condensate $\langle\bar{q}q\rangle$ [52]

is essential to investigate the mechanism of generating hadron mass. But unfortunately the quark condensate $\langle\bar{q}q\rangle$ is not an observable and need the probe to investigate the effect of chiral symmetry restoration. According to the QCD sum rule, which can relate the hadronic spectral function to the QCD condensate, a modification of the hadron mass spectra, especially low mass vector mesons (ρ, ω, ϕ), are expected due to the partial chiral symmetry restoration in hot and/or dense environment [57]. Therefore, the low mass vector meson is powerful probe and the measurement of mass modification at hot and/or dense environment must be great interest.

1.3.3 Low mass vector meson

The light vector mesons (ρ, ω, ϕ) are theoretically most powerful probe to obtain the information related to quark condensate $\langle\bar{q}q\rangle$ as its mass modification in hot and/or dense medium due to their short life times which means larger probability of decaying in medium [57]. In addition, there are decay mode to di-lepton pairs of e^+e^- and $\mu^+\mu^-$. Di-leptons are excellent tool to study possible in-medium modification of vector mesons in the hot and/or dense medium, since the final state lepton is not strongly interact with the medium. Therefore, measurement of vector mesons via di-lepton pairs can extract clean information of mass in the medium. The large mounts of experimental efforts have been reported and continued by using various collision

system in CERES(NA45) [58,59], NA60 [60] at CERN, E325 [61–64] at KEK, E01-112(g7) [65] at J-Laboratory and CBELSA/TAPS [66].

1.4 Motivation and scopes of this thesis

Precise measurements of hadron production in $p+p$ collisions are essential for deeply understanding QCD phenomena such as parton dynamics and hadronization. That also provide a valuable baseline for particle production in heavy ion collision.

At high p_T region, the hadron spectra for the invariant differential cross section can be described by perturbative QCD as shown Section 1.2 and display a power-law behavior called "hard" process. On the other hand, at low p_T region, typically $p_T < 2$ GeV/c, the perturbative approach is not applicable. In addition, the contribution of the multiple parton interaction makes difficult to describe the behavior. The spectra at low p_T region is expected to be exponential behavior like thermal model called "soft" process in heavy ion collisions but it's not established in $p+p$ collision. In this way, the phenomena still has not been fully understood even so in case of $p+p$ collisions.

The observation of the mass modification for the light vector meson due to the partial chiral symmetry restoration in heavy ion collisions is expected as introduced in Section 1.3.2. But it is challenging assignment due to the large combinatorial background from other hadrons. Therefore, it is important to provide the baseline in $p+p$ collisions for analyzing mass spectra of light vector mesons in heavy ion collisions. In $p+p$ collisions, the modification of the mass spectra is not expected, since the system size crating the collision is much smaller than the life time of ϕ and ω mesons. The procedure to evaluate the mass shape assuming with modification in $p+p$ collisions will be considered as baseline for heavy ion physics.

We, PHENIX collaboration, are able to measure various hadrons simultaneously at mid-rapidity in $p+p$ collisions at $\sqrt{s}=200$ GeV. In this study, we measured the production of ω and ϕ meson via e^+e^- decay channel at lower transverse momentum range $0 < p_T < 4$ GeV/c in $p+p$ collisions at $\sqrt{s} = 200$ GeV. Moreover we will mention about analysis result of mass spectra of ω and ϕ meson and the scaling property of various hadrons (π , K , η , ω , ϕ , J/Ψ) at mid-rapidity in $p+p$ collisions at $\sqrt{s}=200$ GeV.

This thesis consists of follows. Chapter 2 gives a description of the PHENIX experimental setup and detector subsystems. Chapter 3 describes the analysis methods including electron identification, reconstruction of ω and ϕ mesons via e^+e^- decay channel and simulation studies. Chapter 4 shows results of ω and ϕ meson production including discussions of mass spectra and scaling properties. Chapter 5 is finally the conclusion of this analysis.

Chapter 2

Experimental Setup

The RHIC complex and PHENIX detector are overviewed in this chapter. The description of the RHIC complex is described in Section 2.1, and the PHENIX detectors is described in Section 2.2.

2.1 Relativistic Heavy Ion Collider (RHIC)

The Relativistic Heavy Ion Collider (RHIC) [69] at Brookhaven National Laboratory (BNL) in the United States was built to study the nuclear physics. The maximum energy at RHIC for heavy ion is 100GeV per nucleon and that for proton is 250GeV. The heavy ion and proton produced at the source are transported through a Tandem Van de Graaff and proton linac, respectively, and accelerate at Booster Synchrotron and the Alternating Gradient Synchrotron (AGS), after that, injected to RHIC. The RHIC ring has a circumference of 3.8km with the maximum bunch of 120 and the designed luminosity is $2 \times 10^{26} \text{ cm}^{-2} \text{ s}^{-1}$ for Au ion and $2 \times 10^{32} \text{ cm}^{-2} \text{ s}^{-1}$ for proton. The RHIC consists of two quasi-circular concentric rings, one("Blue Ring") for clockwise and the other("Yellow Ring") for counter-clockwise. The rings cross at six interaction points. Four experiments, PHENIX, STAR, BRAHMS and PHOBOS are built in each one of six interaction points.

The PHENIX, the Pioneering High Energy Nuclear Interaction eXperiment [71], is one of four experiments and specialized experiment for measurement of lepton and photon. In this analysis, the data collected by PHENIX was used. The Detector design is described in the next subsection.

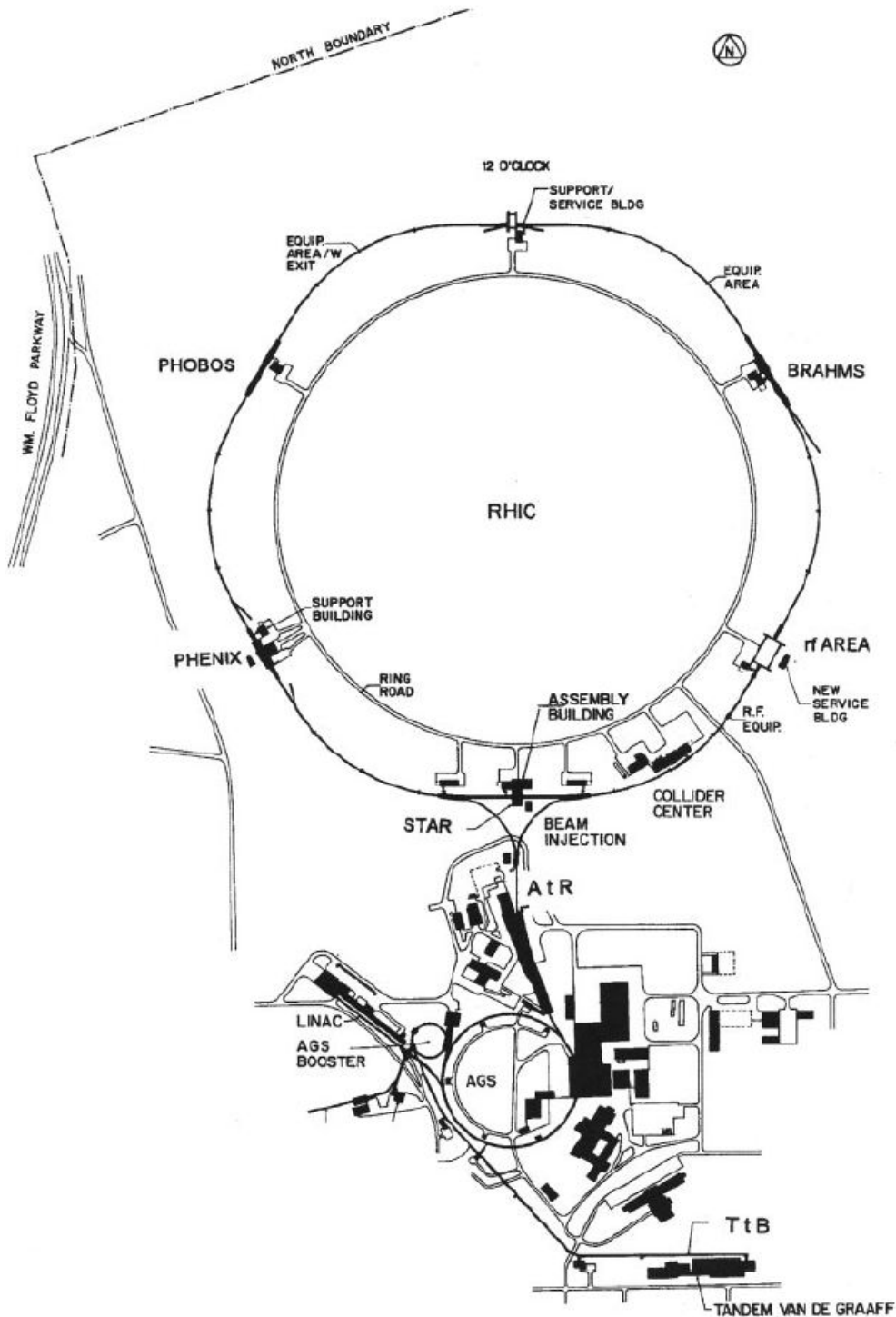


Figure 2.1: Overview of Brookhaven National Laboratory accelerator complex, consisting of LINAC, booster, AGS and RHIC [70]

RUN	Year	Species	$\sqrt{S_{NN}}$	$\int L dt$
01	2000	Au+Au	130	$1 \mu b^{-1}$
02	2001/2002	Au+Au	200	$24 \mu b^{-1}$
		p+p	200	$0.15 pb^{-1}$
03	2002/2003	d+Au	200	$2.74 nb^{-1}$
		p+p	200	$0.35 pb^{-1}$
04	2004	Au+Au	200	$241 \mu b^{-1}$
		Au+Au	62.4	$9 \mu b^{-1}$
05	2004/2005	Cu+Cu	200	$3 nb^{-1}$
		Cu+Cu	62.4	$0.19 nb^{-1}$
		Cu+Cu	22.5	$2.7 \mu b^{-1}$
		p+p	200	$3.8 pb^{-1}$
06	2006	p+p	200	$10.7 pb^{-1}$
		p+p	62.4	$0.1 pb^{-1}$
07	2007	Au+Au	200	$0.813 nb^{-1}$
08	2008	d+Au	200	$80 nb^{-1}$
		p+p	200	$5.2 pb^{-1}$
09	2009	p+p	500	$10 pb^{-1}$
		p+p	200	$16 pb^{-1}$
10	2010	Au+Au	200	$1.3 nb^{-1}$
		Au+Au	62.4	$0.11 nb^{-1}$
		Au+Au	39	$40 \mu b^{-1}$
		Au+Au	7.7	$0.26 \mu b^{-1}$

Table 2.1: summary of the RHIC operation. The integrated luminosity is recorded in PHENIX.

2.2 the PHENIX Detector

The PHENIX detector was optimized for precision measurement with particular focus on electromagnetic probe. The PHENIX have selective triggers, high rate capability, and multiple fast detector systems to track and identify particles emitting from collisions. The PHENIX detector consists of 2 central arms [78, 82, 84] which has pseudo-rapidity coverage of ± 3.5 and 180° azimuthal angle in total, 2 muon arms [85] which has pseudo-rapidity coverage of $\pm (1.2-2.4)$, and beam detectors [72] which is near the beam pipe.

2.2.1 Beam Beam Counters (BBC)

Beam Beam Counters(BBC) [73] are located on North and South side at 144.35 cm along beam pipe from the nominal collision point. The BBC covers pseude-rapidity $3.1 < |\eta| < 3.9$ and full azimuthal angle $\Delta\phi = 2\pi$. Each of them consists of 64 Čerenkov detector elements, which consist quartz Čerenkov radiator and mesh-dynode type photo multiplier tube (PMT).

BBC have four major tasks, to trigger the Minimum Bias events, to measure the collision vertex, to obtain the collision timing and determine the centrality. In addition, the reaction plain is determined by hit pattern of BBC in heavy ion collisions. The collision vertex and timing are determined by the difference and average hit time to north and South counters;

$$\text{collision vertex} = \frac{(T_S - T_N)}{2} \times c \quad (2.1)$$

$$\text{collision time} = \frac{T_S + T_N - (2 \times L)/c}{2} \quad (2.2)$$

where T_N and T_S are the averaged hit time of incoming particles, c is the light velocity and L is the distance from nominal collision point ($z = 0$) to both BBC location, $L = 144.35$ cm.

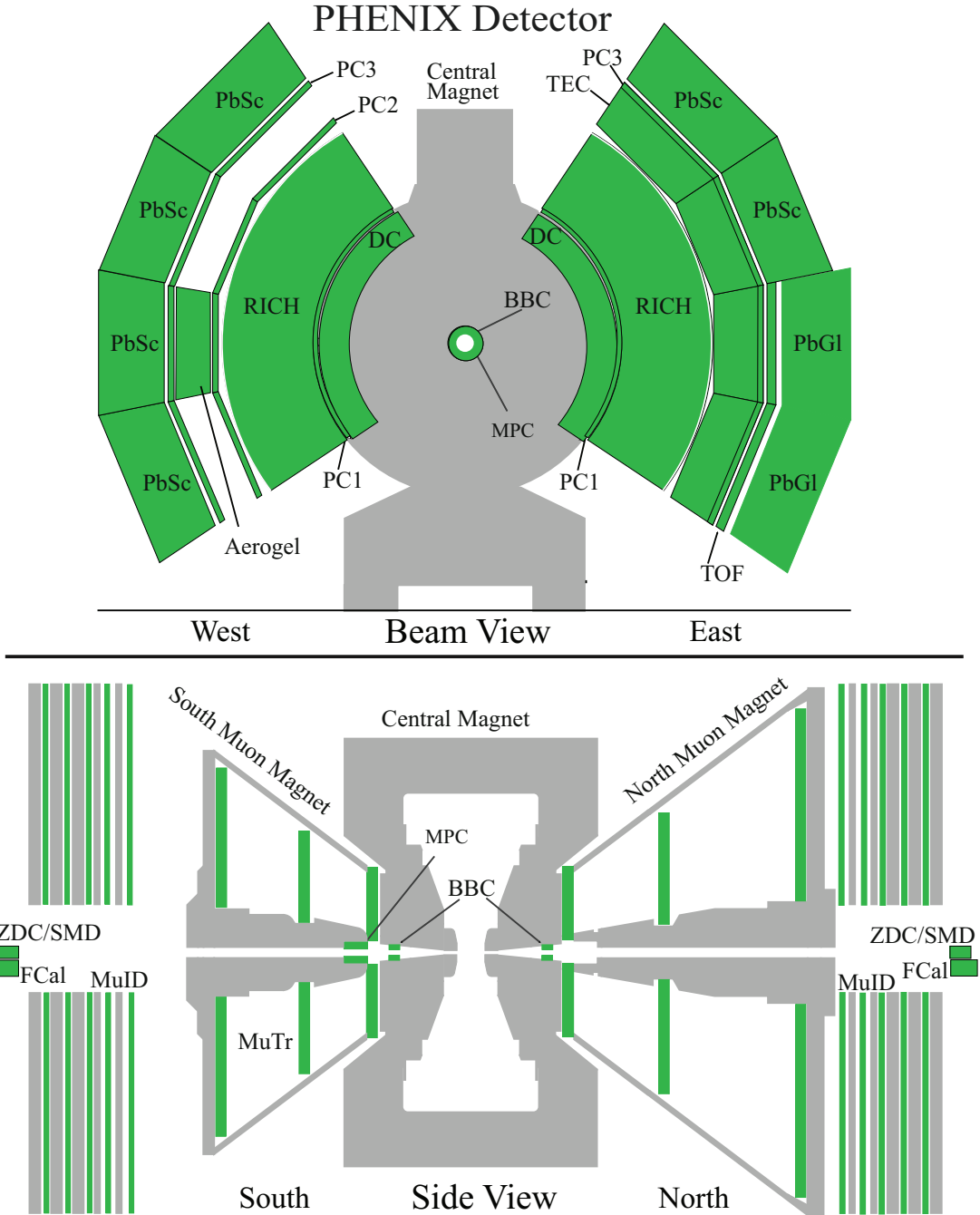


Figure 2.2: The PHENIX Detector configuration [88]. The upper panel shows the beam view. Two central arms and central magnet can be seen. The bottom panel shows side view. Two muon arms and muon magnet can be seen.

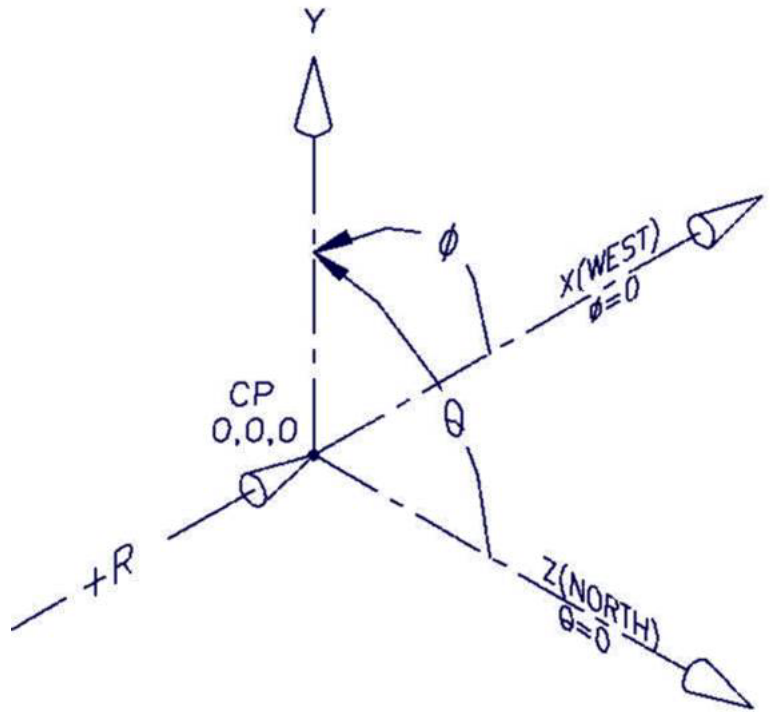


Figure 2.3: the PHENIX global coordinate system.

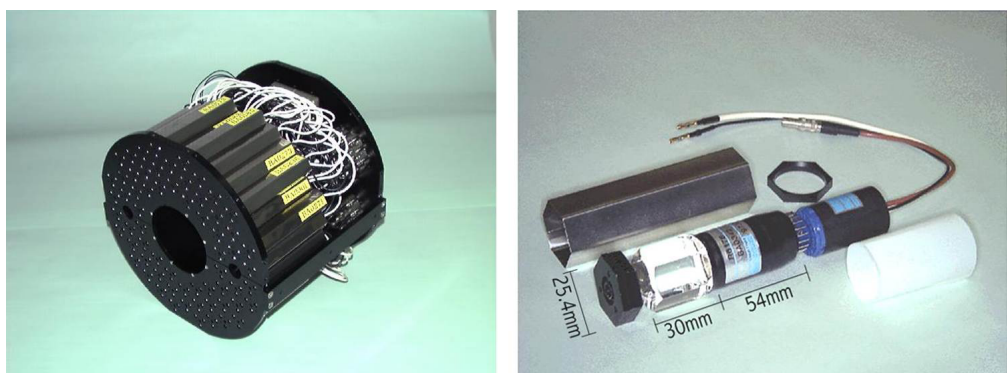


Figure 2.4: Left) BBC arrays consisting 64 elements. Right) One of the BBC elements consisting quartz Čerenkov radiator and mesh-dynode type PMT.

2.2.2 Zero Degree Counters (ZDC)

Zero Degree Calorimeters(ZDC) [74] are hadron calorimeter located at 18m North and South side along beam pipe from the collision point. Since the both north and south ZDC sit at just the upstream of the last bending magnet on the RHIC ring, most of charged particles are swept out from the acceptance. So, ZDC works as the minimum bias trigger counter and monitor the beam luminosity since ZDC measured neutrons from spectator part of heavy ion collision.

2.2.3 PHENIX tracking system

Magnet

The PHENIX has three magnet systems [75], one is the central magnet, others are north and south muon magnets. The central magnet provide a magnetic field around the collision point which is parallel to the beam. And the Central magnet consist of inner and outer coil, which can be optimized separately, together, or in opposition. During the run for this work, both inner and outer magnets are energized and integrated magnetic field is $1.15 T \cdot m$. the momentum of charged particles can be obtained by measuring the curvature of the track which is bended due to magnetic field.

Drift Chamber (DC)

The PHENIX Drift Chambers(DC) [77] are cylindrically shaped and located in the region from 2 to 2.4 m from the beam axis and 2 m along the beam axis. This places them in a residual magnet field with a maximum of 0.6 kG. Each DC measures charged particle trajectories to determine transverse momentum of each particles. The DC also participates in the pattern recognition at high particle track densities by providing position information that is used to link tracks thought the various PHENIX detectors. The good double track spatial resolution for the highest multiplicities at heavy ion collisions is required and the single wire two track separation batter than 1.5 mm.

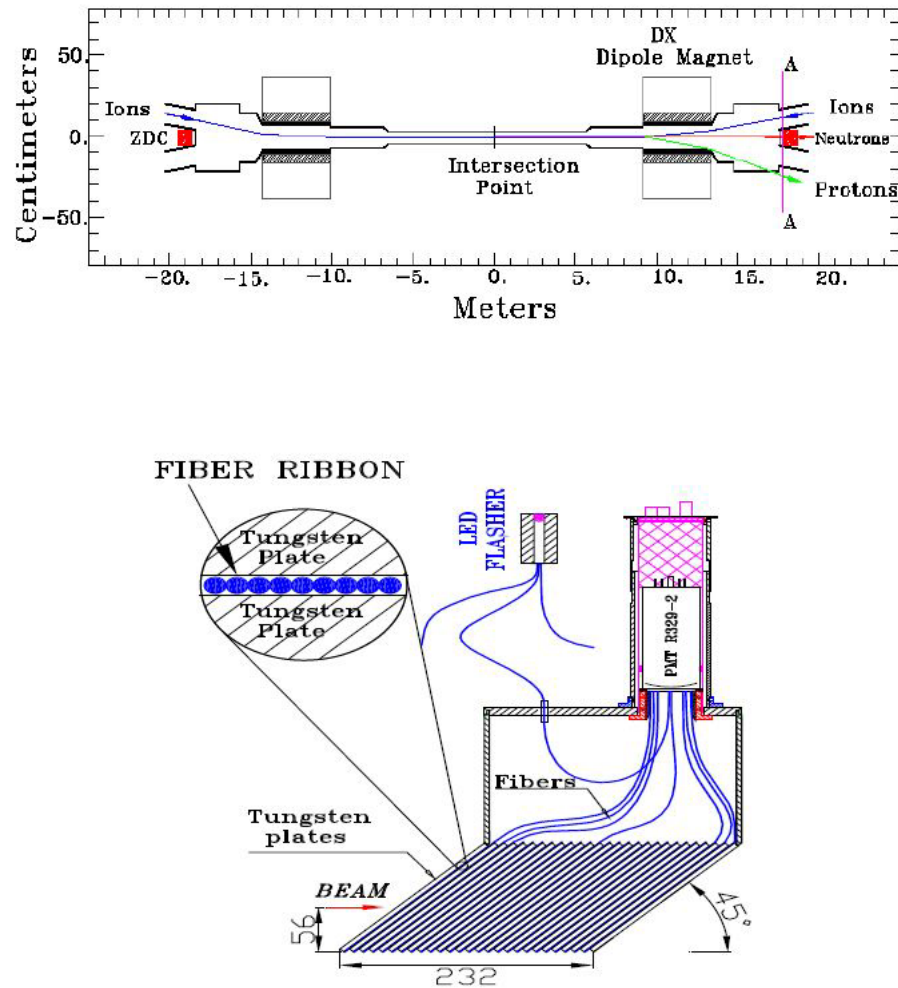
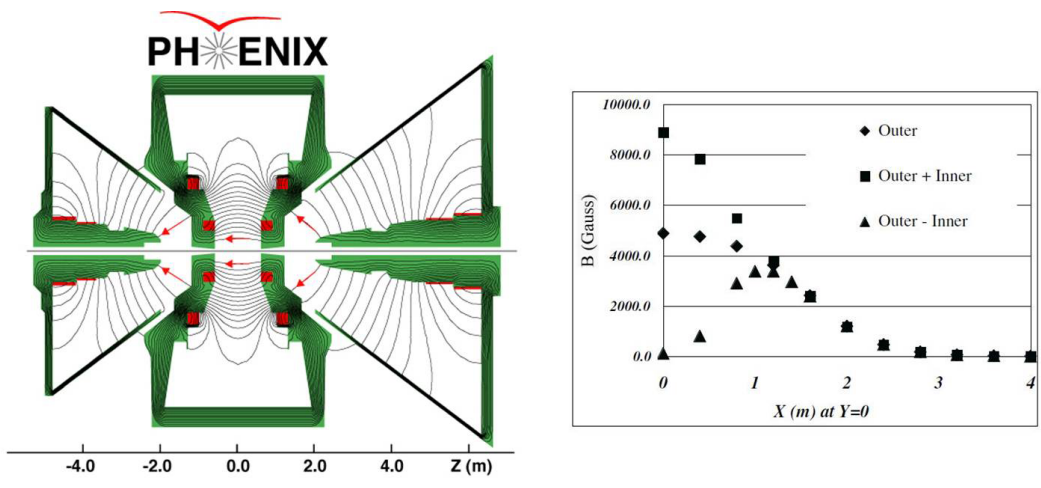


Figure 2.5: schematic view of the ZDC location including deflection of protons and charged fragments [74]



Magnetic field lines for the two Central Magnet coils in combined (++) mode

Figure 2.6: Left) overview of the PHENIX Magnets. The line shows the contour of the magnetic. Right) total magnetic field strength as a function of R at the $\theta=0$ symmetry plane of the Central Magnet for +(outer), ++(Outer+Inner), and +- (Outer-Inner) configuration .

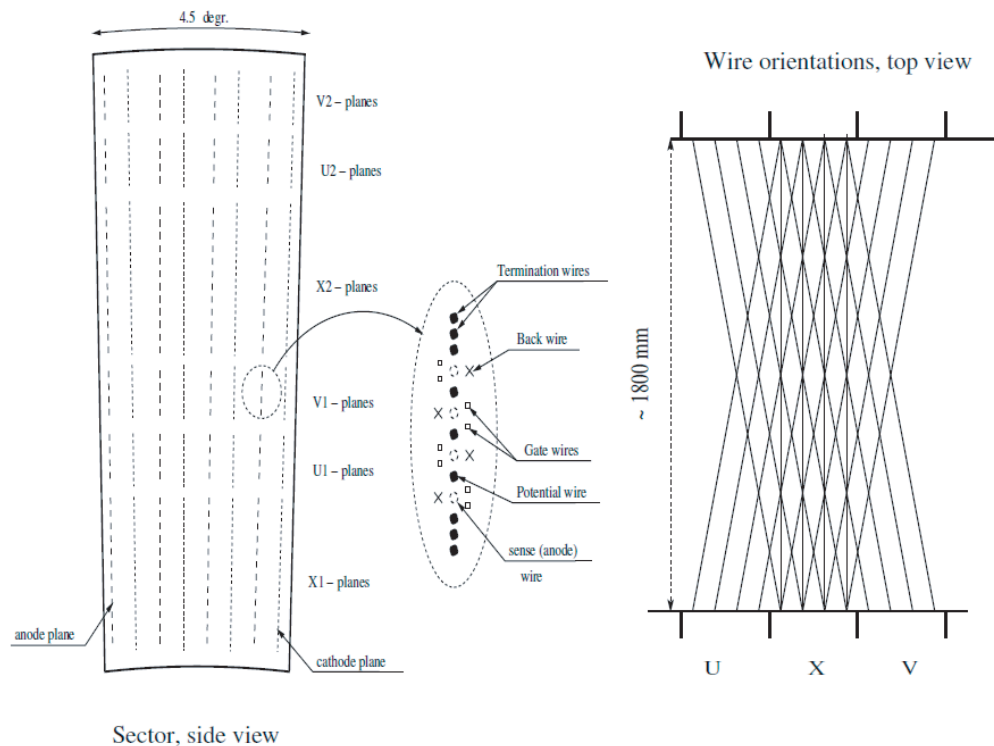


Figure 2.7: The layout of wire position of DC. The X1 and X2 wire cells runs in parallel to the beam to perform precise track measurements in $r\phi$. U1, V1, U2, V2 wires have stereo angle of about 6° relative to the X wires and measure the z coordination of track [78].

Pad Chamber (PC)

The PHENIX Pad Chambers(PC) [76] are multiwire proportional chambers that form three separate layers. Each detectors consists of a single plane of wire inside a gas volume bounded by two cathode plane. One cathode is finely segmented int an array of pixels. The charge induced on a number of pixels when a charged particle starts an avalanche on an anode wire, is read out thorough specially designed read out electronics. The PC system determines space points along the straight line particle trajectories outside the magnetic field. Fig.2.3 shows position of PCs relative to the other detectors. The innermost pad chamber called PC1 is essential for determining the three-dimensional momentum vector by providing the z coordinate at the exit of the DC.

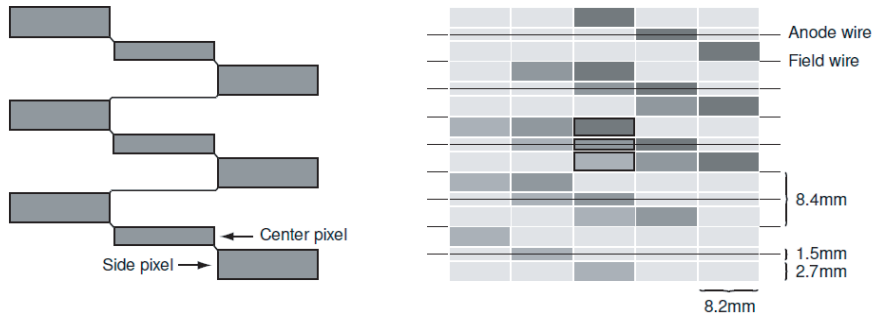


Figure 2.8: the pad and pixel geometry(left), A cell defined by three pixels is at the center of the right picture [78].

Track reconstruction

Charged particles emitted from collision vertex pass through the magnetic field and bend along with a plane perpendicular to beam pipe until reaching the DC. These particles reaching DC goes away in straight lines, since there is almost zero strength of the magnetic field at the outside of DC. Fig. 2.9 shows definition of track parameters for describing a charged particle trajectory though the magnetic field in PHENIX up to PC1 [78, 79].

The parameters measured with DC and PC1 and used to reconstruct the particle trajectory are defied as follows:

- α : The angle between the projection of trajectory in the x - y plane and the radial direction, at the interaction point of trajectory with the circle of reference radius $R_{DC} = 2.2$ m.

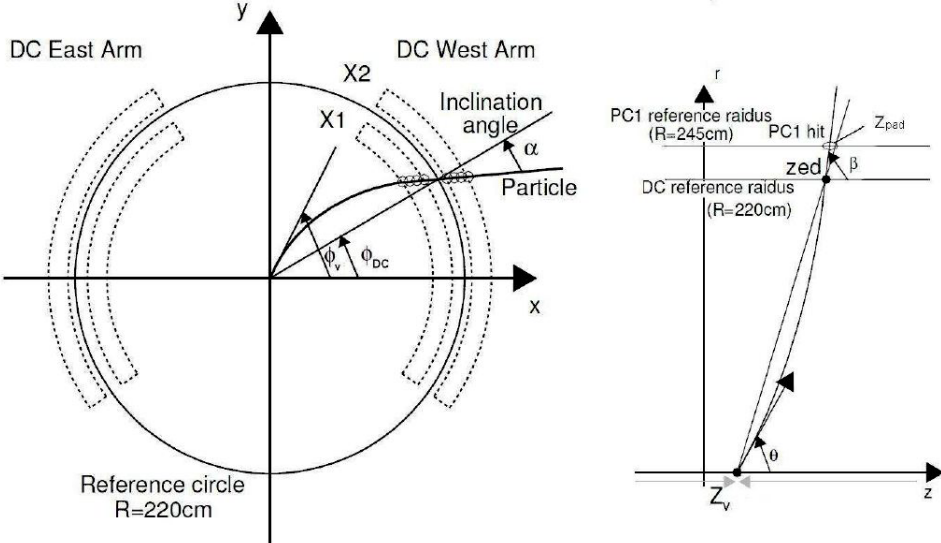


Figure 2.9: Illustration of the track reconstruction in the PHENIX up to PC1 on x - y plane and r - z plane.

- ϕ_{DC} : The azimuthal angle of the interaction point of the trajectory with the circle of radius R_{DC} .
- z_{pad} : The z coordinate of the interaction point of the trajectory with PC1 surface radius $R_{PC1} = 2.45$ m.
- β : The angle between the projection of trajectory in the r - z plane and the z -axis.
- ϕ_v : The initial azimuthal angle of the particle trajectory
- θ : The angle between the initial direction of particle trajectory and z -axis.

The track finding algorithm assumes that the all tracks originated at the collision vertex. The collision vertex is assumed to be $(0,0)$ in (x, y) plane and z position is determined by the timing information of BBC as described in Sec.2.2.1 The track reconstruction within DC is performed using a Hough transform technique [80]. In this technique, the DC hits in X1 and X2 are mapped for all possible X1-X2 hits combinations into a feature space defined by the azimuthal angle ϕ_{DC} and the track bending angle α . The basic assumption is that tracks are straight lines within the DC. In the case of that

all hit pairs of a given track will have the same ϕ and α , then result have maximum in the mapped space of ϕ and α . The reconstructed tracks are then associated with X1 and X2 hits. Once a track is found in ϕ and α plane, the z -coordinate of the track is determined using the Hough Transform with the associated PC1 cluster and the stereo U and V wire informations of the DC.

The momentum, p of the charged particle is determined using the θ and α measured in DC and PC1. The transverse momentum, p_T (GeV/c) and the α -angle (mrad) have the following approximate relation:

$$\alpha \approx \frac{K}{p_T}, \quad (2.3)$$

where $K \approx 0.10$ (rad GeV/c) is the effective field integral between the collision vertex and the DC, expressed as:

$$K = \frac{e}{R} \int l B dl. \quad (2.4)$$

Here, e is the elementary charge in the hybrid unit ($e = 0.2998$ GeV/c T⁻¹ m⁻¹) and R is the DC reference radius.

The resolution of momentum depends on the intrinsic angular resolution of the DC and the contribution of multiple scattering. The momentum resolution is finally determined to be $\delta p/p = 0.7\% \oplus 1.0\% \times p$ (GeV/c) [81]

The quality of track reconstructed by track finding algorithm with DC and PC is defined using the hit information of the X and the stereo U and V wires and the associated PC1 cluster. This *Quality* is defined as a binary pattern of 6 bit valuable as follow :

$$Quality = A \times 2^0 + B \times 2^1 + C \times 2^2 + D \times 2^3 + E \times 2^4 + F \times 2^5, \quad (2.5)$$

where A, B, C, D, E, F are quality bits defined as follows:

- A=1: X1-wire used
- B=1: X2-wire used
- C=1: UV-wire found
- D=1: UV-wire unique
- E=1: PC1 found
- F=1: PC1 unique

If the track is reconstructed by both X1 and X2 sections of DC and is uniquely associated with hits in U or V stereo wires, the value of *quality* is 63 (in case a unique PC1 hit is found) or 31 (in case the PC1 hit is found but ambiguous). In this analysis, the tracks of quality of 63 or 31 are used.

		ABCDEF	quality		
PC1 found/unique	no UV	1100xx	49	50	51
PC1 found/unique	UV found/unique	1111xx	61	62	63
PC1 found/ambiguous	no UV	0100xx	17	18	19
PC1 found/ambiguous	UV found	0101xx	21	22	23
PC1 found/ambiguous	UV found/unique	0111xx	29	30	31

Table 2.2: Summary of the track quality

2.2.4 Ring Image Cherenkov Counters (RICH)

The Ring Image Cherenkov Counters(RICH) [83] is occupies the radial region between 2.575 and 4.1 m from the beam line. Each of the detectors in the east and west central arms has a volume of 40cm². the minimum thickness of the radiator gas, which is CO₂, is 87 cm, the maximum is about 150 cm. The RICH is provides e/π discrimination below the π Cherenkov threshold, which is set at 4.65 GeV/c. The Cherenkov photon produced in the radiator gas are reflected on the mirror and are detected by the photon multiplier tubes (PMTs). The average size of the Cherenkov ring is 8 cm and average number of the Cherenkov photon produced by electron is 10.8 on the plane where the PMTs are sitting. Fig.rich show the cut through view of RICH detector.

2.2.5 Electro Magnetic Calorimeter (EMC)

The Electro Magnetic Calorimeter (EMCal) is designed primarily to measure the energies and spatial position of photon and electrons. It also plays a major role of in particle identification and is an important part of the PHENIX trigger system. The EMCal system can trigger on rare events with high transverse momentum photons and electrons. The EMCal system consists of a total of 24768 individual detector modules divided between the Pb-Scintillator calorimeter (PbSc), which provides 6 sectors of central arm and the Pb-Glass calorimeter (PbGl) comprised of 2 sectors.

The PbSc is a sampling calorimeter made of alternating tile of Pb and scintillator consisting of 15552 individual towers and covering an area of approximately 48 m². The basic block is a module consisting of 4 towers, which are optically isolated, and are read out individually. The tower has 5.52 × 5.25 cm² cross section and 3.75 cm in length. Figure 2.11 show the interior view of the module. A super-module is composed of 12 × 12 towers and a sector is composed of 18(12×12) super-modules.

The PbGl is a Cherenkov type calorimeter. A lead glass has 4.0 × 4.0

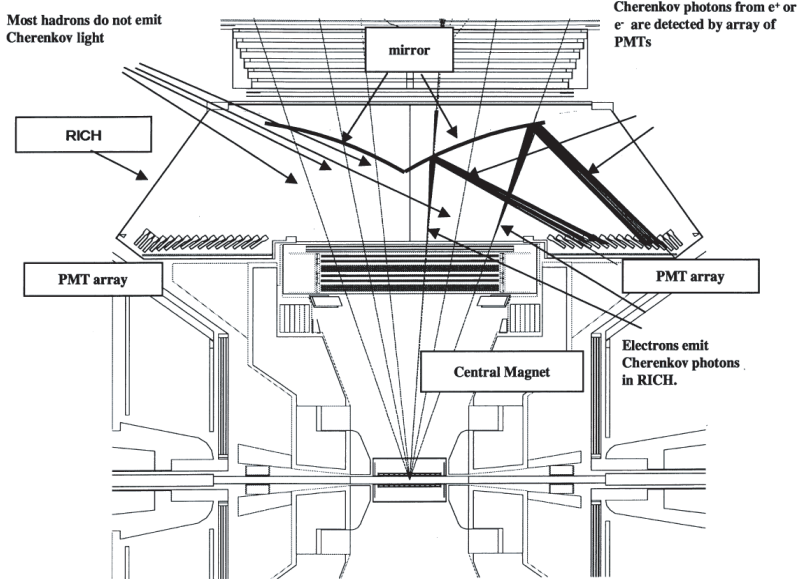


Figure 2.10: A cut through view of RICH detector

parameter	PbSc	PbGl
Radiation length (X_0)	2.1 cm	2.8 cm
Moliere radius	~ 3.0 cm	3.7 cm
Nuclear interaction length (λ_I)	44 cm	38 cm
Total η coverage	0.7	0.7
Total ϕ coverage	$\pi/2 + \pi/4$	$\pi/4$
Number of towers in one sector	72×36	96×48
Total depth	37.5 cm ($18X_0, 0.85\lambda_I$)	40 cm ($14X_0, 1.05\lambda_I$)

Table 2.3: Summary of parameters of two type of PHENIX EMCal

cm² cross section and 40 cm length. Figure 2.12 shows the interior view of one super-module, composed by 4×6 towers. A sector is composed of 192(12×12) super-modules.

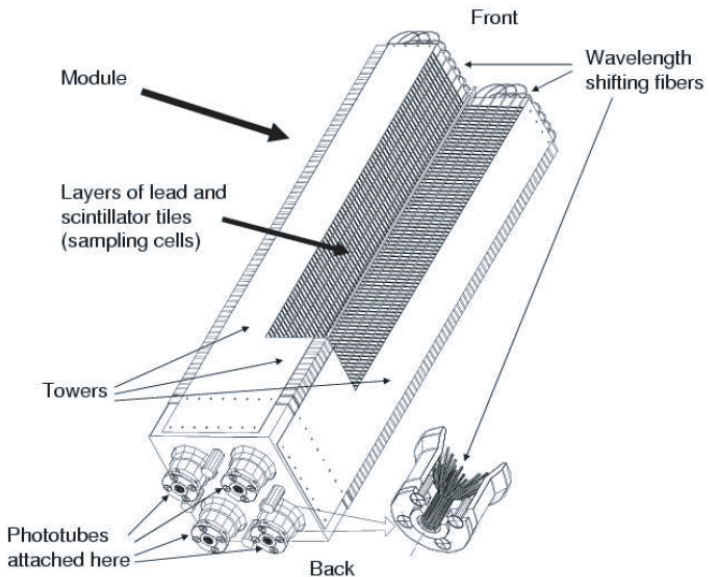


Figure 2.11: Interior view of a lead-scintillator calorimeter module

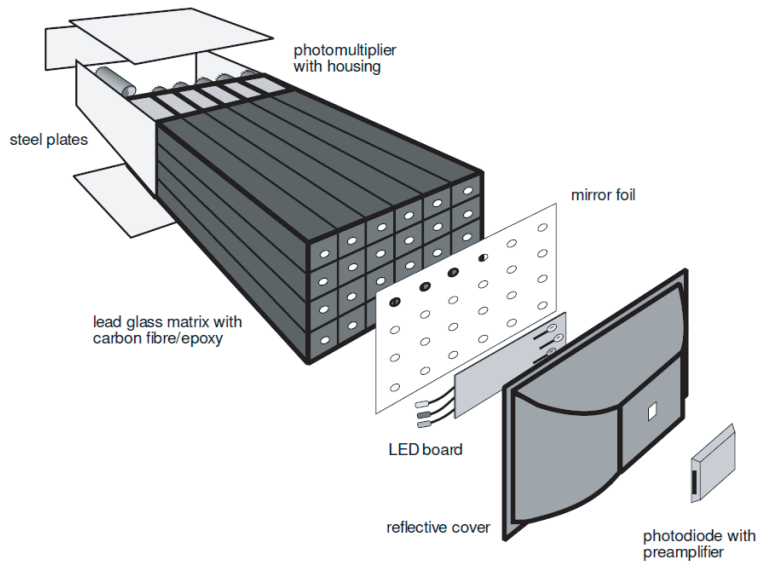


Figure 2.12: Exploded view of a lead-glass detector supermodule

2.3 Data Acquisition system (DAQ)

PHENIX is designed to make measurements on a variety of collision system from p+p to Au+Au. The occupancy in the detector varies from a few tracks in p+p interaction to approximately 10% of all detector channels in central Au+Au interactions. The interaction rate at design luminosity varies from a few kHz for Au+Au central collisions to approximately 500 kHz for minimum bias p+p collisions. The PHENIX DAQ system was designed to seamlessly accommodate improvements in the design luminosity. This was accomplished through the pipelined and deadtimeless features to the detector front ends and the ability to accommodate higher-level triggers.

In PHENIX it is necessary to measure low-mass lepton pair and low p_T particles in a high-background environment. In order to preserve the high interaction-rate capability of PHENIX a flexible system that permits tagging of events was constructed. The On-Line system has two levels of triggering denoted of LVL1 and LVL2. The LVL1 trigger is fully pipelined, therefore the On-Line system is free of deadtime through LVL1. Buffering is provided that is sufficient to handle fluctuations in the event rate so that deadtime is reduced to less than 5% for full RHIC luminosity. The LVL1 trigger and lower levels of the readout are clock-driven by bunch-crossing signals from the 9.4 MHz RHIC clock. The higher levels of readout and the LVL2 trigger are data-driven where the results of triggering and data processing propagate to the next higher level only after processing of a given event is completed.

The general schematic for the PHENIX On-Line system is shown in Fig. 2.13. Signals from the various PHENIX subsystems are processed by Front End Electronics (FEE) that convert detector signals into digital event fragments. This involves analog signal processing with amplification and shaping to extract the optimum time and/or amplitude information, development of trigger input data and buffering to allow time for data processing by the LVL1 trigger and digitization. This is carried out for all detector elements at every beam crossing synchronously with the RHIC beam clock. The timing signal is a harmonic of the RHIC beam clock and is distributed to the FEM's by the PHENIX Master Timing System (MTS). The LVL1 trigger provides a fast filter for discarding empty beam crossings and uninteresting events before the data is fully digitized. It operates in a synchronous pipelined mode, generates a decision every 106 ns and has an adjustable latency of some 40 beam crossings.

Once an event is accepted the data fragments from the FEM's and primitives from the LVL1 trigger move in parallel to the Data Collection Modules (DCM). The PHENIX architecture was designed so that all detector-specific electronics end with the FEM's, so that there is a single set of DCM's that

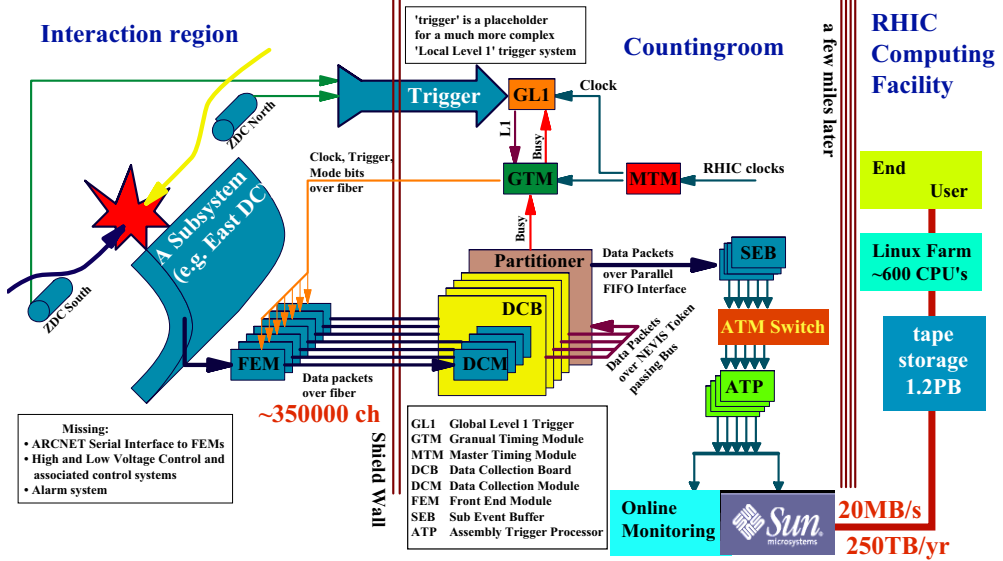


Figure 2.13: block diagram of DAQ [88]

communicate with the rest of the DAQ system. The only connection between the Interaction Region (IR) where the FEM's are located and the Counting House (CH) where the DCM's are located is by fiber-optic cable. The DCM's perform zero suppression, error checking and data reformatting. Many parallel data streams from the DCM's are sent to the Event Builder (EvB). The EvB performs the final stage of event assembly and provides an environment for the LVL2 trigger to operate. In order to study the rare events for which PHENIX was designed, it is necessary to further reduce the number of accepted events by at least a factor of six. This selection is carried out by the LVL2 triggers while the events are being assembled in the Assembly and Trigger Processors (ATP) in the EvB. The EvB then sends the accepted events to the PHENIX On-line Control System (ONCS) for logging and monitoring. The logged data, which is named as PHENIX Raw Data File(PRDF), are send to RHIC Computing Facility(RCF) for sinking on the tape in High Performance Storage System(HPSS). The data in the HPSS are analyzed and converted into an intermediated data format in the linux computer at RCF and Computing Center in Japan(CCJ).

2.4 Event trigger

The PHENIX has had various kinds of the Level 1 triggers corresponding to aim of physics. In this section, two type triggers of BBCLL1 trigger as Minimum Bias trigger and EMCAL RICH level 1 are introduced.

Minimum Bias Trigger

The Minimum Bias trigger in PHENIX is generated by BBCLL1 based on hit information of BBCs. It requires the coincidence of BBC north and south with at least one hit for each side and reconstructed collision vertex is within 30cm of nominal interaction point.

$$\text{Min.Bias} \equiv (\text{BBCN} \geq 1) \& \& (\text{BBCS} \geq 1) \& \& (|\text{vertex}| < 38\text{cm}) \quad (2.6)$$

Since the low event multiplicity in $p+p$ collisions for the rapidity coverage of BBCs, the Minimum Bias trigger accepts only part of the total cross section. This efficiency of minimum bias trigger is estimated to be $54.5 \pm 5\%$ of total inelastic cross section of $\sigma_{inel}^{pp} = 42 \pm 3\text{mb}$ for $p+p$ collisions in $\sqrt{s} = 200\text{GeV}$. Namely, the Minimum Bias trigger absolute cross section is $23\text{mb} \pm 9.7\%$. The fraction of events with particles in the central arm acceptance is $\epsilon_{bias} = 79 \pm 2\%$ with p_T and physics process independent, which determined from the ratio of data collected with and without required the Minimum Bias trigger. Therefore, the measured particles yield is divided by $0.79/0.545$ to correct the fraction of the event missed by the Minimum Bias trigger in $p+p$ collisions.

EMCal and RICH Trigger

The other is the EMCal and RHIC trigger(ERT) designed to enhance the electron, positron, pair of electron and positron, high $p_T \pi_0$. The ERT trigger is crucial for e^+e^- measurement since the events including e^+e^- pairs are rare. The ERT trigger requires a minimum energy deposit of 400MeV in 2×2 EMCal towers matched to a hit in the RICH and coincidence with the Minimum Bias trigger. The schematic view of ERT trigger is shown in Figure 2.15.

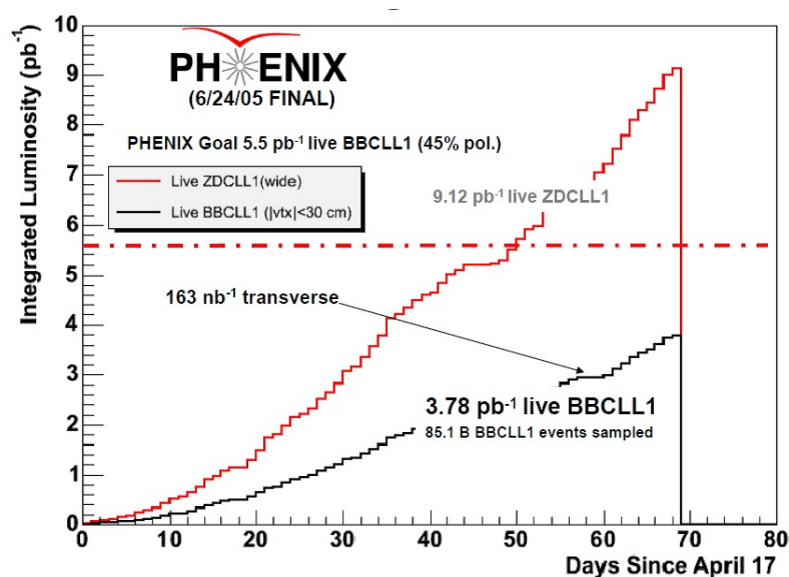


Figure 2.14: Integrated luminosity as a function of date for 200GeV $p+p$ collisions collected by PHENIX in year 2004/2005.

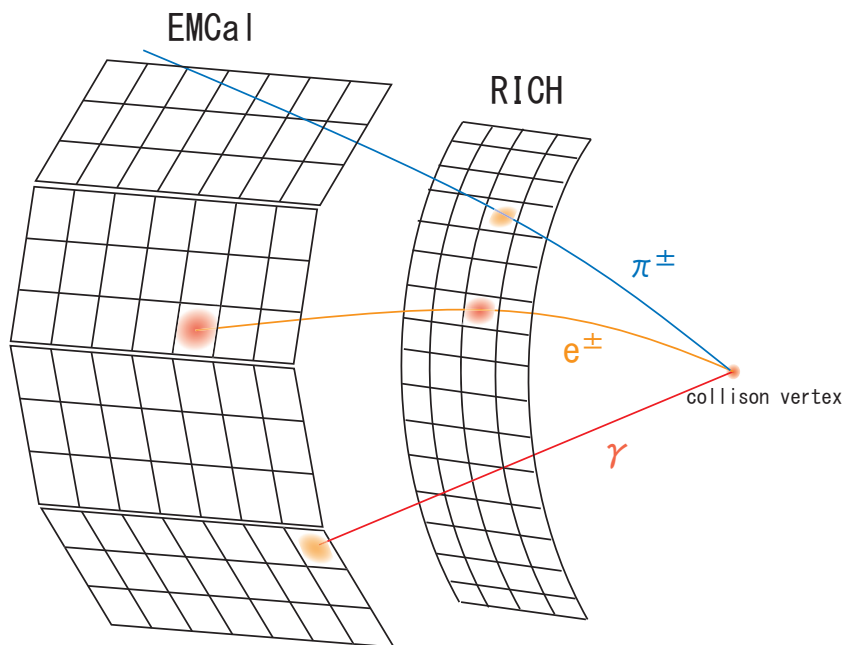


Figure 2.15: schematic view of EMCal RICH level1 Trigger: Both the super-Module of EMCal and RICH are fired for e^+, e^- . Only the EMCal is fired for photon, while only the RICH is fired for high p_T pion. We are able to effectively collect the events including e^+e^- pair.

Chapter 3

Analysis

3.1 Outline of Analysis

In this section, the outline of the analysis is introduced. First, the run and trigger selection is explained in Section 3.2. The methods of track selection to extract electrons from charged hadrons background are described in Section 3.3. By using extracted electrons, the invariant mass of electron and positron are kinematically reconstructed. The procedure of invariant mass reconstruction are introduced in Section 3.4. The background component to invariant mass distribution is explained in Section 3.5. The extraction of raw yield for ω and ϕ is described in Section 3.6. The acceptance, electron ID efficiency and trigger efficiency calculated by using Monte-Carlo simulation are explained in Section 3.7. Finally, the ω and ϕ cross section and systematic uncertainties are presented in Section 3.8.

3.2 Run and Trigger Selection

In proton-proton collisions in year 2004 to 2005 (RUN05), the PHENIX collected 3.8 pb^{-1} as total integrated luminosities which contains 262TByte data as a PRDF(PHENIX Raw Data File) format. 16587 DST(Data Summary Tape) files were made from PRDF. The run number which correspond to $p + p$ collisions in RUN05 is from run168314 to run179846. Run171595 to run172080 are the converter runs where an additional converter (a thin brass sheet of $1.67\% X_0$) was installed around the beam pipe. Run176417 to run176613 are the higher energy runs at $\sqrt{s} = 410 \text{ GeV}$. The normal runs (non-converter runs and $\sqrt{s} = 200 \text{ GeV}$ runs) are analyzed in this work.

The vertex distribution for Minimum Bias triggered events reconstructed by timing information of BBCs is shown in Fig. 3.1. Fig. 3.2 shows the

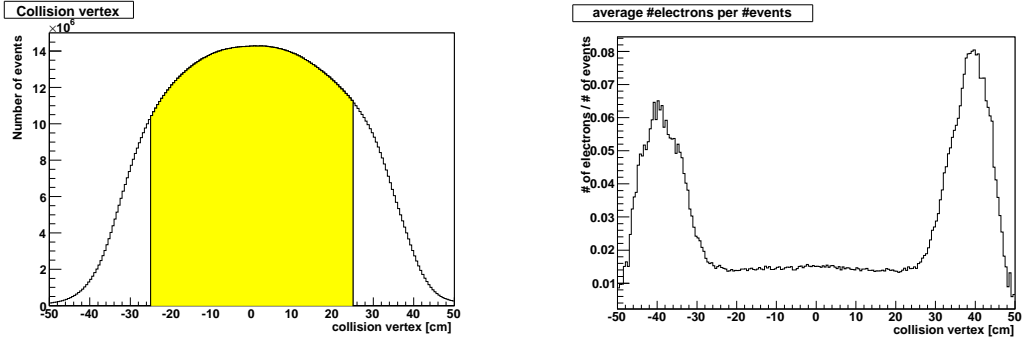


Figure 3.1: Collision vertex distribution. The events in yellow band range are selected for this analysis.

Figure 3.2: number of electrons per events as a function of collision vertex.

average number of electrons per event as a function of the collision vertex. the events with the collision vertex out of ± 25 cm contains the large mounts of conversion electrons generated in detector materials. Therefore, the events with the collision vertex within ± 25 cm of nominal interaction point is selected.

This analysis have done using data samples collected by the Minimum bias trigger(and the ERT trigger that introduced in Section2.4, with the energy threshold setting of 400MeV on the 2x2 EMCAL tower. Fig.3.3 shows the number of electrons per Minimum Bias triggered event as function of run number. If electron yield is less than 2×10^{-4} , these run were rejected from our analysis since the detectors condition were not stable in these run. The yield is very stable until run178937. The electron yield drops after run178937 since two of RICH data packets for ERT trigger were disable. The efficiency for ERT triggered electrons in run169645-169667, 169719-169884, 175815-175831, 175945-175978 were not consistent with one of the nominal runs due to the wrong setting of EMCAL High Voltage. Number of events including these run periods were about 2 % of total luminosity, which were small and removed in this analysis.

Fig.2.4 shows the ratio of the number of Minimum Bias triggered event in the ERT triggered sample and the number of ERT triggered event in the Minimum Bias triggered sample. If there is no file segment lost during data reconstruction, this ratio is equal to unity. Runs with the ratio > 2 or < 0.5 were removed from this analysis.

In PHENIX, the Minimum Bias event in $p + p$ collisions were not fully recorded due to the limited bandwidth of data acquisition as compared to trigger rate. A fraction between recorded and all minimum bias events follows

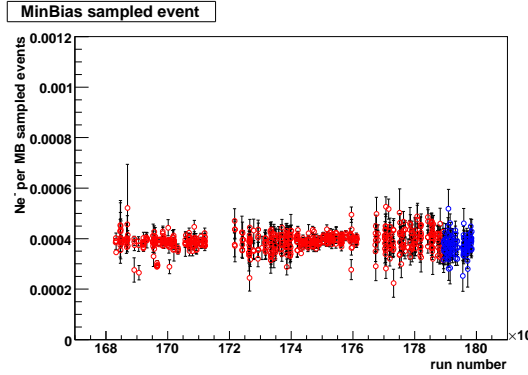


Figure 3.3: Number of electron in $0.3 < p_T < 4.0 \text{ GeV}/c$ per sampled Minimum Bias triggered event as a function of run number.

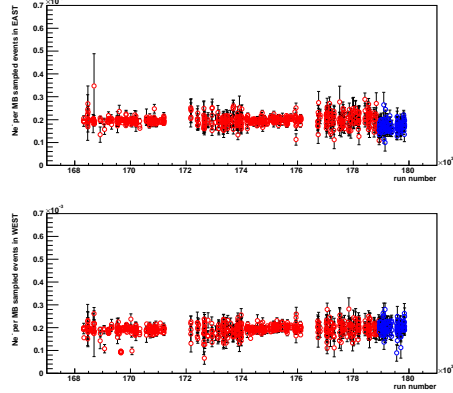


Figure 3.4: Number of electron detected in EAST (top) and WEST (bottom) arms per sampled Minimum Bias triggered event.

the scale down factor, which was specified at the beginning of each run for each triggers and depends on the beam conditions. After run selection, the total number of samples Minimum Bias events corresponding to the ERT trigger set were calculated as follow:

$$\begin{aligned} N_{MB}^{sampled} &= \sum_{run} N_{MB} \times f_{\text{Scale-Down-Factor}} \\ &= 55831.6M \end{aligned} \quad (3.1)$$

where N_{MB} is the number of events recorded with the Minimum Bias trigger and $f_{scale-down-factor}$ is scaled down factor for each run.

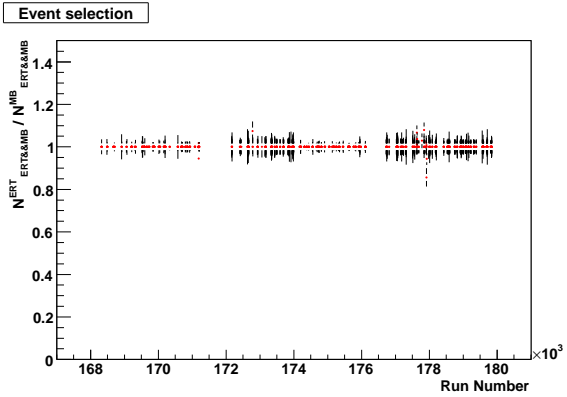


Figure 3.5: $N_{ERT \& MB}^{ERT} / N_{ERT \& MB}^{MB}$ as a function of run number. This ratio should be unity when there is no file segment lost at data reconstruction.

3.3 Track Selection and electron identification (eID)

In this section, the methods of electron identification from charged hadron background are introduced. The fraction of produced electrons in all of charged hadron, mainly pions, is less than 1%. Electrons are identified with RICH and EMCal.

3.3.1 Number of Hit PMT (n0)

The number of fired RICH PMTs in a ring with inner radius of 3.4 and outer radius of 8.4 cm around the projection point of the track onto the PMT plane of RICH. The expected radius of a Cherenkov ring emitted by an electron is 5.9 cm, the width of ± 2.5 cm around it corresponds to the position resolution of the PMT hits.

3.3.2 RHIC match

The absolute displacement of the projection ring center to the measured ring center, determined from RICH PMTs in the ring area between 3.4 and 8.4 cm. The measured ring center is the weighted average of the hit PMT position.

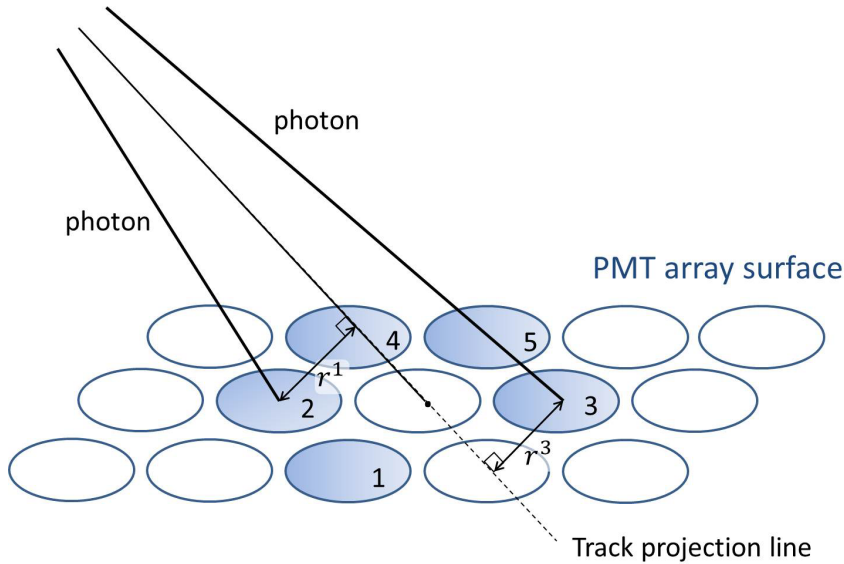


Figure 3.6: Schematic description of the definitions of variable which characterized the RICH ring. The five fit PMTs are shown as an example.

3.3.3 EMC match

EMCal match ($\Delta\phi$)

Distance in ϕ direction between the position of the associated EMCal cluster and the projection on the track onto the EMCal. The distance is normalized by its standard deviation $\sigma_{\Delta\phi}$.

$$\Delta\phi = \frac{\phi_{projection} - \phi_{hit}}{\sigma(\Delta\phi)} \quad (3.2)$$

EMCal match (Δz)

Distance in z direction between the position of the associated EMCal cluster and the projection on the track onto the EMCal. The distance is normalized by its standard deviation $\sigma_{\Delta z}$.

$$\Delta z = \frac{z_{projection} - z_{hit}}{\sigma(\Delta z)} \quad (3.3)$$

The mean and sigma of variables $\sigma_{\Delta\phi}$ and $\sigma_{\Delta z}$ should be zero and one, respectively.

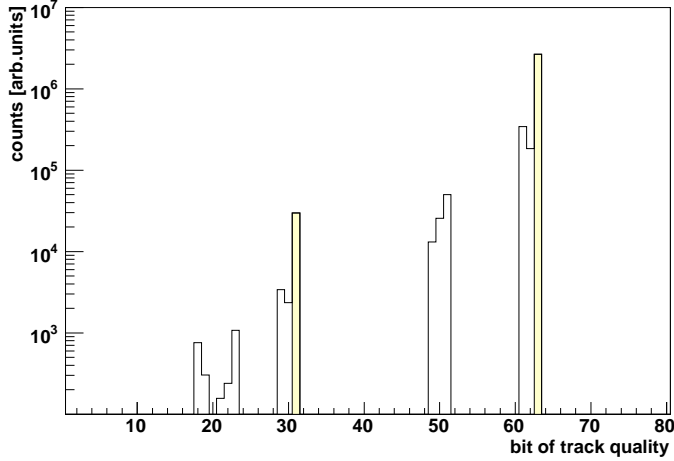
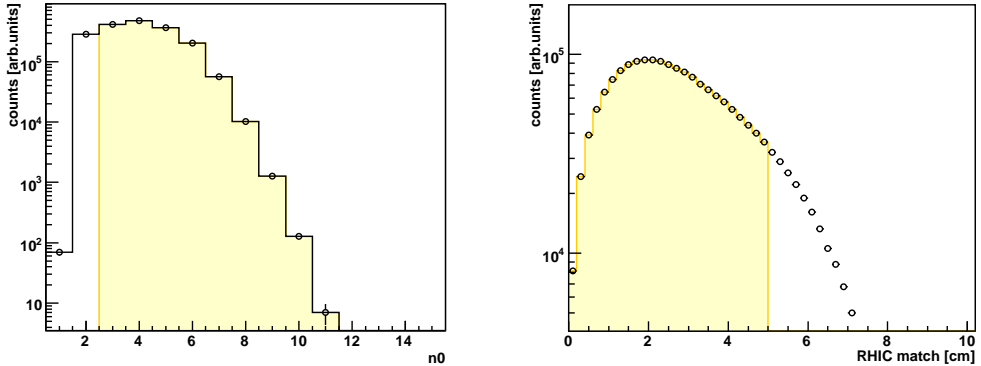


Figure 3.7: Track quality distribution.

Figure 3.8: (distribution of n_0 (left) and $RICH$ matching(right)).

3.3.4 deposition energy over momentum ratio (dep)

The relative deviation of $E/p - 1$, where E is the energy measured by EMCAL, p is the momentum of the track.

$$dep = \frac{E/p - 1}{\sigma(E/p)} \quad (3.4)$$

Figure 3.10 shows the E/p distribution for all charged tracks(black) and for electron candidates(red) which fulfill all the eID cuts listed in Table 3.1 except the dep. The electron mass is light compared to its momentum $p > 200 MeV/c$. In case of electron, deposition Energy into EMCAL(E) over momentum(p) ratio will be $E/p \simeq 1$, since its all energy is deposited into the

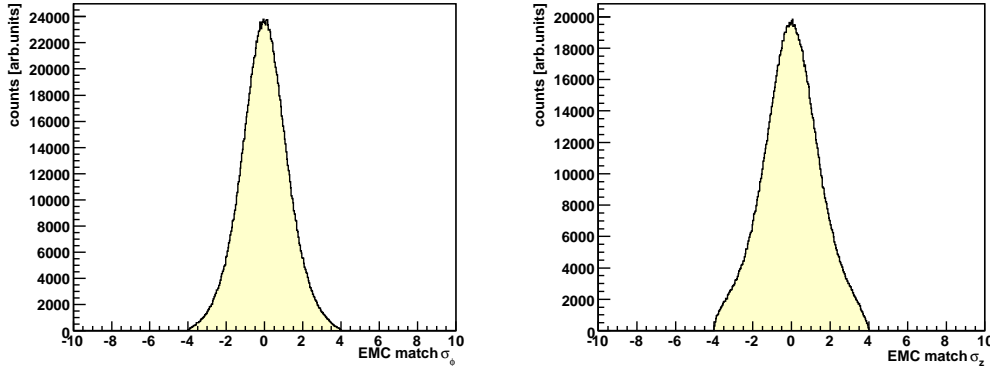


Figure 3.9: distribution of *EMCal matching* for σ_ϕ (left) and σ_z (right)

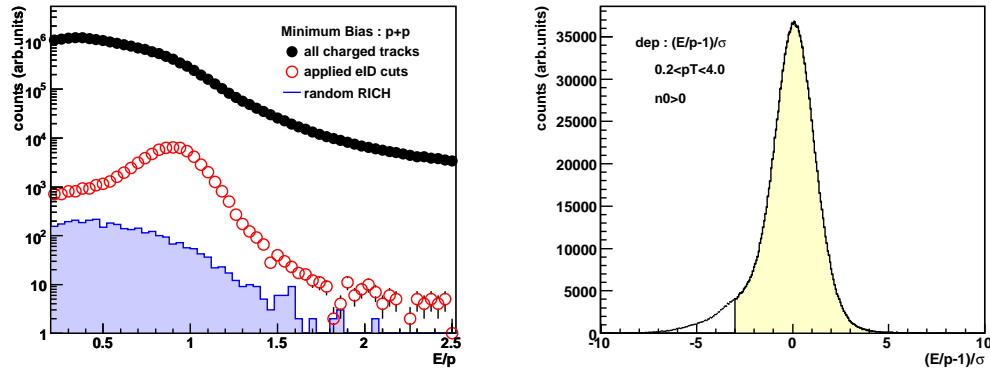


Figure 3.10: (left) E/p distribution in minimum bias event for all charged tracks, for electron candidates and for randomly associated hadrons .(right) dep distribution applying $n0 > 0$.

EMCal due to electromagnetic shower. In contrast, the hadrons only deposit fraction of their energy into EMCal as the result of ionization loss. Therefore, It does't leads the peak structure in E/p distribution. While the distribution of all charged tracks are not seen clear electron peak, the clear peak at $E/p \simeq 1$ is seen when applying eID cuts. Signal-to-background ratio is improved by requiring the eID cuts.

3.4 Fiducial cut

For selecting stable detector condition through the analyzing period, unstable area of DC and EMCal were removed. The relation between the board number

eID cuts	
Track quality	$31 \cup 63$
Number of Hit PMT (n0)	> 2
RHIC match	$< 5 \text{ cm}$
EMC match $\sqrt{\sigma_{\Delta\phi}^2 + \sigma_{\Delta z}^2}$	$< 4 \sigma$
deposition energy over momentum ratio (dep)	$> -3 \sigma$

Table 3.1: Electron ID cuts used in this analysis.

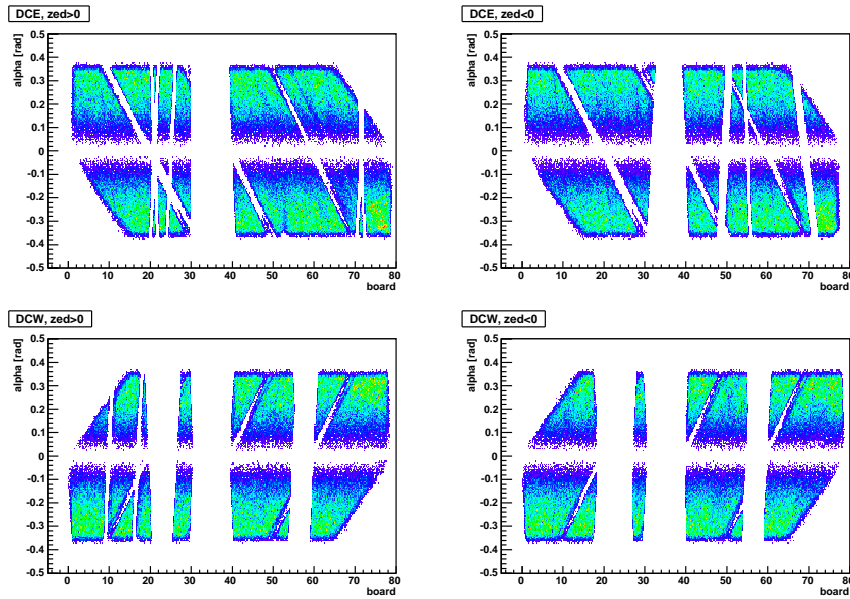


Figure 3.11: Alpha vs board distribution for both sides of the DC East and West after applying the fiducial cuts

in the DC and the azimuthal angle ϕ is as follows:

$$\begin{aligned}
 (\text{East arm})\text{board} &= (3.72402 - \phi + 0.008047 \times \cos(\phi + 0.87851)) / 0.01963496 \\
 (\text{West arm})\text{board} &= (0.573231 + \phi - 0.0046 \times \cos(\phi + 0.05721)) / 0.01963496
 \end{aligned}$$

Using the hardware related coordinates as *board* number can easily identify the malfunction part of detector. Fig.3.11 shows track bending angle α vs *board* distribution for track reconstructed in the East and West side DC after applied the fiducial cuts. Fig.3.12 shows occupancies of EMCAL sectors removed dead and warm towers after applied the fiducial cuts.

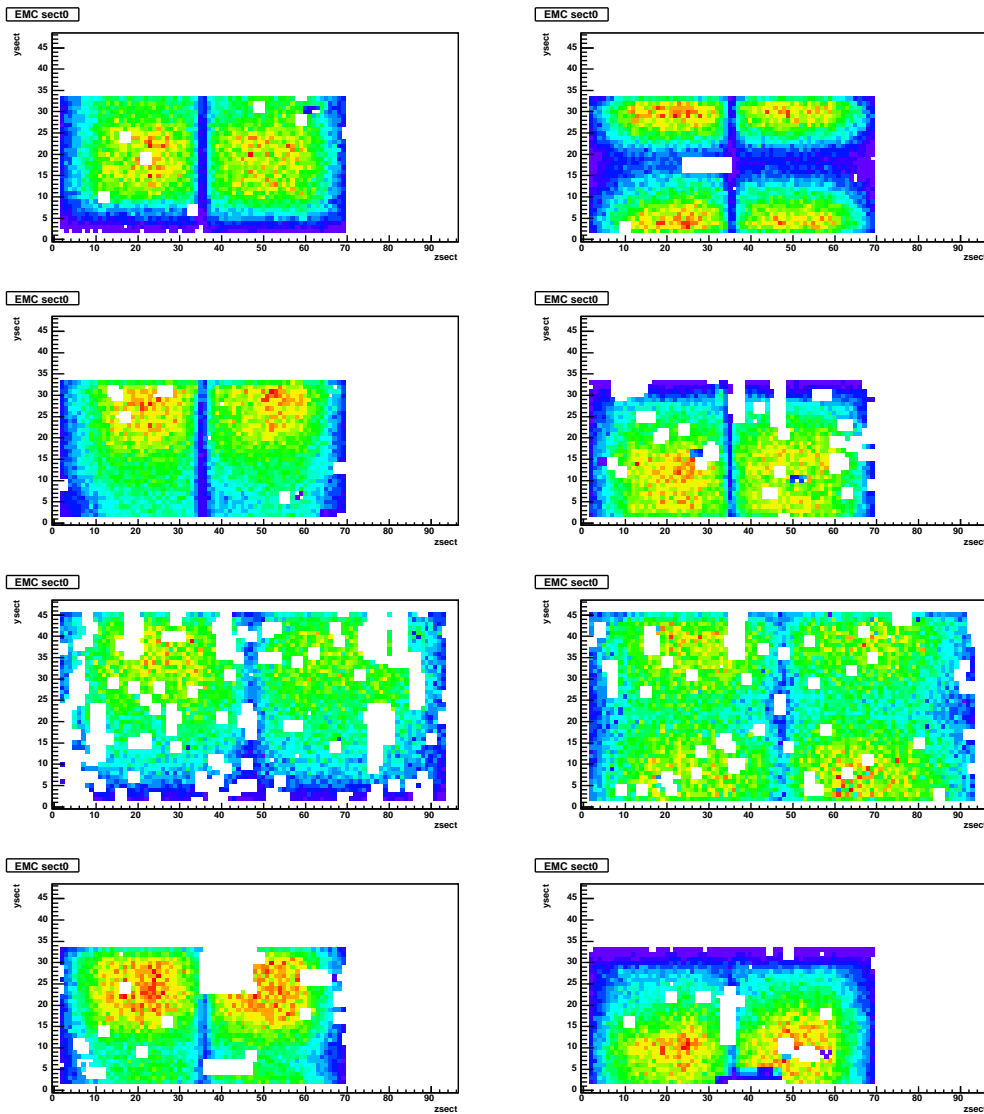


Figure 3.12: Occupancy of EMCal sectors after applying the fiducial cuts

3.5 Pair reconstruction

The invariant mass of electron and positron pairs are calculated from measured energy and momentum of electron and position itself.

$$M_{ee} = \sqrt{(E_{e^+} + E_{e^-})^2 - (\vec{p}_{e^+} + \vec{p}_{e^-})^2} \quad (3.5)$$

where E is the energy of the particle, \vec{p} is particle momentum,

$$(E_{e^+} + E_{e^-})^2 = (\sqrt{m_{e^+}^2 + p_{e^+}^2} + \sqrt{m_{e^-}^2 + p_{e^-}^2})^2 \quad (3.6)$$

and,

$$(\vec{p}_{e^+} + \vec{p}_{e^-})^2 = (p_{e^+x} + p_{e^-x})^2 + (p_{e^+y} + p_{e^-y})^2 + (p_{e^+z} + p_{e^-z})^2. \quad (3.7)$$

p_x, p_y, p_z is written as following,

$$\begin{aligned} p_x &= p \times \sin \theta \cos \phi \\ p_y &= p \times \sin \theta \sin \phi \\ p_z &= p \times \cos \theta \end{aligned}$$

where θ is the polar angle measured from the beam axis and ϕ is the azimuthal angle. The invariant mass distribution are derived by combination all identified e^+e^- pairs.

3.6 Background subtraction

The obtained invariant mass spectra contains all identified electron and positron pairs. To improve signal/background ratio of ω and ϕ mesons, we need to understand source of background and remove it.

1. The background contributed from following is possible to identify in pair-by-pair.
 - (a) Fake electron pair
 - (b) photon conversion pair
2. On the other hand, the following background components are impossible to identified in pair-by-pair. but we are able to subtract statistically.
 - (a) uncorrelated combinatorial background
 - (b) e^+e^- continuum from hardron decay

3.6.1 Fake electron pairs

If the tracks are closer in the detectors, the pairs are candidate of fake electron pairs.

Two tracks share the same Cerenkov ring projection on RICH PMT plane due to the spherical mirror optics of RICH when a track is parallel to a true electron while passing through the RICH radiator. These pairs have a small and correlated opening angle and therefore made correlation in the invariant mass spectrum around $0.5 \text{ GeV}/c^2$.

To eliminate the fake pairs, the cut for the distance between two tracks on z and ϕ plane of each detectors are applied. In Drift Chamber, the cuts applied $\Delta z < 0.5\text{cm}$ and $\Delta\phi < 0.02 \text{ rad}$. In RICH, the cuts applied $\Delta z < 28\text{cm}$ and $\Delta\Phi < 0.07 \text{ rad}$. In addition, the the case of RICH, the cut defined as the angle between two tracks at Drift Chamber called "PFOA(Post-Field Opening Angle)" is also used. Fig.3.14 shows correlation between PFOA(Post-Field Opening Angle) and $\Delta RICH$. $\Delta RICH$ is defined as

$$\Delta RICH \equiv \sqrt{(|\Delta z_{RICH}|/\sigma_z)^2 + (|\Delta\phi_{RICH}|/\sigma_\phi)^2} \quad (3.8)$$

where σ_z and σ_ϕ means 1σ for Δz_{RICH} and $\Delta\phi_{RICH}$ distribution, respectively. If any two tracks fulfill $|\Delta RICH| < 3\sigma$ and PFOA $< 0.25 \text{ rad}$, both of the tracks are eliminated. These cut parameters were determined by comparing real with mixed event as mentioned in Section 3.6.3.

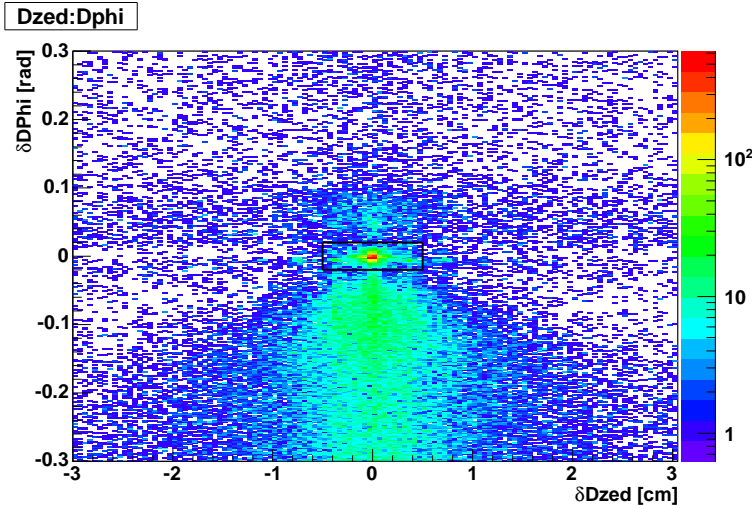


Figure 3.13: $\Delta\phi$ and Δz distribution for pairs of the tracks in DC. The box represents the cut for removed fake pairs in DC.

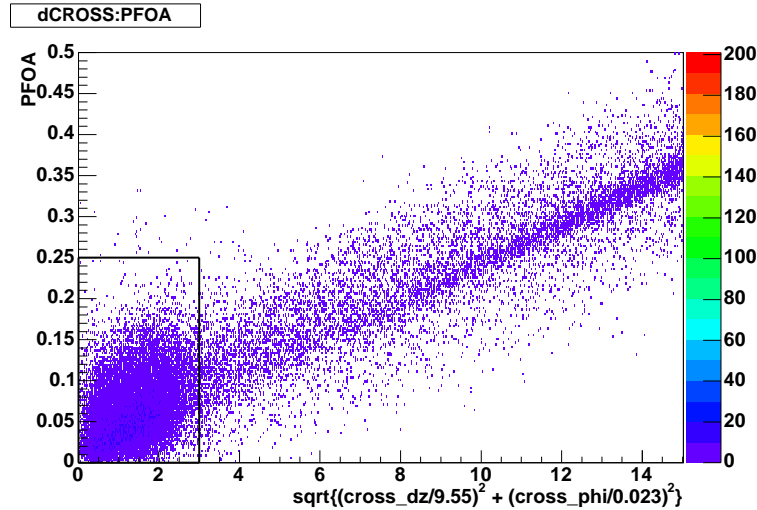


Figure 3.14: The distribution for $PFOA$ and $\Delta RICH$. The detail is in the sentence. The box represents the cut for removed fake pairs for ring sharing tracks.

3.6.2 Photon conversion

The pairs originating from photon conversion in the detector material is reconstructed as background. Tracking algorithm assumes all particles come from collision vertex corresponding azimuthal radial distance $R = 0$. Therefore pairs from photon conversion occurring off vertex($R > 0$ cm) are reconstructed incorrect momentum. Their reconstructed momentum is higher which leads to an fake invariant mass that increase with radial distance between collision vertex and conversion point.

beam pipe material ($R=4$ cm)	$m_{ee} = 20 MeV/c^2$
detector support structures ($R=25$ cm)	$m_{ee} = 125 MeV/c^2$
from the entrance window of DC	$m_{ee} < 300 MeV/c^2$

The procedure to identify the pair of photon conversion is shown below. The opening angle of Conversion pairs is exactly zero since photon is massless. They are bent only azimuthal direction by magnetic field along the beam axis \vec{z} .

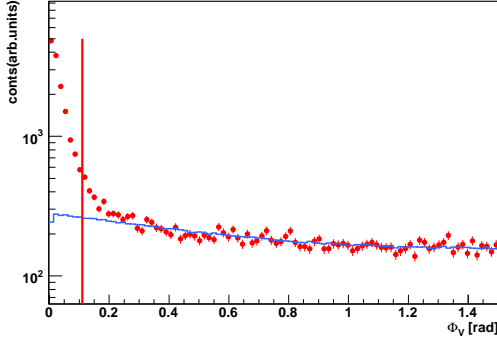


Figure 3.15: Φ_V distribution in the mass range $30 < m_{ee} < 90 \text{ MeV}/c^2$. Blue line shows the Φ_V distribution reconstructed in event mixing which is normalized arbitrary range. Vertical red line on $0.035\pi[\text{rad}]$ indicates cut value in this mass region

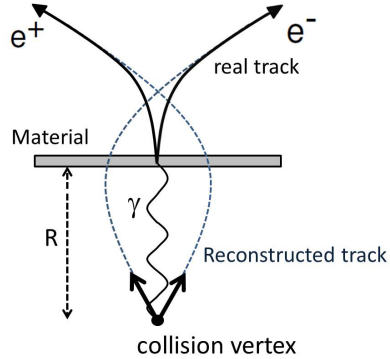


Figure 3.16: Schematic view of conversion pair. The electrons produced at $R > 0$ are reconstructed with incorrect momentum.

$$\vec{u} = \frac{\vec{p}_+ + \vec{p}_-}{|\vec{p}_+ + \vec{p}_-|} \quad (3.9)$$

$$\vec{v} = \frac{\vec{p}_+}{|\vec{p}_+|} \times \frac{\vec{p}_-}{|\vec{p}_-|} \quad (3.10)$$

$$(3.11)$$

We can define the orientation of the actual opening angle as

$$\vec{w} = \vec{u} \times \vec{v} \quad (3.12)$$

We can also define the expected orientation of the opening angle for conversion pairs

$$\vec{w}_c = \vec{u} \times \vec{z} \quad (3.13)$$

Finally, we can define Φ_v as the angle between these two vectors

$$\Phi_V = \cos^{-1}(\vec{w} \cdot \vec{w}_c) \quad (3.14)$$

The filled blue histogram in Fig.3.17 for di-electron mass distribution is shown as contribution of the conversion pairs.

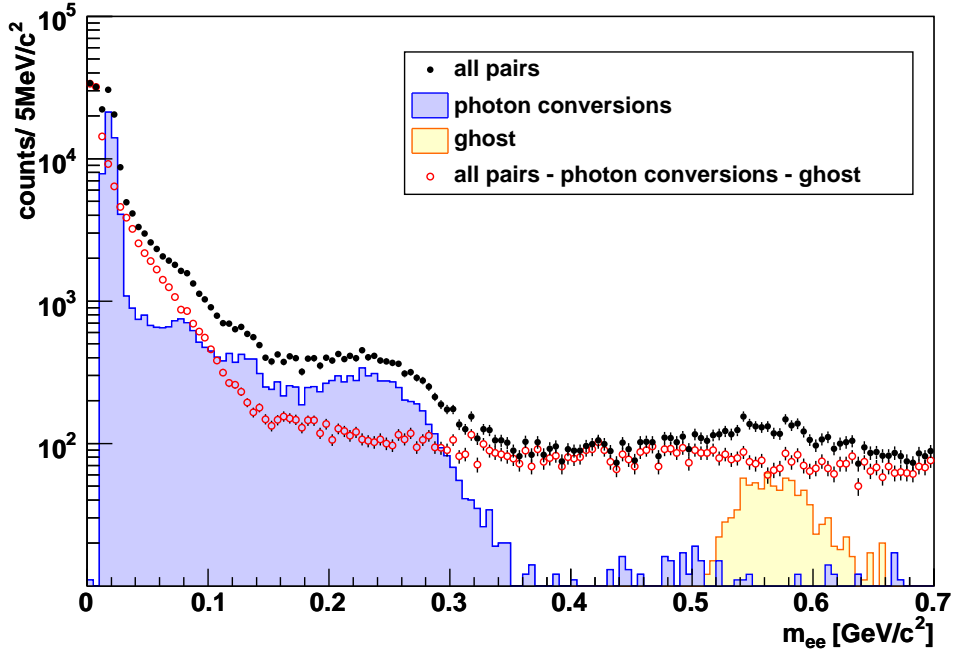


Figure 3.17: Invariant mass distribution for all e^+e^- pairs. The filled yellow histogram shows the ghost pairs. The filled blue histogram shows the pairs removed by the phiV angle cut.

3.6.3 Combinatorial background

Combinatorial background arise as a result of all the combinations of two electrons which origin is uncorrelated. Uncorrelated combinatorial background can be statistically reproduced by mixed event technique, which combines tracks from different events. The mixed event is generated by combining the all of the electrons in one event and the all the electrons in another events which have the similar event topology. Since the tracks are from different events, this technique reproduces the uncorrelated background by definition. This technique also generate the background shape with negligible statistical errors since the background has much statistics related to accumulate number of event in buffer.

In this analysis, we used ERT trigger event sample in which at least one high p_T electron must be required at event by event. If mixed events background is reconstructed using ERT trigger event sample, the background can't represent true uncorrelated background shape due to the trigger bias. Therefore The mixed events background should be constructed from Minimum Bias event sample requiring that at least one of the two electrons fired the ERT

trigger. That pairs can represent true uncorrelated background reconstructed in ERT trigger event sample.

The reproduced combinatorial background is needed to be normalized. unlike-sign spectrum N_{+-} reconstructed e^+e^- pairs in same event, like-sign spectra N_{++} and N_{--} reconstructed e^+e^+ and e^-e^- in same event, respectively.

$$N_{+-} = N_{+-}(m_{ee}, p_T), \quad B_{+-} = B_{+-}(m_{ee}, p_T) \quad (3.15)$$

$$N_{++} = N_{++}(m_{ee}, p_T), \quad B_{++} = B_{++}(m_{ee}, p_T) \quad (3.16)$$

$$N_{--} = N_{--}(m_{ee}, p_T), \quad B_{--} = B_{--}(m_{ee}, p_T) \quad (3.17)$$

As long as both electrons and positrons are produced in one event, the size of the unlike-sign combinatorial background is given by the geometric mean of the number of positive and negative like-sign pairs: $B_{+-} = 2\sqrt{B_{++}B_{--}}$.

Measured all unlike-sign pairs contains correlated pairs originating from other hadron decay as shown in Section 3.6.4. In case of like-sign pairs, there is no contribution from other hadron decay due to no existence decay into e^+e^+ or e^-e^- pairs. But even if the measured like-sign pairs has correlation parts which origin from follows:

- the pairs originating from same jet which have strong correlation on $\Delta\phi \sim 0$ or $\pi[\text{rad}]$
- pairs from decay in $\pi 0 \rightarrow (e^+e^-\gamma \text{ or } \gamma\gamma) \rightarrow e_1^+e_1^-e_2^+e_2^-$

By study of Monte Carlo simulation, we found the region as shown in Fig. 3.18 in 2 dimensional space of p_T vs mass is less contributed from correlated like-sign pairs [89]. Integration of the N_{++} and N_{--} in region A is used for calculation of normalization factors to avoid counting the number of correlated pairs.

$$N'_{++} = B_{++} \frac{\int_A N_{++}}{\int_A B_{++}} dm_{ee} dp_T \quad (3.18)$$

$$N'_{--} = B_{--} \frac{\int_A N_{--}}{\int_A B_{--}} dm_{ee} dp_T \quad (3.19)$$

The absolute normalization factor α is expressed as follow:

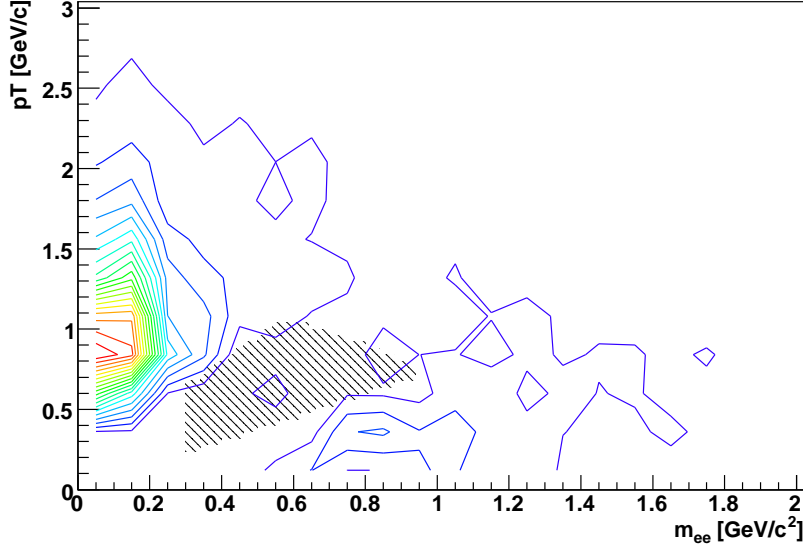


Figure 3.18: like-sign pairs distribution as a function of mass and pair p_T after subtraction of mixed event background. The background is normalized in the normalization area A shown as the dashed area.

$$\alpha = \frac{2\sqrt{N'_{++} \times N'_{--}}}{B_{+-}} \quad (3.20)$$

$$= \frac{2\sqrt{B_{++} \frac{\int_A N_{++}}{\int_A B_{++}} \times B_{--} \frac{\int_A N_{--}}{\int_A B_{--}}}}{B_{+-}} \quad (3.21)$$

$$= \sqrt{\frac{\int_A N_{++} \times \int_A N_{--}}{\int_A B_{++} \times \int_A B_{--}}} \quad (3.22)$$

The invariant mass distribution are shown in Fig.3.19 for all p_T and Fig.3.20 as divided by nine p_T bins of $0 < p_T < 0.25$, $0.25 < p_T < 0.5$, $0.5 < p_T < 0.75$, $0.75 < p_T < 1.0$, $1.0 < p_T < 1.25$, $1.25 < p_T < 1.5$, $1.5 < p_T < 1.0$, $1.5 < p_T < 2.0$, $2.0 < p_T < 4.0$. The combinatorial background contribution evaluated by event mixing technique and normalized by absolute normalization factor α is shown as blue line in Fig.3.19 and Fig.3.20.

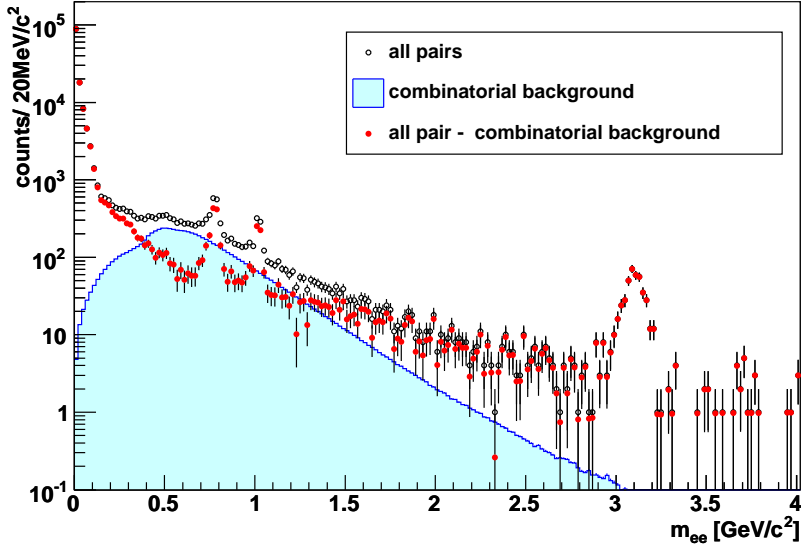


Figure 3.19: invariant e^+e^- mass spectrum. The blue line indicate combinatorial background evaluated by the event mixing method.

3.6.4 continuum contribution

In the remaining di-electron mass spectra represents contribution of correlated pairs so-called continuum, originated from various hadron decay into di-electron mainly as follows; $\pi^0 \rightarrow \gamma e^+e^-$, $\eta \rightarrow \gamma e^+e^-$, $\rho, \omega, \phi \rightarrow e^+e^-$, $J/\Psi \rightarrow e^+e^-$ and open charm $c\bar{c}$. The shape of continuum from other hadrons in the mass range of 0.5 to 1.2 GeV/c^2 and assumed as exponential function + constant. The amount of the contribution for ω and ϕ mesons were approximately less than factor of 0.1 and 0.3, respectively.

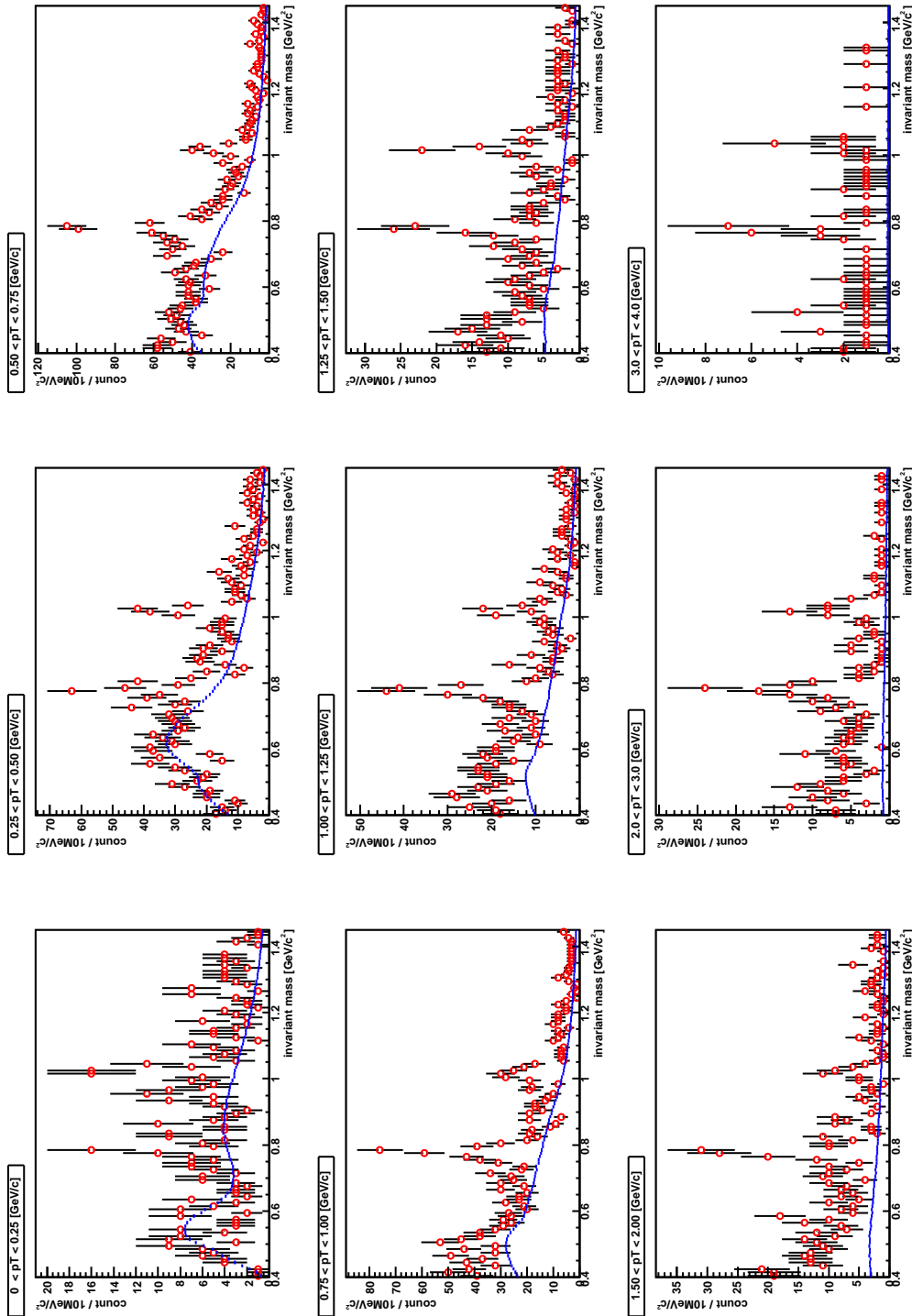


Figure 3.20: Invariant mass spectra divided by pT bins. The blue line indicate combinatorial background evaluated by the event mixing method.

3.7 Signal Extraction

3.7.1 Spectral Shape of Resonances

Spectral shape of resonances were generated using the relativistic Breit-Winger distribution

$$rBR(m) = \frac{m^2 \Gamma_{tot}(m) \Gamma_{ee}(m)}{(m^2 - m_0^2)^2 + m_0^2 \Gamma_{tot}(m)^2} \quad (3.23)$$

with the pole mass, m_0 , total decay width, $\Gamma_{tot}(m)$ and the energy dependent partial decay width of the vector meson going to e^+e^- , $\Gamma_{ee}(m)$.

$\Gamma_{tot}(m)$ and $\Gamma_{ee}(m)$ can be parametrized as

$$\Gamma_{tot}(m) = \frac{m}{m_0} \Gamma_{tot} \quad (3.24)$$

$$\Gamma_{ee}(m) = \frac{m_0^3}{m^3} \Gamma_{ee} \quad (3.25)$$

where Γ_{tot} is the natural decay width, Γ_{ee} is the partial width of the vector meson decaying into e^+e^- . The values of the natural decay widths and pole masses of vector mesons are shown in table 3.2

Due to the finite detector resolution, the spectral shape smeared. therefore the relativistic Breit-Winger function is convoluted by Gaussian. The sigma of the Gaussian is obtained by simulation as mention later in Sec.xxx.

	mass [MeV/ c^2]	Γ_{tot} [MeV/ c^2]	$c\tau$ [fm]	Γ_{ee}/Γ_{tot}
ρ	771.1	149.2	1.3	0.454×10^{-4}
ω	782.57	8.44	23.2	0.695×10^{-4}
ϕ	1019.456	4.26	46.2	2.96×10^{-4}

Table 3.2: The pole masses and natural decay widths of the vector mesons taken from the PDG [48]

Radiative tail correction

The internal radiative correction to e^+e^- was estimated. The observation of radiative decays $J/\psi \rightarrow e^+e^-\gamma$ was reported and the result is consistent with a QED calculation based on final state radiation [90]. The internal radiative decay is described by the diagrams shown Figure 3.21.

An analytic formula for the di-lepton mass spectra in radiative decays is derived [91]. The fraction of decays corresponding to the emission of hard

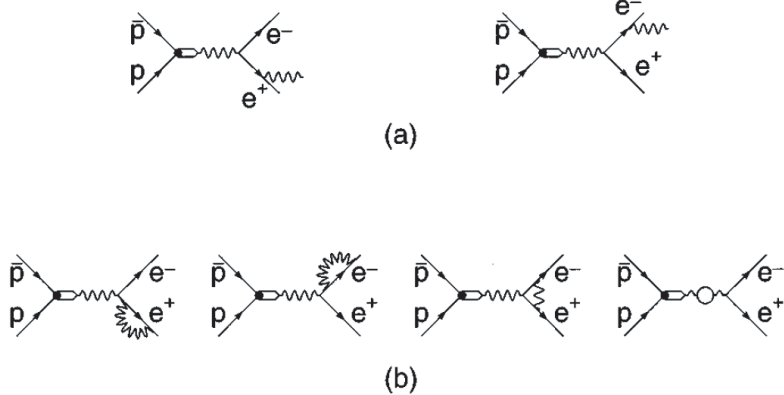


Figure 3.21: Diagrams for final state radiation [90]. The decay into $e^+e^-\gamma$ is described by (a). The infrared divergence in the decay is canceled by interference with the diagrams in (b).

photons is

$$C_{hard} = \frac{\alpha}{2\pi} \left[4 \ln \frac{M}{2E_{min}} \left(\ln \frac{M^2}{m_l^2} - 1 \right) - 3 \ln \frac{M^2}{m_l^2} - \frac{2}{3}\pi^2 + \frac{11}{2} \right] \quad (3.26)$$

where E_{min} is the minimal photon energy, M is a mass of parent particle and m_l is a mass of leptons. The di-lepton mass m is shifted by photon emission

$$m = \sqrt{M(M - 2E_\gamma)} \approx M - E_\gamma (E_\gamma \leq M) \quad (3.27)$$

Hard photon emission cause a tail towards lower mass in the di-lepton mass spectrum. The distribution $P(m)$ of the di-lepton mass in the radiative decay is described as

$$P(m) = \frac{\alpha}{\pi} \frac{2m}{(M^2 - m^2)} \left(1 + \frac{m^4}{M^4} \right) \left(\ln \frac{1+r}{1-r} - r \right) \quad (3.28)$$

where $r = \sqrt{1 - 4m_l^2/m^2}$ is also a function of m . For instance, fig. 3.22 shows the de-electron mass spectra in the radiative decay $\phi \rightarrow e^+e^-\gamma$ for $E_{min} = 10\text{MeV}$. The broad curve is expressed as smeared spectra by detector mass resolution of $10\text{MeV}/c^2$.

Measured resonance peak of ω and ϕ meson were fit into the function of relativistic Breit-Wigner plus radiative tail which were convoluted by Gaussian as the detector mass resolution obtained Monte Carlo simulation as shown in Section 3.8.1.

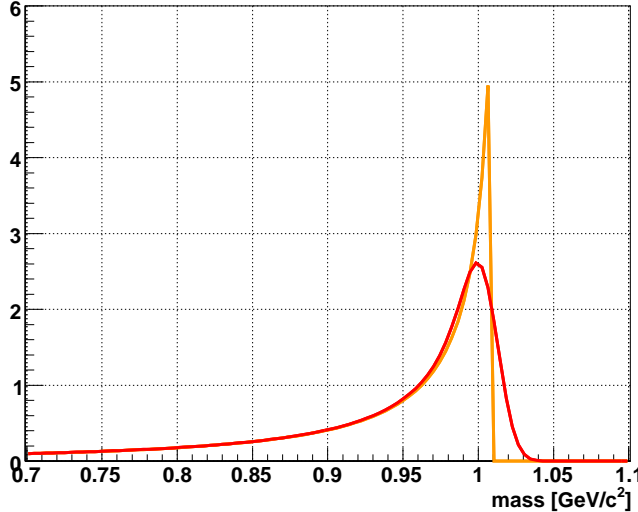


Figure 3.22: e^+e^- mass spectrum in the radiative decay $\phi \rightarrow e^+e^-\gamma$ for $E_{min} = 10\text{MeV}$ (orange) smeared with 10MeV (red).

3.7.2 Signal extraction

Number of signal S was obtained $N^{+-} - B$. The remaining background is contribution from continuum of other hadons. We assumed the shape of the continuum on the mass range of ω and ϕ is exponential. To obtain background contribution on the mass range of ω and ϕ meson, the invariant mass distribution is fit into following function

$$\begin{aligned}
 f(m_{ee}) &= \text{Gaussian convoluted (r.BW + radiative tail)} \\
 &+ \text{Breit Wigner} \\
 &+ \text{(exponential + constant)}
 \end{aligned} \tag{3.29}$$

The first term is for ω and ϕ mesons. The second term, Breit-Winger, is for ρ mesons. Finally, the function of exponential + constant is for remaining background by continuum contribution.

The fitting parameters for ω and ϕ mesons were the peak amplitude, mass center and the width Γ_{tot} while the experimental mass resolution are fixed to the value obtained by Monte Carlo simulation as mention Section xx. In addition, mass center and the width Γ_{tot} for ρ mesons are fixed to PDG value. The experimental mass resolution is not included for ρ mesons since the Γ_{tot}

of ρ meson is much broader than resolution. The ratio between the number of ρ and ω meson were fixed. The ω / ρ ratio is fixed to 1.53, which obtained by ration of branching into $e^+ + e^-$ with the assumption that the production yields of ω and ρ were same. Then, we assumed that the production cross section of ω and ρ is same. The fitting result for invariant mass spectra as a function of p_T were shown in Fig.3.23.

The number of ω and ϕ was obtained by counting the number of entries within 3σ on the each peaks, and subtracted the contribution of background B contained hadron continuum and ρ meson.

Fig.3.24 shows raw yields for ω and ϕ mesons, ρ meson contribution, combinatorial background, remaining background as exponential function + constants and the sum of all components, divided by bin width of p_T and number of used events as a function of p_T .

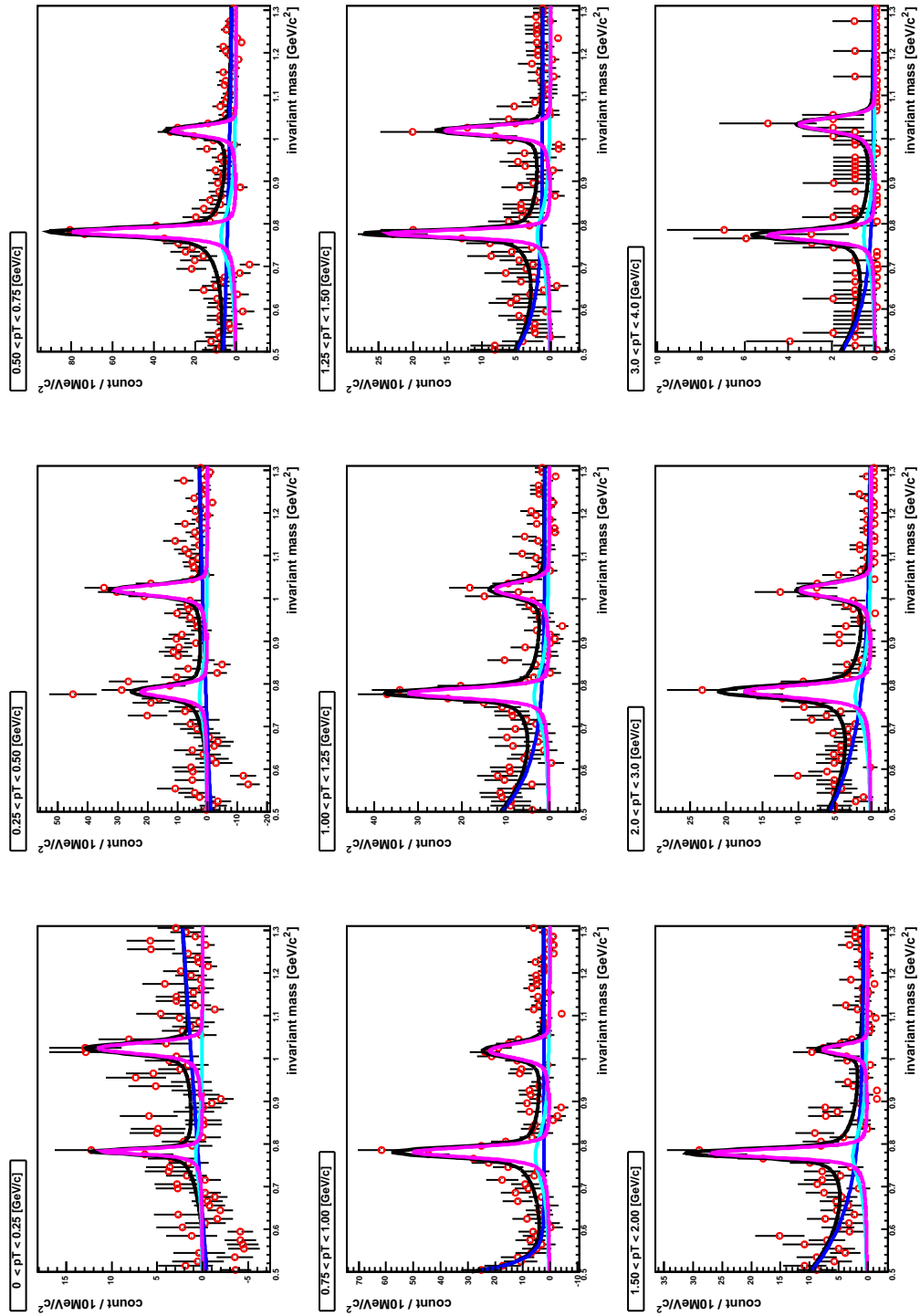


Figure 3.23: Invariant mass spectra divided by pT bins after background subtraction. The black line are the fitting result, which is sum of the known decays, ω (left magenta line), ϕ (right magenta line), radiative decay of ω and ϕ (orange line) and BG(blue line).

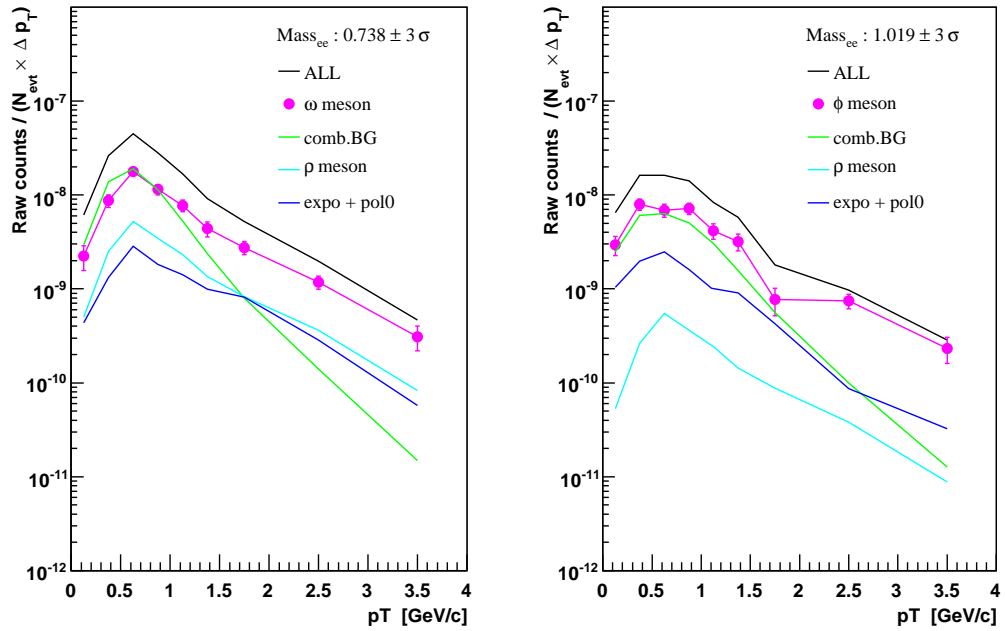


Figure 3.24: Raw counts in counting range for ω (left) and ϕ (right) mesons as a function of p_T . The black lines show all contributions, the magenta points show ω (left) and ϕ (right) mesons including statistical errors, green line lines show combinatorial background, the light blue lines show ρ mesons, and blue lines show exponential+polynomial as contribution of other hadron continuum.

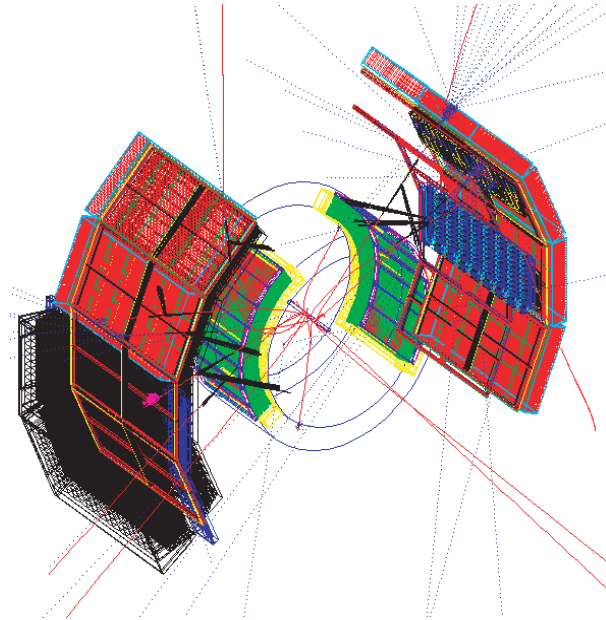


Figure 3.25: The PHENIX central arm detectors represented in GEANT simulation

3.8 Monte Carlo simulation

3.8.1 Reconstruction efficiency

The detector acceptance was determined by single particle Monte Carlo simulation. The ω and ϕ mesons were generated and decay into e^+e^- by using single particle event generator, EXODUS. The ϕ and ω mesons were uniformly generated within $|y| < 0.5$ in rapidity and full azimuthal angle of $0 < \Phi < 2\pi$, and the z-vertex within $|z| < 30\text{cm}$. The generated transverse momentum range was 0 to $5\text{GeV}/c$ which enough covered the measured range of signal extracted from data. The generated transverse momentum spectra were weighted to much the measured particle spectra.

The PHENIX detector simulation was based on GEANT code, called PISA ("PHENIX Integrated Simulation Application"), which including detector performance of momentum, spacial, energy resolutions. In addition, PISA tracks secondary particles generated from the interaction with represented detector materials. Indeed the simulation data should be reproduced same detector performance with real data. The detector acceptance for single electron on ϕ and z direction, each electron identification parameters were compared to confirm consistency between simulation and real data. In fig.3.28 shows the ϕ distribution for single electron and positron with North

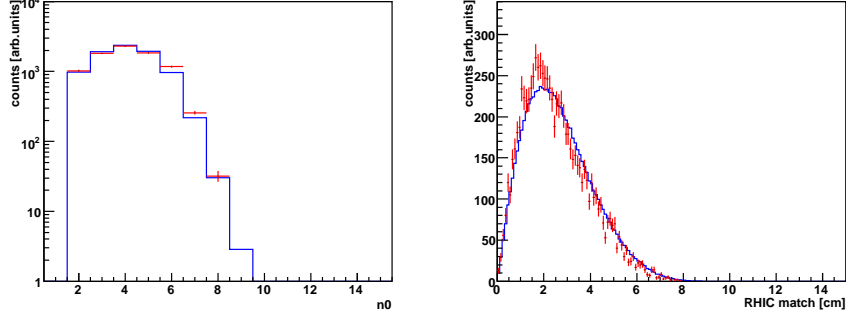


Figure 3.26: Left panel) RICH n0. Right panel) RICH displacement.

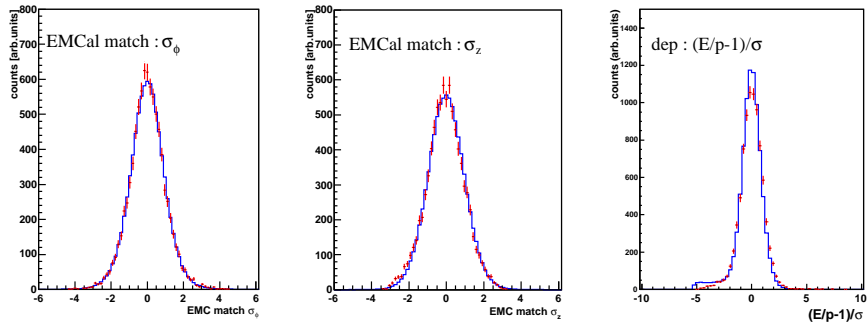


Figure 3.27: Left panel) EMC match for ϕ direction. Middle panel) EMC match for z direction. Right panel) Energy over momentum ratio normalized that width : *dep* direction.

and South side of Drift Chamber in the real and simulated data. The simulated ϕ distribution is weighted by appropriate electron p_T distribution in real data. The simulated data is scaled such that the integral of the whole range of ϕ distribution in the real and simulated data are agreed.

The electron identification parameters of RICH, $n0$ and displacement are shown in Fig.???. The electron identification parameters of EMCal matching for ϕ and z direction are shown in Fig.???. The electron identification parameters of Energy momentum ratio is shown in Fig.???. The systematic uncertainty of the acceptance is estimated due to a little discrepancy of the acceptance between the real and simulation data.

The same analysis code was used for reconstruction of simulated and real data. The invariant mass spectra for ω and ϕ mesons reconstructed e^+e^- in simulation are shown in left panel of Fig.3.30 and Fig.3.31, respectively. The spectra can be described by the function of Gaussian convoluted relativistic Breit-Wigner, where the term of the width of Gaussian will reproduce the

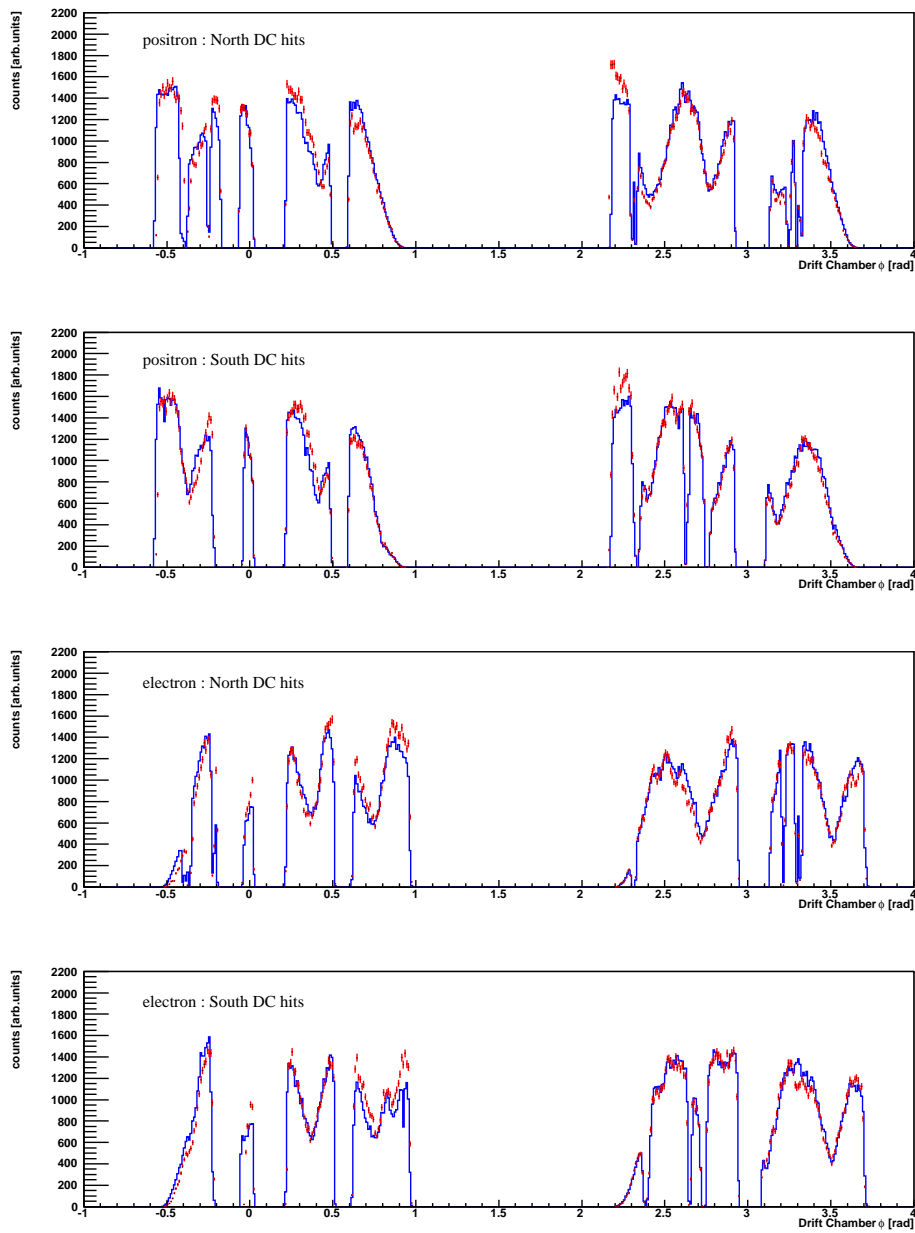


Figure 3.28: Comparison of Drift Chamber hit distribution for ϕ direction in the real data(red) and simulation data(blue). The p_T range of the electron is $0.3 < p_T < 4.0 \text{GeV}/c$ for both real and simulation data.

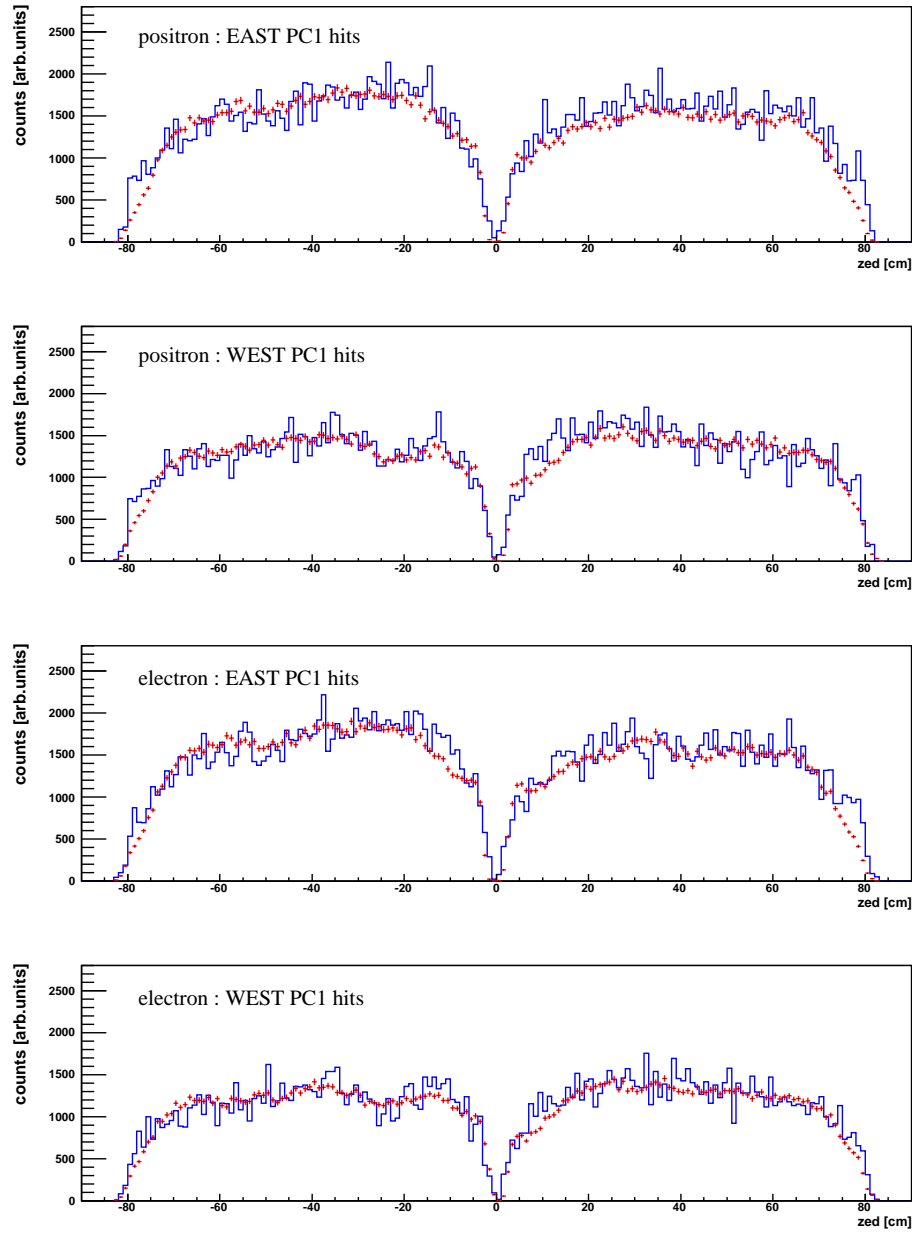


Figure 3.29: Comparison of PC1 hit distribution for *z* direction in the real data(red) and simulation data(blue). The p_T range of the electron is $0.3 < p_T < 4.0 \text{ GeV}/c$ for both real and simulation data.

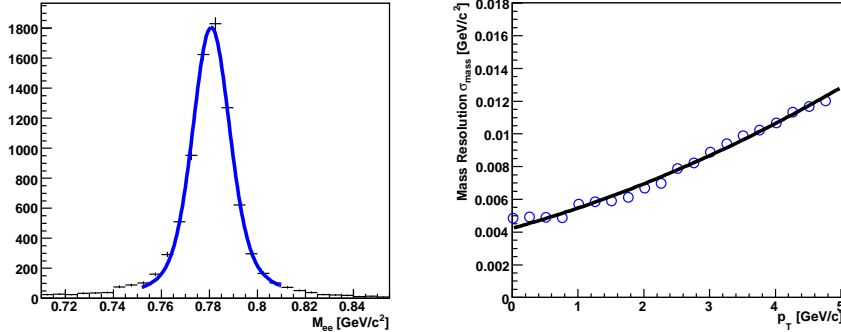


Figure 3.30: Left panel) The invariant mass spectra for ω meson reconstructed e^+e^- in simulation for the $1.0 \leq p_T < 1.25$ GeV/ c . The solid line shows Gaussian convoluted relativistic Breit-Winger function. Right panel) p_T dependent detector mass resolution.

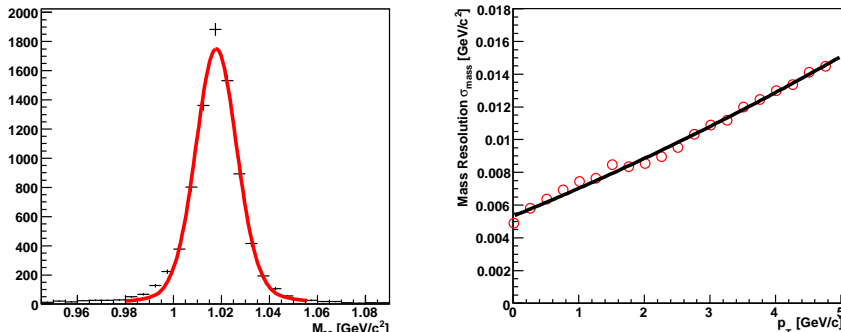


Figure 3.31: Left panel) The invariant mass spectra for ϕ meson reconstructed e^+e^- in simulation for the $1.0 \leq p_T < 1.25$ GeV/ c . The solid line shows Gaussian convoluted relativistic Breit-Winger function. Right panel) p_T dependent detector mass resolution.

detector mass resolution mainly related to momentum resolution of PHENIX detectors. The detector mass resolution for the mass range of ω and ϕ mesons are shown as a function of p_T in right panel of Fig.3.30 and Fig.3.31, respectively.

The reconstruction efficiency is calculated as the ratio of the number of fully reconstructed particle to the number of generated particle. Fig3.32 shows the reconstruction efficiency as a function of transverse momentum of ω and ϕ meson. the curve take into account for the detector geometry, particle decay kinematics, analysis cuts for electron identification.

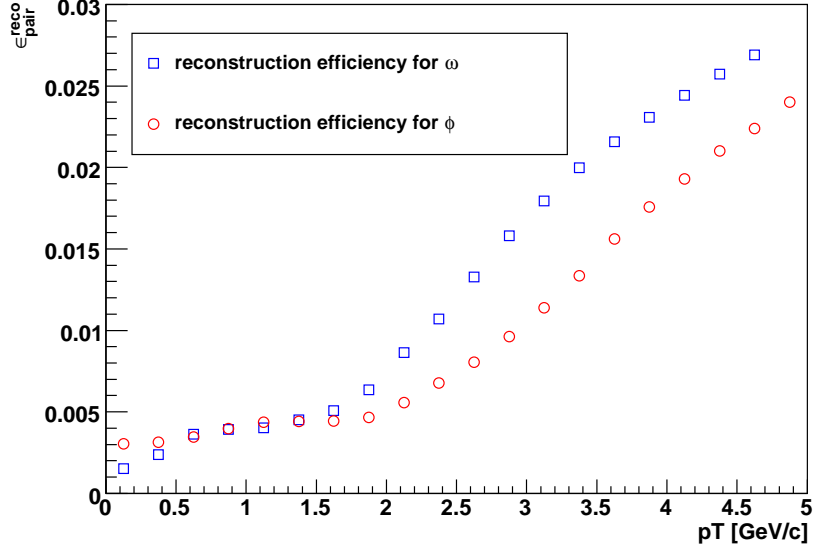


Figure 3.32: Reconstruction efficiency for ω and ϕ mesons ϵ_{pair}^{reco} as a function of p_T .

3.8.2 ERT trigger efficiency

The efficiency of ERT trigger for single electron is determined in sector-by-sector using Min.Bias event sample therefore Min.Bias trigger sample contains ERT trigger sample. We are able to identified the electron which fires ERT trigger tile(both RICH and EMCAL Super Module). The single electron ERT trigger efficiency was calculated as the ratio of number of triggered electrons to number of all electrons for each sectors and shown in Fig.3.33 as a function of transverse momentum.

The curve is steeply growing up and half of the hight is corresponding to approximately EMCAL trigger threshold of 400MeV. The reason why trigger efficiency is below 100% is due to the inactive area of the RICH ERT efficiency.

The curve of trigger efficiency for single electron is described as

$$f(p_T) = \epsilon \times Erf(\frac{p_T - a}{\sigma}) \quad (3.30)$$

$$Erf(x) = \frac{2}{\sqrt{\pi}} \int_0^x e^{-t^2} dt \quad (3.31)$$

where ϵ , a , σ are free parameters.

For the evaluating the ERT trigger efficiency for ω and ϕ meson this curve for single electron is embedded into Monte Carlo simulation as was used for reconstruction efficiency calculation. At first we required that the both

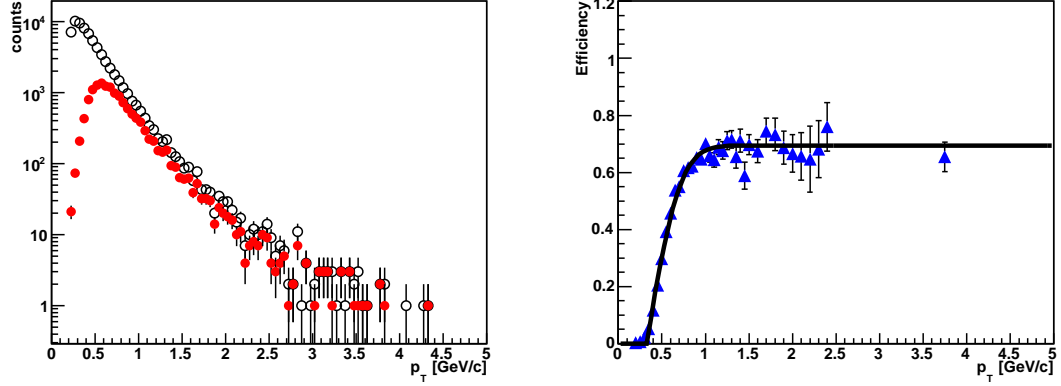


Figure 3.33: (left) The p_T distribution for single electron in MB(black) and fired ERT(red). (right) Trigger efficiency for single elecrons ϵ_{single}^{ERT} as a function of p_T .

electron and positron are reconstructed within PHENIX acceptance without the ERT trigger requirement. Then, for the all sectors of EMCAL associated with electrons, we generated a random number between 0 to 1 and compared it to the magnitude of the curve shown Eq.xx at the same transverse momentum. The particle was considered to fire the ERT trigger if at least one of the randomly generated numbers was lower than the corresponding magnitude of the curve. The probability of fire the ERT trigger for ω and ϕ mesons is shown in Fig.3.34.

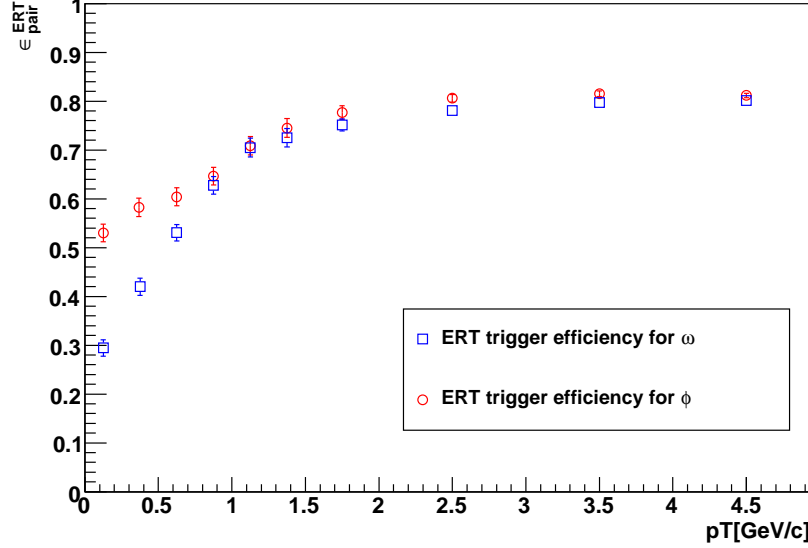


Figure 3.34: Trigger efficiency for ω (blue) and ϕ (red) mesons $\epsilon_{\text{pair}}^{\text{ERT}}$ as a function of p_T .

3.9 Invariant differential cross section

The invariant differential cross section for ϕ and ω production as a function of p_T in $p + p$ collisions can be written as follows;

$$\frac{E}{dp^3} \frac{d^3\sigma}{dp^3} = \frac{1}{2\pi p_T} \frac{d^2\sigma}{dp_T dy} \quad (3.32)$$

$$= \frac{1}{2\pi p_T} \frac{1}{\mathcal{L}} \frac{1}{BR} \frac{1}{\epsilon_{\text{bias}} \epsilon_{\text{pair}}^{\text{reco}} \epsilon_{\text{pair}}^{\text{ERT}}} \frac{N_{\omega,\phi}(\Delta p_T)}{\Delta p_T \Delta y} \quad (3.33)$$

with integrated luminosity

$$\mathcal{L} = \frac{N_{\text{event}}^{MB}}{\sigma_{BBC}}, \quad (3.34)$$

where

- N_{event} is the Number of MinBias sampled events.
- BR is branching ratio into e^+e^- , $7.28 \pm 0.14 \times 10^{-5}$ for ω meson and $2.95 \pm 0.03 \times 10^{-4}$ for ϕ meson.
- Δp_T is the width of p_T bin.

- ϵ_{pair}^{reco} is the acceptance and reconstruction efficiency.
- ϵ_{pair}^{ERT} is the ERT trigger efficiency.
- $\sigma_{BBC} = 23.0 \pm 2.2 [\text{mb}]$ is the Minimum Bias trigger cross section. The efficiency of the minimum bias trigger is estimated to be $55 \pm 5\%$ of total inelastic cross section of $\sigma_{inel}^{pp} = 42 \pm 3 \text{mb}$.
- $\epsilon_{bias} = 0.79 \pm 0.02$ is the minimum bias trigger efficiency for events containing meson.

Bin shift correction

The bin shift correction was applied to take into account the finite width of p_T bins used in the analysis. The measured yield in each p_T bins is not the value at the center of p_T bin but the average in the p_T bin. The bin width is large and/or the spectra is steeply fall, then this effect is more significant. To correct for this effect, we moved the data point vertically and leave the p_T of the data point.

The procedure is below. At first the data points were fit into the Levy function $f(p_T)$ which can be approximately described real spectra shape. the correction factor r , which is the ratio between the average yield in this p_T bin and the value of the function at the bin center p_T^C , can be calculated as

$$r = \frac{\frac{1}{\Delta} \int_{p_T^C - \Delta/2}^{p_T^C + \Delta/2} f(p_T) dp_T}{f(p_T^C)} \quad (3.35)$$

where Δ is the bin width. The corrected yield in the given p_T bin is then calculated as

$$dN/dp_T|_{corrected} = \frac{dN/dp_T|_{uncorrected}}{r} \quad (3.36)$$

The effect of this bin shift correction is approximately a few % in $\Delta p_T = 1 \text{GeV}/c$ and shown in Fig.3.35 and Fig.3.36.

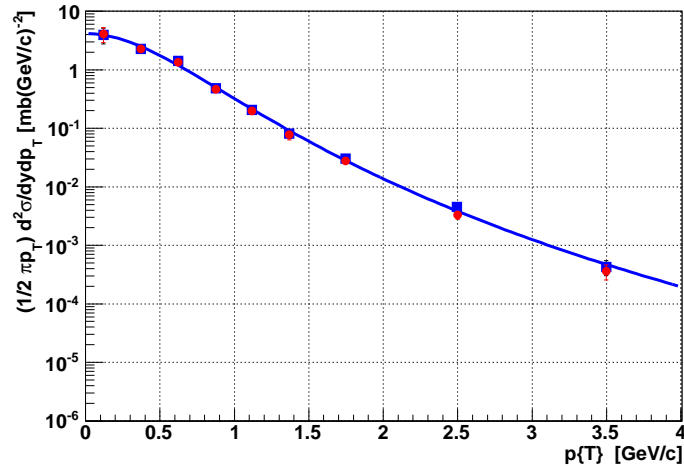


Figure 3.35: Bin shift correction for ω . Blue point and line shows before correction, and red point shows after correction.

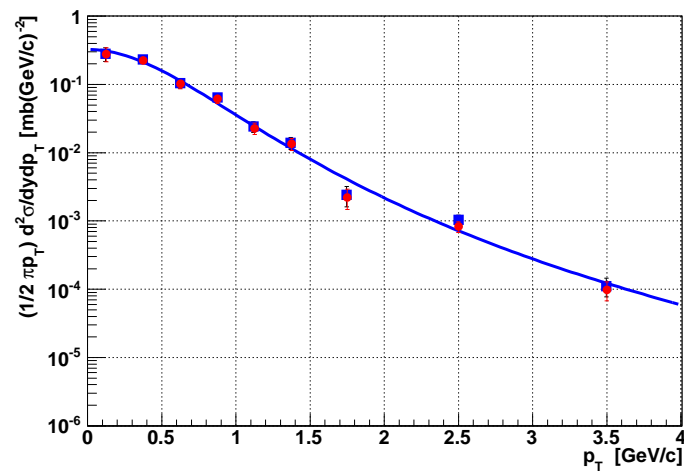


Figure 3.36: Bin shift correction for ϕ . Blue point and line shows before correction, and red point shows after correction.

3.10 Systematic Uncertainty

This section summarizes the source of the systematic uncertainties that contribute to invariant cross section as follows:

signal extraction

This is the uncertainty for methods of signal extraction for the window to count the signal, fitting range, background shape, threshold emitting gamma energy for radiative tail. The uncertainties are evaluated by varying 1)the window to count the signal to 2σ and 4σ , 2)the fitting range to $0.5\text{-}1.15\text{GeV}/c^2$ and $0.4\text{-}1.25\text{GeV}/c^2$, 3)background shape to 2nd polynominal and 3rd polynominal, 4)threshold of emitting gamma energy for radiative tail to 5MeV and 15MeV. For each case, the raw yield was extracted and the resulting RMS of these yield for each p_T bins are assigned as systematic errors.

Acceptance

This is the uncertainty in how well the acceptance of PHENIX detectors in the simulation agrees with real data. We evaluate this comparing the phi distribution of hit position in the data and simulation.

electron ID

This is the uncertainty of electron identification efficiency for RHIC cut, EMC track matching and energy momentum ratio. We evaluate this by varying each eID cuts parameters in both of real and simulation, and monitoring the deviation of recalculating cross section from basic value as systematic errors.

ERT trigger efficiency

The uncertainties in the ERT trigger efficiency are evaluated by varying the single electron efficiency curve for every EMCAL sectors in simulation.

bin shift correction

The uncertainty for bin shift correction due to function shape assumed to fit real data was evaluate to use other functions; Hagedron function and exponential function.

3.10.1 Total systematic error

Various systematic errors are summarized in Table 3.3, 3.4.

pT	0.-0.25	0.25-0.5	0.5-0.75	0.75-1.0	1.0-1.25	1.25-1.5	1.5-2.0	2.0-3.0	3.0-4.0
signal	10.5%	17.3%	5.4%	7.6%	8.4%	8.1%	5.9%	6.7%	5.5%
acceptance						4.5%			
electron ID						8.9%			
ERT trigger	2.4%	2.0%	1.8%	1.1%	1.2%	1.3%	1.3%	1.1%	1.1%
bin shift	2.7%	1.7%	0.4%	0.3%	0.5%	0.4%	0.6%	5.1%	10.3%
σ_{BBC}						9.6%			
ϵ_{bias}						2.5%			
Total	17.9%	22.5%	15.2%	16.0%	16.4%	16.3%	15.3%	16.4%	18.3%

Table 3.3: Total systematic error for ω meson

pT	0.-0.25	0.25-0.5	0.5-0.75	0.75-1.0	1.0-1.25	1.25-1.5	1.5-2.0	2.0-3.0	3.0-4.0
signal	16.7%	6.0%	3.8%	5.7%	8.7%	5.2%	15.8%	9.6%	6.0%
acceptance						4.5%			
electron ID						8.1%			
ERT trigger	1.1%	1.2%	2.0%	1.8%	1.5%	1.4%	1.1%	1.2%	1.1%
bin shift	1.6%	1.0%	0.7%	0.4%	0.3%	0.4%	2.2%	12.6%	16.3%
σ_{BBC}						9.6%			
BBC bias						2.5%			
Total	21.6%	14.9%	14.3%	14.9%	16.2%	14.6%	21.0%	20.9%	22.1%

Table 3.4: Total systematic error for ϕ meson

Chapter 4

Results and Discussions

In this section, we show the result of ω and ϕ meson production via di-electron decay channels in p+p collisions at $\sqrt{s} = 200\text{GeV}$; the spectra of invariant cross section as a function of p_T , total cross section for ω and ϕ and the particle ratio of ω/π^0 , ϕ/π^0 . We also present the transverse mass(m_T) spectra for various mesons and scaling behavior. In addition, the di-electron mass distribution is analyzed with simple model to evaluate mass shift quantitatively.

4.1 Spectra of the invariant cross sections

Figure 4.1 shows the invariant cross section for ω and ϕ production measured in di-electron decay channel in p+p collisions at $\sqrt{s} = 200\text{GeV}$, as a function of p_T . Bars and boxes represent statistical and systematic errors, respectively.

In addition, we already measured ω and ϕ mesons via other decay modes, $\omega \rightarrow \pi^0\pi^+\pi^-$, $\omega \rightarrow \gamma\pi^0$ [93] and $\phi \rightarrow K^+K^-$ [42], in the PHENIX experiment. Figure 4.2 and 4.2 show the invariant cross section for ω and ϕ production measured in dielectron and hadronic decay modes for wide p_T range, $0 < p_T < 13\text{GeV}/c$ for ω and $0 < p_T < 7\text{GeV}/c$ for ϕ , in p+p collisions at $\sqrt{s} = 200\text{GeV}$, as a function of p_T , respectively. The error bars of the cross section measured in hadronic decay modes show statistic uncertainties added in quadrature with the systematic uncertainties.

The underlying physics for particle production at low p_T and high p_T is different. According to pQCD calculation as shown Section 1.2, a pure power-law spectrum describes the high p_T region of particle spectra. A similarly good agreement is observed for π^0 with modified power-law function [92] :

$$E \frac{d^3\sigma}{dp^3} = A(1 + \frac{p_T}{b})^{-n} \quad (4.1)$$

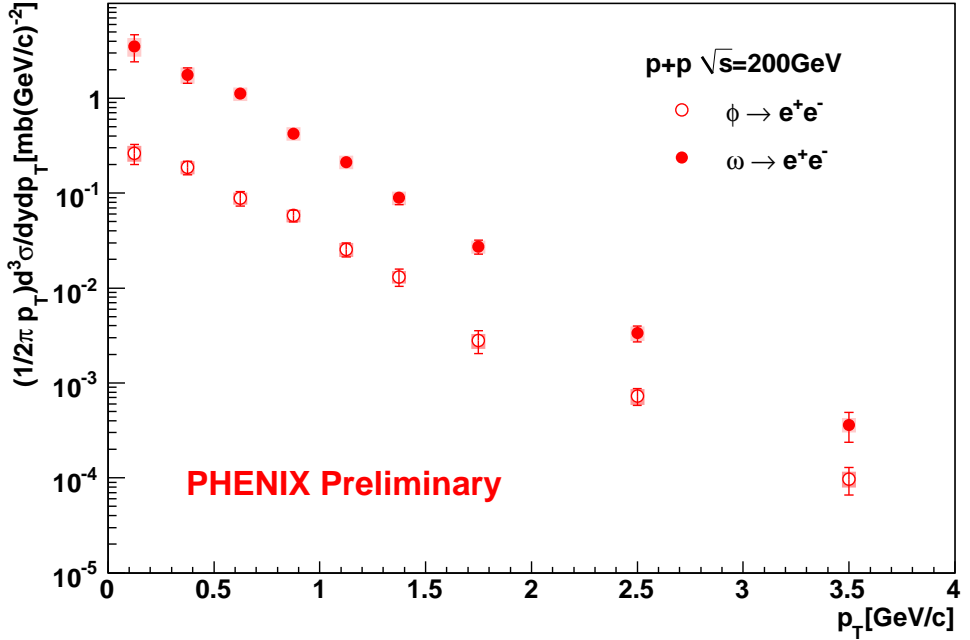


Figure 4.1: Invariant cross section of ω and ϕ production in $p + p$ collision at $\sqrt{s}= 200\text{GeV}$ measured in $\omega \rightarrow e^+e^-$ and $\phi \rightarrow e^+e^-$ decay channels as a function of p_T . Bars and boxes represent statistical and systematic errors, respectively.

where, A , b and the power n are the parameters of this function. However the power law is seen to fail in region below $p_T = 3\text{GeV}/c$. At low p_T region, where particle are largely produced in soft(thermal-like) process, the shape of the spectrum can be well described by:

$$E \frac{d^3\sigma}{dp^3} = \frac{1}{2\pi T^2} \frac{d\sigma}{dy} \exp^{-\frac{p_T}{T}} \quad (4.2)$$

where, $\frac{d\sigma}{dy}$ and the inverse slope parameter T are parameters of this function.

The Tsallis statistics extend Boltzman-Gibbs statistic [107]. The p_T spectra of particle production are well described by a Levy function based on Tsallis statistics:

$$E \frac{d^3\sigma}{dp^3} = \frac{1}{2\pi} \frac{d\sigma}{dy} \frac{(n-1)(n-2)}{(nT+m_0(n-1)(nT+m_0))} \left(\frac{nT + \sqrt{p_T^2 + m_0^2}}{nT + m_0} \right)^{-n} \quad (4.3)$$

where $\frac{d\sigma}{dy}$ is the integrated production cross section, m_0 is the rest mass corresponding to particle species, T is the inverse slope parameter, and n is the

related to power. All the parameters except m_0 are free parameters in fit. In the limiting case of $1/n \rightarrow \inf$, the Levy function approached an exponential function. In the another limiting case of $m_0 \rightarrow 0$, the Levy function approached similar function of Eq.4.1.

The solid (red) curve in Figure 4.2,4.3 shows levy function fit to the both data measured in di-electron and hadronic decay modes in $0 < p_T < 13 \text{ GeV}/c$ for ω and $0 < p_T < 7 \text{ GeV}/c$ for ϕ . We also try to fit by modified power-law (Eq. 4.1) as shown the solid curve(green) which can well describe the data at higher p_T region above $3 \text{ GeV}/c$. In contrast, the exponential function as shown the dash curve(black) well describes the data at lower p_T region below $3\text{GeV}/c$. The ratio of data to levy fit are shown in bottom Fig. 4.2 and Fig. 4.3. The levy fit is in an good agreed with data in the wide p_T range.

The spectra measured via di-electron and hadronic decay modes are smoothly connected. It notes that there are only a few data points within overlap p_T range of $2.0 < P_T < 4.0 \text{ GeV}/c$ for ω production, since the p_T range in di-electron decay modes is limited by statistics at high pT and the p_T range in hadronic decay modes is limited by decreasing detector acceptance and trigger efficiency at low p_T .

Comparison with PYTHIA

The PYTHIA event generator is frequently used for the description of high-energy hadron+hadron collisions. We have used PYTHIA version 6.421, with Tune *A* for in-elastic cross section and including preset for multiple parton scattering process [108]. In this setting, the Lund symmetric fragmentation function $D_Q^h(z, \mu^2)$ [109, 110] and Leading order Parton Distribution Function (CTEQ 5L) [3] is used. Fig. 4.4 and Fig.4.5 show the invariant cross section compared with PYTHIA for ω and ϕ meson, respectively. It is in a good agreement with data within experimental error.

4.2 Integrated cross sections

First measurement of the ω and ϕ measured in di-electron decay mode extend the p_T region to zero momentum and allow a direct calculation of the integrated cross section $d\sigma/dy$. The $d\sigma/dy$ was calculated by summing up the data points:

$$\frac{d\sigma}{dy} = 2\pi \sum_i \left(\frac{d\sigma_i}{dp_T dy} \times p_T^i \times \Delta p_T^i \right) \quad (4.4)$$

The statistic and systematic errors on the data points are added quadrature, respectively.

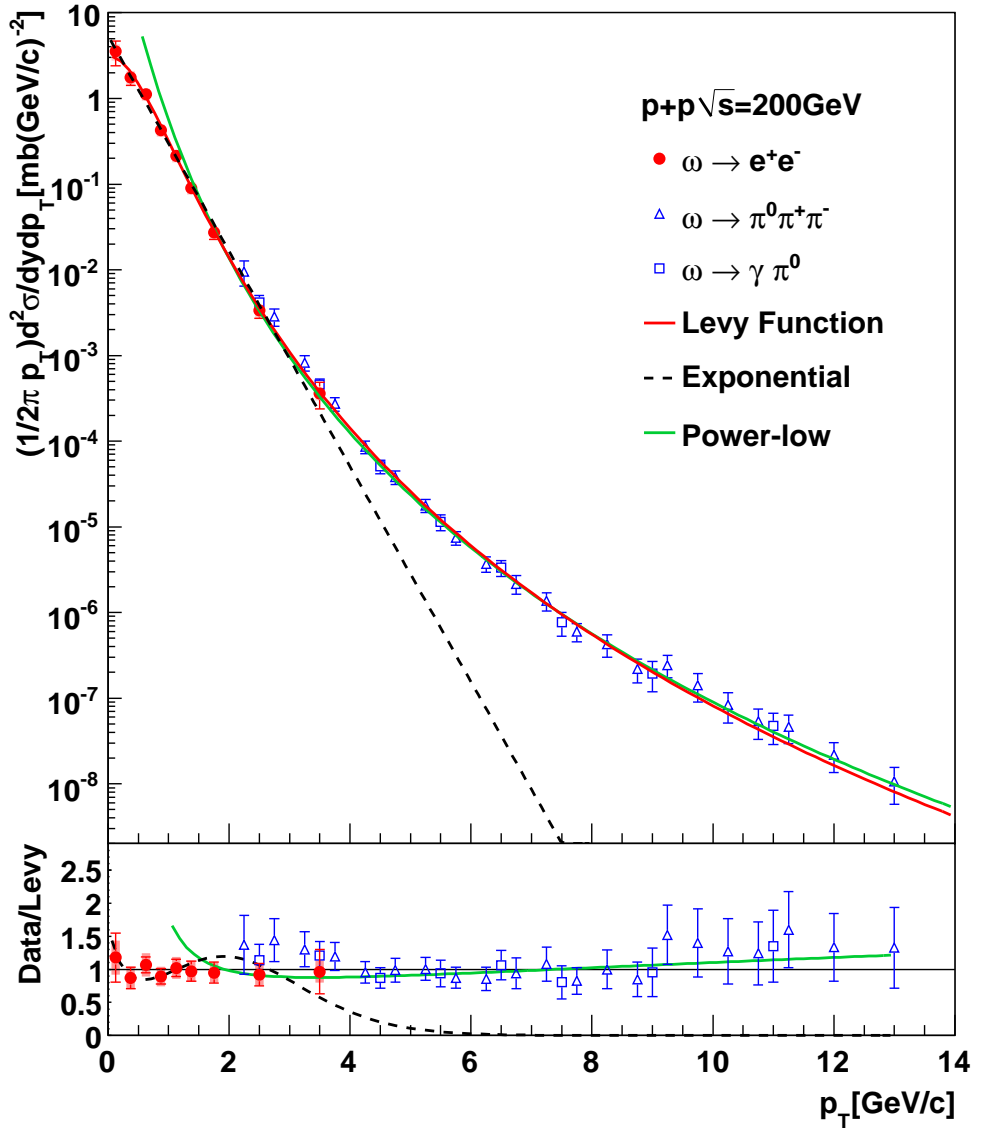


Figure 4.2: (Top) The invariant cross section of ω production in $p + p$ collision at $\sqrt{s} = 200\text{GeV}$ measured in $\omega \rightarrow e^+e^-$, $\pi^0\pi^+\pi^-$ and $\pi^0\gamma$ decay channels. The curves show Levy(red), modified Power-law(Green) and Exponential(black) fit to the data measured in both dilepton and hadronic decay modes. (Bottom)Ratio of the data and Levy fit.

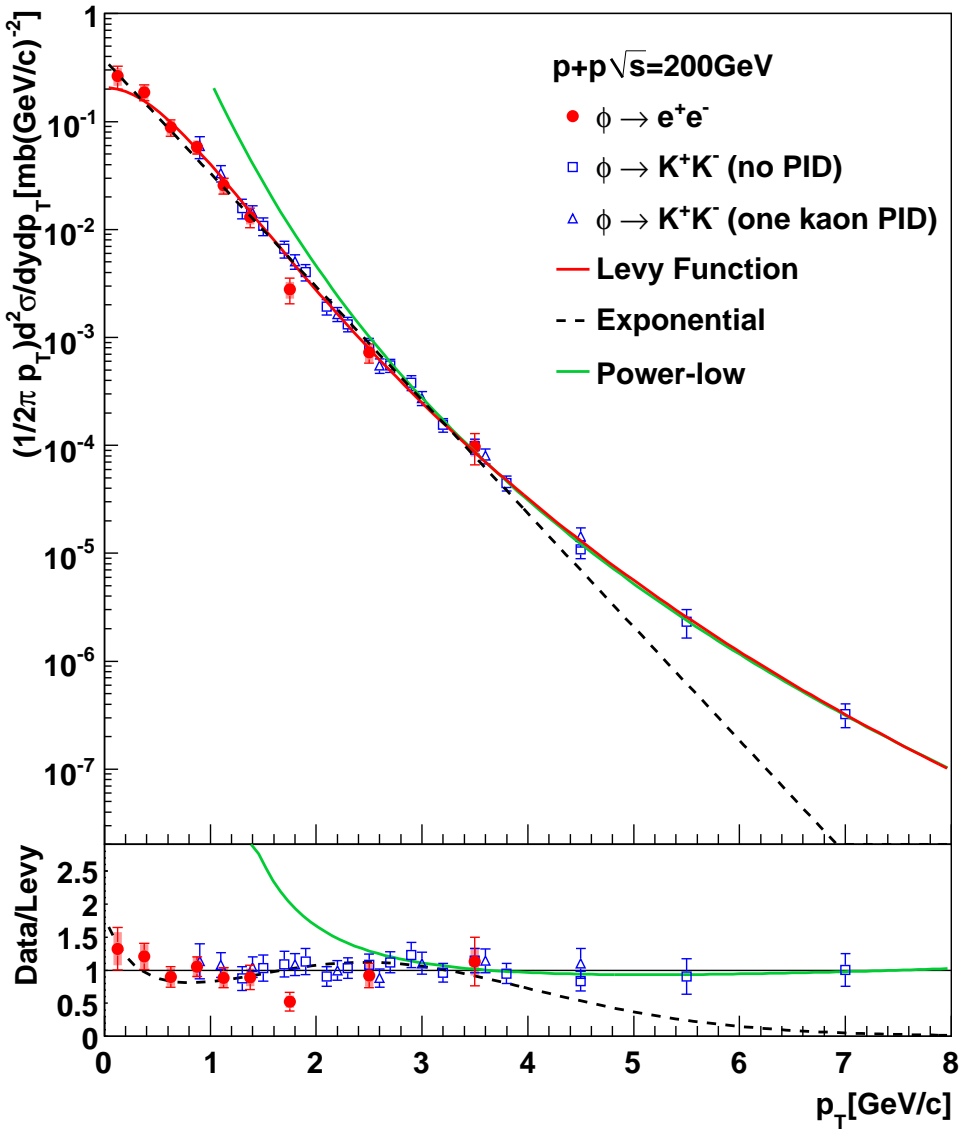


Figure 4.3: Invariant cross section of ϕ production in $p + p$ collision at $\sqrt{s}=200\text{GeV}$ measured in $\phi \rightarrow e^+e^-$, K^+K^- decay channels. The curves show Levy(red), modified Power-law(Green) and Exponential(black) fit to the data measured in both delepton and hadronic decay modes. (Bottom)Ratio of the data and Levy fit.

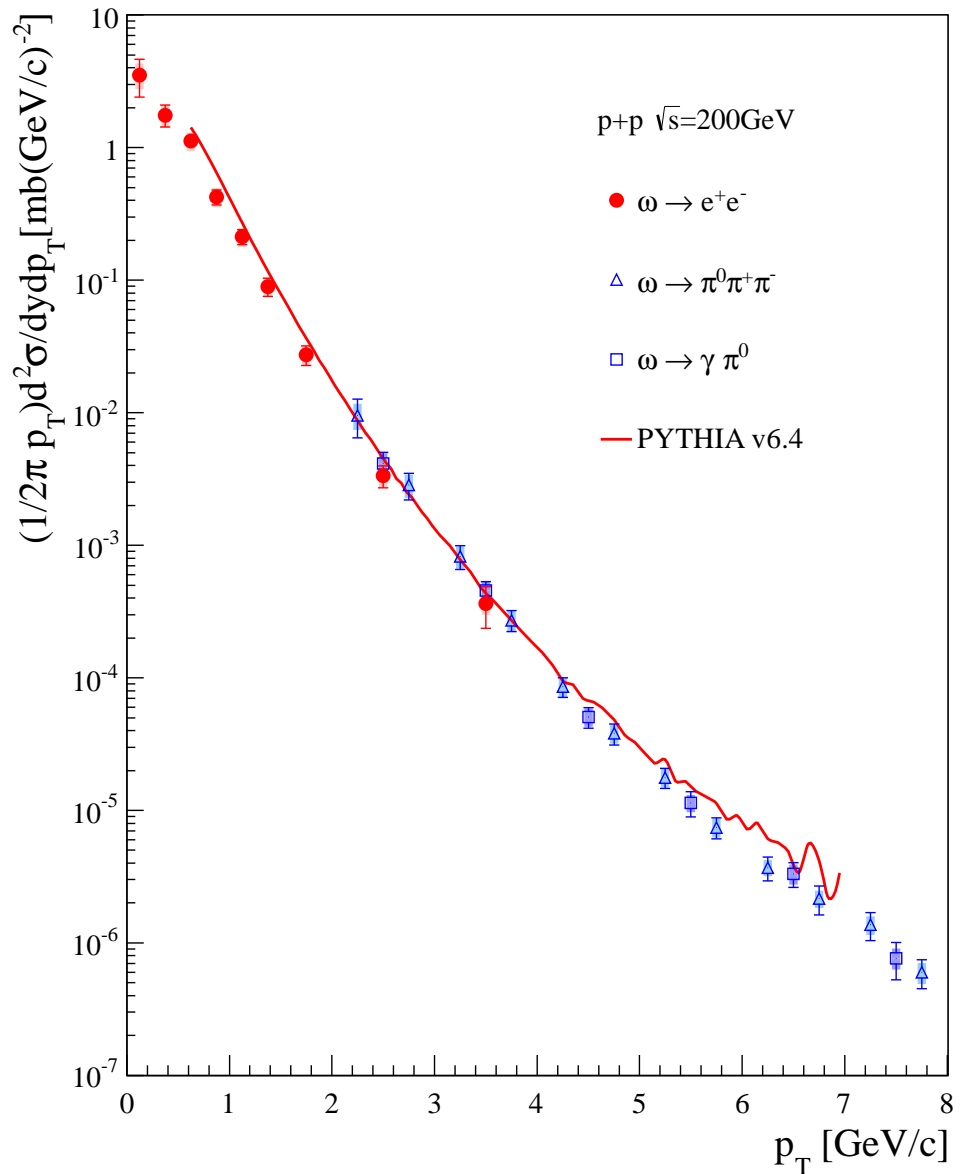


Figure 4.4: The invariant cross section of ω production in $p + p$ collision at $\sqrt{s}= 200\text{GeV}$ compared with PYTHIA version 6.421 with Tune *A*.

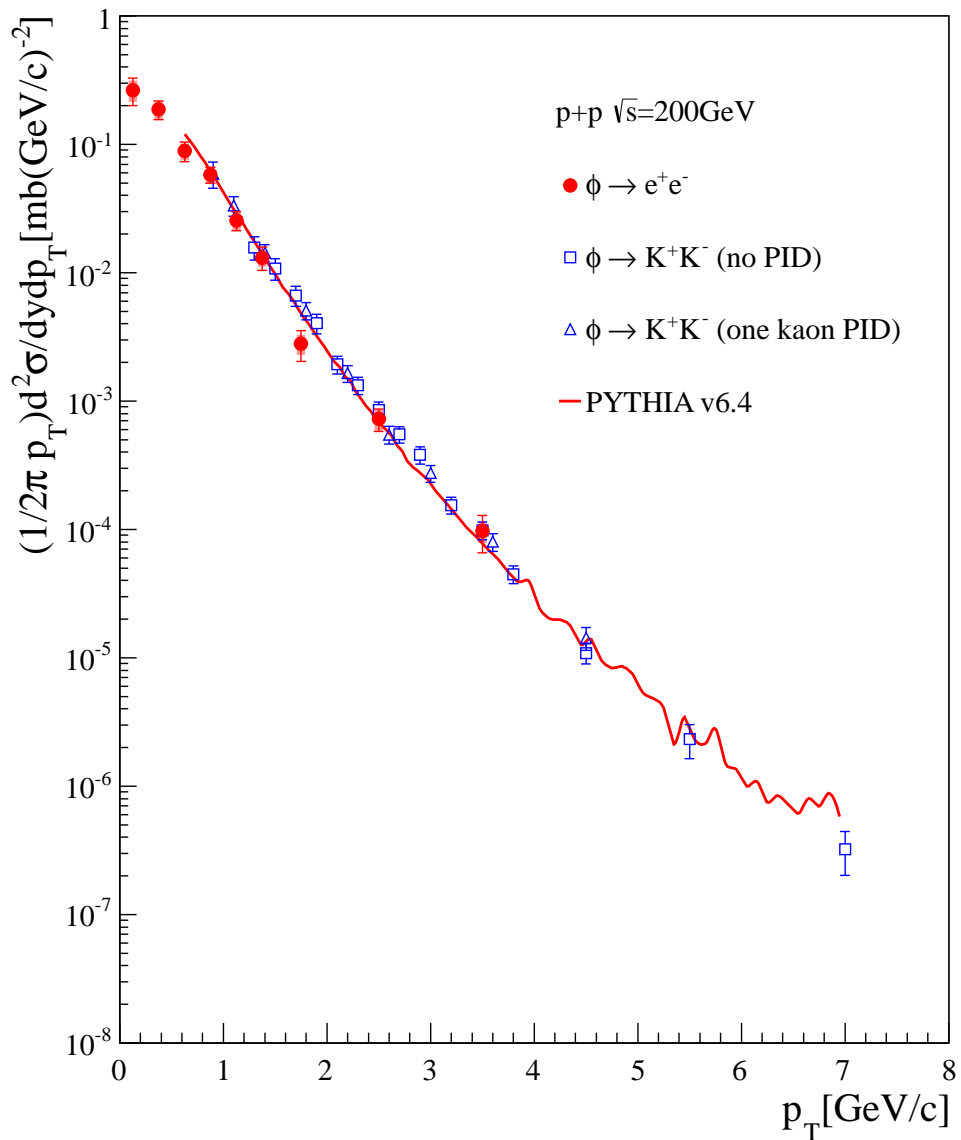


Figure 4.5: Invariant cross section of ϕ production in $p + p$ collision at $\sqrt{s}=200\text{GeV}$ compare with PYTHIA version 6.421 with Tune *A*.

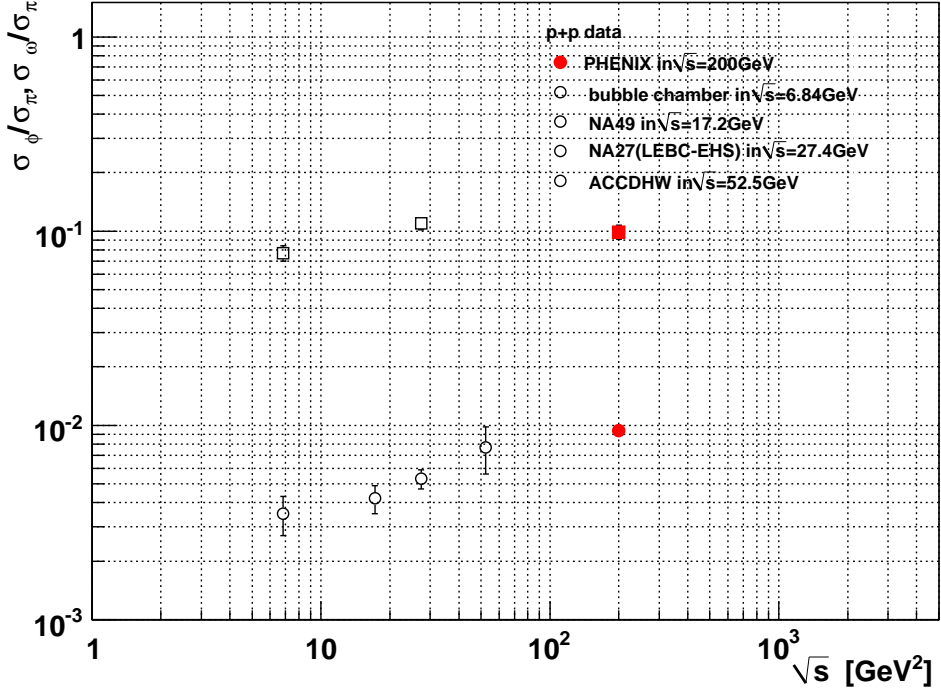


Figure 4.6: Ratio of cross section, σ_ω/σ_π (square) and σ_ϕ/σ_π (circle), measured for $p + p$ data as a function of center-of-mass energy.

The results for ω and ϕ are $d\sigma^\omega/dy = 4.19 \pm 0.33^{stat.} \pm 0.33^{sys.}$ mb and $d\sigma^\phi/dy = 0.431 \pm 0.031^{stat.} \pm 0.028^{sys.}$ mb which are consistent with one obtained by Levy fit within statistic error. The results are summarized in Table 4.1.

	Function	Fit range[GeV/c]	$d\sigma/dy[\text{mb}]$	n	χ^2/NDF
$\phi \rightarrow ee \& KK$	Summing	$0 < p_T < 7.0$	$0.431 \pm 0.031 \pm 0.028$	—	—
	Levy	$0 < p_T < 4.0$	0.430 ± 0.035	11.0 ± 1.1	$19.0/29$
	exponential	$3 < p_T < 7.0$	0.400 ± 0.028	—	$26.7/27$
$\phi \rightarrow ee$	power-law	—	—	9.8 ± 0.5	$2.8/6$
	Levy	$0.5 < p_T < 4.0$ (Overlap region)	0.419 ± 0.063	6.5 ± 1.9	$3.1/4$
	exponential	$0.5 < p_T < 4.0$ (Overlap region)	0.418 ± 0.063	—	$7.3/5$
$\phi \rightarrow ee$	power-law	—	—	6.7 ± 0.3	$6.8/4$
$\phi \rightarrow KK$	Levy	$0 < p_T < 4.0$	0.454 ± 0.071	10.5 ± 2.1	$6.3/17$
	exponential	$0.5 < p_T < 4.0$ (Overlap region)	0.402 ± 0.038	—	$15.0/18$
	power-law	—	—	7.8 ± 0.1	$21.7/17$
	Function	Fit range[GeV/c]	$d\sigma/dy$	n	χ^2/NDF
$\omega \rightarrow ee \& \pi^0\gamma \& \pi^0\pi\pi$	Summing	$0 < p_T < 13.0$	$4.19 \pm 0.33 \pm 0.33$	—	—
	Levy	$0.5 < p_T < 3.0$	4.23 ± 0.41	9.7 ± 0.4	$16.7/35$
	exponential	$4.0 < p_T < 13.0$	4.05 ± 0.55	—	$5.6/7$
$\omega \rightarrow ee$	pow-law	—	—	9.2 ± 0.2	$6.1/20$
	Levy	$0 < p_T < 4.0$ (Full range)	4.12 ± 0.45	9.6 ± 2.6	$0.9/6$
	exponential	$0.5 < p_T < 3.0$	4.48 ± 0.64	—	$1.0/4$
$\omega \rightarrow \pi^0\gamma \& \pi^0\pi\pi$	Levy	$2.0 < p_T < 13.0$ (Full range)	36.64 ± 39.20	8.3 ± 0.5	$8.5/26$
	pow-law	$4.0 < p_T < 13.0$	—	8.1 ± 0.2	$5.0/20$

Table 4.1: Summary of fitting parameters

4.3 particle ratio of ω and ϕ to π

The distributions of the particle ratios for ω/π and ϕ/π as a function of p_T in $p + p$ collision at $\sqrt{s} = 200\text{GeV}$ were shown Fig.4.7 and 4.8, respectively. The π meson yields were obtained by Tsallis fit results to $(\pi^+ + \pi^-)/2$ and π^0 spectra measured by PHENIX [95, 102]. In high p_T region, $p_T > 3\text{ GeV}/c$, the were constant of $\omega/\pi = 0.79 \pm 0.04^{stat}$. and $\phi/\pi = 0.023 \pm 0.007^{stat}$. It means that these mesons have same power n of power law function. This implied that the fragmentation functions to the mesons were same and it is consistent picture with pQCD expectation.

4.4 Scaling properties

The invariant cross section of K^\pm , K_s^0 , η and J/ψ meson in $p+p$ collision at $\sqrt{s} = 200\text{GeV}$ are also measured by PHENIX experiment [94, 103–106]. The spectra of invariant differential cross section for $(\pi^+ + \pi^-)/2$, π^0 , $(K^+ + K^-)/2$, K_s^0 , η , ω , ϕ and J/ψ mesons as a function of p_T is shown in Fig.4.9. The fit of the Tsallis distribution to the spectra for each particles were shown as dash lines in Fig.4.9. This function consists only 2 parameters, since the m_0 is fixed to the mass corresponding to particle species. Nevertheless, the Tsallis function can describe the spectra of various particle species with masses are 0.1 to 3 GeV/c^2 .

The Fig.4.10 shows the spectra of all measured mesons normalized to π_0 at $p_T = 6\text{ GeV}/c$. The solid line show pure power law function fit into the range of $5 < p_T < 20\text{ GeV}/c$ for all points. According to pQCD calculation, the power law behavior represented at high p_T region and this results consistent with pQCD picture.

In addition, the spectra of $(\pi^+ + \pi^-)/2$, π^0 , $(K^+ + K^-)/2$, K_s^0 , η , ω , ϕ and J/ψ as a function of transverse mass, m_T ($= \sqrt{p_T^2 + m_0^2}$), in $p+p$ collision at $\sqrt{s} = 200\text{GeV}$ were shown in Fig.4.11. The bottom figure shows the ratio of theses spectra to Tsallis functional form fit into π meson spectrum. The ratio is approximately constant and it means that the spectra shape as a function of m_T for all particle species are very similar.

Fig.4.12 shows m_T spectra for all mesons normalized ar one point of $p_T = 10\text{ GeV}/c$. It is clear that the spectra shape for all particles are very similar forms for wide m_T region when plotted as a function of m_T . The Eq.4.3 can be expressed for transverse mass as follow:

$$E \frac{d^3\sigma}{dp^3} = \frac{1}{2\pi} \frac{d\sigma}{dy} \frac{(n-1)(n-2)}{(nT + m_0(n-1)(nT + m_0))} \left(\frac{nT + m_T}{nT + m_0} \right)^{-n} \quad (4.5)$$

In the limit of $m_0 \rightarrow 0$ Eq.4.6 becomes

$$E \frac{d^3\sigma}{dp^3} = \frac{1}{2\pi} \frac{d\sigma}{dy} \frac{(n-1)(n-2)}{(nT)^2} \left(1 + \frac{m_T}{nT}\right)^{-n}. \quad (4.6)$$

This form is very similar to expression inspired by QCD called Hagedorn formula [111] used fits to experimental data with success [112, 113]. In this case, the form was written as a function of m_T instead of p_T . All the normalized points for all particles were fit simultaneously with Eq.4.6 and follows m_T scaling well as $\sqrt{s} = 200$ GeV.

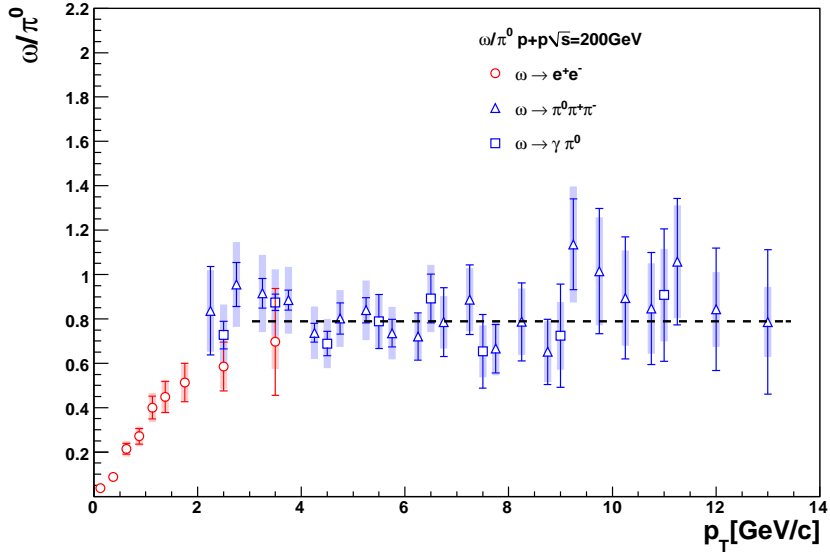


Figure 4.7: Measured ω/π^0 as a function of p_T in p+p collisions at $\sqrt{s} = 200\text{GeV}$. Straight lines show fits to a constant for $2 < p_T < 3\text{GeV}/c$

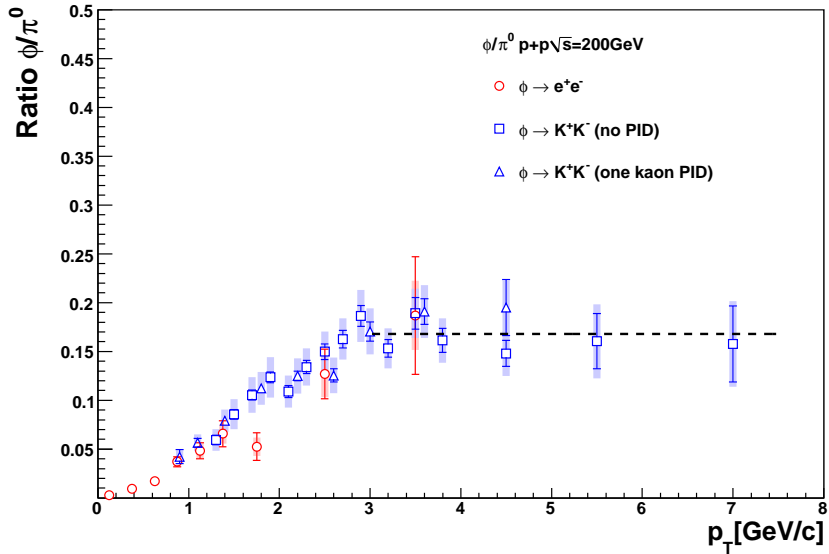


Figure 4.8: Measured ϕ/π^0 as a function of p_T in p+p collisions at $\sqrt{s} = 200\text{GeV}$. Straight lines show fits to a constant for $3 < p_T < 7\text{GeV}/c$

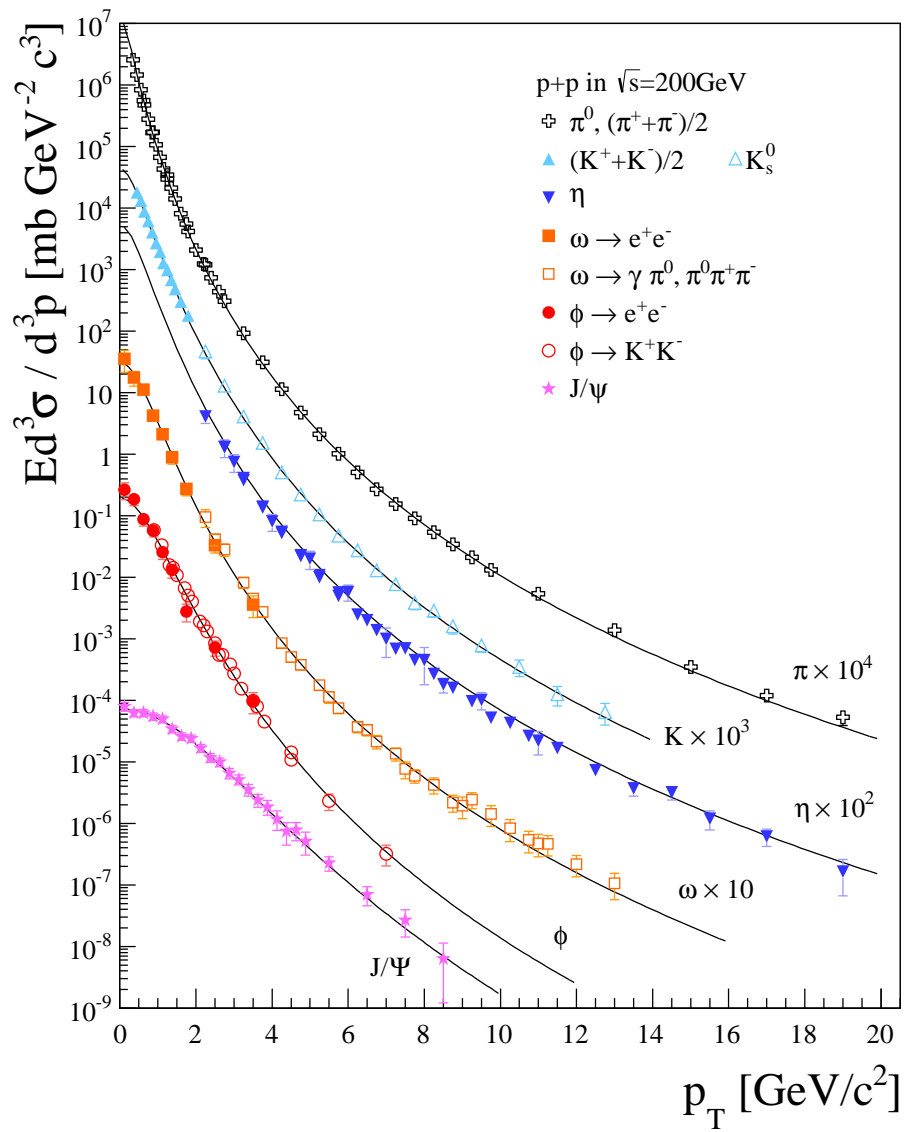


Figure 4.9: Spectra of invariant differential cross section as a function of p_T for $(\pi^+ + \pi^-)/2$, π^0 , $(K^+ + K^-)/2$, K_s^0 , η , ω , ϕ and J/ψ in $p + p$ collision at $\sqrt{s} = 200$ GeV at mid-rapidity.

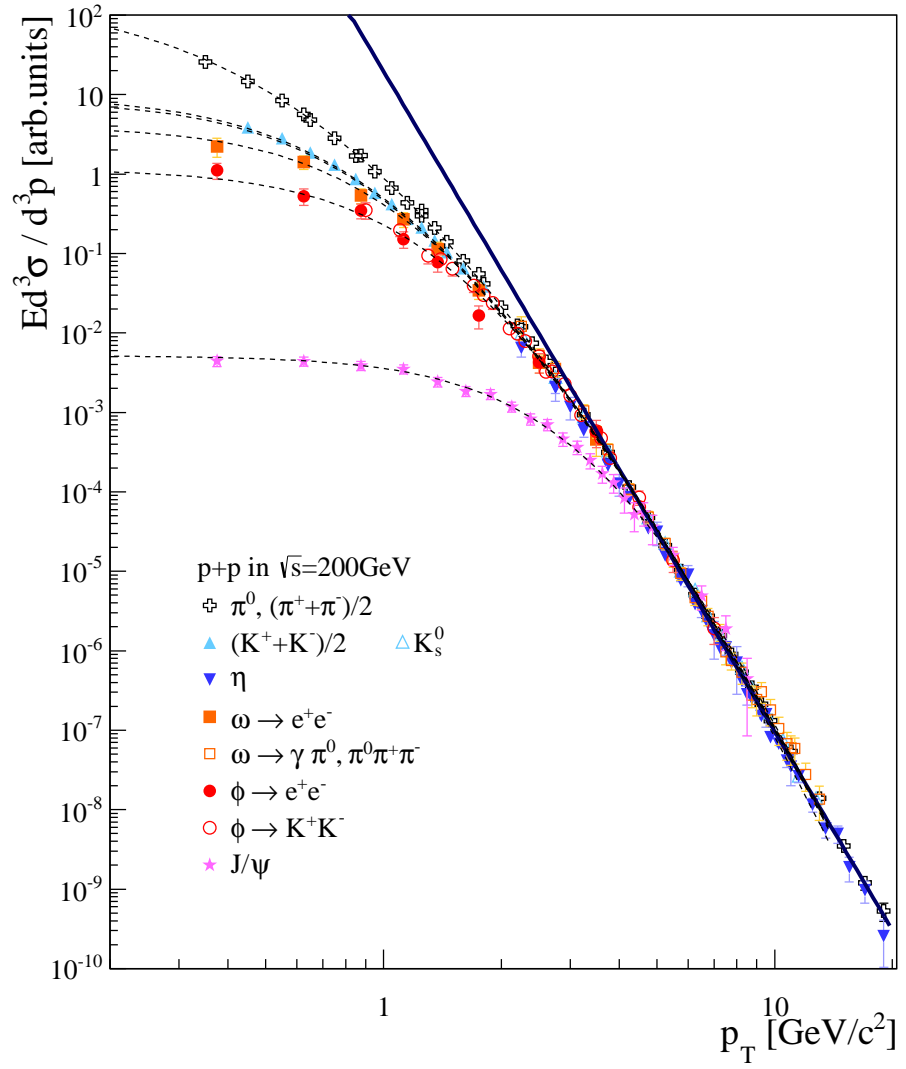


Figure 4.10: Scaled spectra of invariant differential cross section as a function of p_T for $(\pi^+ + \pi^-)/2$, π^0 , $(K^+ + K^-)/2$, K_s^0 , η , ω , ϕ and J/ψ in $p+p$ collision at $\sqrt{s} = 200$ GeV at mid-rapidity. Solid line expressed pure power law function fitted in $5.0 < p_T < 20$ GeV/c.

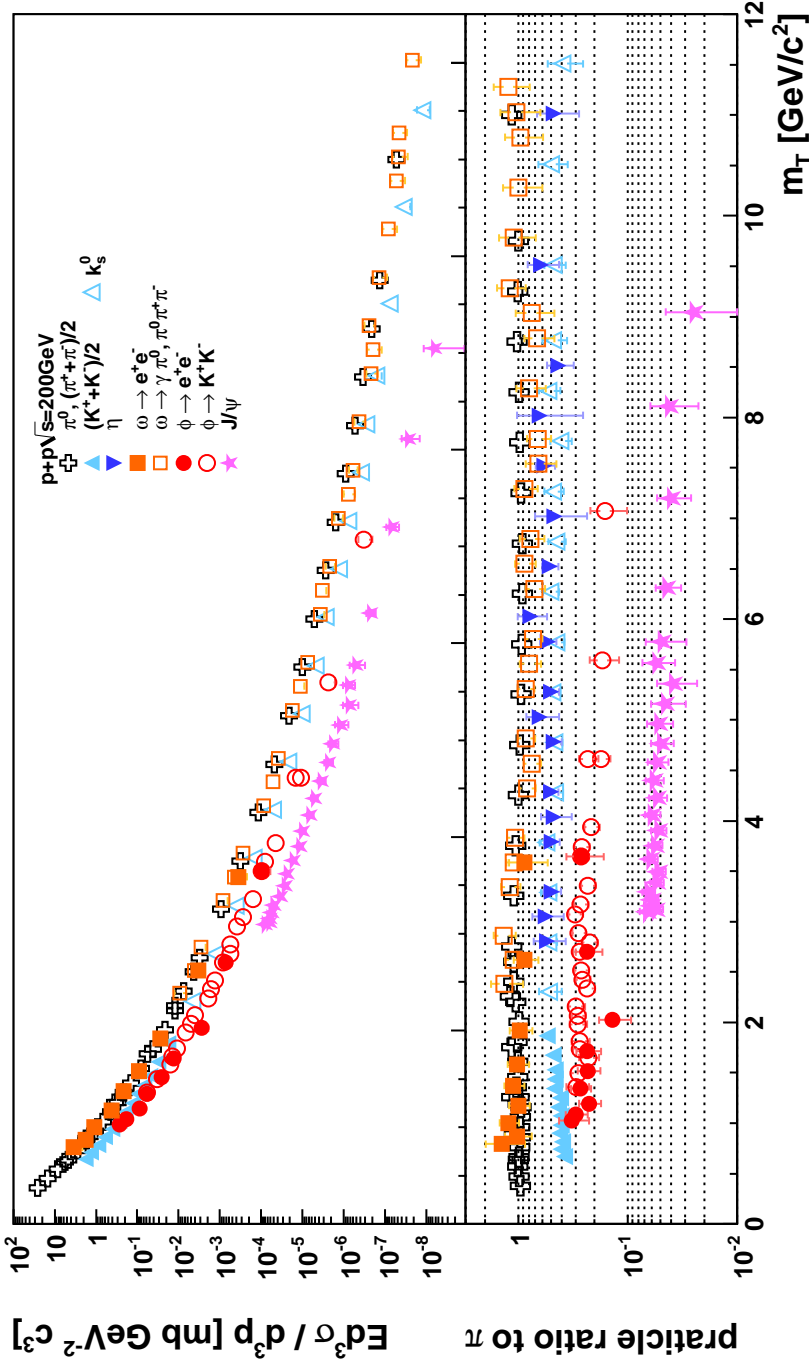


Figure 4.11: (top) m_T spectra for $(\pi^+ + \pi^-)/2$, π^0 , $(K^+ + K^-)/2$, K_s^0 , η , ω , ϕ and J/ψ in $p + p$ collision at $\sqrt{s} = 200$ GeV at mid-rapidity. (Bottom) The ratio of the spectra to Levy fit to π . Bars show uncertainties combined with statistical and systematic errors.

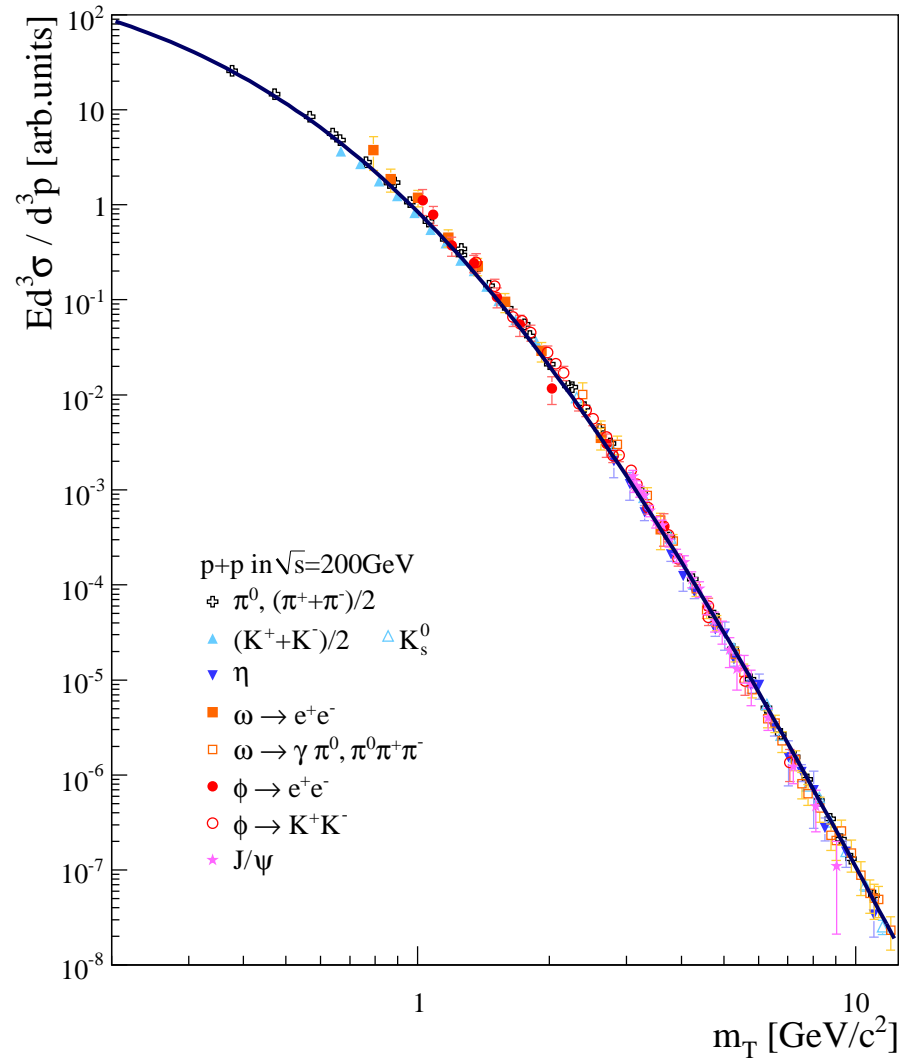


Figure 4.12: Scaled m_T spectra for $(\pi^+ + \pi^-)/2$, π^0 , $(K^+ + K^-)/2$, K_s^0 , η , ω , ϕ and J/ψ in $p + p$ collision at $\sqrt{s} = 200$ GeV at mid-rapidity.

4.5 Mass line shape analysis

Due to the chiral symmetry restoration in the hot matter created by the high energy heavy ions collisions, the possible observation of mass modification of ω and ϕ mesons are expected. On the other hand, the observation of the mass modification is not expected in case of $p+p$ collisions, since the matter created by $p+p$ collisions should be much smaller than the life time of these mesons. The analyzing invariant mass distribution in $p+p$ collisions provides crucial baseline for challenging studies for measurement of ω and ϕ meson mass spectra due to the huge combinatorial background in heavy ion collisions.

The model of this analysis consists two parameters to consider mass shift quantitatively. Then one of the parameters, Δ were defined as the ratio how much center of mass were shifted:

$$M' = (1 + \Delta)M \quad (4.7)$$

If Δ equal to zero, it means no mass shift was observed. In the assumption of that the temperature of hot medium is stable, the Δ should be constant since the modification depend on temperature. Then, if the mesons decayed inside the medium, the position of center of reconstructed mass peak should be M' .

In addition, another parameter as the fraction of the meson yield decaying inside medium was defined as R ;

$$R = \frac{\text{Yield}_{\text{decay inside medium}}}{\text{Yield}_{\text{total}}} \quad (4.8)$$

where R is in the range of 0 to 1. We assumed that R depends $1/\beta\gamma$ corresponding to that the decay probability inside medium increase as moving slower.

Then, the total invariant mass spectra for the vector mesons represent as follows;

$$F(m_{ee}) = A \times (R \times f' + (1 - R) \times f) \quad (4.9)$$

Here

$$f(m_{ee}) = \text{Gaussian convoluted (r.BW + radiative tail)} \quad (4.10)$$

$$f'(m_{ee})|_{\text{mod}} = \text{Gaussian convoluted (r.BW + radiative tail)} \quad (4.11)$$

where A is normalization factor, $f'(m_{ee})|_{\text{mod}}$ represents mass spectra fully including mass shift as shown Eq.4.7. The center of mass and natural width Γ were fixed to PDG value as shown Table3.2. The ρ meson contamination

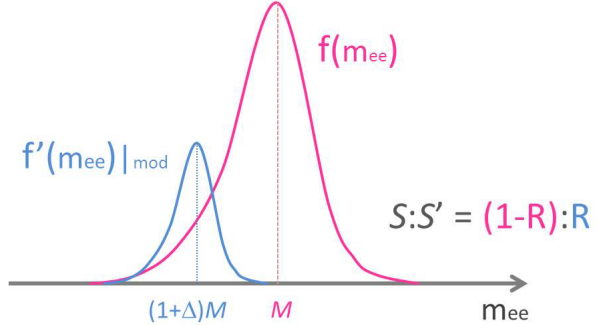


Figure 4.13: Schematic representation of the model to evaluate mass spectra with mass shift. The shapes of $f(m_{ee})$ and $f'(m_{ee})$ represent the measured spectra of vector meson decaying outside and inside medium, respectively.

into the mass spectra of ω meson was considered. The ratio of ω/ρ was fixed to 1.35 determined by their e^+e^- decay branching ratio in vacuum with the assumption of the ratio of the total production yield $\sigma_\rho/\sigma_\omega = 1.15$, consistent with jet fragmentation [89].

The invariant mass distribution reconstructed via e^+e^- in $p+p$ collisions analyzed by the function $F(m_{ee})$ were shown in Fig.4.14 and Fig.4.17 for ω and ϕ mesons, respectively. The invariant mass distributions were divided by three p_T binning correspond to the weighted average of $\langle\beta\gamma\rangle = 1.01, 2.04, 4.85$ and $\langle\beta\gamma\rangle = 0.74, 1.82, 3.68$ for ω and ϕ mesons, respectively. In the figures, the blue line shows $F(m_{ee})$, the magenta and light blue line correspond to f and f' , respectively. The dash line shows the fit result in case of $\Delta = 1$ and $R = 0$. And the green line shows contribution of ρ meson.

The best fit value of Δ and R were obtained as the result of global fit into the invariant mass distribution for these three p_T binning. In addition, statistical errors of Δ and R were estimated by χ^2 distribution as shown in Fig. 4.15 and Fig. 4.18 for ω and ϕ mesons, respectively. The best fit value for Δ and R with statistical errors were $\Delta = -3.3^{+2.4}_{-3.8}\%$, $R = 7.5^{+4.9}_{-4.9}\%$ for ω meson and $\Delta = -1.2^{+0.9}_{-0.8}\%$, $R = 9.7^{+8.0}_{-8.0}\%$ for ϕ meson. The χ^2 distributions for 2-dimensional space of Δ and R were shown in Fig.4.16 and Fig.4.19 for ω and ϕ mesons. The red points are the best fit value and the bars show statistic errors for Δ and R . If there were no mass shift, the parameters of Δ and R should be $\Delta = 0$ and/or $R = 0$. The obtained results including error are close to the $\Delta = 0$ and/or $R = 0$. The results for ω and ϕ mesons are consistent with assumption that no mass shift was observed in $p+p$ collisions within 1.4σ , respectively.

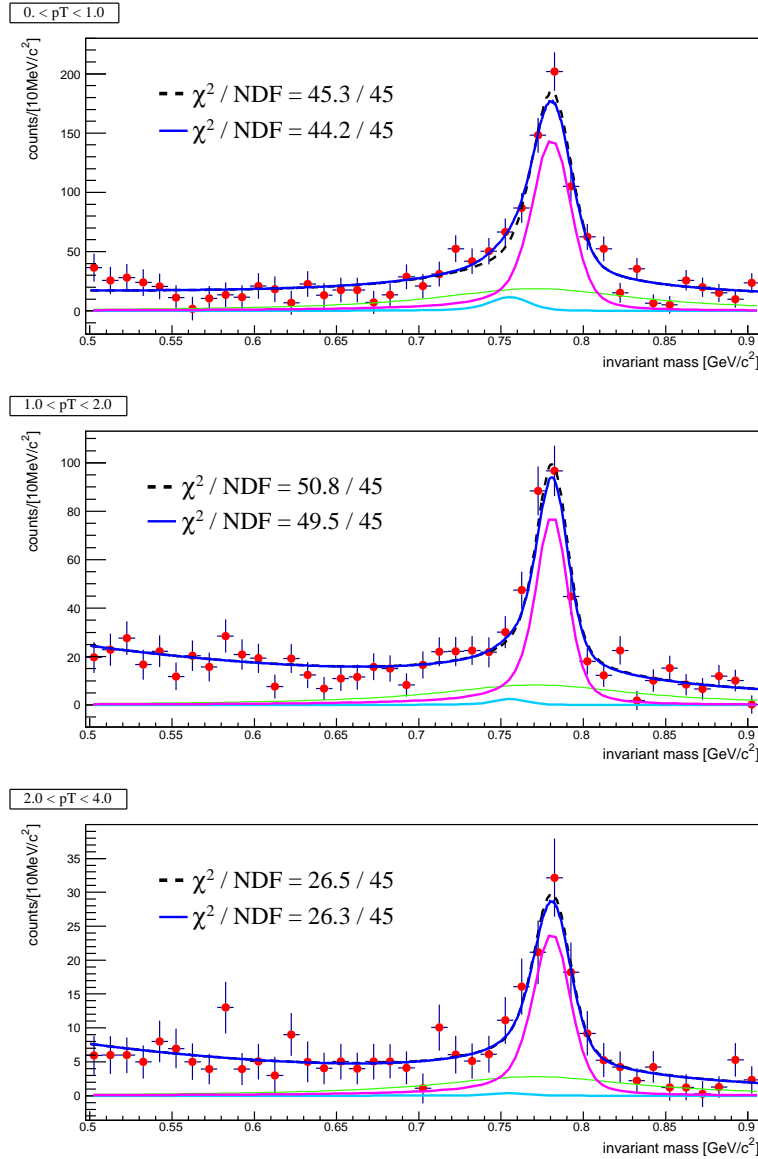


Figure 4.14: Invariant mass distribution with fitting results for ω mesons for three p_T bins corresponding to the weighted average of $\langle\beta\gamma\rangle = 1.01, 2.04, 4.85$. Blue line shows $F(m_{ee})$, magenta and light blue line correspond to f and f' , respectively. The dash line shows the fit result with $\Delta = 0$ and $R = 0$. The green line shows ρ meson contribution.

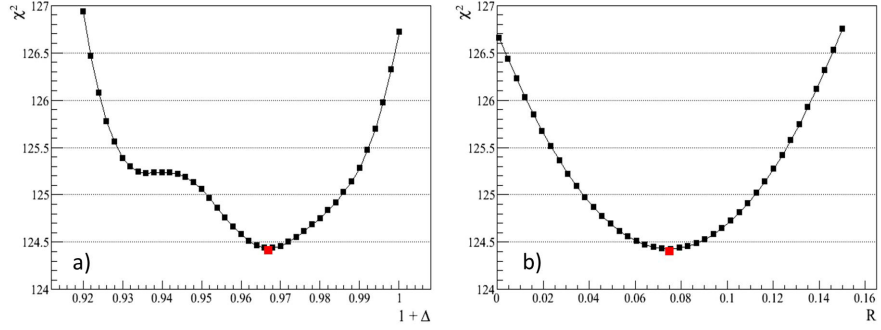


Figure 4.15: a) and b) show χ^2 distribution as a function of $(1+\Delta)$ and R for ω meson, respectively. The red points are best fit value.

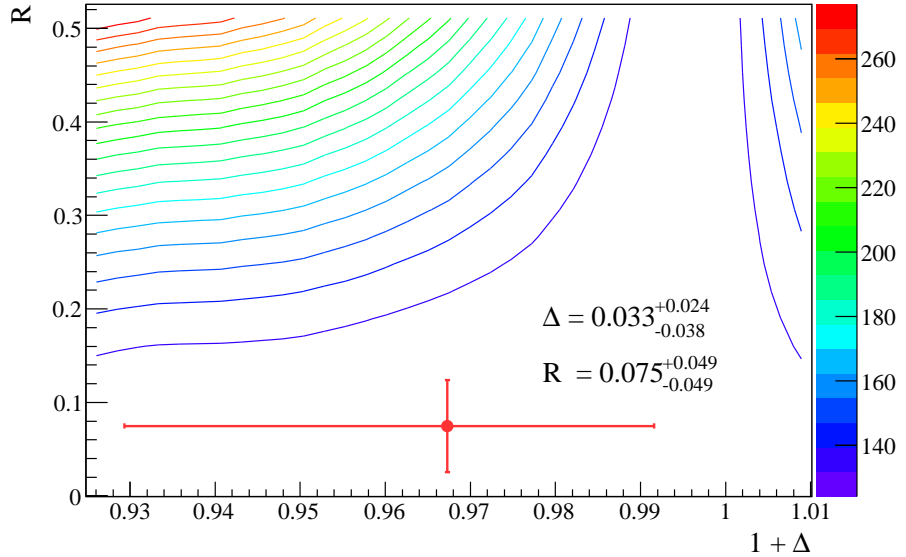


Figure 4.16: χ^2 distribution in 2-dimensional space for $(1 + \Delta)$ and R for ω meson. The red point is best fit value and the bars are statistical errors corresponding to $\Delta\chi^2 = +1$

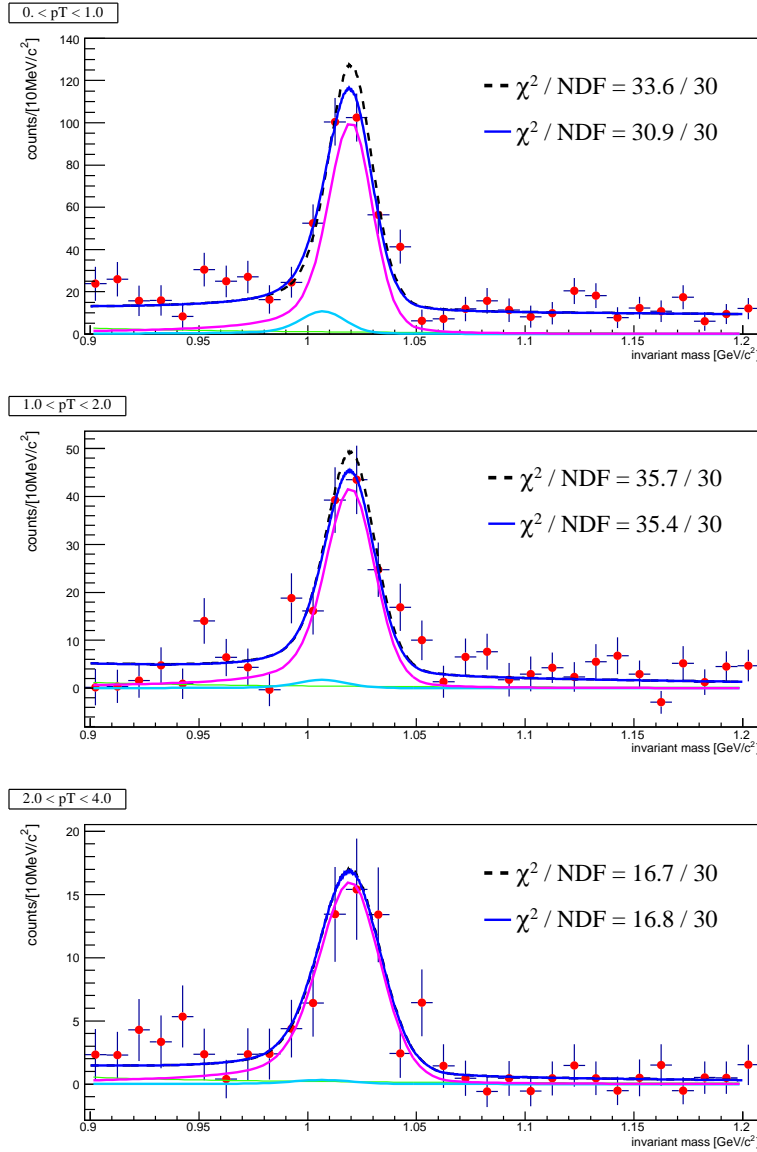


Figure 4.17: Invariant mass distribution with fitting results for ω mesons for three p_T bins corresponding to weighted average of $\langle\beta\gamma\rangle = 0.74, 1.82, 3.68$. Blue line shows $F(m_{ee})$, magenta and light blue line correspond to f and f' , respectively. The dash line shows the fit result with $\Delta = 0$ and $R = 0$. The green line shows ρ meson contribution.

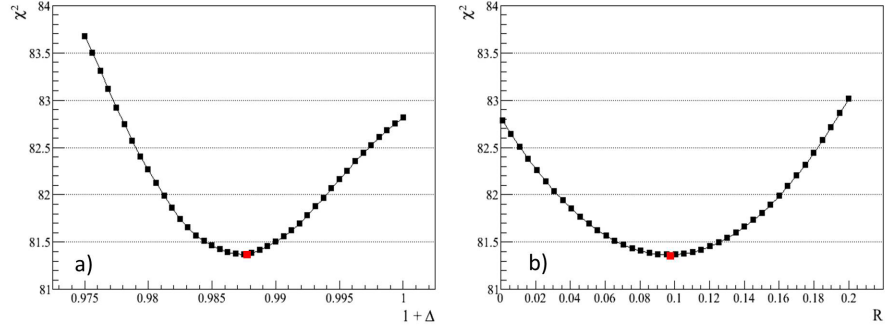


Figure 4.18: a) and b) show χ^2 distribution as a function of $(1 + \Delta)$ and R for *phi* meson, respectively. The red points are best fit value.

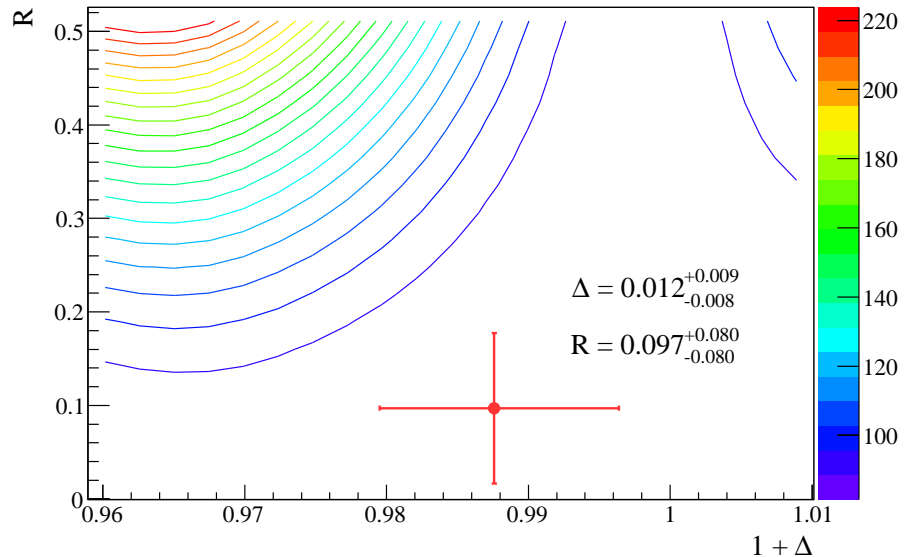


Figure 4.19: χ^2 distribution in 2-dimensional space for $(1 + \Delta)$ and R for ϕ meson. The red point is best fit value and the bars are statistical errors corresponding to $\Delta\chi^2 = +1$

Chapter 5

Summary and Conclusions

We have measured spectra of differential cross sections of ω and ϕ mesons as a function of transverse momentum in the range of $0 < p_T < 4 \text{ GeV}/c$. We analyzed data sample representing a total integrated luminosity of 3.8pb^{-1} accumulated by the PHENIX experiment in year 2004/2005 in $p+p$ collision at $\sqrt{s} = 200 \text{ GeV}$.

The ω and ϕ were identified from invariant mass spectra reconstructed by electron and positron pairs identified from large background of hadrons. The yield of ω and ϕ were statistically subtracted from large amount of background which comes from combinatorial pairs mainly due to π^0 Dalitz decay, photon conversion and other hadron decay. After applying correction for geometrical acceptance of PHENIX detector, electron identification efficiency, trigger efficiency obtained by simulation based on GEANT, the cross section of ω and ϕ meson be obtained.

Measurements of ω and ϕ vis di-electron decay mode in $p+p$ collisions at $\sqrt{s} = 200\text{GeV}$ extend the p_T coverage to zero and allows direct calculation of the integrated cross section $d\sigma^\omega/dy = 4.19 \pm 0.33^{stat.} \pm 0.33^{sys.} \text{ mb}$ and $d\sigma^\phi/dy = 0.431 \pm 0.031^{stat.} \pm 0.028^{sys.} \text{ mb}$.

The spectra of invariant cross sections of ω and ϕ were measured in wide p_T ranges, $0 < p_T < 13 \text{ GeV}/c$ for ω and $0 < p_T < 7 \text{ GeV}/c$ for ϕ utilizing both of di-electron and hadronic decay modes. The spectra measured in di-electron and hadronic decay modes are smoothly connected within overlap p_T range. There were described by the Tsallis distributions which represent an exponential shape at low p_T and power low shape at high p_T . The measured spectra is in a good agreement with results of an event generator PYTHIA based on perturbative Quantum ChromoDynamics(pQCD) calculations.

The particle ratios ω/π and ϕ/π were constant in the high p_T region of $pT > 3\text{GeV}/c$. The results of a fit to a constant are $\omega/\pi = 0.79 \pm 0.04^{stat.}$ and $\phi/\pi = 0.023 \pm 0.007^{stat.}$.

The Tsallis distribution with parameters of T and n described various meson spectra $(\pi^+ + \pi^-)/2$, π^0 , $(K^+ + K^-)/2$, K_s^0 , η , ω , ϕ and J/ψ measured by PHENIX for wide p_T range. Having same power n for all mesons implied that the fragmentation functions to the mesons were same and it is consistent picture with pQCD expectation. The m_T spectra of $(\pi^+ + \pi^-)/2$, π^0 , $(K^+ + K^-)/2$, K_s^0 , η , ω , ϕ and J/ψ were presented. The spectra shape for all particle species were similar for wide m_T region in spite of that its contained both production process of soft and hard. Thesis scaling results suggest a similar production mechanism of mesons in $p+p$ collisions at $\sqrt{s} = 200$ GeV. By using the model of this analysis for evaluating mass modification, two parameters corresponding to the ratio of mass shift Δ and the fraction of modified meson yield R were estimated, and the best value were $\Delta = -3.3^{+2.4}_{-3.8}$ %, $R = 7.5^{+4.9}_{-4.9}$ % for ω meson and $\Delta = -1.2^{+0.9}_{-0.8}$ %, $R = 9.7^{+8.0}_{-8.0}$ % for ϕ meson. The results for ω and ϕ mesons are consistent with assumption that no mass shift was observed in $p+p$ collisions within 1.4σ , respectively. The baseline for study of mass modification in heavy ion interactions was provided by considering the procedure to evaluate measured mass spectra in $p+p$ collisions.

We conclude that the these results for ω and ϕ meson production in $p+p$ provided a crucial data as a solid baseline to understand physics of heavy ion interactions.

Acknowledgment

I would like to thank Prof. T. Sugitate for his continuous guidance, constructive comment and his work as the leader of our laboratory in Hiroshima University and PHENIX BBC subsystem group. I would like to express my sincere gratitude to my supervisor Prof. K. Shigaki for giving me an long-standing and continuous guidance, support and for all the opportunities he has provided for my studies. I could not have done this work without his support. I would like to appreciate Dr. K. Homma for providing interesting physics theme for no only high energy nuclear physics and his many thoughtful comments, suggestion and also his work for PHENIX BBC subsystem group.

I deeply acknowledge Dr. K. Ozawa and Prof. S. Esumi for their works on the financial supports of PHENIX-J. In addition, I wish to also thank Dr. K. Ozawa for his advice on research. I could not start the di-electron analysis without his help. I appreciate chief scientist Dr. H. En'yo for giving financial support to attend international conference.

I would like to acknowledge all PHENIX collaboration. I have had a lot of supports from PHENIX spokesperson, Prof. W. A. Zajc and Prof. B. V. Jacak and paper preparation group, Dr. A.Milov, Dr. Y.Riabov, Dr. V.Riabov, Dr. D. Ivanishchev, Dr. M. Naglis, Dr. A. Toia, Dr. D. Morrison. I am very thank to Prof. R. Seto and Dr. D. Sharma for providing the opportunity to discuss and their help for my analysis.

I would like to thank Mr. Y. Nakamiya, Ms. M. Ouchida, Mr. D. Watanabe, Mr. M. Nihashi for working together for the BBC operation and maintenance. With their help, I could face difficulties and enjoy working and discussion. In addition, I offer warm thanks to Yoshihide for his help and support with daily tasks, issues and in not only research as well. I also appreciate Dr. J. S. Haggerty, Dr. C. Y. Chi, Dr. S. Bathe, Dr. S. Stoll, Dr. M. Chiu for their cooperation of the BBC operation. We could not provide data by BBC without their help. I would like to express deep thank for Dr. Y. Akiba, Dr. T. Sakaguchi, Dr. K. Okada, Dr. I. Nakagawa. I would like to thanks to Dr. H. Torii, Dr. T. Horaguchi, Dr. T. Hachiya, Dr. M. Hachiya,

Dr. H. Masui Dr. A. Enokizono, Dr. M. Konno, Dr. T. Gunji, Dr. T. Isobe, Dr. M. Togawa, Dr. Y. Fukao, Dr. Y. Morino, Dr. K. Miki, Dr. Y. Yamaguchi, Dr. Y. Aramaki, Mr. Y. Ikeda, Mr. K. Watanabe, Mr. M. Sano, Mr. T. Todoroki. I had a very good time to discuss and to talk with them. I wish to thank Dr. K. Kondo, Dr. T. Kanesue, Dr. K Karatsu, Mr. K. Nakamura, Mr. K. Watanabe for the great time we spend together at BNL. I could really enjoy BNL life.

I would also like to thank all the member of quark physics laboratory at Hiroshima University, Dr. H. Harada, Mr. K. Haruna, Mr. H. Sakata, Mr. K. Hosokawa, Mr. K. Yamaura, Mr. K. Kubo, Mr. T. Narita, Mr. K. Kadokami, Mr. K. Mizoguchi, Mr. Y. Iwanaga, Mr. Y. Okada, Mr. Y. Maruyama, Mr. F. Chuman, Ms. A. Hiei, Mr. Iwasaki, Mr. H. Sakaguchi, Mr. M. Saka, Ms. T. Yamamoto, Mr. J. Midori, Mr. H. Obayashi, Mr. T. Hiasa, Mr. S. Yano, Mr. T. Hoshino, Mr. S. Sakurai, Mr. K. Kume, Mr. D. Sato, Mr. T. Hasebe, Ms. A. Tuji, Mr. T. Okubo. I would like to acknowledge Dr. T. Nakamura and Mr. Y. Tsuchimoto. I could learn many techniques of the experiments and analysis from them and could enjoy the research with their discussion.

Many thanks to my friends, Mr. H. Fuji, Mr. G. Fujimoto, Ms. H. Kobara, Ms. M. Nakata, Ms. H. Okawachi, Ms. K. Shiraishi and my senior, Mr. H. Takahashi, Mr. Y. Ikagawa for their unfailing friendship and encouragement.

Finally, but the mostly I wish to express my deepest gratitude to my parents. Akira and Kinuyo, and my brother Sintaro, for their support and encouragements of continuing my work. I could not continue and finish this work without their understanding and supports. I would like to dedicate this thesis to my father.

Bibliography

- [1] C.Amsler *et al.* Phys.Lett.**B667**, (2008)37
- [2] D.J.Gross, F.Wilczek, Phys.Rev.**B8**, 3633 (1973)
- [3] H.L.Lai *et al.* (CTEQ Collaboration), Eur.Phys.J.**C12**, 375 (2000)
- [4] M.G. Albrow *et al.* (CHLM Collaboration) Nucle. Phys. **B56**, 333 (1973)
- [5] B.Alper *et al.* (British-Scandinavian Collaboration) Nucle. Phys. **B87**, 19 (1975)
- [6] B.Alper *et al.* (British-Scandinavian Collaboration) Nucle. Phys. **B100**, 237 (1975)
- [7] K.Guettler *et al.* (British-Scandinavian-MIT Collaboration) Nucle. Phys. **B116**, 77 (1976)
- [8] D.Antreasyan *et al.*, Phys.Rev. **D19**, 764 (1979)
- [9] D.E.Jaffe *et al.* (FNAL-E605 Collaboration) Phys.Rev.**D40**, 2777 (1989)
- [10] J.Adams *et al.* (STAR Collaboration), Phys.Lett. **B637**, 161 (2006)
- [11] B.Abelev *et al.* (STAR Collaboration), Phys.Rev. **C79**, 034909 (2009)
- [12] B.Abelev *et al.* (STAR Collaboration), Phys.Rev. **C75**, 064901 (2007)
- [13] B.Abelev *et al.* (STAR Collaboration), Phys.Rev. Lett. **97**, 132301 (2006)
- [14] B.Abelev *et al.* (STAR Collaboration), Phys.Lett. **B616**, 8 (2005)
- [15] D.Acosta *et al.* (CDF Collaboration) Phys.Rev.**D72**, 052001 (2005)
- [16] J.Schaffner-Bielich *et al.* nucl-th/0202054 (2002)
- [17] D.Buskulic *et al.* (ALEPH Collaboration), Z.Phys.C**73**, 409 (1997)

- [18] R.Barate *et al.* (ALEPH Collaboration), Phys.Rept, **249**, 1 (1998)
- [19] G.Alexander *et al.* (OPAL Collaboration), Z.Phys.C**72**, 191 (1996)
- [20] K.Ackerstaff *et al.* (OPAL Collaboration), Z.Phys.C**75**, 193 (1997)
- [21] G.Abbiendi *et al.* (OPAL Collaboration), Eur.Phys.J.C**16**, 185 (2000) [hep-ex/0002012]
- [22] G.Abbiendi *et al.* (OPAL Collaboration), Eur.Phys.J.C**27**, 467 (2003) [hep-ex/0209048]
- [23] P.Abreu *et al.* (DELPHI Collaboration), Eur.Phys.J.C**6**, 19 (1999)
- [24] B.Adeva *et al.* (L3 Collaboration), Phys.Lett.B**259**, 199 (1991)
- [25] D.Bender *et al.*, Phys.Rev.D**31**, 1 (1985)
- [26] A.Petersen *et al.*, Phys.ReV.D**37**, 1 (1988)
- [27] G.S.Abrams *et al.*, Phys.Rev.Lett.**64**, 1334 (1990)
- [28] H.Aihara *et al.* (TPC/Two Gamma Collaboration), Phys.Rev.Lett.**61**, 1263 (1988)
- [29] R.Brandelik *et al.* (TASSO Collaboration), Phys.Lett.B**114**, 65 (1982)
- [30] W.Braunschweig *et al.* (TASSO Collaboration), Z.Phys.C**47**, 187 (1990)
- [31] Y.K.Li *et al.* (AMY Collaboration), Phys.Rev.D**41**, 2675 (1990)
- [32] Y.Hatta and T.Ikeda, Phys.Rev.D**67**, 014028(2003)
- [33] A.Andronic,P.Braun-Munzinger,J.Stachel. Nucl.Phys.A**722**, 167-199(2006)
- [34] K.Rajagopal, Nucl.Phys.A**661**, 150 (1999)
- [35] F. Karsch, J. Phys. G**31**, S633 (2005), hep-lat/0412038.
- [36] A. Adare *et al.* (PHENIX Collaboration), Phys. Rev. Lett. **101**, 232301 (2008)
- [37] S.S.Adler *et al.* (PHENIX Collaboration), Phys. Rev. Lett. **91**, 072301 (2003)
- [38] S.S.Adler *et al.* (PHENIX Collaboration), Phys. Rev. C **69**, 034910 (2004)

- [39] K.Adcox *et al.* (PHENIX Collaboration), Phys. Rev. Lett. **88** 022301 (2001)
- [40] A.Adare *et al.* (PHENIX Collaboration), Phys. Rev. C**82**, 011902(R) (2010)
- [41] A.Adare *et al.* (PHENIX Collaboration), Phys. Rev. C **84** 044902 (2011)
- [42] A.Adare *et al.* (PHENIX Collaboration), Phys. Rev. C**83**, 024909 (2011)
- [43] A.Adare *et al.* (PHENIX Collaboration), Phys. Rev. Lett. **98**, 232301 (2007)
- [44] J. W. Cronin *et al.*, Phys. Rev. D**11**, 3105 (1975)
- [45] D.Kharzeev and K.Tuchin, Nucl. Phys. A**770**, 40 (2006)
- [46] J.L.Nagle *et al.*, Phys.Rev. C**84**, 044911 (2011)
- [47] K.Hagiwara, *et al.* Review of Particle Physics. *Phys.Rev.D*, 66:010001, 2002.
- [48] K.Nakamura *et al.* *The Review of Particle Physics* J.Phys.**G37**,075021(2010)
- [49] Y.Nambu and G.Jona-Lasinio, Phys. Rev. **122**, 345 (1961)
- [50] Y.Nambu and G.Jona-Lasinio, Phys. Rev. **124**, 246 (1961)
- [51] K.Yagi, T.Hatsuda and Y.Miake, "Quark-Gluon-Plasma: From Big Bang to Little Bang", Cambridge, Univ. Pr. (2005)
- [52] W.Weise, Nucl. Phys. A**553**, 59c-72c (1993)
- [53] A.Baldit *et al.* (NA51 Collaboration), Phys.Lett.**B322**,244(1994)
- [54] E.A.Hawker *et al.* (FNAL E866/NuSea Collaboration), Phys.Rev.Lett.**80**,3715(1998)
- [55] H.Fukaya, *et al.* Phys.Rev.Lett.**98**, 172001(2007)
- [56] P.M.Stevenson, Phys.Rev.D**23**,2916 (1981)
- [57] T.Hatsuda and S.H.Lee, Phys.Rev.C**46** R34 (1992)
- [58] G. Agakichiev *et al.*, Eur. Phys. J. C **4**, 231 (1998)

- [59] J. P. Wessels *et al.*, Nucl. Phys. A**715**, 262 (2003)
- [60] R. Arnaldi *et al.* (NA60 Collaboration), Phys. Rev. Lett. **96**, 162302 (2006)
- [61] M. Naruki *et al.* (KEK-PS E325 Collaboration), Phys. Rev. Lett **96**, 092301 (2006)
- [62] R. Muto *et al.* (KEK-PS E325 Collaboration), Phys. Rev. Lett **98**, 042501 (2007)
- [63] F. Sakuma *et al.* (KEK-PS E325 Collaboration), Phys. Rev. Lett **98**, 152302 (2007)
- [64] K. Ozawa *et al.* (KEK-PS E325 Collaboration), Phys. Rev. Lett **86**, 5019 (2001)
- [65] M.H.Wood *et al.* (CLAS Collaboration), Phys. Rev. C **78**, 015201 (2008)
- [66] M. Nanova *et al.* (CBELSA/TAPS Collaboration), Eur. Phys. J. A**47**, 16 (2011)
- [67] Brown,G.E and M.Rho, Phys.Rep.**363**,85(2002)
- [68] Rapp,R. and J.Wambach, Adv.Nucl.Phys.**25**,1(2000)
- [69] Nuclear Instruments and Methods A **499**(2003) 235-244
- [70] M. Harrison, *et al.* Annu. Rev. Nucl. Part. Sci. **52**(2002) 425-469
- [71] Nuclear Instruments and Methods A **499**(2003) 423-432
- [72] Nuclear Instruments and Methods A **499**(2003) 549-559
- [73] T.Nakamura
<http://www.phenix.bnl.gov/WWW/run/03/focus/talks/bbc/focus/bbc.ppt>
- [74] Nuclear Instruments and Methods A **499**(2003) 433-436
- [75] Nuclear Instruments and Methods A **499**(2003) 480-488
- [76] K. Adcox *et al.* Nucl. Instr. and Meth., **A497**, 263 (2003)
- [77] K. Adcox *et al.* (PHENIX Collaboration), Nuclear Instruments and Methods **A499**, 489 (2003)
- [78] J.T.Mitchell *et al.* Nuclear Instruments and Methods **A482**, 491 (2002)

- [79] A.Chikanian *et al.* Nuclear Instruments and Methods **A371**, 480 1996)
- [80] M. Ohlsson *et al.*, Comp. Phys. Commun. **71**, 77 (1992)
- [81] S.S.Adler *et al.* (PHENIX Collaboration), Phys.Rev.C**69**, 034910 (2004)
- [82] Nuclear Instruments and Methods A **499**(2003) 508-520
- [83] Nuclear Instruments and Methods A **433**(1999) 143-148
- [84] Nuclear Instruments and Methods A **499**(2003) 521-536
- [85] Nuclear Instruments and Methods A **499**(2003) 537-548
- [86] Nuclear Instruments and Methods A **499**(2003) 560-592
- [87] Nuclear Instruments and Methods A **499**(2003) 593-602
- [88] website of the PHENIX experiment:
<http://www.phenix.bnl.gov/WWW/run/drawing/>
- [89] A.Adare *et al.* (PHENIX Collaboration), Phys. Rev. C**81**, 034911 (2010)
- [90] T.A.Armstrong, *et al.* (E760 Collaboration) Phys.Rev.D **54**(1996) 7067-7070
- [91] A.Spiridonov hep-ex/ **0510076**
- [92] S.S.Adler *et al.* (PHENIX Collaboration), Phys.Rev.Lett.**91**, 241803, (2003).
- [93] S.S.Adler *et al.* (PHENIX Collaboration), Phys.Rev.C**104**, 051902(R), (2007).
- [94] A.Adare *et al.* (PHENIX Collaboration), Phys. Rev. D**83**, 052004 (2011)
- [95] S.S.Adler *et al.* (PHENIX Collaboration), Phys.Rev.C**74**, 024904, (2006).
- [96] A.Adare *et al.* (PHENIX Collaboration), Phys.Rev.Lett., **104**, 132301, (2010).
- [97] J.Adams *et al.* (STAR Collaboration) Phys.Lett.B**612**, 181, (2005).
- [98] C.Tsallis, J.Stat.Phys**52**, 479, (1988).
- [99] G.Wilk and Z.Włodarczyk, Phys.Rev.Lett.**84**, 2770-2773, (2000).

- [100] B.Alper *et al.* Nucl.Phys.**B87**, 19, (1975).
- [101] J.Schaffner-Bielich *et al.* nucl-th.**020254** (2002).
- [102] S.S.Adler *et al.* (PHENIX Collaboration) Phys.Rev.**D76**, 051106, (2007).
- [103] S.S.Adler *et al.* (PHENIX Collaboration) Phys.Rev.**C75**, 024909, (2007).
- [104] A.Adare *et al.* (PHENIX Collaboration) Phys.Rev.Lett.**98**, 232002, (2007).
- [105] A.Adare *et al.* (PHENIX Collaboration) Phys.Rev.**D82**, 012001, (2010).
- [106] A.Adare *et al.* (PHENIX Collaboration) Phys.Rev.**C83**, 064903, (2011).
- [107] C.Tsallis, J.Stat.Phys.**52**,479(1998)
- [108] T.Sjostrand and M.v.Zijl, Phys.Rev. **D36**, 2019 (1987)
- [109] B.Andersson *et al.* Phys. Rept. **97**, 31-145 (1983)
- [110] T.Sjostrand, Nucl.Phys.**B248**, 469 (1984)
- [111] R.Hagedorn, Riv. Nuovo Cimento Soc. Ital. Fis. **6N10**, 1 (1983)
- [112] G.Arison *et al.* Phy.lett.**B118**, 167 (1982)
- [113] M.Biyajima *et al.* (UA1 Collaboration) Eur.Phys. J. **C48**, 597 (2006)

公表論文

- (1) Measurement of neutral mesons in $p+p$ collisions at $\sqrt{s} = 200\text{GeV}$ and scaling properties of hadron production
A.Adare, K.M.Kijima *et al.*, (別紙、共著者リスト 1 参照)
Physical Review C83, 052004 (2011).

Letter of Acceptance

This letter is to state that Mr. Kotaro M. Kijima has my approval to preferentially apply the following article as part of his doctoral dissertation at Hiroshima University.

Article: PHYSICAL REVIEW D 83, 052004 (2011)

Title: Measurement of neutral mesons in p +p collisions at $\sqrt{s} = 200$ GeV and scaling properties of hadron production

Spokesperson of the PHENIX Collaboration:

Barbara V. Jacak

Professor of Physics and Astronomy at SUNY Stony Brook University

Date: January 10, 2012

Signature:

A handwritten signature in black ink, appearing to read "Barbara V. Jacak".

Measurement of neutral mesons in $p + p$ collisions at $\sqrt{s} = 200$ GeV and scaling properties of hadron production

- A. Adare,¹¹ S. Afanasiev,²⁵ C. Aidala,^{12,36} N. N. Ajitanand,⁵³ Y. Akiba,^{47,48} H. Al-Bataineh,⁴² J. Alexander,⁵³ K. Aoki,^{30,47}
 L. Aphecetche,⁵⁵ R. Armendariz,⁴² S. H. Aronson,⁶ J. Asai,^{47,48} E. T. Atomssa,³¹ R. Averbeck,⁵⁴ T. C. Awes,⁴³
 B. Azmoun,⁶ V. Babintsev,²¹ M. Bai,⁵ G. Baksay,¹⁷ L. Baksay,¹⁷ A. Baldissari,¹⁴ K. N. Barish,⁷ P. D. Barnes,³³
 B. Bassalleck,⁴¹ A. T. Basye,¹ S. Bathe,⁷ S. Batsouli,⁴³ V. Baublis,⁴⁶ C. Baumann,³⁷ A. Bazilevsky,⁶ S. Belikov,^{6,*}
 R. Bennett,⁵⁴ A. Berdnikov,⁵⁰ Y. Berdnikov,⁵⁰ A. A. Bickley,¹¹ J. G. Boissevain,³³ H. Borel,¹⁴ K. Boyle,⁵⁴ M. L. Brooks,³³
 H. Buesching,⁶ V. Bumazhnov,²¹ G. Bunce,^{6,48} S. Butsyk,^{33,54} C. M. Camacho,³³ S. Campbell,⁵⁴ B. S. Chang,⁶²
 W. C. Chang,² J.-L. Charvet,¹⁴ S. Chernichenko,²¹ J. Chiba,²⁶ C. Y. Chi,¹² M. Chiu,²² I. J. Choi,⁶² R. K. Choudhury,⁴
 T. Chujo,^{58,59} P. Chung,⁵³ A. Churyn,²¹ V. Cianciolo,⁴³ Z. Citron,⁵⁴ C. R. Cleven,¹⁹ B. A. Cole,¹² M. P. Comets,⁴⁴
 P. Constantin,³³ M. Csanad,¹⁶ T. Csorgo,²⁷ T. Dahms,⁵⁴ S. Dairaku,^{30,47} K. Das,¹⁸ G. David,⁶ M. B. Deaton,¹ K. Dehmelt,¹⁷
 H. Delagrange,⁵⁵ A. Denisov,²¹ D. d'Enterria,^{12,31} A. Deshpande,^{48,54} E. J. Desmond,⁶ O. Dietzsch,⁵¹ A. Dion,⁵⁴
 M. Donadelli,⁵¹ O. Drapier,³¹ A. Drees,⁵⁴ K. A. Drees,⁵ A. K. Dubey,⁶¹ A. Durum,²¹ D. Dutta,⁴ V. Dzhordzhadze,⁷
 Y. V. Efremenko,⁴³ J. Egdemir,⁵⁴ F. Ellinghaus,¹¹ W. S. Emam,⁷ T. Engelmore,¹² A. Enokizono,³² H. En'yo,^{47,48}
 S. Esumi,⁵⁸ K. O. Eyser,⁷ B. Fadem,³⁸ D. E. Fields,^{41,48} M. Finger, Jr.,^{8,25} M. Finger,^{8,25} F. Fleuret,³¹ S. L. Fokin,²⁹
 Z. Fraenkel,^{61,*} J. E. Frantz,⁵⁴ A. Franz,⁶ A. D. Frawley,¹⁸ K. Fujiwara,⁴⁷ Y. Fukao,^{30,47} T. Fusayasu,⁴⁰ S. Gadrat,³⁴
 I. Garishvili,⁵⁶ A. Glenn,¹¹ H. Gong,⁵⁴ M. Gonin,³¹ J. Gosset,¹⁴ Y. Goto,^{47,48} R. Granier de Cassagnac,³¹ N. Grau,^{12,24}
 S. V. Greene,⁵⁹ M. Grosse Perdekamp,^{22,48} T. Gunji,¹⁰ H. -A. Gustafsson,^{35,*} T. Hachiya,²⁰ A. Hadj Henni,⁵⁵
 C. Haegemann,⁴¹ J. S. Haggerty,⁶ H. Hamagaki,¹⁰ R. Han,⁴⁵ H. Harada,²⁰ E. P. Hartouni,³² K. Haruna,²⁰ E. Haslum,³⁵
 R. Hayano,¹⁰ M. Heffner,³² T. K. Hemmick,⁵⁴ T. Hester,⁷ X. He,¹⁹ H. Hiejima,²² J. C. Hill,²⁴ R. Hobbs,⁴¹ M. Hohlmann,¹⁷
 W. Holzmann,⁵³ K. Homma,²⁰ B. Hong,²⁸ T. Horaguchi,^{10,47,57} D. Hornback,⁵⁶ S. Huang,⁵⁹ T. Ichihara,^{47,48} R. Ichimiya,⁴⁷
 H. Iinuma,^{30,47} Y. Ikeda,⁵⁸ K. Imai,^{30,47} J. Imrek,¹⁵ M. Inaba,⁵⁸ Y. Inoue,^{49,47} D. Isenhower,¹ L. Isenhower,¹ M. Ishihara,⁴⁷
 T. Isobe,¹⁰ M. Issah,⁵³ A. Isupov,²⁵ D. Ivanischev,⁴⁶ B. V. Jacak,^{54,†} J. Jia,¹² J. Jin,¹² O. Jinnouchi,⁴⁸ B. M. Johnson,⁶
 K. S. Joo,³⁹ D. Jouan,⁴⁴ F. Kajihara,¹⁰ S. Kametani,^{10,47,60} N. Kamihara,^{47,48} J. Kamin,⁵⁴ M. Kaneta,⁴⁸ J. H. Kang,⁶²
 H. Kanou,^{47,57} J. Kapustinsky,³³ D. Kawall,^{36,48} A. V. Kazantsev,²⁹ T. Kempel,²⁴ A. Khanzadeev,⁴⁶ K. M. Kijima,²⁰
 J. Kikuchi,⁶⁰ B. I. Kim,²⁸ D. H. Kim,³⁹ D. J. Kim,⁶² E. Kim,⁵² S. H. Kim,⁶² E. Kinney,¹¹ K. Kiriluk,¹¹ A. Kiss,¹⁶
 E. Kistenev,⁶ A. Kiyomichi,⁴⁷ J. Klay,³² C. Klein-Boesing,³⁷ L. Kochenda,⁴⁶ V. Kochetkov,²¹ B. Komkov,⁴⁶ M. Konno,⁵⁸
 J. Koster,²² D. Kotchetkov,⁷ A. Kozlov,⁶¹ A. Kral,¹³ A. Kravitz,¹² J. Kubart,^{8,23} G. J. Kunde,³³ N. Kurihara,¹⁰
 K. Kurita,^{49,47} M. Kurosawa,⁴⁷ M. J. Kweon,²⁸ Y. Kwon,^{56,62} G. S. Kyle,⁴² R. Lacey,⁵³ Y. S. Lai,¹² J. G. Lajoie,²⁴
 D. Layton,²² A. Lebedev,²⁴ D. M. Lee,³³ K. B. Lee,²⁸ M. K. Lee,⁶² T. Lee,⁵² M. J. Leitch,³³ M. A. L. Leite,⁵¹ B. Lenzi,⁵¹
 P. Liebing,⁴⁸ T. Lika,¹³ A. Litvinenko,²⁵ H. Liu,⁴² M. X. Liu,³³ X. Li,⁹ B. Love,⁵⁹ D. Lynch,⁶ C. F. Maguire,⁵⁹
 Y. I. Makdisi,⁵ A. Malakhov,²⁵ M. D. Malik,⁴¹ V. I. Manko,²⁹ E. Mannel,¹² Y. Mao,^{45,47} L. Maek,^{8,23} H. Masui,⁵⁸
 F. Matathias,¹² M. McCumber,⁵⁴ P. L. McGaughey,³³ N. Means,⁵⁴ B. Meredith,²² Y. Miake,⁵⁸ P. Mike, ^{8,23} K. Miki,⁵⁸
 T. E. Miller,⁵⁹ A. Milov,^{6,54} S. Mioduszewski,⁶ M. Mishra,³ J. T. Mitchell,⁶ M. Mitrovski,⁵³ A. K. Mohanty,⁴ Y. Morino,¹⁰
 A. Morreale,⁷ D. P. Morrison,⁶ T. V. Moukhanova,²⁹ D. Mukhopadhyay,⁵⁹ J. Murata,^{49,47} S. Nagamiya,²⁶ Y. Nagata,⁵⁸
 J. L. Nagle,¹¹ M. Naglis,⁶¹ M. I. Nagy,¹⁶ I. Nakagawa,^{47,48} Y. Nakamiya,²⁰ T. Nakamura,²⁰ K. Nakano,^{47,57} J. Newby,³²
 M. Nguyen,⁵⁴ T. Niita,⁵⁸ B. E. Norman,³³ R. Nouicer,⁶ A. S. Nyanin,²⁹ E. O'Brien,⁶ S. X. Oda,¹⁰ C. A. Ogilvie,²⁴
 H. Ohnishi,⁴⁷ K. Okada,⁴⁸ M. Oka,⁵⁸ O. O. Omiwade,¹ Y. Onuki,⁴⁷ A. Oskarsson,³⁵ M. Ouchida,²⁰ K. Ozawa,¹⁰ R. Pak,⁶
 D. Pal,⁵⁹ A. P. T. Palounek,³³ V. Pantuev,⁵⁴ V. Papavassiliou,⁴² J. Park,⁵² W. J. Park,²⁸ S. F. Pate,⁴² H. Pei,²⁴ J.-C. Peng,²²
 H. Pereira,¹⁴ V. Peresedov,²⁵ D. Yu. Peressounko,²⁹ C. Pinkenburg,⁶ M. L. Purschke,⁶ A. K. Purwar,³³ H. Qu,¹⁹ J. Rak,⁴¹
 A. Rakotozafindrabe,³¹ I. Ravinovich,⁶¹ K. F. Read,^{43,56} S. Rembeczki,¹⁷ M. Reuter,⁵⁴ K. Reygers,³⁷ V. Riabov,⁴⁶
 Y. Riabov,⁴⁶ D. Roach,⁵⁹ G. Roche,³⁴ S. D. Rolnick,⁷ A. Romana,^{31,*} M. Rosati,²⁴ S. S. E. Rosendahl,³⁵ P. Rosnet,³⁴
 P. Rukoyatkin,²⁵ P. Ruika,²³ V. L. Rykov,⁴⁷ B. Sahlmueller,³⁷ N. Saito,^{30,47,48} T. Sakaguchi,⁶ S. Sakai,⁵⁸
 K. Sakashita,^{47,57} H. Sakata,²⁰ V. Samsonov,⁴⁶ S. Sato,²⁶ T. Sato,⁵⁸ S. Sawada,²⁶ K. Sedgwick,⁷ J. Seele,¹¹ R. Seidl,²²
 A. Yu. Semenov,²⁴ V. Semenov,²¹ R. Seto,⁷ D. Sharma,⁶¹ I. Shein,²¹ A. Shevel,^{46,53} T.-A. Shibata,^{47,57} K. Shigaki,²⁰
 M. Shimomura,⁵⁸ K. Shoji,^{30,47} P. Shukla,⁴ A. Sickles,^{6,54} C. L. Silva,⁵¹ D. Silvermyr,⁴³ C. Silvestre,¹⁴ K. S. Sim,²⁸
 B. K. Singh,³ C. P. Singh,³ V. Singh,³ S. Skutnik,²⁴ M. Sluneka,^{8,25} A. Soldatov,²¹ R. A. Soltz,³² W. E. Sondheim,³³
 S. P. Sorensen,⁵⁶ I. V. Sourikova,⁶ F. Staley,¹⁴ P. W. Stankus,⁴³ E. Stenlund,³⁵ M. Stepanov,⁴² A. Ster,²⁷ S. P. Stoll,⁶
 T. Sugitate,²⁰ C. Suire,⁴⁴ A. Sukhanov,⁶ J. Sziklai,²⁷ T. Tabaru,⁴⁸ S. Takagi,⁵⁸ E. M. Takagui,⁵¹ A. Takehara,^{47,48}
 R. Tanabe,⁵⁸ Y. Tanaka,⁴⁰ K. Tanida,^{47,48,52} M. J. Tannenbaum,⁶ A. Tarantenko,⁵³ P. Tarjan,¹⁵ H. Themann,⁵⁴

T. L. Thomas,⁴¹ M. Togawa,^{30,47} A. Toia,⁵⁴ J. Tojo,⁴⁷ L. Tomášek,²³ Y. Tomita,⁵⁸ H. Torii,^{20,47} R. S. Towell,¹ V-N. Tram,³¹ I. Tserruya,⁶¹ Y. Tsuchimoto,²⁰ C. Vale,²⁴ H. Valle,⁵⁹ H. W. van Hecke,³³ A. Veicht,²² J. Velkovska,⁵⁹ R. Vértesi,¹⁵ A. A. Vinogradov,²⁹ M. Virius,¹³ V. Vrba,²³ E. Vznuzdaev,⁴⁶ M. Wagner,^{30,47} D. Walker,⁵⁴ X. R. Wang,⁴² Y. Watanabe,^{47,48} F. Wei,²⁴ J. Wessels,³⁷ S. N. White,⁶ D. Winter,¹² C. L. Woody,⁶ M. Wysocki,¹¹ W. Xie,⁴⁸ Y. L. Yamaguchi,⁶⁰ K. Yamaura,²⁰ R. Yang,²² A. Yanovich,²¹ Z. Yasin,⁷ J. Ying,¹⁹ S. Yokkaichi,^{47,48} G. R. Young,⁴³ I. Younus,⁴¹ I. E. Yushmanov,²⁹ W. A. Zajc,¹² O. Zaudtke,³⁷ C. Zhang,⁴³ S. Zhou,⁹ J. Zimányi,^{27,*} and L. Zolin²⁵

(PHENIX Collaboration)

¹Abilene Christian University, Abilene, Texas 79699, USA

²Institute of Physics, Academia Sinica, Taipei 11529, Taiwan

³Department of Physics, Banaras Hindu University, Varanasi 221005, India

⁴Bhabha Atomic Research Centre, Bombay 400 085, India

⁵Collider-Accelerator Department, Brookhaven National Laboratory, Upton, New York 11973-5000, USA

⁶Physics Department, Brookhaven National Laboratory, Upton, New York 11973-5000, USA

⁷University of California-Riverside, Riverside, California 92521, USA

⁸Charles University, Ovocný trh 5, Praha 1, 116 36, Prague, Czech Republic

⁹Science and Technology on Nuclear Data Laboratory, China Institute of Atomic Energy, Beijing, People's Republic of China

¹⁰Center for Nuclear Study, Graduate School of Science, University of Tokyo, 7-3-1 Hongo, Bunkyo, Tokyo 113-0033, Japan

¹¹University of Colorado, Boulder, Colorado 80309, USA

¹²Columbia University, New York, New York 10027 and Nevis Laboratories, Irvington, New York 10533, USA

¹³Czech Technical University, Zikova 4, 166 36 Prague 6, Czech Republic

¹⁴Dapnia, CEA Saclay, F-91191, Gif-sur-Yvette, France

¹⁵Debrecen University, H-4010 Debrecen, Egyetem tér 1, Hungary

¹⁶ELTE, Eötvös Loránd University, H-1117 Budapest, Pázmány P.s. 1/A, Hungary

¹⁷Florida Institute of Technology, Melbourne, Florida 32901, USA

¹⁸Florida State University, Tallahassee, Florida 32306, USA

¹⁹Georgia State University, Atlanta, Georgia 30303, USA

²⁰Hiroshima University, Kagamiyama, Higashi-Hiroshima 739-8526, Japan

²¹IHEP Protvino, State Research Center of Russian Federation, Institute for High Energy Physics, Protvino, 142281, Russia

²²University of Illinois at Urbana-Champaign, Urbana, Illinois 61801, USA

²³Institute of Physics, Academy of Sciences of the Czech Republic, Na Slovance 2, 182 21 Prague 8, Czech Republic

²⁴Iowa State University, Ames, Iowa 50011, USA

²⁵Joint Institute for Nuclear Research, 141980 Dubna, Moscow Region, Russia

²⁶KEK, High Energy Accelerator Research Organization, Tsukuba, Ibaraki 305-0801, Japan

²⁷KFKI Research Institute for Particle and Nuclear Physics of the Hungarian Academy of Sciences (MTA KFKI RMKI),

H-1525 Budapest 114, P.O. Box 49, Budapest, Hungary

²⁸Korea University, Seoul, 136-701, Korea

²⁹Russian Research Center "Kurchatov Institute", Moscow, Russia

³⁰Kyoto University, Kyoto 606-8502, Japan

³¹Laboratoire Leprince-Ringuet, Ecole Polytechnique, CNRS-IN₂P₃, Route de Saclay, F-91128, Palaiseau, France

³²Lawrence Livermore National Laboratory, Livermore, California 94550, USA

³³Los Alamos National Laboratory, Los Alamos, New Mexico 87545, USA

³⁴LPC, Université Blaise Pascal, CNRS-IN₂P₃, Clermont-Fd, 63177 Aubiere Cedex, France

³⁵Department of Physics, Lund University, Box 118, SE-221 00 Lund, Sweden

³⁶Department of Physics, University of Massachusetts, Amherst, Massachusetts 01003-9337, USA

³⁷Institut für Kernphysik, University of Muenster, D-48149 Muenster, Germany

³⁸Muhlenberg College, Allentown, Pennsylvania 18104-5586, USA

³⁹Myongji University, Yongin, Kyonggi-do 449-728, Korea

⁴⁰Nagasaki Institute of Applied Science, Nagasaki-shi, Nagasaki 851-0193, Japan

⁴¹University of New Mexico, Albuquerque, New Mexico 87131, USA

⁴²New Mexico State University, Las Cruces, New Mexico 88003, USA

⁴³Oak Ridge National Laboratory, Oak Ridge, Tennessee 37831, USA

⁴⁴IPN-Orsay, Université Paris Sud, CNRS-IN₂P₃, BP1, F-91406, Orsay, France

⁴⁵Peking University, Beijing, People's Republic of China

⁴⁶PNPI, Petersburg Nuclear Physics Institute, Gatchina, Leningrad region, 188300, Russia

⁴⁷RIKEN Nishina Center for Accelerator-Based Science, Wako, Saitama 351-0198, JAPAN

⁴⁸RIKEN BNL Research Center, Brookhaven National Laboratory, Upton, New York 11973-5000, USA

⁴⁹Physics Department, Rikkyo University, 3-34-1 Nishi-Ikebukuro, Toshima, Tokyo 171-8501, Japan

⁵⁰Saint Petersburg State Polytechnic University, St. Petersburg, Russia⁵¹Universidade de São Paulo, Instituto de Física, Caixa Postal 66318, São Paulo CEP05315-970, Brazil⁵²System Electronics Laboratory, Seoul National University, Seoul, Korea⁵³Chemistry Department, Stony Brook University, Stony Brook, SUNY, New York 11794-3400, USA⁵⁴Department of Physics and Astronomy, Stony Brook University, SUNY, Stony Brook, New York 11794, USA⁵⁵SUBATECH (Ecole des Mines de Nantes, CNRS-IN₂P₃, Université de Nantes) BP 20722 - 44307, Nantes, France⁵⁶University of Tennessee, Knoxville, Tennessee 37996, USA⁵⁷Department of Physics, Tokyo Institute of Technology, Oh-okayama, Meguro, Tokyo 152-8551, Japan⁵⁸Institute of Physics, University of Tsukuba, Tsukuba, Ibaraki 305, Japan⁵⁹Vanderbilt University, Nashville, Tennessee 37235, USA⁶⁰Waseda University, Advanced Research Institute for Science and Engineering, 17 Kikui-cho, Shinjuku-ku, Tokyo 162-0044, Japan⁶¹Weizmann Institute, Rehovot 76100, Israel⁶²Yonsei University, IPAP, Seoul 120-749, Korea

(Received 20 May 2010; published 16 March 2011)

The PHENIX experiment at the Relativistic Heavy Ion Collider has measured the invariant differential cross section for production of K_S^0 , ω , η' , and ϕ mesons in $p + p$ collisions at $\sqrt{s} = 200$ GeV. Measurements of ω and ϕ production in different decay channels give consistent results. New results for the ω are in agreement with previously published data and extend the measured p_T coverage. The spectral shapes of all hadron transverse momentum distributions measured by PHENIX are well described by a Tsallis distribution functional form with only two parameters, n and T , determining the high- p_T and characterizing the low- p_T regions of the spectra, respectively. The values of these parameters are very similar for all analyzed meson spectra, but with a lower parameter T extracted for protons. The integrated invariant cross sections calculated from the fitted distributions are found to be consistent with existing measurements and with statistical model predictions.

DOI: 10.1103/PhysRevD.83.052004

PACS numbers: 25.75.Dw

I. INTRODUCTION

The PHENIX experiment at the Relativistic Heavy Ion Collider (RHIC) at Brookhaven National Laboratory has measured the production of a wide variety of hadrons (π , K , η , η' , ω , ϕ , p , J/ψ , and ψ') at midrapidity in $p + p$ collisions at $\sqrt{s} = 200$ GeV. The measurements were performed using a time-of-flight technique for charged hadron identification and via reconstruction of various photonic, hadronic, and dielectron decay modes for neutral hadrons. The measured transverse momentum spectra extend over the range from zero to 20 GeV/c. Precise measurements of hadron production in $p + p$ collisions are crucial for a deeper understanding of QCD phenomena such as parton dynamics and hadronization. They also provide a valuable baseline for particle and jet production in heavy ion collisions, essential to the needs of the RHIC heavy ion program.

There exists a large body of experimental data on hadron production in $p + p$ collisions measured at the Intersecting Storage Rings, $S\bar{p}\bar{S}$, Tevatron, and RHIC [1–19]. At high p_T the spectra display a power law behavior that becomes more and more evident as the interaction energy increases. In this regime, the spectra are well described by perturbative QCD together with measured proton structure func-

tions [20]. At low p_T , typically $p_T < 2$ GeV/c, a region which accounts for the bulk of the produced particles, the spectra are governed by processes that belong to the non-perturbative regime of QCD and are not yet fully understood. In this p_T region, the spectra reveal an exponential behavior which can be explained with the assumption that secondary particles are emitted from a thermalized system with, at most, short-range correlations and obeying Boltzmann-Gibbs statistics [21]. In this approach, the inverse slope parameter T can be interpreted as the temperature of the system. However, that would require some mechanism of local thermal equilibrium in $p + p$ collisions which is not yet established. It is also known that the particle spectra are best described by an exponential in m_T rather than in p_T [22]. According to the observation that the temperature parameter T in the exponential function is the same for different particles, the spectral shape is also the same. This observation is consistent with m_T scaling [18,23].

The two regimes described here and the p_T region where their contributions are predominant are commonly designated as “soft” and “hard.” There is no obvious boundary between them, and the distinction between production mechanisms in each region is difficult to determine experimentally. The spectral shapes of all hadrons produced in $p + p$ collisions at $\sqrt{s} = 200$ GeV are well described by one single distribution without making a distinct division into two regions. The Tsallis [24] distribution, also referred to as a Levy distribution [7,25], has only two parameters, T

*Deceased.

†PHENIX Spokesperson.
jacak@skipper.physics.sunysb.edu

and n , that characterize the low- and high- p_T regions of the spectra, respectively. This distribution has been shown by Tsallis to result from a postulated generalization of the Boltzmann-Gibbs entropy. It has been suggested to be relevant for various types of systems, such as those with long-range correlations, or nonergodic filling of the available phase space. Boltzmann statistics and exponential distributions are recovered in the limit that correlations disappear. The parameter T then recovers the usual interpretation as the temperature of the system.

In a number of recent publications [26–30] the Tsallis statistical distribution was successfully applied to describe data for $A + A$ and $p + p$ collisions over a wide range of incident energies and centralities. Discussed in other publications [31–36] are the physical mechanisms responsible for the successful application of the nonextensive statistical approach to the description of the particle spectra. However, the analysis presented in this paper uses the Tsallis formalism primarily as a parametrization to describe the particle spectra and compares it with other parametrizations used for the spectra approximation. Common features and differences revealed in such an approach are data driven and should contribute to a better understanding of particle production mechanisms.

The successful description of the particle spectra with the Tsallis distribution allows us to accurately calculate the integrated particle yield and mean momentum, even for species measured only in a limited momentum range. The integrated particle abundances provide important information on the bulk properties of the soft particle production. In particular, the comparison of the particle yields to statistical model predictions can be used to infer the degree of hadro-chemical equilibration. In the case of heavy ion collisions, the success of statistical model fits to the particle yields [37,38] suggests that hadro-chemical equilibration is essentially complete. These models have also been used to describe particle production in $p + p$ collisions [39,40].

In this paper we present new PHENIX results on the production of neutral mesons in $p + p$ collisions at $\sqrt{s} = 200$ GeV and compare the PHENIX data with the parametrizations commonly used to describe particle spectra in relativistic $p + p$ collisions, including the Tsallis parametrization. It is demonstrated that the latter describes the data in the entire range of measured p_T most accurately. The parameter values extracted from the fits are given for all measured particles.

The paper is organized as follows: Sec. II gives a description of the PHENIX experimental setup and detector subsystems. Section III describes the analysis methods used to measure the transverse momentum spectra of different hadrons for $p + p$ collisions at $\sqrt{s} = 200$ GeV. In Sec. IV the properties of the measured transverse momentum spectra are analyzed. In Sec. V the scaling properties of the particle spectra are discussed and the calculated

integrated yields are compared with published results and with statistical model calculations. The measured invariant cross sections are tabulated in tables given in the Appendix.

II. PHENIX DETECTOR

The PHENIX detector is designed as a high rate and fine granularity apparatus that utilizes a variety of detector technologies to measure global characteristics of the events, and to measure leptons, hadrons, and photons over a wide range of transverse momenta. The experimental setup comprises two central arm spectrometers each covering $\Delta\phi = \pi/2$ in azimuth at midrapidity $|\eta| < 0.35$, and two forward muon spectrometers with full azimuthal coverage in the rapidity interval $1.2 < |\eta| < 2.4(2.2)$ for the north (south) arm and a system of “global” detectors. Each spectrometer provides very good momentum and spatial resolution and particle identification capabilities. The detailed description of the detector can be found elsewhere [41]. The experimental results presented in this paper were obtained using the central spectrometers and global detectors of the PHENIX experiment schematically shown in Fig. 1.

Reconstruction of charged particle tracks and momentum measurements are performed with the drift chambers (DC) and the first layer of the pad chambers (PC1). The fiducial volume of the DC is located outside of the analyzing magnetic field of the detector and has an inner radius of 2.02 m and an outer radius of 2.46 m. Multiple layers of wires measure the track position with an angular resolution of ~ 0.8 mrad in the bending plane perpendicular to the beam axis. The PC1, located just outside the outer radius of the DC, has a spatial resolution of $\sigma_\phi \sim 2.4$ mm and $\sigma_z \sim 1.7$ mm and provides the z coordinate of the track at the

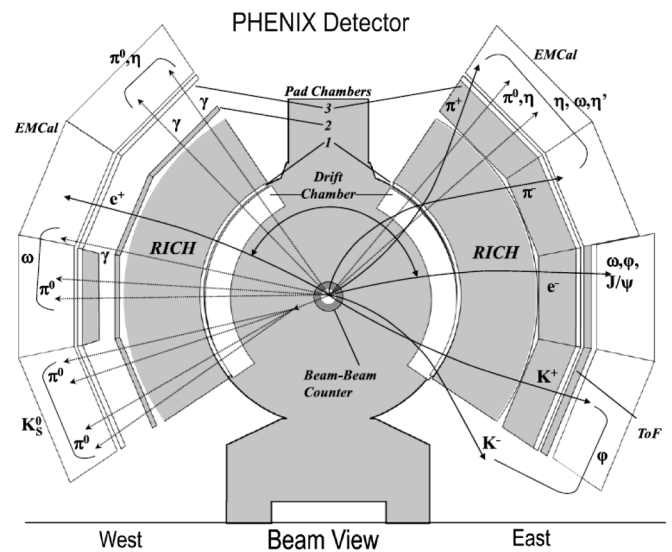


FIG. 1. Schematic view of the PHENIX central spectrometers and particle decay modes analyzed in this paper.

exit of the DC. The momentum of a particle is determined by the measured bending angle in the axial magnetic field of the central magnet [42], assuming that the particle originates from the collision vertex. The DC momentum resolution is estimated to be $\delta p/p = 0.7 \oplus 1.1\%p$ [GeV/c]. Track matching with hits in the second (PC2) and third (PC3) pad chamber layers located at radii of 4.2 m and 5.0 m, respectively, rejects tracks from secondaries originating either from decays of long-lived hadrons or from interactions with the structure of the detector. Such tracks have not passed through the full magnetic field and therefore have improperly determined momenta that are typically overestimated. A detailed description of the PHENIX tracking system can be found in [43,44].

The primary purpose of the PHENIX electromagnetic calorimeter (EMCal) is to measure the position and energy of photons and electrons. The EMCal covers the full acceptance of the central spectrometers and is divided into eight sectors. Six of the EMCal sectors located at a radius of 5.0 m are built of lead scintillator (PbSc) and comprise 15 552 individual towers with a granularity of 5.5×5.5 cm 2 and a depth of $18 X_0$. The two other sectors located at a radius of 5.2 m are built of lead glass (PbGl) and comprise 9216 lead-glass Čerenkov towers with a granularity of 4×4 cm 2 and a depth of $14.4 X_0$. Because of the fine segmentation of the EMCal, the electromagnetic showers typically spread over several towers. This spread provides the means to analyze the position and shape of the shower, and to reject hadrons which produce showers of a different shape. The spatial resolution of the PbSc (PbGl) EMCal sector is $\sigma(E) = 1.55(0.2) \oplus 5.7(8.4)/\sqrt{E[\text{GeV}]}$ mm for particles at normal incidence. The energy resolution of the PbSc (PbGl) calorimeter is $\delta E/E = 2.1(0.8)\% \oplus 8.1(5.9)/\sqrt{E[\text{GeV}]}\%$.

The time-of-flight (TOF) subsystem is used for hadron identification based on momentum measurements in the DC and PC1 combined with flight path length from the collision vertex [45]. The TOF is located between the PC3 and the PbGl at a radius of 5.0 m and covers about 1/3 of the acceptance of one central arm. The TOF detector comprises 10 panels, each containing 96 segments equipped with plastic scintillators and photomultiplier readout from both ends. The time resolution of ~ 120 ps enables π/K and K/p separation in the transverse momentum ranges 0.3–2.5 GeV/c and 0.3–5.0 GeV/c, respectively. The lower limit is defined by the energy loss of different particles in the detector material.

The Ring-Imaging Čerenkov (RICH) detector is the primary detector for e/π separation. It provides an e/π rejection factor of $\sim 10^{-3}$ for tracks with momenta below the pion Čerenkov threshold of ~ 4 GeV/c in the CO₂ used as a radiator gas. The RICH detector, in each arm, has a mirror measuring 20 m 2 that focuses the light onto an array of 2560 photomultipliers. The material of the PHENIX central arm that precedes the RICH detector has been kept to just $\sim 2\%$ of a radiation length in order

to minimize the background contribution of electrons from γ conversion. The PHENIX RICH and TOF detectors are described in more detail in [45].

The Beam-Beam Counter (BBC) detectors [46] are used for triggering, determination of the collision time, and location of the vertex along the beam axis, z_{vtx} . Each BBC comprises 64 Čerenkov counters surrounding the beam pipe, and located at a distance of ± 1.44 m from the center of the interaction region. Each BBC covers the full azimuth and the pseudorapidity interval $3.1 < |\eta| < 3.9$. The z coordinate of the collision vertex is determined with a typical resolution of 2 cm in $p + p$ collisions by the timing difference of the signals from each BBC. The time average of all BBC signals gives a start time for the time-of-flight measurements. The minimum bias trigger in $p + p$ collisions is generated when there is at least one count from each BBC, and the collision vertex calculated online is $|z_{\text{vtx}}| < 38$ cm. The efficiency of the minimum bias trigger is estimated to be $(55 \pm 5)\%$ of the total inelastic cross section of $\sigma_{\text{inel}}^{pp} = 42 \pm 3$ mb. Further details about the BBC subsystem of the PHENIX detector can be found in [46].

Because of the high rate of $p + p$ collisions at RHIC, PHENIX employs several specialized triggers which enable the experiment to sample more of the delivered luminosity for rare events. Besides the minimum bias trigger, the experimental results presented in this paper were obtained using the EMCal-RICH Trigger (ERT).

The EMCal is used to trigger on rare events with a large energy deposit originating primarily from high-energy photons or electrons. The analog sum of signals from 4×4 adjacent towers is compared with a trigger threshold of 1.4 GeV. In addition, a combination of the EMCal and the RICH signals is used to build the ERT trigger, which is designed to select events containing electrons. The trigger fires when the analog sum of signals from 2×2 adjacent towers in the EMCal exceeds a threshold of 0.4 GeV (setting used in the 2005 physics run) or 0.6 GeV (used in 2006) in geometrical coincidence with a signal in the associated RICH trigger tile (4×5 PMTs) determined using a lookup table.

III. NEUTRAL MESON MEASUREMENTS

In this section we describe the analysis details of the $K_S^0 \rightarrow \pi^0 \pi^0$, $\omega \rightarrow \pi^0 \pi^+ \pi^-$, $\omega \rightarrow \pi^0 \gamma$, $\omega \rightarrow e^+ e^-$, $\eta' \rightarrow \eta \pi^+ \pi^-$, $\phi \rightarrow K^+ K^-$, and $\phi \rightarrow e^+ e^-$ measurements in $p + p$ collisions at $\sqrt{s} = 200$ GeV. These measurements complete and extend previous neutral meson spectra results measured by the PHENIX experiment and published in [2,3,5,6,47,48].

The measurements are based on a data sample representing a total integrated luminosity of 2.5 pb^{-1} within a vertex cut of $|z_{\text{vtx}}| < 30$ cm accumulated by the PHENIX experiment in 2005. The data were collected using minimum bias and ERT triggers.

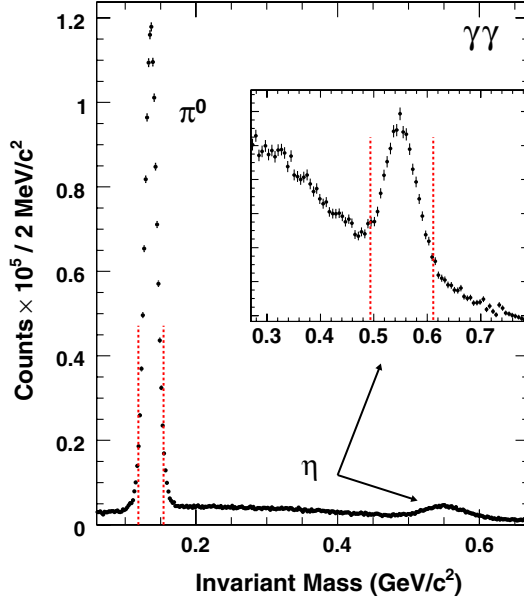


FIG. 2 (color online). Invariant mass distribution for $\gamma\gamma$ pairs in the range $4 < p_T$ (GeV/c) < 6 . The inset shows an enlargement of the region around the η mass.

A. Reconstruction of neutral mesons

Here we discuss the analysis details and main parameters of the invariant mass distributions reconstructed for different decay modes.

1. Selection of the π^0 , $\eta \rightarrow \gamma\gamma$ candidates

Most particles studied in this section decay, producing a π^0 or η meson in the final state, which in turn decays into a $\gamma\gamma$ pair at the point of primary decay. The analysis procedures for the measurement of the inclusive π^0 and η invariant transverse momentum spectra in $p + p$ collisions have been published previously [2,3,6,47]. Meson candidates were reconstructed from pairs of clusters in the

EMCal with energy $E_\gamma > 0.2$ GeV, assuming that they correspond to photons originating from the collision vertex. A shower profile cut was used to reject broader showers predominantly produced by hadrons [49]. The invariant mass distribution for cluster pairs is shown in Fig. 2.

The width of the peaks is determined largely by the EMCal energy resolution. For $\pi^0(\eta)$ meson candidates the width decreases from $12(40)$ MeV/c 2 to $9(30)$ MeV/c 2 between 1 GeV/c and 3 GeV/c of the pair transverse momentum.

The reconstructed positions and widths of the peaks are in agreement with simulation results once detector resolution and trigger biases have been taken into account. The measured mass peaks were parametrized as a function of the $\gamma\gamma$ pair p_T . For further analyses involving π^0 or η mesons in the final state, we selected pairs with $p_T > 1$ GeV/c and an invariant mass within 2 standard deviations of the measured peak position. All $\gamma\gamma$ pairs satisfying these criteria were assigned the nominal mass of the meson [50] and the photon energies were rescaled by the ratio of the nominal to the reconstructed masses.

2. $\omega \rightarrow \pi^0\gamma$ and $K_S^0 \rightarrow \pi^0\pi^0$

The reconstruction of $\omega \rightarrow \pi^0\gamma$ and $K_S^0 \rightarrow \pi^0\pi^0$ decays was performed by combining π^0 candidates with either all other photons with energy $E_\gamma > 1$ GeV [4] or with all other π^0 candidates from the same event. Combinations using the same EMCal clusters more than once were rejected.

Invariant mass distributions for $\pi^0\gamma$ and $\pi^0\pi^0$ decays are shown in Fig. 3. The width of the ω meson peak is ~ 30 MeV and has a weak p_T dependence. The width of the K_S^0 peak is ~ 15 MeV. The signal-to-background ratio (S:B) increases from 1:30 (1:4) to 1:5 (1:2) for ω (K_S^0) mesons as the transverse momentum increases from 2 to 12 GeV/c.

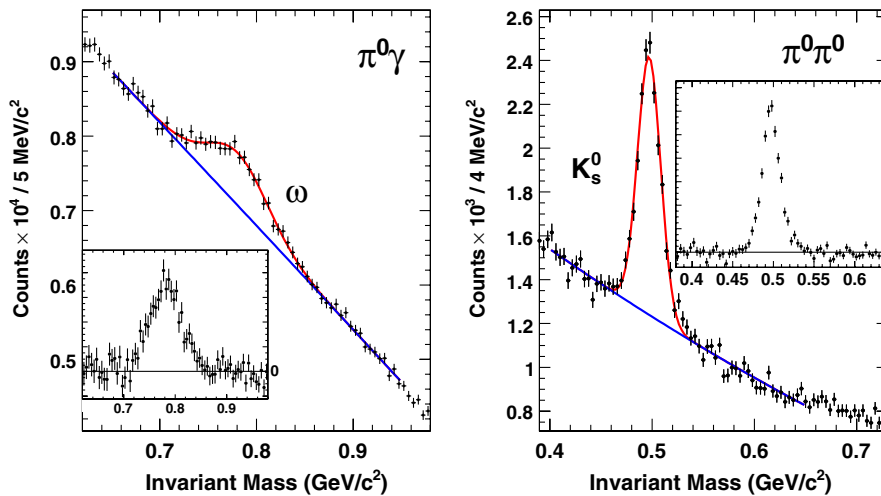


FIG. 3 (color online). Invariant mass distribution for $\pi^0\gamma$ (left panel) and $\pi^0\pi^0$ (right panel) decays at $4 < p_T$ (GeV/c) < 6 .

The main difference in the analysis of the ω and K_S^0 decays was due to the large lifetime of the K_S^0 meson. Neutral pions coming from the decays of high- p_T K_S^0 originate from a displaced vertex, and their reconstructed mass and width need to be parametrized in a different way compared to pions coming from the primary event vertex. This effect was studied using the PHENIX Monte Carlo calculations. The correction was based on the mass and width of π^0 's coming from kaon decays with a realistic p_T distribution, and on π^0 's produced at the collision vertex with the inclusive p_T distribution.

3. $\omega, \eta \rightarrow \pi^0\pi^+\pi^-$, $\eta' \rightarrow \eta\pi^+\pi^-$

For the reconstruction of $\omega, \eta \rightarrow \pi^0\pi^+\pi^-$ and $\eta' \rightarrow \eta\pi^+\pi^-$ decay modes, we combined $\pi^0(\eta)$ candidates with all pairs of oppositely charged tracks in the same event [2,4]. Charged tracks accepted for this analysis were required to have momenta in the range $0.2 < p_T (\text{GeV}/c) < 8$, and were assigned the charged pion mass. Tracks with momentum below $0.2 \text{ GeV}/c$ do not go through the entire detector due to their large bending angle in the axial magnetic field of the central magnet. Tracks that appear to have momenta above $8 \text{ GeV}/c$ are, for the most part, low momentum secondaries coming from the decay of long-lived primaries. Because they do not originate from the collision vertex, their momenta are not calculated correctly. Invariant mass distributions for $\pi^0(\eta)\pi^+\pi^-$ triples are shown in Fig. 4. The two peaks in the distribution shown in the left panel correspond to decays of η and ω mesons. The width of $\sim 8 \text{ MeV}/c^2$ for the reconstructed η meson peak is similar to that of the η' meson peak shown in the right panel of Fig. 4. The width of the ω -meson peak is $\sim 17 \text{ MeV}/c^2$, which is narrower than that in the $\omega \rightarrow \pi^0\gamma$ decay mode. This is due to the smaller difference between the masses of the primary particle and their decay products and to the better momentum

resolution of the tracking system as compared to the EMCAL in this momentum range. The signal-to-background ratio in the range of measurements changes from 1:10 (1:5) to 1:3 (1:2) for $\omega(\eta')$ mesons. More details on the analysis of η and ω mesons can be found in [2,4].

4. $\phi \rightarrow K^+K^-$

Reconstruction of the $\phi \rightarrow K^+K^-$ decay was done by combining pairs of oppositely charged tracks. The tracks were required to have a momentum in the range $0.3 < p_T (\text{GeV}/c) < 8$. Each track was assigned the charged kaon mass. Invariant mass distributions were accumulated in two different configurations: (i) combining all tracks reconstructed in the PHENIX tracking system and (ii) combining all tracks of one sign with tracks of the opposite sign identified as a kaon in the TOF subsystem. Examples of the invariant mass distributions for the two cases are shown in the left and right panels of Fig. 5, respectively.

The use of particle identification improved the signal-to-background ratio by a factor of more than 2 at the expense of a more limited acceptance, resulting in a factor of 5 loss in statistics. At low and intermediate p_T , where the combinatorial background is high but the data sample has large statistics, this method is preferable. The method without particle identification was more effective at intermediate and high p_T because of the significant gain in the acceptance. The highest p_T reachable with this method is limited by the available statistics in the minimum bias data sample. The two methods described here use different detector subsystems and produce different shapes of combinatorial background and signal-to-background ratios. Use of the two methods allowed us to extend the p_T coverage of the measurement and provided a consistency check between the results obtained in the overlap region between $1.5 \text{ GeV}/c$ and $4.5 \text{ GeV}/c$. The signal-to-background

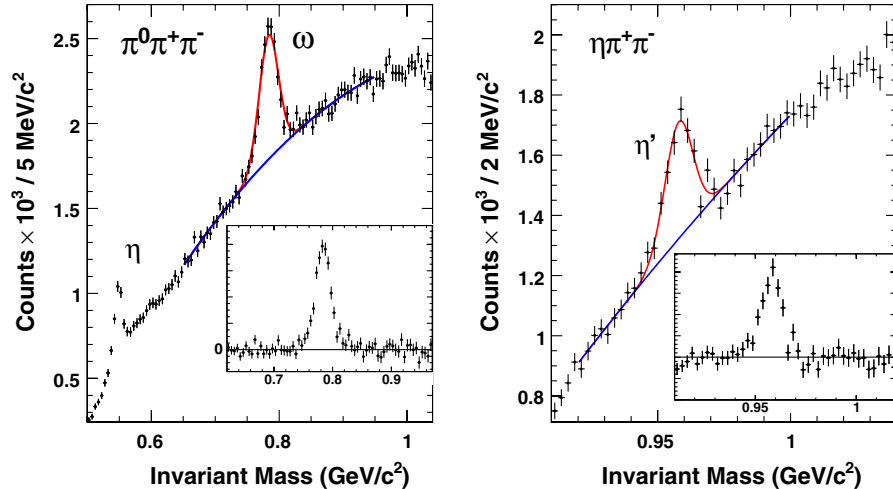


FIG. 4 (color online). Invariant mass distribution for $\pi^0\pi^+\pi^-$ (left panel) and $\eta\pi^+\pi^-$ (right panel) triplets in the momentum range $4 < p_T (\text{GeV}/c) < 6$. The inset shows the invariant mass distribution after the background removal explained in Sec. III B.

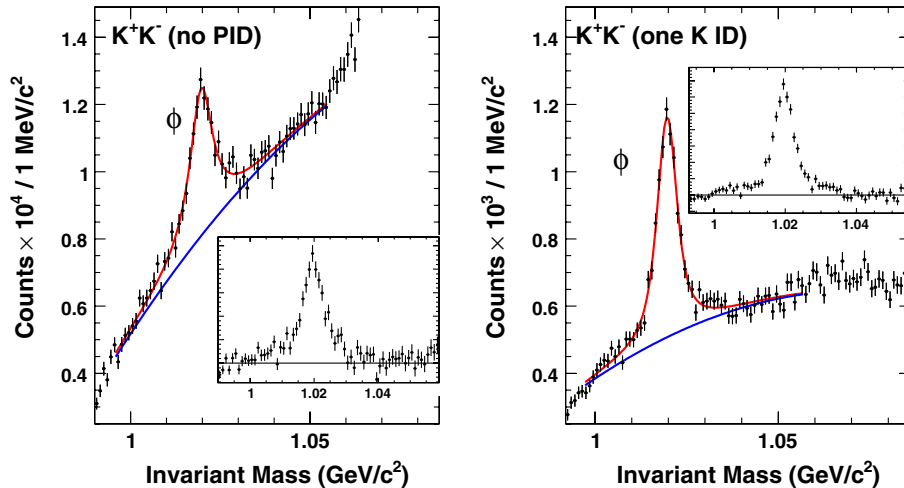


FIG. 5 (color online). Invariant mass distribution for K^+K^- accumulated without particle identification (left panel) and with one K -meson identification (right panel) in the momentum range $4 < p_T$ (GeV/c) < 6 . The inset shows the invariant mass distribution after the background removal explained in Sec. III B.

ratio changes from 1:10 to 2:1 depending on the analysis method and the p_T bin. More details on this measurement can be found in [51].

5. $\omega, \phi \rightarrow e^+e^-$

Electrons are reliably identified by the PHENIX detector in the momentum range $0.2 < p_T$ (GeV/c) < 4 . Electron identification is accomplished using the information from the RICH and EMCAL subsystems by requiring at least two RICH phototubes to fire within the ring-shaped area associated with a charged track. In addition, the ratio of the associated cluster energy measured in the EMCAL to the momentum measured in the tracking system must satisfy $|E/p - 1| < 0.5$. The invariant mass distribution obtained by combining identified e^+ and e^- pairs is shown in Fig. 6

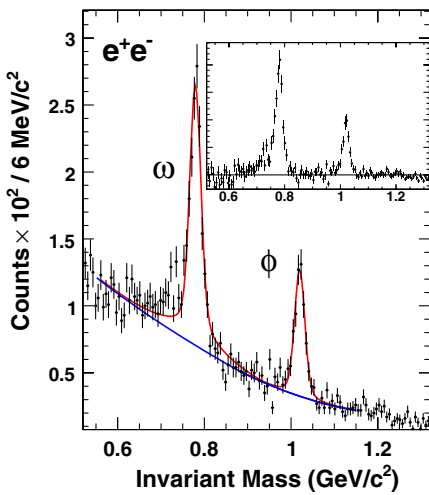


FIG. 6 (color online). Invariant mass distribution for e^+e^- pairs in the momentum range $0.5 < p_T$ (GeV/c) < 0.75 . The inset shows the invariant mass distribution after the background removal explained in Sec. III B.

for pairs in the range $0.5 < p_T$ (GeV/c) < 0.75 . The two peaks correspond to $\omega + \rho$ and ϕ mesons. The widths of the ω (ϕ) meson peaks vary from $6.1(6.0)$ MeV/c^2 to $9.0(11)$ MeV/c^2 , from the lowest p_T to the highest p_T of the electron pairs. The signal-to-background ratio in the region of the ω (ϕ) meson peaks changes from 1:2 (2:1) to 3:1 (6:1).

B. Raw yield extraction

To extract the raw yields the invariant mass distributions near each peak were parametrized as the sum of signal and background contributions.

For the signal, we used a Breit-Wigner function convolved with a Gaussian function (BW * G). The Breit-Wigner function describes the natural shape of the measured resonance, and the Gaussian takes into account the detector resolution. Depending on the decay channel being analyzed, one or the other contribution may dominate; e.g. the Gaussian part is more important in decays like $\omega \rightarrow \pi^0\gamma$ or $K_s^0 \rightarrow \pi^0\pi^0$, and the Breit-Wigner part in decays like $\phi \rightarrow K^+K^-$ or $\omega, \phi \rightarrow e^+e^-$. In most cases the parameters of the BW * G function when fitted to the data were consistent with the values expected from simulation.

The $\phi \rightarrow K^+K^-$ decay mode was treated somewhat differently. Kaons decaying in flight before passing completely through the PHENIX tracking system modify the shape of the invariant mass distribution compared to those passing through the detector without decays. This results in non-Gaussian tails of the detector response function, and thus the Breit-Wigner and Gaussian width parameters in the BW * G convolution mix together. To account for this effect a Monte Carlo sample was produced with the natural width of the ϕ set to zero and the kaon lifetime set to infinity. Using these samples allowed us to disentangle the effects related to the kaon decays in flight.

Our analysis verified that the peak positions and widths obtained from the fits to the data were in agreement with the simulated values within the error bars. In the highest p_T bins, where the available statistics prevents unconstrained extraction of the Gaussian width from the data, we constrained the fitted width to be within 10% of the value found in the simulation. In the measurement of the ω , $\phi \rightarrow e^+ e^-$ decays, other terms were added to the $BW * G$ shape to account for ρ decays and for internal conversions taken from [52,53]. The contribution of ρ underneath the ω peak was estimated using Breit-Wigner parametrization, with the assumption that the production ratio of ρ and ω is 1; in the fit their ratio was determined by their $e^+ e^-$ branching ratios in vacuum equal to 1.53.

To properly estimate the background under the peak, it is necessary to assume that the shape of the background does not change rapidly. With this assumption one can expand the background shape in a Taylor series around the peak position and take the most significant terms of the expansion. A natural choice is to use a second order polynomial. The regions outside the resonance peak, where the background dominates, define the parameters of the fit. For a second order polynomial fit, the background varies smoothly under the peak. This may not be the case for higher order polynomial fits to the background.

The combinatorial background in the data has two main contributions. The first comes from the random association of uncorrelated tracks. Its shape is defined by the detector acceptance and the p_T distribution of particles in the event. This part of the background remains smooth in the mass interval comparable to the width of the peaks shown in Figs. 3–6. The correlated part of the combinatorial background comes from partially or incorrectly reconstructed decays of true particles and jets, and may have a faster changing shape. In several analyses the most significant contributions to the correlated background were studied to verify that they do not affect the raw yield extraction procedure. For example, the decay $\eta \rightarrow \gamma\gamma$ produces an $\eta\gamma$ peak at around $0.6 \text{ GeV}/c^2$ in the invariant mass distribution of $\pi^0\gamma$. Also, the decay of $K_s^0 \rightarrow \pi^+\pi^-$ produces a peak at $\sim 1.07 \text{ GeV}/c^2$ in the K^+K^- invariant mass distribution when two pions are erroneously assigned the kaon mass. In some cases these processes limit the mass range available for the background determination. The mass range used for the determination of the background did not include regions where one could expect the appearance of such peaks.

The raw yields were measured in the following way. First, the invariant mass distributions in different p_T bins were fitted with the $BW * G$ plus background in the mass range of ± 5 combined widths of the $BW * G$ around the nominal mass of the meson. The exact range varied slightly depending on particle species and the p_T bin. The background contribution, estimated by the polynomial part of the fit function, was subtracted from the measured

invariant mass distribution, and the resulting histogram was used to count the raw yield. Bins lying within ± 2.5 combined widths of the $BW * G$ function around the mass peak contributed to the yield. The same procedure was used to calculate the raw yield in the Monte Carlo calculations used for the acceptance evaluation.

The systematic uncertainty of the raw yield extraction is usually the main contributor to the total systematic uncertainty. We evaluated this uncertainty by modifying the analysis procedure. The main goal was to change the shape of the background around the resonance peak in a manner similar to that shown in Fig. 5. To achieve this goal, analyses of the same decay modes were performed in different ways—for example, by requiring PC3 or EMCAL hit matching for charged tracks, varying the minimum energy of γ clusters, or modifying the selection criteria for π^0 (η) candidates. Independent of this we also varied the parameters of the fit functions, such as the fit range and the order of the polynomial. Typically, six to ten raw yield values were accumulated for each p_T bin. After fully correcting each of them for the corresponding reconstruction efficiency, the rms of the results was taken as the systematic uncertainty.

C. Invariant mass resolution

The invariant mass resolution of the detector plays an important role in the analyses described in this section. It depends on several factors. Use of the detector tracking system or EMCAL makes a large difference. The momentum range of the analyzed particles is less important. The difference between the mass of the particle and its decay products contributes directly to the invariant mass resolution. To demonstrate this we consider the limiting case of a particle decaying into two massless products. In this case, one can approximate the invariant mass resolution with the simple relation $\delta m/m = (1/\sqrt{2})\delta p_T/p_T$. The single particle momentum resolution was discussed in Sec. II. Figure 7 compares this approximation with the widths of the peaks shown in Figs. 2–6. The measured widths are plotted as a function of the mass difference between the particle and its decay products. The two lines in the plot are calculated for two-body decays reconstructed either with the tracking system only or with the EMCAL only at a pair p_T of $4 \text{ GeV}/c$.

As can be seen, the simple approximation describes the measured mass widths for the two-body decays reasonably well. The widths of the e^+e^- decay modes are somewhat narrower due to the use of a lower momentum range. The results for the J/ψ and ψ' , which are not shown in the plot, are also consistent with the trend of the “tracking” line. The $\phi \rightarrow K^+K^-$ represents the case where the assumption of massless products is least valid; nevertheless, the agreement is still reasonable.

The widths of the invariant mass peaks reconstructed with both the EMCAL and the tracking systems are

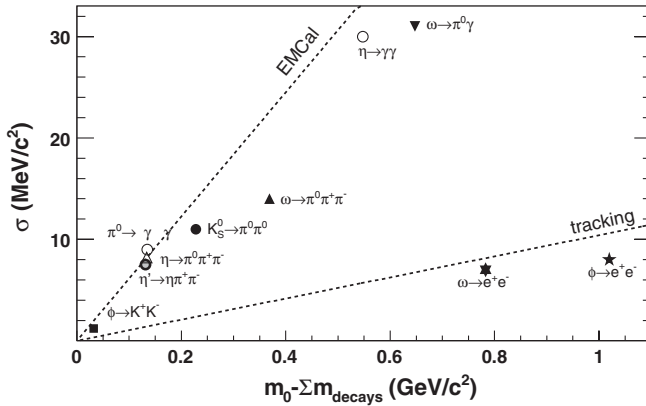


FIG. 7. Invariant mass resolution of the PHENIX detector for different decay modes measured in the momentum range $4 < p_T (\text{GeV}/c) < 6$, except for the e^+e^- mode that is measured in the range $0.5 < p_T (\text{GeV}/c) < 0.75$. The lines indicate the expected detector mass resolution.

dominated by the EMCAL resolution. However, due to the energy correction applied to the γ clusters forming π^0 or η candidates, the widths of the peaks reconstructed with three and four particles are below the “EMCal” line.

D. Detector acceptance and efficiency

1. Geometrical acceptance and the analysis cuts

The determination of the detector acceptance was done using a single particle Monte Carlo simulation. Particles were uniformly generated within $|y| < 0.5$ in rapidity and in full azimuthal angle. The range of the transverse momentum distributions was chosen to produce sufficient statistics in all p_T bins for which the signal could be extracted from the data. For the acceptance calculation the generated spectra were weighted to match the measured particle spectra. This procedure was done iteratively. Kinematics of the three-body decays of the η , ω , and η' mesons assumed the experimentally measured phase space density distributions [54–59].

The PHENIX detector simulation is based on the GEANT code, which properly reproduces the momentum, spatial, and timing resolution of all detector subsystems and fully describes inactive areas. The simulated positions and widths of the π^0 , K_s^0 , η , ω , η' , and ϕ peaks were consistent with the values measured in real data at all p_T 's. The same analysis code was used for the reconstruction and analysis of the simulated and real data.

The detector acceptance, calculated as the ratio of the number of fully reconstructed particles to the number of generated particles, is shown in Fig. 8. All curves take into account the detector geometry, particle decay kinematics, performance of the detector subsystems including particle identification, and the analysis cuts. The efficiencies strongly depend on the particle momentum and rapidly decrease at low p_T for all species studied in this analysis, establishing a low p_T edge for the measurements.

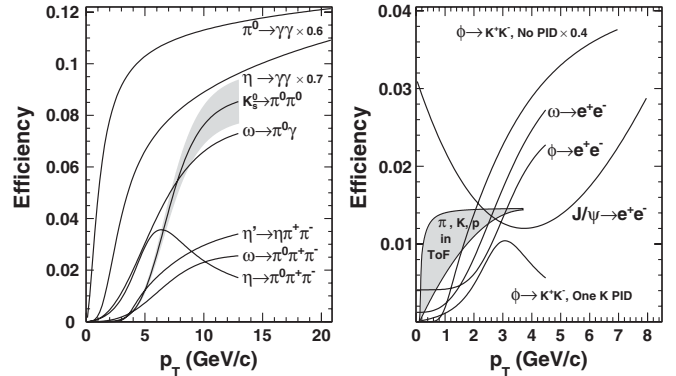


FIG. 8. Detector acceptance as a function of transverse momentum for different particles measured with the PHENIX experiment. The scaling factors allow clear comparison of the p_T dependence of the efficiency of rare and common decay channels. The band in the left panel shows the largest relative systematic uncertainty among all curves.

2. ERT trigger efficiency

The analysis of several decay modes was based on data samples accumulated with the ERT trigger described in Sec. II. The ERT trigger efficiency was extracted using the minimum bias event sample. Each EMCAL cluster which set the ERT trigger bit to indicate a γ cluster or electron was identified. The track or cluster had to also satisfy the analysis cuts of a particular decay mode, and match the region where the trigger bit was generated. The trigger efficiency was calculated as the energy spectra of such clusters divided by the energy spectra of all accepted clusters or electrons. Trigger efficiencies of photons and electrons measured for one of the PbSc sectors as a function of cluster energy are shown in the left panel of Fig. 9.

The trigger efficiencies grow steeply with energy, reaching 50% at values approximately corresponding to the online trigger threshold setting of 0.6 GeV for electrons and 1.4 GeV for photons. The curves saturate at approximately twice the threshold energy. The level of saturation is below 100% because of inactive areas of the ERT and the RICH efficiency.

For the analyzed decay modes the trigger efficiency evaluation was done using the same Monte Carlo sample as was used for the acceptance calculation. First we required the particle to be reconstructed in PHENIX without the ERT trigger requirement. Then, for all EMCAL clusters associated with photons or electrons in the final state of the decay, we generated a random number between 0 and 1 and compared it to the magnitude of the curve shown in the left panel of Fig. 9 at the energy of the cluster. The particle was considered to fire the ERT trigger if at least one of the randomly generated numbers was lower than the corresponding value of the curve. The probability to fire the ERT trigger for all analyzed mesons is shown in the right panel of the same figure.

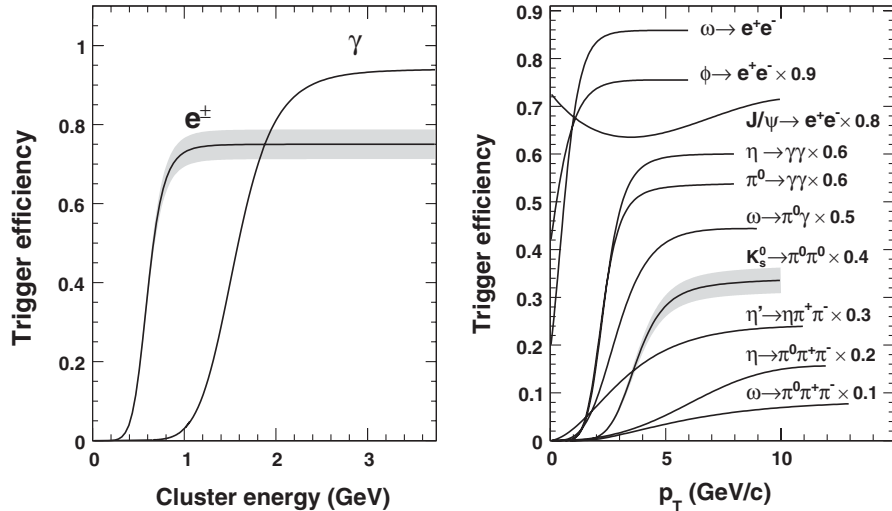


FIG. 9. Efficiencies of the ERT 4×4 and ERT 2×2 triggers for single γ clusters and electrons as a function of energy (left panel). Trigger efficiencies for different meson decays as determined from Monte Carlo simulation (right panel). The band shows the largest relative systematic uncertainty among all curves. The scaling factors are used for visual clarity.

3. Electron identification efficiency

The electron identification efficiency is included in the acceptance efficiencies shown in Fig. 8. It was evaluated using a full detector Monte Carlo simulation which was tuned to adequately reproduce the RICH and the EMCAL detector responses. To ensure that the electron identification efficiency was properly done in the simulation, it was confirmed to agree with the efficiency measured with real data.

For this comparison the data samples accumulated during special PHENIX runs were used. In those runs a 1.7%

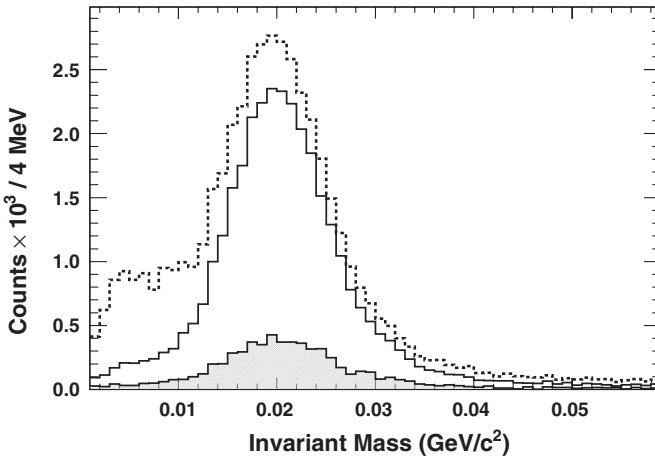


FIG. 10. Invariant mass distribution for $e^+ e^-$ pairs, where one track is identified as an electron and the second track is any track (dashed line), the same for pairs which open up in the plane perpendicular to the detector magnetic field (solid line), and among those pairs, the ones in which the second track fails the electron identification cut (filled histogram).

radiation length brass converter was installed around the RHIC beam pipe in the PHENIX interaction region. In this sample we selected electrons of both signs using very strict electron identification requirements. Those electrons were paired with all other tracks in the event. The invariant mass distribution of such pairs is shown by the upper histogram in Fig. 10.

One can see the characteristic shape of the partially reconstructed π^0 Dalitz decays and a peak at around $22 \text{ MeV}/c^2$ corresponding to γ conversions close to the beam pipe. Since the conversion electrons originate at the displaced converter vertex, and therefore skip the first 3.8 cm of the magnetic field, the reconstructed invariant mass peak is shifted from zero. Among these pairs a further selection was made to choose those which open up in the plane perpendicular to the detector magnetic field. This requirement effectively suppresses the combinatorial background and pairs coming from the π^0 Dalitz decays, but does not suppress $\gamma \rightarrow e^+ e^-$ pairs having small opening angles. The middle histogram in Fig. 10 shows that the conversion peak significantly dominates the residual Dalitz contribution and the combinatorial background. Finally, we applied the electron identification requirements to the second track. The invariant mass distribution of the pairs where the second track fails to be identified as an electron is shown by the filled histogram. The ratio of the lowest to the middle histogram under the peak is the electron identification loss. It reaches 20% below $0.5 \text{ GeV}/c$ and saturates at $\sim 10\%$.

E. Calculation of invariant cross sections

The invariant cross section for a particle in each p_T bin was calculated as

TABLE I. Relative systematic uncertainties (in percent) for different decay modes. Given ranges indicate the variation of the systematic uncertainty over the p_T range of the measurement.

Particle decay	K_s^0 $\pi^0\pi^0$	$\pi^0\pi^+\pi^-$	ω $\pi^0\gamma$	e^+e^-	η' $\eta\pi^+\pi^-$	K^+K^-	ϕ e^+e^-	Uncertainty type
Acceptance	8	5	6	5	5	5–7	5	B
EMCal energy resolution	4–5	2–5	2–3		2–4			B
EMCal, DC scale	4–6	2–6	3–17	2–11	2–5	1–5	2–10	B
π^0, η selection	5–10	3	3		3			B
ERT trigger efficiency	2–12	3–10	2–7	1–3	2–4		1–2	B
Peak extraction MC	2	1	1	1	1	3	1	A, B
Raw yield extraction	4–19	5–17	5–12	4–15	6–25	8–25	3–11	A, B
γ conversion	6	3	5		3			C
e identification					10		9	B
Branching ratio	0	1	3	1.7	3	1	1.3	C
MinBias trigger	9.7	9.7	9.7	9.7	9.7	9.7	9.7	C
Total	17–29	13–24	15–26	16–24	14–29	14–28	15–18	

$$\frac{1}{2\pi p_T} \frac{d^2\sigma}{dp_T dy} = \frac{1}{2\pi p_T} \frac{1}{\mathcal{L} \text{BR}} \frac{1}{\varepsilon(p_T) \varepsilon_{\text{BBC}}} \frac{N(\Delta p_T)}{\Delta p_T \Delta y}, \quad (1)$$

where $N(\Delta p_T)$ is the number of reconstructed particles in a given p_T bin, \mathcal{L} is the integrated luminosity sampled by the minimum bias trigger, $\varepsilon(p_T)$ is the acceptance and reconstruction efficiency, BR is the branching ratio, and ε_{BBC} is the minimum bias trigger efficiency for events containing mesons, estimated to be 0.79 ± 0.02 . The cross section sampled by the BBC trigger, $\sigma_{\text{tot}}^{pp} = 23.0 \pm 2.2$ mb, was used to determine the integrated luminosity. For the analyses with the minimum bias data sample, $\varepsilon(p_T)$ corrects for the acceptance and reconstruction efficiency, while for analyses with the ERT data sample, it includes the ERT trigger efficiencies as well. A bin shift correction was applied to take into account the finite width of the p_T bins used in the analyses. The correction is made by shifting the data points along the vertical axis according to the procedure described in [60].

Finally, in the $\omega \rightarrow \pi^0\pi^+\pi^-$ and $K_s^0 \rightarrow \pi^0\pi^0$ analyses, the cross sections measured with the ERT and with the minimum bias triggers were averaged in the overlapping p_T region, taking into account the statistical and systematic uncertainties.

F. Systematic uncertainties

In addition to the systematic uncertainties described in the corresponding analysis sections, uncertainties of the ERT trigger efficiency and acceptance corrections were estimated by varying the analysis cuts, and by varying the energy and momentum scales of the EMCal and DC by 1%. The resulting systematic uncertainties for the different decay modes of $K_s^0, \eta, \omega, \eta'$, and ϕ mesons are summarized in Table I. The uncertainties are categorized by types: (A) uncorrelated between p_T bins, (B) p_T correlated, all points moving in the same direction but not by the same factor, and (C) an overall normalization uncertainty in which all points move by the same factor, independent of p_T . The type C

uncertainty is predominantly due to the uncertainty of the minimum bias trigger efficiency in $p + p$ collisions, equal to 9.7% [1,2]. The uncertainty of the raw yield extraction is estimated as described in Sec. III B. It dominates the total uncertainty and is split into type A and type B contributions.

G. Neutral meson spectra

The invariant differential cross sections calculated using Eq. (1) are tabulated in Tables X and XI in the Appendix and plotted in Fig. 11. Different symbols are used to show results for different decay modes. One can see a very good

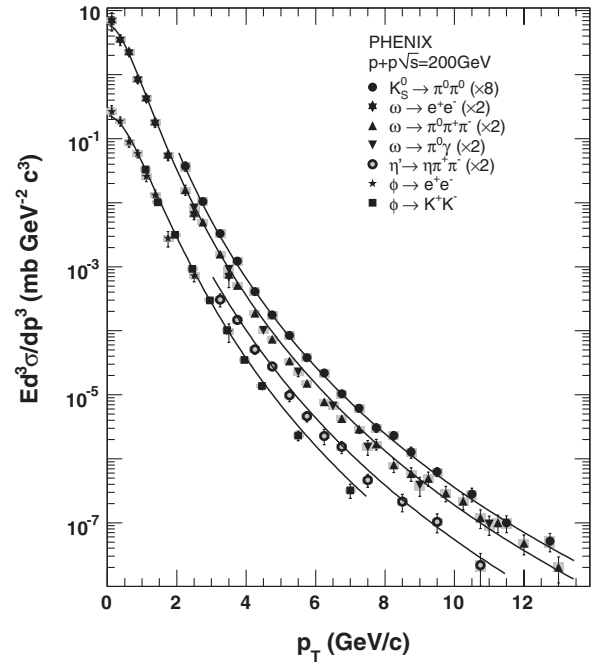


FIG. 11. Invariant differential cross section of neutral mesons measured in $p + p$ collisions at $\sqrt{s} = 200$ GeV in various decay modes. The lines are fits to the spectra as described further in the text.

agreement between the particle spectra measured in the different decay modes. Results for low p_T bins for particles reconstructed through decays in the e^+e^- mode allow an accurate measurement of the integrated particle yield. The integrated yield at midrapidity for the ω is measured to be $d\sigma^\omega/dy = 4.20 \pm 0.33^{\text{stat}} \pm 0.52^{\text{syst}}$ mb, and for the ϕ it is measured to be $d\sigma^\phi/dy = 0.432 \pm 0.031^{\text{stat}} \pm 0.051^{\text{syst}}$ mb. The mean transverse momenta for these particles are $\langle p_T^\omega \rangle = 0.664 \pm 0.037^{\text{stat}} \pm 0.012^{\text{syst}}$ GeV/c and $\langle p_T^\phi \rangle = 0.752 \pm 0.032^{\text{stat}} \pm 0.014^{\text{syst}}$ GeV/c.

IV. ANALYSIS OF PARTICLE SPECTRA

In this section we analyze the measured invariant transverse momentum spectra for a variety of hadrons in $p + p$ collisions at $\sqrt{s} = 200$ GeV and search for common features. All measurements are quoted as the invariant differential cross sections at midrapidity averaged over the rapidity interval $|y| \leq 0.35$.

$$E \frac{d^3\sigma}{dp^3} = \sigma_{\text{inel}}^{\text{pp}} \times \frac{1}{2\pi p_T} \frac{1}{N_{\text{events}}} \frac{d^2N}{dy dp_T}, \quad (2)$$

where $\sigma_{\text{inel}}^{\text{pp}} = 42$ mb.

A. Data samples

The procedures used for the reconstruction of the particle transverse momentum spectra are described above in Sec. III and in other PHENIX publications listed in Table II. Figure 11 shows the new results presented in

TABLE II. Data samples used in the analysis of particle spectra. The X and XI in the Reference column refer to Tables X and XI in the Appendix.

Particle	Mode	Physics run	p_T (m_T) range GeV/c, GeV/c ²	Reference
π^0	$\gamma\gamma$	5	0.5–20	[3]
π^+, π^-	TOF	3	0.3–2.7	[1]
K^+, K^-	TOF	3	0.4–1.9	[1]
K_S^0	$\pi^0\pi^0$	5	2–13.5	XI
η	$\gamma\gamma$	3	2–12	[2]
η	$\gamma\gamma$	6	2–20	[6]
η	$\pi^0\pi^+\pi^-$	3	2.5–8.5	[2]
ω	e^+e^-	5	0–4	X
ω	$\pi^0\pi^+\pi^-$	5	2–13.5	X
ω	$\pi^0\pi^+\pi^-$	3	2.5–10	[4]
ω	$\pi^0\gamma$	5	2–12	X
ω	$\pi^0\gamma$	3	2–7	[4]
η'	$\eta\pi^+\pi^-$	5	3–11.5	XI
ϕ	e^+e^-	5	0–4	XI
ϕ	K^+K^-	5	1–8	XI
J/ψ	e^+e^-	5	0–9	[5]
J/ψ	e^+e^-	6	0–9	[48]
ψ'	e^+e^-	6	0–7	[61]
p, \bar{p}	TOF	3	0.6–3.7	[1]

this paper, and Fig. 12 shows these results compared with previous PHENIX results. All meson spectra used in this paper are not corrected for feed-down.

Figure 12 demonstrates a very good agreement between the new results and previously published data. The results presented in this paper greatly enhance the p_T range of the previously measured particles and add results for particles that have not been previously analyzed.

For each particle we considered all available measurements of the invariant momentum distributions together with their statistical and systematic uncertainties categorized as types A, B, and C, as explained in Sec. III F.

For the analysis of the shape of the transverse momentum distributions, the data for all particles of the same isospin multiplet were combined into one p_T spectrum to be fitted. All data for positively and negatively charged particles measured in the same analysis and in the same p_T bins were averaged. All data for neutral particles, measured via different decay channels, were added together. The notation π is used to denote a combined spectrum of π^0 and $(\pi^+ + \pi^-)/2$, K is used for a combined spectra of K_S^0 and $(K^+ + K^-)/2$, p denotes $(p + \bar{p})/2$, and so forth. Independent measurements of the same particle performed using different data samples or different decay modes were also added together but not averaged. For data samples where the results were published as dN/dp_T , a conversion was made using Eq. (2).

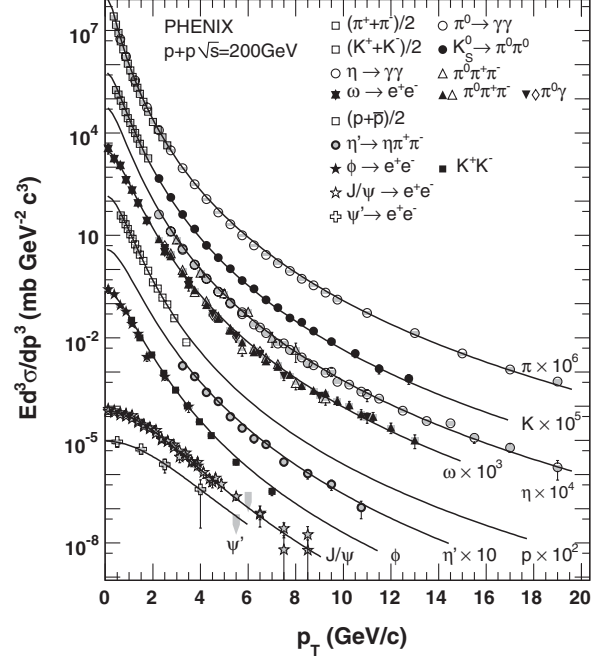


FIG. 12. Invariant differential cross sections of different particles measured in $p + p$ collisions at $\sqrt{s} = 200$ GeV in various decay modes. The spectra published in this paper are shown with closed symbols, and previously published results are shown with open symbols. The curves are the fit results discussed in the text.

B. Particle spectra fit distributions

It is widely known from experimental data that, as expected from pQCD calculations (e.g. [62]), a pure power law shape successfully describes the high- p_T region of particle spectra:

$$E \frac{d^3\sigma}{dp^3} = A p_T^{-\nu}, \quad (3)$$

where the shape is determined by the power ν and A is a normalization constant. However, the power law shape is seen to fail in the region below about $p_T = 3\text{--}5 \text{ GeV}/c$, where the spectra exhibit a more exponential shape.

The exponential shape of the particle spectra at low p_T suggests a thermal interpretation in which the bulk of the produced particles is emitted by a system in thermal equilibrium with a Boltzmann-Gibbs statistical description of their spectra:

$$E \frac{d^3\sigma}{dp^3} = C_b e^{-E/T}, \quad (4)$$

where C_b is a normalization factor and E is the particle energy. At midrapidity one can replace E by $m_T = (p_T^2 + m_0^2)^{1/2}$, where m_0 is the particle rest mass.

In recent years a variety of publications [7,26–30,63] have used the Tsallis distribution [24] to fit particle spectra. The Tsallis distribution derives from a generalized form of the Boltzmann-Gibbs entropy and is written as

$$G_q(E) = C_q \left(1 - (1 - q) \frac{E}{T}\right)^{1/(1-q)}, \quad (5)$$

where C_q , E , and T have similar meanings as in Eq. (4) and q is the so-called nonextensivity parameter. For values of $q \neq 1$ the distribution exhibits a power law behavior with power $n = -1/(1 - q)$. In order to associate the Tsallis distribution with a probability distribution, which describes the invariant particle spectra given by Eq. (2) and defined over $0 < E < \infty$, Eq. (5) must satisfy a normalization and energy conservation condition $\langle E \rangle < \infty$. This limits the range of the parameter q to $1 < q < 1\frac{1}{3}$. The Tsallis distribution reduces to the Boltzmann-Gibbs distribution of Eq. (4) in the limit of $q \rightarrow 1$.

To put Eq. (5) into a form appropriate to fit particle spectra, we replace E by $m_T = (p_T^2 + m_0^2)^{1/2}$ and use the requirement of unit normalization to determine the coefficient C_q in Eq. (5) to be equal to

$$C_q = \frac{(2q - 3)(q - 2)}{T(T + m_0) - (q - 1)(q - 2)m_0^2} \times \frac{1}{(1 - (1 - q)\frac{m_0}{T})^{1/(1-q)}}. \quad (6)$$

We replace the parameter q with

$$n = -\frac{1}{1 - q}. \quad (7)$$

The resulting formula used in the fitting procedure is given by

$$E \frac{d^3\sigma}{dp^3} = \frac{1}{2\pi} \frac{d\sigma}{dy} \frac{(n - 1)(n - 2)}{(nT + m_0(n - 1))(nT + m_0)} \left(\frac{nT + m_T}{nT + m_0}\right)^{-n}, \quad (8)$$

where $d\sigma/dy$ is the integrated cross section of the particle production at midrapidity.

In the limit of $m_0 \rightarrow 0$ Eq. (8) becomes

$$E \frac{d^3\sigma}{dp^3} = \frac{1}{2\pi} \frac{d\sigma}{dy} \frac{(n - 1)(n - 2)}{(nT)^2} \left(1 + \frac{m_T}{nT}\right)^{-n}. \quad (9)$$

This form is very similar to the QCD inspired expression suggested by Hagedorn in [22] written as a function of m_T instead of p_T .

The condition that the shapes of the m_T spectra of different particles are the same regardless of their mass is referred to as m_T scaling. m_T scaling is known to provide a good description of the experimental data at low energy, where the spectral shapes are exponential [18,23]. Because of the explicit m_0 mass dependence in Eq. (8) the Tsallis distribution does not satisfy m_T scaling, except in the case $m_0 \rightarrow 0$ or $q \rightarrow 1$, in which case the limiting forms of Eq. (4) or (9) apply. Therefore, the accuracy of fits to the Tsallis distribution and the validity of m_T scaling need to be quantified with data.

The power law behavior at high p_T which appears in Eq. (8) is governed by the parameter n . The parameter n can be related to the simple power law parameter ν that occurs in Eq. (3) through the condition that both expressions have the same power-law slope at a given p_T . From Eqs. (3) and (8) one can write

$$\frac{d \ln(nT + m_T)^{-n}}{d \ln(p_T)} = \frac{d \ln(p_T^{-\nu})}{d \ln(p_T)}, \quad n = \frac{\nu m_T^2}{p_T^2 - \nu T m_T}. \quad (10)$$

At high p_T ($p_T \gg m_0, \nu T$), where one can neglect the difference between m_T and p_T , ν and n coincide. In the p_T region where most particle spectra are measured, n is 15%–25% larger than ν .

The mean m_T of the Tsallis distribution in the form of Eq. (8) is calculated as

$$\begin{aligned} \langle m_T \rangle &= \frac{2nT}{n - 3} + \frac{(n - 2)(n - 1)}{(nT + m_0(n - 1))(n - 3)} m_0^2 \\ &\approx \frac{2nT}{n - 3} + \frac{n - 2}{n - 3} m_0. \end{aligned} \quad (11)$$

The approximate relation requires $m_0 \gg T$. This condition is satisfied for all particles, except pions, for which T and m_0 are about the same. Similarly, the mean p_T can be well approximated for all measured particles with a linear dependence:

$$\langle p_T \rangle \approx \frac{2nT}{n-3} + f(n)m_0. \quad (12)$$

The first contribution is identical to that in Eq. (11), and $f(n)$ has only a weak dependence on m_0 , which we neglect in Eq. (12).

The Tsallis distribution is appealing to use to describe particle spectra because it provides a single functional form that can reproduce the full spectral shape with just two parameters. Tsallis distributions have been used successfully to describe particle spectra in different collision systems and at different energies [7,26–30,64–66]. Tsallis distributions also describe various physics phenomena beyond particle production and have been successfully applied in other fields of science; see [64,67–69] and references therein.

As mentioned above, the Tsallis distribution was derived as the single particle distribution corresponding to a generalization of the Boltzmann-Gibbs entropy through the introduction of the nonextensivity parameter q [24]. Whereas the Boltzmann-Gibbs distributions are found to apply to systems which exhibit an exponential relaxation in time to a stationary state characterized by exponentials in energy at thermal equilibrium, the generalized form is found to apply to systems which exhibit power laws in relaxation time and energy. These are systems which relax with a nonergodic occupation of phase space as a consequence of the microscopic dynamics of the system. Among other examples, this is characteristic of systems with long-range interactions that fall off with distance with a power smaller than the dimensionality of the system. It is an interesting question whether strongly interacting partonic matter might also exhibit power law relaxation. In fact, an analysis of the diffusion of a charmed quark in partonic matter produced in parton cascade calculations found that the parton densities were characterized by Tsallis distributions, rather than Boltzmann-Gibbs distributions [70].

The physical interpretation of the parameter T in Eq. (5), especially in $p + p$ collisions, is not straightforward. One can expect that for larger systems, such as those produced in relativistic heavy ion collisions, T reflects the kinetic freeze-out temperature $\langle T_{\text{kfo}} \rangle$ at which particle scattering ceases to modify the spectral shapes. It is shown below that the magnitudes of $\langle T \rangle$ found in this work are close to $\langle T_{\text{kfo}} \rangle$ extracted in the blast-wave model approach [8,71] applied to $p + p$ data. In applications to $p + p$ collisions it has been shown [25] that the parameter q of the Tsallis distribution of Eq. (5) can be related to the amount of temperature fluctuations in the system as

$$q = 1 + \frac{\text{Var}(\frac{1}{T})}{\langle \frac{1}{T} \rangle^2} = 1 + \frac{1}{n}. \quad (13)$$

C. Fitting procedure

In order to obtain a reliable estimate of the fit uncertainties, the experimental systematic uncertainties must be

treated properly. The various types of systematic uncertainties have been taken into consideration as described here. The p_T -independent systematic uncertainties of type A have been combined in quadrature with the statistical errors, and the p_T -independent systematic uncertainties of type C were reduced by 9.7% due to the trigger uncertainty, common to all analyzed particles. Residual uncertainties of type C and of type B must also be considered in the analysis. The type B uncertainties, by definition, have an unknown p_T dependence. In order to estimate their effect, the particle spectra were varied and fit multiple times. For each fit the y coordinate in each p_T bin was varied by the same amount according to the uncertainty of type C, and by differing amounts according to the type B uncertainties, in a manner similar to that explained in [72].

Variations of the y coordinates were made independently for each fit with the amount of variation chosen randomly according to the p_T -dependent uncertainties for each particle and each sample. For the particle spectra consisting of multiple samples, results of each fit to the entire spectrum were weighted with the probability of the fit estimated from the χ^2 criteria. Such weighting emphasizes variations in which individual samples fluctuate toward each other rather than away from each other, which corresponds to the assumption that the different samples represent measurements of the same true momentum distribution.

As a result of the multiple fits, weighted distributions of the fit parameters were obtained. The mean of the distribution was taken as the parameter value, the rms width of the distribution was taken as the systematic uncertainty, and the statistical uncertainty was taken from the fit to the unmodified data. The number of fits was chosen such that the mean and the rms did not change with an increasing number of trials.

D. Fit results

The fits of Eq. (8) to the data are shown in Fig. 13 with dotted lines. The results are given in Table III.

The fit parameters n and T are strongly correlated. The magnitude of the correlation coefficient between these two parameters for all species listed in Table III exceeds 0.9. Therefore, additional information is needed to constrain the values of n and T . For that purpose one can use a power law given by Eq. (3) fitted to the same data. As discussed above, the parameters n and ν are related to each other through Eq. (10). However, it is found that the results of the power law fit depend on the fit range, but become stable when the fit range begins above $p_T \sim 3.5 \text{ GeV}/c$ for most particles, or above $p_T \sim 5.5 \text{ GeV}/c$ for heavier particles such as the J/ψ . The resulting power law fits are shown in Fig. 13 as dashed lines that have been plotted down to $p_T = 0.5 \text{ GeV}/c$. Spectra without sufficient data above the fit range lower limit were not fitted. The results are given in Table IV.

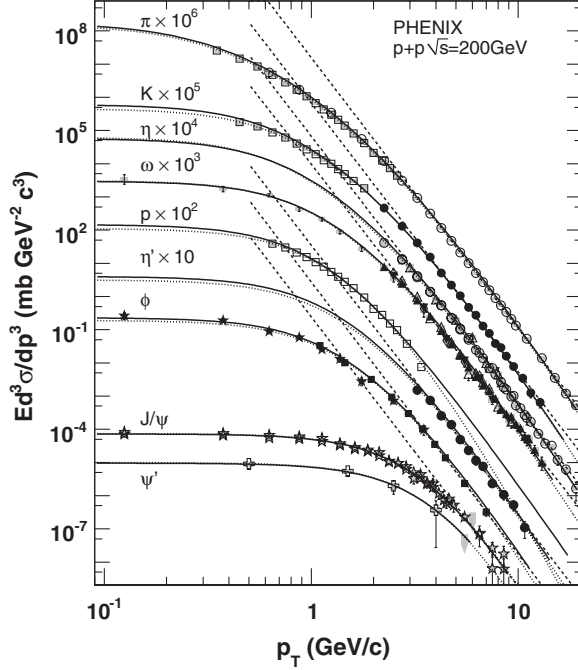


FIG. 13. The p_T spectra of various hadrons measured by PHENIX fitted to the power law fit (dashed lines) and Tsallis fit (solid lines). See text for more details.

The parameters ν of the power law fits and the parameters n and T of the Tsallis fits are shown in Fig. 14 as a function of the particle mass. The parameters have been fit to a linear function to establish if there is a mass dependence. The fits are shown in Fig. 14 as solid lines, with the uncertainties indicated by dashed lines. From Fig. 14 it is evident that the parameters are consistent, with no significant mass dependence. Therefore, the parameters have also been fit with a constant value. The results for the linear and constant fits are summarized in Table V.

The fitted linear coefficients are consistent with zero mass dependence within less than 2 standard deviations of the fit accuracy for all three parameters. At the same time, the parameter ν is more accurately defined compared

TABLE IV. Parameters of the power law fit with Eq. (3). The uncertainties are statistical and systematic. Units of A are $\text{mb}(\text{GeV}/c)^{\nu+2}$.

	ν	A
π	$8.174 \pm 0.035 \pm 0.049$	$16.4 \pm 1.1 \pm 1.6$
K	$8.24 \pm 0.08 \pm 0.11$	$8.8 \pm 0.9 \pm 1.6$
η	$8.169 \pm 0.037 \pm 0.054$	$7.64 \pm 0.46 \pm 0.83$
ω	$7.986 \pm 0.083 \pm 0.080$	$9.5 \pm 1.3 \pm 1.4$
η'	$8.12 \pm 0.21 \pm 0.11$	$3.6 \pm 1.2 \pm 0.8$
ϕ	$8.20 \pm 0.36 \pm 0.15$	$2.8 \pm 1.5 \pm 0.7$
J/ψ	$7.0 \pm 1.2 \pm 0.4$	$0.03 \pm 0.03 \pm 0.02$

to the Tsallis fit parameter n . We can invoke Eq. (10) to constrain the Tsallis fit using the parameter ν . This requires estimating the effective p_T which appears in Eq. (10). Using the mass-independent terms of the fits listed in Table V, the effective p_T is about $7 \text{ GeV}/c$.

This value is large enough to allow one to neglect the difference between m_T and p_T in Eq. (10) for all particles, except the J/ψ and ψ' . These two particles do not constrain the mass dependence of the Tsallis fit parameters due to their large fit uncertainties, as shown in Fig. 14.

Under the assumption that the parameter ν is the same for all particles, the mass dependence of the parameters n and T must either be present or absent together. This can be checked by fixing the parameter n to a constant value of $n = 9.656$ (from Table V) and fitting the data again. The mass-dependent coefficient for the parameter T that results in this case is somewhat different from zero, compared to uncertainties. This is a clear contradiction to Eq. (10) under the assumption of constant ν , and therefore indicates that the parameters n and T have a mass dependence. However, this conclusion is at the limit of the accuracy of the currently available data.

For further analysis the parameter n was fixed to have a linear dependence $n = 9.48 + 0.66m_0 [\text{GeV}/c^2]$ (from Table V), and the particle spectra were fit again. The results are given in Table VI, and the fit to the mass dependence of T is given in Table VII.

TABLE III. Parameters of the Tsallis fit with Eq. (8) with all parameters free to vary. The uncertainties are statistical and systematic. Cross sections are in μb for J/ψ and ψ' , and in mb for all other particles.

	$d\sigma/dy (\text{mb}, \mu\text{b})$	$T (\text{MeV})$	$n = -1/(1-q)$
π	$43.5 \pm 2.0 \pm 1.9$	$112.7 \pm 2.9 \pm 1.1$	$9.57 \pm 0.11 \pm 0.03$
K	$4.0 \pm 0.1 \pm 0.5$	$132.7 \pm 3.8 \pm 7.2$	$10.04 \pm 0.16 \pm 0.27$
η	$5.1 \pm 1.1 \pm 3.9$	$119 \pm 10 \pm 30$	$9.68 \pm 0.18 \pm 0.49$
ω	$4.3 \pm 0.3 \pm 0.4$	$109.7 \pm 6.9 \pm 6.7$	$9.78 \pm 0.24 \pm 0.18$
η'	$0.80 \pm 1.5 \pm 0.7$	$141 \pm 107 \pm 61$	$10.5 \pm 2.2 \pm 1.2$
ϕ	$0.41 \pm 0.02 \pm 0.03$	$139 \pm 16 \pm 15$	$10.82 \pm 0.71 \pm 0.56$
J/ψ	$0.73 \pm 0.01 \pm 0.05$	$149 \pm 56 \pm 82$	$12.3 \pm 1.6 \pm 2.9$
ψ'	$0.13 \pm 0.03 \pm 0.02$	$164 \pm 10^3 \pm 10^2$	$14 \pm 12 \pm 6$
p	$1.63 \pm 0.05 \pm 0.11$	$107 \pm 13 \pm 12$	$12.2 \pm 1.0 \pm 0.7$

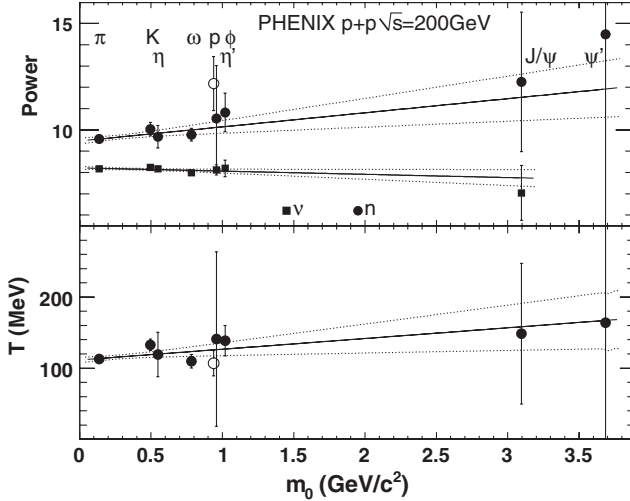


FIG. 14. Particle mass dependence of the fit parameters. Power law parameters ν and n are plotted in the upper panel. Vertical bars denote the combined statistical and systematic uncertainties. The solid lines are linear fits. The dashed lines denote the uncertainty within which the linear fit can be inclined. The lower panel shows the same for the fit parameter T . The proton measurement (open circle) is not used in the fits.

TABLE VII. Constant and linear fits to the Tsallis parameter T of mesons with the fixed parameter n . The last column gives the probability estimated by the $\chi^2/\text{n.d.f.}$ of the fit.

	Fit	Probability
T (MeV)	117.4 ± 2.5	0.64
T (MeV) $(112.6 \pm 3.8) + (11.8 \pm 7.0)m_0$ (GeV/ c^2)		0.83

Comparison of the results listed in Tables III and VI reveals that the parameters of the fit did not change significantly within uncertainties, even for the η and η' mesons which are not measured at low p_T . In addition, with the n parameter constrained, the uncertainty on the parameter T is reduced.

Since there is not yet a published PHENIX measurement of protons at high p_T , the parameter ν cannot be determined for the case of protons. Results published in [7] suggest that the slope of the proton spectra at high p_T is the same as that for mesons. Using this assumption allows us to extract the parameter T for protons, with the results listed in Table VI. The value of T for protons differs from the values extracted for mesons.

TABLE V. Constant and linear fits to the power law and Tsallis fit parameters. The last column gives the probability estimated by the $\chi^2/\text{n.d.f.}$ of the fit.

	Fit	Probability
ν	8.154 ± 0.039	0.75
ν	$(8.22 \pm 0.07) - (0.15 \pm 0.14)m_0$ (GeV/ c^2)	0.79
n	9.656 ± 0.097	0.69
n	$(9.48 \pm 0.14) + (0.66 \pm 0.39)m_0$ (GeV/ c^2)	0.94
T (MeV)	115.3 ± 2.8	0.43
T (MeV)	$(111.5 \pm 4.0) + (15 \pm 12)m_0$ (GeV/ c^2)	0.51

TABLE VI. Parameters of the Tsallis fit with Eq. (8), with the parameter n constrained to a fixed linear dependence on mass (for mesons). The uncertainties for $d\sigma/dy$ and T are statistical and systematic, and are only systematic for n . Cross sections are in μb for J/ψ and ψ' , and in mb for all other particles.

	$d\sigma/dy$ (mb, μb)	T (MeV)	$n = -1/(1-q)$
π	$42.8 \pm 3.1 \pm 2.7$	$112.6 \pm 2.1 \pm 2.8$	9.57 ± 0.10
K	$4.23 \pm 0.09 \pm 0.53$	$125.4 \pm 0.9 \pm 5.3$	9.81 ± 0.13
η	$3.86 \pm 0.30 \pm 0.71$	$124 \pm 2 \pm 12$	9.84 ± 0.14
ω	$4.26 \pm 0.23 \pm 0.33$	$115.5 \pm 2.1 \pm 6.8$	10.00 ± 0.22
η'	$0.63 \pm 0.27 \pm 0.21$	$123 \pm 17 \pm 18$	10.12 ± 0.28
ϕ	$0.427 \pm 0.019 \pm 0.023$	$123.4 \pm 3.0 \pm 8.3$	10.16 ± 0.31
J/ψ	$0.760 \pm 0.014 \pm 0.048$	$148 \pm 8 \pm 35$	11.5 ± 1.1
ψ'	$0.132 \pm 0.029 \pm 0.020$	$147 \pm 127 \pm 54$	11.9 ± 1.3
p	$1.775 \pm 0.044 \pm 0.066$	$58.8 \pm 1.8 \pm 6.1$	9.20 ± 0.28

TABLE VIII. Parameters of the Tsallis fit with Eq. (8), with the parameters n and T constrained to have a fixed linear dependence on mass (for mesons). The uncertainties for $d\sigma/dy$ are statistical and systematic, and are only systematic for T and n . Cross sections are in μb for J/ψ and ψ' , and in mb for all other particles.

	$d\sigma/dy$ (mb, μb)	T (MeV)	$n = -1/(1 - q)$
π	$40.5 \pm 0.3 \pm 5.8$	114.2 ± 4.0	9.57 ± 0.10
K	$4.71 \pm 0.06 \pm 0.48$	118.4 ± 5.2	9.81 ± 0.13
η	$4.46 \pm 0.05 \pm 0.97$	119.0 ± 5.4	9.84 ± 0.14
ω	$3.64 \pm 0.07 \pm 0.77$	121.8 ± 6.7	10.00 ± 0.22
η'	$0.62 \pm 0.04 \pm 0.16$	123.8 ± 7.7	10.11 ± 0.28
ϕ	$0.421 \pm 0.009 \pm 0.054$	124.5 ± 8.1	10.15 ± 0.31
J/ψ	$0.761 \pm 0.013 \pm 0.060$	149 ± 22	11.5 ± 1.1
ψ'	$0.133 \pm 0.024 \pm 0.019$	156 ± 26	11.9 ± 1.3
p	$1.76 \pm 0.03 \pm 0.16$	58.8 ± 6.4	9.20 ± 0.28

Using the linear dependence of the T parameter, $T = 112.6 + 11.8m_0$ (GeV/c^2), extracted from the fits to the Tsallis distribution with fixed linear dependence of the n parameter (from Table VI), the spectra can be fit once again to obtain an improved normalization parameter. The resulting fits are shown in Fig. 13 as the solid lines, and the results of the fit are given in Table VIII.

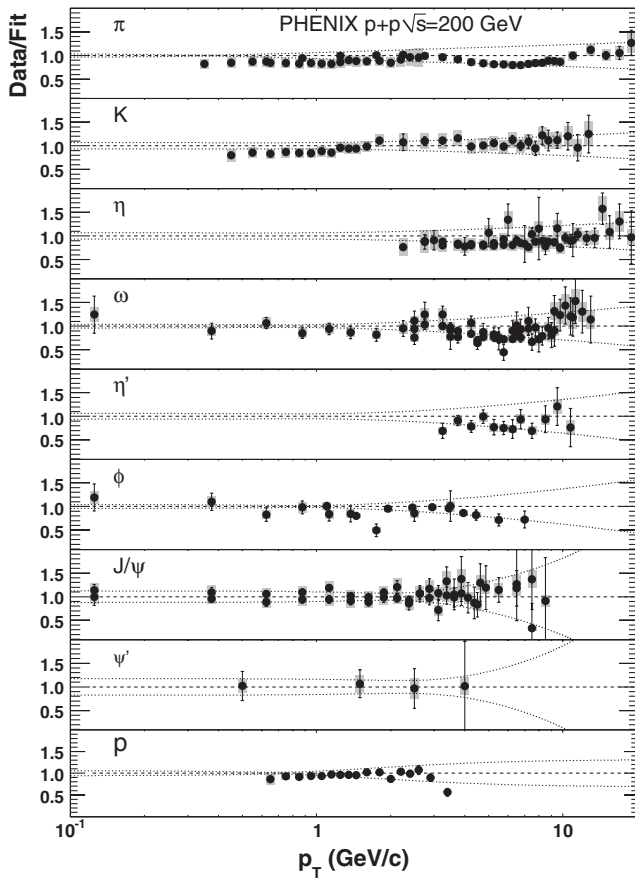


FIG. 15. Data-to-fit ratio for different particles used in the analysis. The systematic uncertainties are the combined uncertainties of type B and type C, excluding the common 9.7% trigger uncertainty.

The parameters n and T , and their errors, are fixed to the values obtained from the fitted linear dependence of the parameters on particle mass, obtained from the fits of Tables V and VII. The systematic error on the integrated yields reflects the variation of the n and T parameters within the errors. It also includes the uncertainty from the variation of the spectral shapes within errors of types B and C, as explained above.

The fits accurately describe the data. To demonstrate the quality of the fits, the data points have been divided by the fit value, and the ratios are plotted in Fig. 15.

Grey error bars show the combined systematic uncertainty of types B and C, with the type B uncertainties dominating. The dashed lines show the fit uncertainty corridor. The rms of the vertical spread of all points plotted in Fig. 15 is 0.17. If each point is normalized to the combined statistical and systematic error of the data point, the rms of the same distribution is much larger, with a value of 0.88, which indicates that the agreement between the data and the fit is well within errors.

V. DISCUSSION

A. Tsallis fit parameters

The analysis of Sec. IV demonstrated the ability of the Tsallis distribution functional form to fit the full transverse momenta spectra for all different species produced in $p + p$ collisions at $\sqrt{s} = 200$ GeV with only two parameters, $n = -1/(1 - q)$ and T . Furthermore, the values of the two parameters extracted from the fits are approximately the same for all measured mesons.

On the other hand, the observation that the pure power law fit of Eq. (3) to the spectra in the region of $p_T > 3.5 \text{ GeV}/c$ yields the same power $\nu = 8.154 \pm 0.039$ for all particles with higher accuracy than the Tsallis fit indicates that a weak mass dependence of the Tsallis parameters is to be expected. Assuming a weak mass dependence, one gets $T = 112.6 \pm 3.8 + (11.8 \pm 7.0)m_0$ [GeV/c^2] MeV and $n = 9.48 \pm 0.14 + (0.66 \pm 0.39)m_0$ [GeV/c^2], which improves the description of the meson spectra with the Tsallis distribution.

The parameters are listed in Tables IV and VIII and plotted in Fig. 14.

The ratios of the data points to the Tsallis parametrization using the global fit parameters n and T for all particles were shown in Fig. 15. Represented are nine different particle species measured over the range $0 < p_T$ (GeV/c) < 20 using six independent data samples and ten different analysis techniques. The parametrization is in good agreement with the experimental data. The average deviation of the points from 1 in all panels of Fig. 15 is 88% of the combined uncertainty of the data and the fit.

The Tsallis distribution fit for the proton measurement yields a parameter $T = 58.8 \pm 6.4$ MeV, significantly lower than that for the mesons. Since the published PHENIX results for protons have a limited p_T range, this result was checked and confirmed using STAR measurements for protons and heavier baryons [7–11]. This result indicates significantly different Tsallis fit parameters between mesons and baryons.

The similarity of the measured parameters T and n for all studied mesons suggests a similar production mechanism in $p + p$ collisions at $\sqrt{s} = 200$ GeV. At the same time, the mechanism of baryon production must have different features. The interpretation of the T parameter of the Tsallis fits is not straightforward. If interpreted as a temperature, the values obtained are seen to be similar to average freeze-out temperatures $\langle T_{\text{fo}} \rangle$ extracted in the blast-wave model approach [8,71] applied to $p + p$ data. As mentioned above, the parameter n can be related to temperature fluctuations as $\sqrt{\text{Var}(1/T)/\langle 1/T \rangle} = 1/n$ in a thermal interpretation. Following this interpretation, one can estimate the fluctuations of the inverse slope parameter $1/T$ to be of order of 0.3.

B. m_T scaling

As discussed in Sec. IV B, m_T scaling can not be an exact scaling when particle spectra follow the Tsallis distribution with $q \neq 1$. However, m_T scaling could be approximately true. The validity of m_T scaling can be studied quantitatively with the assistance of Eq. (9), which gives the Tsallis distribution in the limit $m_0 \rightarrow 0$ with a form explicitly satisfying m_T scaling.

Figure 16 shows the spectra for all particles plotted as a function of m_T and normalized at one single point on the x axis. All normalized spectra are then fit simultaneously with Eq. (9) using fixed parameters taken from Tables V and VII: $n = 9.656$ and $T = 115.3$ MeV for mesons, and $T = 58.8$ MeV for baryons.

The difference in the spectral shapes between mesons and baryons shown in Fig. 16 is due to the large difference in $\langle T \rangle$ between these particle groups. At the same time, the spectra of both mesons and baryons separately are well described by the m_T scaling assumption.

To quantify this statement we restricted the analysis to the PHENIX meson measurements only. After optimization of the normalization point for the different

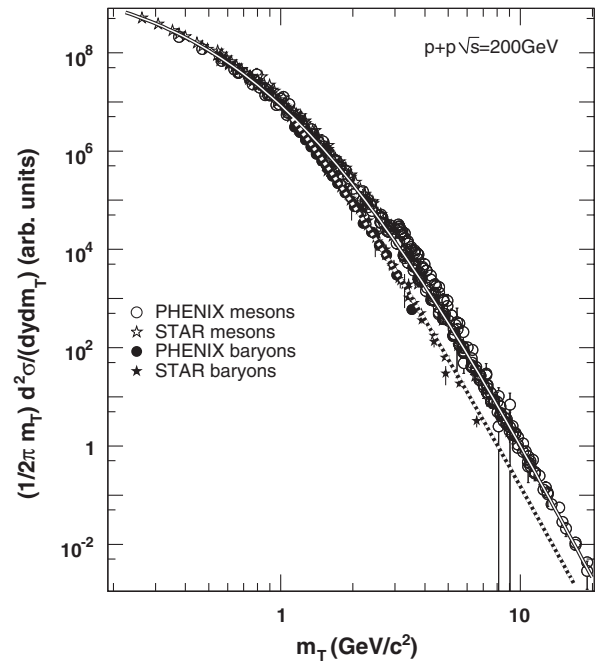


FIG. 16. Particle spectra plotted vs m_T and arbitrarily normalized at $p_T = 10$ GeV/c. Open symbols are mesons and full symbols are baryons measured by PHENIX (circles) and STAR (stars). The lines are the Hagedorn fits by Eq. (9) to mesons (solid) and baryons (dashed) with parameters n and T fixed to average values. Error bars are statistical and point-by-point systematic only.

particles, the rms of the data-to-fit ratio for all points shown in Fig. 16 has a value of 0.25. This is to be compared to the analogous result of Fig. 15 for the Tsallis fit in the p_T coordinate which gave a rms of 0.17. This small increase supports the conclusion that at $\sqrt{s} = 200$ GeV all meson spectra have very similar shapes when plotted as a function of m_T , and thus obey m_T scaling.

C. Integrated yields and $\langle p_T \rangle$

Using the Tsallis functional form and Tables V and VII, one can derive information about $\langle m_T \rangle$ and $\langle p_T \rangle$, based only on the particle mass and the baryon number. Determination of the integrated $d\sigma/dy$ requires experimental measurement of the particle production cross section in at least a limited p_T range.

The results presented below were obtained independently for each particle species without averaging within the same isospin multiplet, unless such averaging was done by the experiment. Different measurements of the same particle were combined together. Published data from the STAR experiment and the references listed in Table IX were also analyzed. To compare PHENIX and STAR results, the spectra and the integrated yields published by STAR, in units of dN/dy , were multiplied by 30 mb, which is the value of the STAR minimum bias cross section in

TABLE IX. Cross sections in mb and $\langle p_T \rangle$ in GeV/c of different particles in $p + p$ collisions at $\sqrt{s} = 200$ GeV. The PHENIX and STAR columns show the values obtained by fits to the experimental spectra with the Tsallis functional form as described in the text. One should state explicitly that these values do not supersede values given in the “Published” column by the experiments, in their publications listed in the last column, or elsewhere. An additional 9.7% systematic uncertainty should be added to all $d\sigma/dy$ values listed in the column “PHENIX” and 12% to the values in the column “STAR” to account for the trigger uncertainties. Values in the column Published are also given without these systematic uncertainties. The column “SM” is the prediction of the statistical model discussed in the text. The characteristic widths of the particle spectra are $\langle p_T \rangle$ for all species except for J/ψ and ψ' , for which the values given in the table are $\langle p_T^2 \rangle$. For ψ' the integration is done in the p_T region below 5 GeV/c . All errors are the combined statistical and systematic uncertainties.

Particle	$d\sigma/dy$ (mb)			$\langle p_T \rangle$ (GeV/c), $\langle p_T^2 \rangle$ (GeV^2/c^2)			Reference
	PHENIX	STAR	Published	SM	Fit	Published	
π^0	41.4 ± 5.8			46.9	0.377 ± 0.012		
π^+	39.4 ± 7.3	43.8 ± 3.3	43.2 ± 3.3	42.1	0.379 ± 0.012	0.348 ± 0.018	[8]
π^-	38.6 ± 7.2	43.2 ± 3.3	42.6 ± 3.3	41.5	0.379 ± 0.012	0.348 ± 0.018	[8]
K^+	4.57 ± 0.61	4.72 ± 0.39	4.50 ± 0.39	4.57	0.567 ± 0.017	0.517 ± 0.030	[8]
K^-	4.20 ± 0.51	4.61 ± 0.18	4.35 ± 0.39	4.38	0.567 ± 0.017	0.517 ± 0.030	[8]
K_S^0	5.28 ± 0.53	4.26 ± 0.15	4.02 ± 0.34	4.40	0.569 ± 0.017	0.605 ± 0.025	[9]
η	4.47 ± 0.96			4.93	0.595 ± 0.018		
ρ		6.55 ± 0.37	7.8 ± 1.2	5.58	0.714 ± 0.019	0.616 ± 0.062	[73]
ω	3.65 ± 0.77		4.20 ± 0.47	5.03	0.718 ± 0.022	0.664 ± 0.039	This work
η'	0.62 ± 0.17			0.365	0.808 ± 0.026		
$(K^{*+} + K^{*-})/2$		1.46 ± 0.10		1.57	0.774 ± 0.022		
$(K^{*0} + \bar{K}^{*0})/2$		1.525 ± 0.091	1.52 ± 0.19	1.55	0.776 ± 0.022	0.81 ± 0.14	[63]
ϕ	0.421 ± 0.055		0.432 ± 0.035	0.339	0.839 ± 0.027	0.752 ± 0.043	This work
ϕ		0.525 ± 0.018	0.540 ± 0.086	0.339	0.839 ± 0.025	0.820 ± 0.051	[74]
$J/\psi (\times 10^3)$	0.759 ± 0.053		0.746 ± 0.089		4.464 ± 0.606	4.60 ± 0.19	[5]
$\psi' (\times 10^3)$	0.133 ± 0.031		0.126 ± 0.034		4.807 ± 0.443	4.7 ± 1.3	[61]
p		4.06 ± 0.23	4.14 ± 0.30	4.47	0.648 ± 0.019	0.661 ± 0.022	[8]
\bar{p}		3.28 ± 0.23	3.39 ± 0.36	3.59	0.648 ± 0.019	0.661 ± 0.022	[8]
Λ		1.33 ± 0.13	1.31 ± 0.12	1.30	0.742 ± 0.023	0.775 ± 0.040	[9]
$\bar{\Lambda}$		1.20 ± 0.12	1.19 ± 0.11	1.11	0.742 ± 0.023	0.763 ± 0.040	[9]
Ξ^-		0.094 ± 0.020	0.078 ± 0.028	0.092	0.850 ± 0.030	0.924 ± 0.054	[9]
$\bar{\Xi}^+$		0.091 ± 0.019	0.087 ± 0.031	0.082	0.850 ± 0.030	0.881 ± 0.051	[9]
$\Sigma^{*+} + \bar{\Sigma}^{*-}$		0.358 ± 0.026	0.321 ± 0.044	0.308	0.882 ± 0.032	1.020 ± 0.073	[10]
$\bar{\Sigma}^{*+} + \bar{\Sigma}^{*-}$		0.310 ± 0.025	0.267 ± 0.038	0.260	0.882 ± 0.032	1.010 ± 0.061	[10]
$\bar{\Lambda}^* + \Lambda^*$		0.127 ± 0.013	0.104 ± 0.017	0.168	0.955 ± 0.038	1.08 ± 0.10	[10]
$\Omega^- + \bar{\Omega}^+ (\times 10^3)$		11.5 ± 4.6	10.2 ± 5.7	17.1	1.035 ± 0.046	1.08 ± 0.30	[9]

$p + p$ collisions at $\sqrt{s} = 200$ GeV, including the nonsingle diffractive part of $p + p$ interactions (cf. [8]).

The particle spectra published by the STAR experiment were fit to the Tsallis functional form given by Eq. (8) with the parameters $n = 9.48 + 0.66m_0$ [GeV/c^2] and $T = 112.6 + 11.8m_0$ [GeV/c^2] taken from the global fit to the PHENIX data. The same parameters determined independently for the STAR data give consistent results for mesons. For baryons the STAR data showed a dependence of the parameter T on the mass of the particle; however, the fit uncertainties were too large to make a definite statement. The value of T averaged over all baryon measurements made by STAR agrees with the PHENIX result for the proton measurement. Calculation of $d\sigma/dy$ for p and \bar{p} measured by PHENIX was not done because the spectra are feed-down corrected and the extrapolation to low

p_T requires additional evaluation of the systematic uncertainties.

Figure 17 shows a comparison of the experimentally measured integrated spectral characteristics to the results obtained using the Tsallis fits. The ratio of the measured characteristic width to the width calculated from the Tsallis fit is shown in the upper panel. For most particles the width is taken to be $\langle p_T \rangle$, but for the J/ψ and ψ' the comparison is done for $\langle p_T^2 \rangle$ because this is the parameter published in the corresponding articles. Statistical and systematic uncertainties of the published results are shown at each data point, and the uncertainties of the Tsallis fit values are shown by the band around $y = 1$.

For all mesons the agreement between the published values and the values from the Tsallis fit analysis is consistent with the published uncertainties. This demonstrates

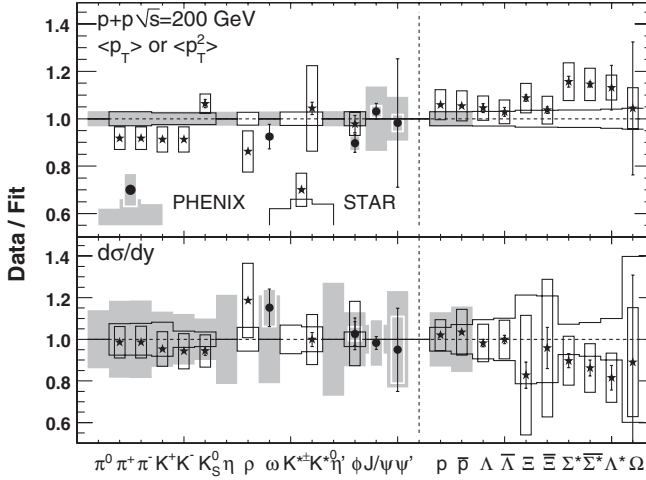


FIG. 17. Comparison of the integrated parameters of the particle spectra. The upper panel shows the ratio of the published result divided by the result of the constrained Tsallis fit for $\langle p_T \rangle$ ($\langle p_T^2 \rangle$) for the J/ψ and the same for ψ' integrated in the p_T range below $5 \text{ GeV}/c$. The lower panel shows the ratio for $d\sigma/dy$. The statistical and systematic uncertainties shown at each point are from the published data only. The band around $y = 1$ shows the uncertainty of the values extracted from the Tsallis function. The trigger efficiency scale uncertainties of 9.7% for PHENIX and 12% for STAR are not plotted. There are no points outside the plot boundaries. The vertical dashed line separates mesons and baryons.

the accuracy to which the Tsallis functional form describes the experimental spectral shapes.

Equation (12) suggests that the mass dependence of the $\langle p_T \rangle$ should be approximately linear. A fit to the average mean momentum of all mesons extracted from the Tsallis distribution fits as a function of their mass gives $\langle p_T \rangle = (0.319 \pm 0.007) [\text{GeV}/c] + (0.491 \pm 0.009)m_0$. A fit to the published data directly gives a similar consistent result of $\langle p_T \rangle = (0.284 \pm 0.015) [\text{GeV}/c] + (0.506 \pm 0.033)m_0$. For baryons the agreement with the linear fit is reasonable based on the data published by the STAR experiment.

In the original work of R. Hagedorn [22] a nearly linear dependence of the $\langle p_T \rangle$ was derived based on the assumption of Boltzmann-Gibbs statistics to describe the particle spectra at low p_T . The difference between mesons and baryons would follow from the bosonic and fermionic nature of these particles. However, quantitatively the values of the particle $\langle p_T \rangle$ and the magnitude of the meson-to-baryon difference are not the same as would follow from the mechanisms discussed in [22].

The lower panel of Fig. 17 shows the ratio of the integrated yields published by the experiment to the integrated yields extracted from the Tsallis function fits. The common uncertainties on all integrated yields of 9.7% for PHENIX and 12% for STAR are not included. Most of the ratios equal 1 within uncertainties. From Fig. 17 and Table IX one may conclude that the constrained Tsallis fit reproduces the measured integrated cross section with

high accuracy for all identified particles in $p + p$ collisions at $\sqrt{s} = 200 \text{ GeV}$. This gives justification to use the constrained Tsallis fit results to obtain $d\sigma/dy$ for particles which have only been measured in a limited p_T range, such as π^0 , η , and η' mesons. The resulting $d\sigma/dy$ for such particles are also given in Table IX.

It should be noted explicitly that the $d\sigma/dy$ and $\langle p_T \rangle$ values given in Table IX determined using the Tsallis parametrization do not supersede, or presume to be more accurate than, the corresponding values published by the experiments in the original papers. They are given to validate the method. In those cases where no values have been published, the Tsallis fit result values in the table represent a best attempt to obtain the cross section or $\langle p_T \rangle$ based on the validity of the Tsallis fit distribution.

D. Statistical model calculation

Figure 18 shows the ratio of the constrained Tsallis fit results for the integrated particle yields to the predicted yields from a statistical model (SM) calculation [75]. The data-to-model ratio for PHENIX data is shown in the upper panel, and for STAR data in the lower panel. The statistical model calculation parameters were chosen to reproduce the integrated yields published by the STAR experiment [8–10, 63, 73, 74], which may explain the larger discrepancies in the comparison to the PHENIX results.

Although statistical models are not commonly used to describe $p + p$ data, the agreement of the statistical model calculation with the STAR results was found to be accurate for most particles except for the ρ , ϕ , and Λ^* [40]. Leaving

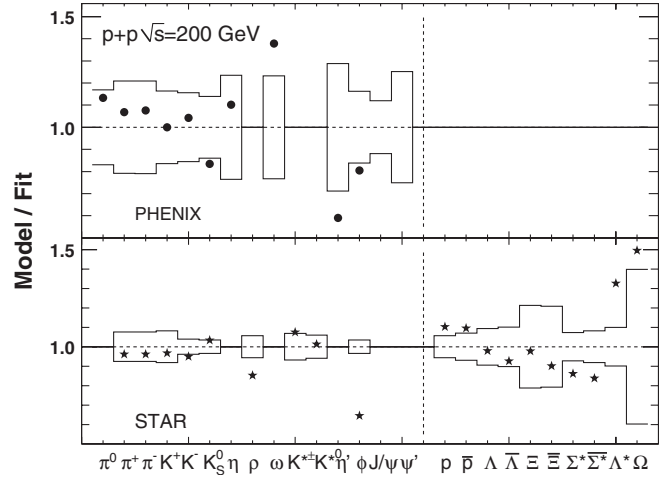


FIG. 18. Ratio of integrated yields predicted by the statistical model [40] to those of the constrained Tsallis fits for various particles. Results for fits to PHENIX data are shown in the upper panel and STAR data in the lower panel. The band reflects the uncertainty of the Tsallis fit results and includes the trigger uncertainty of 9.7% for PHENIX. The lower panel has smaller uncertainties because the model prediction was based on published STAR data given in Table IX. There are no points outside the plot boundaries. The vertical dashed line separates mesons and baryons.

aside baryons, for which the calculations of the $d\sigma/dy$ requires additional assumptions, as explained above, the Tsallis fit also has difficulty reproducing the result for the ρ meson, as shown in Fig. 17. This can be explained by the large systematic uncertainty of the published value [73].

For the PHENIX data the SM calculations agree with the production rates for most mesons because the Tsallis fit results of the PHENIX and STAR data agree. The production rates of π^0 , η , ω , η' , and ϕ were not measured by STAR and so were not used in the determination of the SM parameters. Among them, the predicted yields of π^0 and η mesons are in very good agreement with the PHENIX data. The predictions of the SM for the ω , η' , and ϕ yields are less accurate, with ratios just outside of errors.

VI. SUMMARY

A systematic study of neutral meson production in $p + p$ collisions at $\sqrt{s} = 200$ GeV has been performed by the PHENIX experiment at RHIC with results presented in this paper. New measurements by PHENIX of K_S^0 , ω , ϕ , and η' meson production have been presented.

The measurement of the K_S^0 invariant differential cross section via the $\pi^0\pi^0$ decay channel in the momentum range $2 < p_T (\text{GeV}/c) < 13.5$ extends previously published K^\pm measurements [1].

We present the first measurement of the ϕ invariant differential cross section in the K^+K^- decay mode using several different techniques. The combined spectrum reaches to $p_T = 8 \text{ GeV}/c$.

This work also presents the first measurement of the invariant differential cross section of η' production measured via the $\eta\pi^+\pi^-$ decay mode with results that cover the range $3 < p_T (\text{GeV}/c) < 11$.

Measurements of ω meson production in nonleptonic decay channels extend the p_T coverage of the previous PHENIX ω measurement [4], obtained with a smaller data sample, to $13.5 \text{ GeV}/c$.

These first measurements of the ω and ϕ in the e^+e^- decay channel extend the p_T coverage for these two particles down to zero momentum and allow a direct calculation of the integrated yields and mean transverse momenta with the following results: $d\sigma^\omega/dy = 4.20 \pm 0.33^{\text{stat}} \pm 0.52^{\text{syst}} \text{ mb}$ and $d\sigma^\phi/dy = 0.432 \pm 0.031^{\text{stat}} \pm 0.051^{\text{syst}} \text{ mb}$, and $\langle p_T^\omega \rangle = 0.664 \pm 0.037^{\text{stat}} \pm 0.012^{\text{syst}} \text{ GeV}/c$ and $\langle p_T^\phi \rangle = 0.752 \pm 0.032^{\text{stat}} \pm 0.014^{\text{syst}} \text{ GeV}/c$.

All measured results were found to be consistent between the different decay modes and analysis techniques, as well as with previously published data. The results are shown in Figs. 11 and 12, and the measured cross sections are tabulated in the Appendix.

The invariant differential cross sections for all measured hadrons produced in $p + p$ collisions at $\sqrt{s} = 200$ GeV presented in this work, as well as in previous PHENIX publications, were shown to be described well over the

entire momentum range by the Tsallis distribution functional form with only two parameters, T and n , characterizing the low- and high- p_T regions, respectively. Furthermore, the values of the two parameters extracted from the fits are approximately the same for all measured mesons with a weak mass dependence: $T = 112.6 \pm 3.8 + (11.8 \pm 7.0)m_0 [\text{GeV}/c^2]\text{MeV}$ and $n = 9.48 \pm 0.14 + (0.66 \pm 0.39)m_0 [\text{GeV}/c^2]$.

The meson spectral shapes have very similar forms when plotted as a function of m_T and hence follow m_T scaling well at $\sqrt{s} = 200$ GeV. On the other hand, the proton spectra are described with a significantly lower parameter value of $T = 58.8 \pm 6.4 \text{ MeV}$ and do not follow the m_T -scaling form observed for mesons.

The ability to successfully describe all particle spectra in $p + p$ collisions at $\sqrt{s} = 200$ GeV with a common functional form allows one to calculate the invariant differential cross section for any particle. This allows the absolute integrated yield to be derived from any experimental measurement of the hadron spectrum, even with limited p_T range. The values of $d\sigma/dy$ and $\langle p_T \rangle$ are tabulated in Table IX for hadrons measured by PHENIX, as well as those measured by the STAR experiment using the set of values of Tables V and VII. For all measured mesons the average transverse momentum of the particle depends linearly on the mass m_0 and can be parametrized with the relation $\langle p_T \rangle = (0.319 \pm 0.007) [\text{GeV}/c] + (0.491 \pm 0.009)m_0$.

The predictions of statistical model calculations based on data published by the STAR experiment [40] were shown to be in good agreement with the integrated yields calculated from the Tsallis distribution fits for most particles. Some deviations are seen for the ω , the η' , and the ϕ mesons.

ACKNOWLEDGMENTS

We thank the staff of the Collider-Accelerator and Physics Departments at Brookhaven National Laboratory and the staff of the other PHENIX participating institutions for their vital contributions. We also thank F. Becattini of the University of Florence for providing us with the statistical model predictions, and G. Wilk of SINS, Warsaw for useful discussions about applications of the Tsallis distribution. We acknowledge support from the Office of Nuclear Physics in the Office of Science of the Department of Energy, the National Science Foundation, a sponsored research grant from Renaissance Technologies LLC, Abilene Christian University Research Council, Research Foundation of SUNY, and Dean of the College of Arts and Sciences, Vanderbilt University (U.S.); Ministry of Education, Culture, Sports, Science, and Technology and the Japan Society for the Promotion of Science (Japan); Conselho Nacional de Desenvolvimento Científico e Tecnológico and Fundação de Amparo à Pesquisa do Estado de São Paulo (Brazil); Natural Science Foundation of China (People's Republic of China); Ministry of Education, Youth and Sports (Czech Republic); Centre National de la

Recherche Scientifique, Commissariat à l'Énergie Atomique, and Institut National de Physique Nucléaire et de Physique des Particules (France); Ministry of Industry, Science and Technologies, Bundesministerium für Bildung und Forschung, Deutscher Akademischer Austausch Dienst, and Alexander von Humboldt Stiftung (Germany); Hungarian National Science Fund, OTKA (Hungary); Department of Atomic Energy (India); Israel Science Foundation (Israel); National Research Foundation (Korea); Ministry of Education and Science, Russia Academy of Sciences, Federal Agency of Atomic Energy

(Russia); VR and the Wallenberg Foundation (Sweden); the U.S. Civilian Research and Development Foundation for the Independent States of the Former Soviet Union; the U.S.-Hungarian Fulbright Foundation for Educational Exchange; and the U.S.-Israel Binational Science Foundation.

APPENDIX

Tables X and XI show the measured invariant differential cross section $\frac{1}{2\pi p_T} \frac{d^2\sigma}{dy dp_T}$.

TABLE X. The invariant differential cross section $\frac{1}{2\pi p_T} \frac{d^2\sigma}{dy dp_T}$ of ω meson production measured in the indicated decay channel. Notations are as follows: V is the differential cross section, and A, B, and C are the three types of errors described in the text.

Meson	Decay channel	p_T GeV/c	V mb/(GeV/c) ²	A	B	C
ω	$e^+ e^-$	0.125	3.5	1.1	0.4	0.2
		0.375	1.76	0.33	0.19	$8. \times 10^{-2}$
		0.625	1.12	0.12	0.12	$5. \times 10^{-2}$
		0.875	0.425	5.6×10^{-2}	4.6×10^{-2}	1.9×10^{-2}
		1.125	0.213	2.8×10^{-2}	2.3×10^{-2}	$2. \times 10^{-3}$
		1.375	9.0×10^{-2}	1.4×10^{-2}	$1. \times 10^{-2}$	$4. \times 10^{-3}$
		1.75	2.73×10^{-2}	4.6×10^{-3}	2.9×10^{-3}	1.2×10^{-3}
		2.5	3.34×10^{-3}	6.3×10^{-4}	3.5×10^{-4}	1.5×10^{-4}
		3.5	3.6×10^{-4}	1.2×10^{-4}	$4. \times 10^{-5}$	$2. \times 10^{-5}$
		2.25	8.0×10^{-3}	1.4×10^{-3}	$8. \times 10^{-4}$	2.6×10^{-4}
		2.75	2.50×10^{-3}	2.5×10^{-4}	2.4×10^{-4}	$8. \times 10^{-5}$
		3.25	7.89×10^{-4}	5.8×10^{-5}	7.4×10^{-5}	2.6×10^{-5}
		3.75	2.56×10^{-4}	1.7×10^{-5}	2.3×10^{-5}	$8. \times 10^{-6}$
		4.25	9.41×10^{-5}	5.9×10^{-6}	8.0×10^{-6}	3.1×10^{-6}
		4.75	3.69×10^{-5}	2.5×10^{-6}	3.5×10^{-6}	1.2×10^{-6}
		5.25	1.68×10^{-5}	1.3×10^{-6}	1.5×10^{-6}	$5. \times 10^{-7}$
		5.75	7.57×10^{-6}	7.1×10^{-7}	7.1×10^{-7}	2.5×10^{-7}
		6.25	3.89×10^{-6}	4.1×10^{-7}	3.7×10^{-7}	1.3×10^{-7}
		6.75	2.13×10^{-6}	2.8×10^{-7}	2.2×10^{-7}	$7. \times 10^{-8}$
ω	$\pi^0 \pi^+ \pi^-$	7.25	1.45×10^{-6}	2.2×10^{-7}	1.6×10^{-7}	$5. \times 10^{-8}$
		7.75	8.5×10^{-7}	1.6×10^{-7}	1.0×10^{-7}	$3. \times 10^{-8}$
		8.25	4.03×10^{-7}	9.8×10^{-8}	4.6×10^{-8}	1.3×10^{-8}
		8.75	2.93×10^{-7}	7.0×10^{-8}	3.6×10^{-8}	1.0×10^{-8}
		9.25	2.48×10^{-7}	6.2×10^{-8}	3.5×10^{-8}	$8. \times 10^{-9}$
		9.75	1.49×10^{-7}	4.0×10^{-8}	2.2×10^{-8}	$5. \times 10^{-9}$
		10.25	1.09×10^{-7}	3.0×10^{-8}	1.7×10^{-8}	$4. \times 10^{-9}$
		10.75	6.0×10^{-8}	1.9×10^{-8}	$1. \times 10^{-8}$	$2. \times 10^{-9}$
		11.25	5.1×10^{-8}	1.6×10^{-8}	$8. \times 10^{-9}$	$2. \times 10^{-9}$
		12.	2.41×10^{-8}	8.3×10^{-9}	3.6×10^{-9}	$8. \times 10^{-10}$
		13.	1.02×10^{-8}	4.4×10^{-9}	1.7×10^{-9}	$3. \times 10^{-10}$
		2.5	4.15×10^{-3}	5.0×10^{-4}	5.5×10^{-4}	2.3×10^{-4}
		3.5	4.54×10^{-4}	3.2×10^{-5}	4.9×10^{-5}	2.5×10^{-5}
ω	$\pi^0 \gamma$	4.5	5.07×10^{-5}	4.8×10^{-6}	5.2×10^{-6}	2.8×10^{-6}
		5.5	1.14×10^{-5}	1.8×10^{-6}	1.1×10^{-6}	$6. \times 10^{-7}$
		6.5	3.33×10^{-6}	4.5×10^{-7}	3.8×10^{-7}	1.8×10^{-7}
		7.5	7.7×10^{-7}	2.0×10^{-7}	1.0×10^{-7}	$4. \times 10^{-8}$
		9.	1.94×10^{-7}	6.4×10^{-8}	2.9×10^{-8}	1.1×10^{-8}
		11.	4.8×10^{-8}	1.6×10^{-8}	1.0×10^{-8}	$3. \times 10^{-9}$

TABLE XI. The invariant differential cross section $\frac{1}{2\pi p_T} \frac{d^2\sigma}{dy dp_T}$ of K_S^0 , η' , and ϕ meson production measured in the indicated decay channel. Notations are as follows: V is the differential cross section, and A, B, and C are the three types of errors described in the text.

Meson	Decay channel	p_T GeV/c	V mb/(GeV/c) ²	A	B	C
K_S^0	$\pi^0 \pi^0$	2.25	4.66×10^{-3}	7.7×10^{-4}	7.4×10^{-4}	3.0×10^{-4}
		2.75	1.30×10^{-3}	1.1×10^{-4}	1.8×10^{-4}	8.0×10^{-5}
		3.25	4.14×10^{-4}	2.5×10^{-5}	5.5×10^{-5}	2.6×10^{-5}
		3.75	1.54×10^{-4}	8.0×10^{-6}	2.0×10^{-5}	1.0×10^{-5}
		4.25	5.09×10^{-5}	2.8×10^{-6}	6.6×10^{-6}	3.2×10^{-6}
		4.75	2.22×10^{-5}	1.2×10^{-6}	2.9×10^{-6}	1.4×10^{-6}
		5.25	1.06×10^{-5}	6.0×10^{-7}	1.4×10^{-6}	7.0×10^{-7}
		5.75	4.74×10^{-6}	3.3×10^{-7}	6.1×10^{-7}	3.0×10^{-7}
		6.25	2.74×10^{-6}	2.2×10^{-7}	3.6×10^{-7}	1.7×10^{-7}
		6.75	1.30×10^{-6}	1.3×10^{-7}	1.7×10^{-7}	8.0×10^{-8}
		7.25	7.70×10^{-7}	1.0×10^{-7}	1.0×10^{-7}	5.0×10^{-8}
		7.75	3.82×10^{-7}	6.0×10^{-8}	5.3×10^{-8}	2.4×10^{-8}
		8.25	2.88×10^{-7}	4.4×10^{-8}	4.1×10^{-8}	1.8×10^{-8}
		8.75	1.59×10^{-7}	3.1×10^{-8}	2.3×10^{-8}	1.0×10^{-8}
		9.50	7.80×10^{-8}	1.2×10^{-8}	1.1×10^{-8}	4.9×10^{-9}
		10.5	3.49×10^{-8}	8.5×10^{-9}	5.6×10^{-9}	2.2×10^{-9}
		11.5	1.25×10^{-8}	3.7×10^{-9}	2.2×10^{-9}	8.0×10^{-10}
		12.75	6.50×10^{-9}	2.1×10^{-9}	1.3×10^{-9}	4.1×10^{-10}
η'	$\eta \pi^+ \pi^-$	3.25	1.53×10^{-4}	3.6×10^{-5}	1.6×10^{-5}	$7. \times 10^{-6}$
		3.75	7.38×10^{-5}	8.9×10^{-6}	7.3×10^{-6}	3.3×10^{-6}
		4.25	2.55×10^{-5}	4.1×10^{-6}	2.5×10^{-6}	1.1×10^{-6}
		4.75	1.39×10^{-5}	2.0×10^{-6}	1.3×10^{-6}	$6. \times 10^{-7}$
		5.25	4.9×10^{-6}	1.0×10^{-6}	$5. \times 10^{-7}$	$2. \times 10^{-7}$
		5.75	2.32×10^{-6}	4.3×10^{-7}	2.3×10^{-7}	1.0×10^{-7}
		6.25	1.13×10^{-6}	3.1×10^{-7}	1.1×10^{-7}	$5. \times 10^{-8}$
		6.75	7.7×10^{-7}	1.7×10^{-7}	$8. \times 10^{-8}$	$3. \times 10^{-8}$
		7.5	2.33×10^{-7}	5.4×10^{-8}	2.7×10^{-8}	1.0×10^{-8}
		8.5	1.07×10^{-7}	3.3×10^{-8}	1.2×10^{-8}	$5. \times 10^{-9}$
ϕ	$e^+ e^-$	9.5	5.2×10^{-8}	1.7×10^{-8}	$6. \times 10^{-9}$	$2. \times 10^{-9}$
		10.75	1.09×10^{-8}	5.8×10^{-9}	2.1×10^{-9}	4.9×10^{-10}
		0.125	0.264	6.3×10^{-2}	2.6×10^{-2}	1.1×10^{-2}
		0.375	0.188	3.1×10^{-2}	1.8×10^{-2}	$8. \times 10^{-3}$
		0.625	8.9×10^{-2}	1.5×10^{-2}	$9. \times 10^{-3}$	$4. \times 10^{-3}$
		0.875	5.83×10^{-2}	8.2×10^{-3}	5.8×10^{-3}	2.5×10^{-3}
		1.125	2.57×10^{-2}	4.3×10^{-3}	2.5×10^{-3}	1.2×10^{-3}
		1.375	1.31×10^{-2}	2.7×10^{-3}	1.3×10^{-3}	$6. \times 10^{-4}$
		1.75	2.79×10^{-3}	7.5×10^{-4}	2.8×10^{-4}	1.3×10^{-4}
		2.5	7.2×10^{-4}	1.5×10^{-4}	$7. \times 10^{-5}$	$3. \times 10^{-5}$
ϕ	$K^+ K^-$	3.5	9.7×10^{-5}	3.1×10^{-5}	1.0×10^{-5}	$4. \times 10^{-6}$
		1.1	3.32×10^{-2}	2.6×10^{-3}	2.6×10^{-3}	$4. \times 10^{-4}$
		1.45	1.01×10^{-2}	$7. \times 10^{-4}$	$5. \times 10^{-4}$	$1. \times 10^{-4}$
		1.95	3.16×10^{-3}	1.9×10^{-4}	1.7×10^{-4}	$4. \times 10^{-5}$
		2.45	9.28×10^{-4}	5.6×10^{-5}	5.3×10^{-5}	1.1×10^{-5}
		2.95	2.99×10^{-4}	1.9×10^{-5}	1.8×10^{-5}	$4. \times 10^{-6}$
		3.45	1.02×10^{-4}	$6. \times 10^{-6}$	$6. \times 10^{-6}$	$1. \times 10^{-6}$
		3.95	3.49×10^{-5}	2.6×10^{-6}	2.3×10^{-6}	$4. \times 10^{-7}$
		4.45	1.38×10^{-5}	1.8×10^{-6}	$9. \times 10^{-7}$	$2. \times 10^{-7}$
		5.5	2.31×10^{-6}	4.1×10^{-7}	1.6×10^{-7}	$3. \times 10^{-8}$
		7.	3.21×10^{-7}	7.9×10^{-8}	2.4×10^{-8}	$4. \times 10^{-9}$

- [1] S.S. Adler *et al.* (PHENIX Collaboration), Phys. Rev. C **74**, 024904 (2006).
- [2] S.S. Adler *et al.* (PHENIX Collaboration), Phys. Rev. C **75**, 024909 (2007).
- [3] A. Adare *et al.* (PHENIX Collaboration), Phys. Rev. D **76**, 051106 (2007).
- [4] S.S. Adler *et al.* (PHENIX Collaboration), Phys. Rev. C **75**, 051902 (2007).
- [5] A. Adare *et al.* (PHENIX Collaboration), Phys. Rev. Lett. **98**, 232002 (2007).
- [6] A. Adare *et al.* (PHENIX Collaboration), Phys. Rev. D **83**, 032001 (2011).
- [7] J. Adams *et al.* (STAR Collaboration), Phys. Lett. B **637**, 161 (2006).
- [8] B. Abelev *et al.* (STAR Collaboration), Phys. Rev. C **79**, 034909 (2009).
- [9] B. Abelev *et al.* (STAR Collaboration), Phys. Rev. C **75**, 064901 (2007).
- [10] B. Abelev *et al.* (STAR Collaboration), Phys. Rev. Lett. **97**, 132301 (2006).
- [11] J. Adams *et al.* (STAR Collaboration), Phys. Lett. B **616**, 8 (2005).
- [12] D. Antreasyan *et al.*, Phys. Rev. D **19**, 764 (1979).
- [13] D.E. Jaffe *et al.* (FNAL-E605 Collaboration), Phys. Rev. D **40**, 2777 (1989).
- [14] B. Alper *et al.* (British-Scandinavian Collaboration), Nucl. Phys. **B100**, 237 (1975).
- [15] F.W. Busser *et al.*, Nucl. Phys. **B106**, 1 (1976).
- [16] M.G. Albrow *et al.* (CHLM Collaboration), Nucl. Phys. **B56**, 333 (1973).
- [17] K. Guettler *et al.* (British-Scandinavian-MIT Collaboration), Nucl. Phys. **B116**, 77 (1976).
- [18] K. Guettler *et al.* (British-Scandinavian-MIT Collaboration), Phys. Lett. **64B**, 111 (1976).
- [19] D.E. Acosta *et al.* (CDF Collaboration), Phys. Rev. D **72**, 052001 (2005).
- [20] G. Sterman *et al.*, Rev. Mod. Phys. **67**, 157 (1995).
- [21] R. Hagedorn, Nuovo Cimento Suppl. **3**, 147 (1965).
- [22] R. Hagedorn, Riv. Nuovo Cimento Soc. Ital. Fis. **6N10**, 1 (1984).
- [23] J. Bartke *et al.* (Aachen-Berlin-Bonn-CERN-Cracow-Heidelberg-Warsaw Collaboration), Nucl. Phys. **B120**, 14 (1977).
- [24] C. Tsallis, J. Stat. Phys. **52**, 479 (1988).
- [25] G. Wilk and Z. Włodarczyk, Phys. Rev. Lett. **84**, 2770 (2000).
- [26] M. Biyajima, M. Kaneyama, T. Mizoguchi, and G. Wilk, Eur. Phys. J. C **40**, 243 (2005).
- [27] M. Biyajima *et al.*, Eur. Phys. J. C **48**, 597 (2006).
- [28] Z. Tang *et al.*, Phys. Rev. C **79**, 051901 (2009).
- [29] M. Shao *et al.*, J. Phys. G **37**, 085104 (2010).
- [30] V. Khachatryan *et al.* (CMS Collaboration), J. High Energy Phys. **02** (2010) 041.
- [31] M. Nauenberg, Phys. Rev. E **67**, 036114 (2003).
- [32] C. Tsallis, Phys. Rev. E **69**, 038101 (2004).
- [33] M. Nauenberg, Phys. Rev. E **69**, 038102 (2004).
- [34] A.S. Parvan, Phys. Lett. A **360**, 26 (2006).
- [35] T.S. Biro and G. Purcsel, arXiv:0809.4768.
- [36] Q.A. Wang *et al.*, Europhys. Lett. **65**, 606 (2004).
- [37] J. Cleymans and H. Satz, Z. Phys. C **57**, 135 (1993).
- [38] P. Braun-Munzinger *et al.*, Phys. Lett. B **465**, 15 (1999).
- [39] F. Becattini and U.W. Heinz, Z. Phys. C **76**, 269 (1997).
- [40] F. Becattini, P. Castorina, A. Milov, and H. Satz, Eur. Phys. J. C **66**, 377 (2010).
- [41] K. Adcox *et al.* (PHENIX Collaboration), Nucl. Instrum. Methods Phys. Res., Sect. A **499**, 469 (2003).
- [42] S. Aronson *et al.* (PHENIX Collaboration), Nucl. Instrum. Methods Phys. Res., Sect. A **499**, 480 (2003).
- [43] K. Adcox *et al.* (PHENIX Collaboration), Nucl. Instrum. Methods Phys. Res., Sect. A **499**, 489 (2003).
- [44] K. Adcox *et al.* (PHENIX Collaboration), Nucl. Instrum. Methods Phys. Res., Sect. A **497**, 263 (2003).
- [45] M. Aizawa *et al.* (PHENIX Collaboration), Nucl. Instrum. Methods Phys. Res., Sect. A **499**, 508 (2003).
- [46] M. Allen *et al.* (PHENIX Collaboration), Nucl. Instrum. Methods Phys. Res., Sect. A **499**, 549 (2003).
- [47] S.S. Adler *et al.* (PHENIX Collaboration), Phys. Rev. Lett. **91**, 241803 (2003).
- [48] A. Adare *et al.* (PHENIX Collaboration), Phys. Rev. D **82**, 012001 (2010).
- [49] L. Aphecetche *et al.* (PHENIX Collaboration), Nucl. Instrum. Methods Phys. Res., Sect. A **499**, 521 (2003).
- [50] C. Amsler *et al.* (PDG Collaboration), Phys. Lett. B **667**, 1 (2008 and 2009 partial update for the 2010 edition).
- [51] A. Adare *et al.* (PHENIX Collaboration), arXiv:1004.3532.
- [52] T. Armstrong *et al.* (FNAL-E760 Collaboration), Phys. Rev. D **54**, 7067 (1996).
- [53] A. Spiridonov, arXiv:hep-ex/0510076; Internal Note No. DESY-04-105.
- [54] C. Alff *et al.*, Phys. Rev. Lett. **9**, 325 (1962).
- [55] J.S. Danburg *et al.*, Phys. Rev. D **2**, 2564 (1970).
- [56] S. Giovannella *et al.* (KLOE Collaboration), arXiv:hep-ex/0505074.
- [57] M.L. Stevenson *et al.*, Phys. Rev. **125**, 687 (1962).
- [58] R.A. Briere *et al.* (CLEO Collaboration), Phys. Rev. Lett. **84**, 26 (2000).
- [59] N. Beisert and B. Borasoy, Nucl. Phys. **A705**, 433 (2002).
- [60] G.D. Lafferty and T.R. Wyatt, Nucl. Instrum. Methods Phys. Res., Sect. A **355**, 541 (1995).
- [61] A. Adare *et al.* (PHENIX Collaboration) (to be published).
- [62] D. de Florian and R. Sassot, Phys. Rev. D **69**, 074028 (2004).
- [63] J. Adams *et al.* (STAR Collaboration), Phys. Rev. C **71**, 064902 (2005).
- [64] G. Wilk and Z. Włodarczyk, Eur. Phys. J. A **40**, 299 (2009).
- [65] G. Wilk and Z. Włodarczyk, Nucl. Phys. B, Proc. Suppl. **75**, 191 (1999).
- [66] I. Bediaga *et al.*, Physica A (Amsterdam) **286**, 156 (2000).
- [67] C. Tsallis, Physica A (Amsterdam) **344**, 718 (2004).
- [68] F. Navarra *et al.*, Physica A (Amsterdam) **344**, 568 (2004).
- [69] C. Tsallis (updated), <http://tsallis.cat.cbpf.br/biblio.htm>.

- [70] D. B. Walton and J. Rafelski, *Phys. Rev. Lett.* **84**, 31 (2000).
- [71] K. Adcox *et al.* (PHENIX Collaboration), *Phys. Rev. C* **69**, 024904 (2004).
- [72] A. Adare *et al.* (PHENIX Collaboration), *Phys. Rev. C* **77**, 064907 (2008).
- [73] J. Adams *et al.* (STAR Collaboration), *Phys. Rev. Lett.* **92**, 092301 (2004).
- [74] J. Adams *et al.* (STAR Collaboration), *Phys. Lett. B* **612**, 181 (2005).
- [75] F. Becattini and R. Fries, arXiv:0907.1031.

参考論文

- (1) Nuclear modification factors of ϕ mesons in $d+\text{Au}$, $\text{Cu}+\text{Cu}$ and $\text{Au}+\text{Au}$ collisions at $\sqrt{s_{NN}} = 200\text{GeV}$
A.Adare, K.M.Kijima *et al.*, (別紙、共著者リスト 2 参照)
Physical Review C83, 024909 (2011).
- (2) Identified charged hadron production in $p+p$ collisions at $\sqrt{s} = 200$ and 62.4GeV
A.Adare, K.M.Kijima *et al.*, (別紙、共著者リスト 3 参照)
Physical Review C83, 064903 (2011).

Nuclear modification factors of ϕ mesons in $d + \text{Au}$, $\text{Cu} + \text{Cu}$, and $\text{Au} + \text{Au}$ collisions at $\sqrt{s_{NN}} = 200 \text{ GeV}$

- A. Adare,¹¹ S. Afanasiev,²⁶ C. Aidala,^{12,40} N. N. Ajitanand,⁵⁷ Y. Akiba,^{51,52} H. Al-Bataineh,⁴⁶ J. Alexander,⁵⁷ A. Al-Jamel,⁴⁶
 A. Angerami,¹² K. Aoki,^{33,51} N. Apadula,⁵⁸ L. Aphecetche,⁵⁹ Y. Aramaki,¹⁰ R. Armendariz,⁴⁶ S. H. Aronson,⁵ J. Asai,⁵²
 E. T. Atomssa,³⁴ R. Averbeck,⁵⁸ T. C. Awes,⁴⁷ B. Azmoun,⁵ V. Babintsev,²² M. Bai,⁴ G. Baksay,¹⁸ L. Baksay,¹⁸ A. Baldissari,¹⁴
 K. N. Barish,⁶ P. D. Barnes,³⁶ B. Bassalleck,⁴⁵ A. T. Basye,¹ S. Bathe,⁶ S. Batsouli,^{12,47} V. Baublis,⁵⁰ F. Bauer,⁶ C. Baumann,⁴¹
 A. Bazilevsky,⁵ S. Belikov,^{5,25,*} R. Belmont,⁶³ R. Bennett,⁵⁸ A. Berdnikov,⁵⁴ J. H. Bhom,⁶⁶ A. A. Bickley,¹¹
 M. T. Bjorndal,¹² D. S. Blau,³² J. G. Boissevain,³⁶ J. S. Bok,⁶⁶ H. Borel,¹⁴ N. Borggren,⁵⁷ K. Boyle,⁵⁸ M. L. Brooks,³⁶
 D. S. Brown,⁴⁶ D. Bucher,⁴¹ H. Buesching,⁵ V. Bumazhnov,²² G. Bunce,^{5,52} J. M. Burward-Hoy,³⁶ S. Butsyk,^{36,58}
 S. Campbell,⁵⁸ A. Caringi,⁴² J.-S. Chai,²⁸ B. S. Chang,⁶⁶ J. L. Charvet,¹⁴ C. H. Chen,⁵⁸ S. Chernichenko,²² J. Chiba,²⁹
 C. Y. Chi,¹² M. Chiu,^{5,12,23} I. J. Choi,⁶⁶ J. B. Choi,⁸ R. K. Choudhury,³ P. Christiansen,³⁸ T. Chujo,^{62,63} P. Chung,⁵⁷ A. Churyn,²²
 O. Chvala,⁶ V. Cianciolo,⁴⁷ Z. Citron,⁵⁸ C. R. Cleven,²⁰ Y. Cobigo,¹⁴ B. A. Cole,¹² M. P. Comets,⁴⁸ Z. Conesa del Valle,³⁴
 M. Connors,⁵⁸ P. Constantin,^{25,36} M. Csan  d,¹⁶ T. Cs  rg  ,³⁰ T. Dahms,⁵⁸ S. Dairaku,^{33,51} I. Danchev,⁶³ K. Das,¹⁹ A. Datta,⁴⁰
 G. David,⁵ M. K. Dayananda,²⁰ M. B. Deaton,¹ K. Dehmelt,¹⁸ H. Delagrange,⁵⁹ A. Denisov,²² D. d'Enterria,¹²
 A. Deshpande,^{52,58} E. J. Desmond,⁵ K. V. Dharmawardane,⁴⁶ O. Dietzsch,⁵⁵ A. Dion,^{25,58} M. Donadelli,⁵⁵ L. D'Orazio,³⁹
 J. L. Drachenberg,¹ O. Drapier,³⁴ A. Drees,⁵⁸ K. A. Drees,⁴ A. K. Dubey,⁶⁵ J. M. Durham,⁵⁸ A. Durum,²² D. Dutta,³
 V. Dzhordzhadze,^{6,60} S. Edwards,¹⁹ Y. V. Efremenko,⁴⁷ J. Egdemir,⁵⁸ F. Ellinghaus,¹¹ W. S. Emam,⁶ T. Engelmore,¹²
 A. Enokizono,^{21,35,47} H. En'yo,^{51,52} B. Espagnon,⁴⁸ S. Esumi,⁶² K. O. Eyser,⁶ B. Fadem,⁴² D. E. Fields,^{45,52} M. Finger Jr.,^{7,26}
 M. Finger,^{7,26} F. Fleuret,³⁴ S. L. Fokin,³² B. Forestier,³⁷ Z. Fraenkel,^{65,*} J. E. Frantz,^{12,58} A. Franz,⁵ A. D. Frawley,¹⁹
 K. Fujiwara,⁵¹ Y. Fukao,^{33,51} S. Y. Fung,⁶ T. Fusayasu,⁴⁴ S. Gadrat,³⁷ I. Garishvili,⁶⁰ F. Gastineau,⁵⁹ M. Germain,⁵⁹
 A. Glenn,^{11,35,60} H. Gong,⁵⁸ M. Gonin,³⁴ J. Gosset,¹⁴ Y. Goto,^{51,52} R. Granier de Cassagnac,³⁴ N. Grau,^{12,25} S. V. Greene,⁶³
 G. Grim,³⁶ M. Gross Perdekamp,^{23,52} T. Gunji,¹⁰ H.-Å. Gustafsson,^{38,*} T. Hachiya,^{21,51} A. Hadj Henni,⁵⁹ C. Haegemann,⁴⁵
 J. S. Haggerty,⁵ M. N. Hagiwara,¹ K. I. Hahn,¹⁷ H. Hamagaki,¹⁰ J. Hamblen,⁶⁰ J. Hanks,¹² R. Han,⁴⁹ H. Harada,²¹
 E. P. Hartouni,³⁵ K. Haruna,²¹ M. Harvey,⁵ E. Haslum,³⁸ K. Hasuko,⁵¹ R. Hayano,¹⁰ M. Heffner,³⁵ T. K. Hemmick,⁵⁸ T. Hester,⁶
 J. M. Heuser,⁵¹ X. He,²⁰ H. Hiejima,²³ J. C. Hill,²⁵ R. Hobbs,⁴⁵ M. Hohlmann,¹⁸ M. Holmes,⁶³ W. Holzmann,^{12,57} K. Homma,²¹
 B. Hong,³¹ T. Horaguchi,^{21,51,61} D. Hornback,⁶⁰ S. Huang,⁶³ M. G. Hur,²⁸ T. Ichihara,^{51,52} R. Ichimiya,⁵¹ H. Iinuma,^{33,51}
 Y. Ikeda,⁶² K. Imai,^{33,51} M. Inaba,⁶² Y. Inoue,^{53,51} D. Isenhower,¹ L. Isenhower,¹ M. Ishihara,⁵¹ T. Isobe,¹⁰ M. Issah,^{57,63}
 A. Isupov,²⁶ D. Ivanishev,⁵⁰ Y. Iwanaga,²¹ B. V. Jacak,^{58,†} J. Jia,^{5,12,57} X. Jiang,³⁶ J. Jin,¹² O. Jinnouchi,⁵² B. M. Johnson,⁵
 T. Jones,¹ K. S. Joo,⁴³ D. Jouan,⁴⁸ D. S. Jumper,¹ F. Kajihara,^{10,51} S. Kametani,^{10,64} N. Kamihara,^{51,61} J. Kamin,⁵⁸ M. Kaneta,⁵²
 J. H. Kang,⁶⁶ H. Kanou,^{51,61} J. Kapustinsky,³⁶ K. Karatsu,³³ M. Kasai,^{53,51} T. Kawagishi,⁶² D. Kawall,^{40,52} M. Kawashima,^{53,51}
 A. V. Kazantsev,³² S. Kelly,¹¹ T. Kempel,²⁵ A. Khanzadeev,⁵⁰ K. M. Kijima,²¹ J. Kikuchi,⁶⁴ A. Kim,¹⁷ B. I. Kim,³¹
 D. H. Kim,⁴³ D. J. Kim,^{27,66} E. J. Kim,⁸ E. Kim,⁵⁶ Y.-J. Kim,²³ Y.-S. Kim,²⁸ E. Kinney,¹¹  . Kiss,¹⁶ E. Kistenev,⁵
 A. Kiyomichi,⁵¹ J. Klay,³⁵ C. Klein-Boesing,⁴¹ L. Kochenda,⁵⁰ V. Kochetkov,²² B. Komkov,⁵⁰ M. Konno,⁶² J. Koster,²³
 D. Kotchetkov,⁶ D. Kotov,⁵⁴ A. Kozlov,⁶⁵ A. Kr  l,¹³ A. Kravitz,¹² P. J. Kroon,⁵ J. Kubart,^{7,24} G. J. Kunde,³⁶ N. Kurihara,¹⁰
 K. Kurita,^{53,51} M. Kurosawa,⁵¹ M. J. Kweon,³¹ Y. Kwon,^{60,66} G. S. Kyle,⁴⁶ R. Lacey,⁵⁷ Y. S. Lai,¹² J. G. Lajoie,²⁵ A. Lebedev,²⁵
 Y. Le Bornec,⁴⁸ S. Leckey,⁵⁸ D. M. Lee,³⁶ J. Lee,¹⁷ K. B. Lee,³¹ K. S. Lee,³¹ M. K. Lee,⁶⁶ T. Lee,⁵⁶ M. J. Leitch,³⁶
 M. A. L. Leite,⁵⁵ B. Lenzi,⁵⁵ P. Lichtenwalner,⁴² P. Liebing,⁵² H. Lim,⁵⁶ L. A. Linden Levy,¹¹ T. Li  ka,¹³ A. Litvinenko,²⁶
 H. Liu,³⁶ M. X. Liu,³⁶ X. Li,⁹ X. H. Li,⁶ B. Love,⁶³ D. Lynch,⁵ C. F. Maguire,⁶³ Y. I. Makdisi,^{4,5} A. Malakhov,²⁶ M. D. Malik,⁴⁵
 V. I. Manko,³² E. Mannel,¹² Y. Mao,^{49,51} L. Ma  ek,^{7,24} H. Masui,⁶² F. Matathias,^{12,58} M. C. McCain,²³ M. McCumber,⁵⁸
 P. L. McGaughey,³⁶ N. Means,⁵⁸ B. Meredith,²³ Y. Miake,⁶² T. Mibe,²⁹ A. C. Mignerey,³⁹ P. Mike  ,^{7,24} K. Miki,⁶²
 T. E. Miller,⁶³ A. Milov,^{5,58} S. Mioduszewski,⁵ G. C. Mishra,²⁰ M. Mishra,² J. T. Mitchell,⁵ M. Mitrovski,⁵⁷ A. K. Mohanty,³
 H. J. Moon,⁴³ Y. Morino,¹⁰ A. Morreale,⁶ D. P. Morrison,⁵ J. M. Moss,³⁶ T. V. Moukhanova,³² D. Mukhopadhyay,⁶³
 T. Murakami,³³ J. Murata,^{53,51} S. Nagamiya,²⁹ Y. Nagata,⁶² J. L. Nagle,¹¹ M. Naglis,⁶⁵ M. I. Nagy,³⁰ I. Nakagawa,^{51,52}
 Y. Nakamiya,²¹ K. R. Nakamura,³³ T. Nakamura,^{21,51} K. Nakano,^{51,61} S. Nam,¹⁷ J. Newby,³⁵ M. Nguyen,⁵⁸ M. Nihashi,²¹
 B. E. Norman,³⁶ R. Nouicer,⁵ A. S. Nyanin,³² J. Nystrand,³⁸ C. Oakley,²⁰ E. O'Brien,⁵ S. X. Oda,¹⁰ C. A. Ogilvie,²⁵
 H. Ohnishi,⁵¹ I. D. Ojha,⁶³ K. Okada,⁵² M. Oka,⁶² O. O. Omiwade,¹ Y. Onuki,⁵¹ A. Oskarsson,³⁸ I. Otterlund,³⁸ M. Ouchida,²¹
 K. Ozawa,¹⁰ R. Pak,⁵ D. Pal,⁶³ A. P. T. Palounek,³⁶ V. Pantuev,⁵⁸ V. Papavassiliou,⁴⁶ I. H. Park,¹⁷ J. Park,⁵⁶ S. K. Park,³¹
 W. J. Park,³¹ S. F. Pate,⁴⁶ H. Pei,²⁵ J.-C. Peng,²³ H. Pereira,¹⁴ V. Peresedov,²⁶ D. Yu. Peressounko,³² R. Petti,⁵⁸ C. Pinkenburg,⁵
 R. P. Pisani,⁵ M. Proissl,⁵⁸ M. L. Purschke,⁵ A. K. Purwar,^{36,58} H. Qu,²⁰ J. Rak,^{25,27,45} A. Rakotozafindrabe,³⁴ I. Ravinovich,⁶⁵
 K. F. Read,^{47,60} S. Rembeczki,¹⁸ M. Reuter,⁵⁸ K. Reygers,⁴¹ V. Riabov,⁵⁰ Y. Riabov,⁵⁰ E. Richardson,³⁹ D. Roach,⁶³
 G. Roche,³⁷ S. D. Rolnick,⁶ A. Romana,^{34,*} M. Rosati,²⁵ C. A. Rosen,¹¹ S. S. E. Rosendahl,³⁸ P. Rosnet,³⁷ P. Rukoyatkin,²⁶
 P. Ru   ka,²⁴ V. L. Rykov,⁵¹ S. S. Ryu,⁶⁶ B. Sahlmueller,⁴¹ N. Saito,^{29,33,51} T. Sakaguchi,^{5,10,64} S. Sakai,⁶² K. Sakashita,^{51,61}
 H. Sakata,²¹ V. Samsonov,⁵⁰ S. Sano,^{10,64} H. D. Sato,^{33,51} S. Sato,^{5,29,62} T. Sato,⁶² S. Sawada,²⁹ K. Sedgwick,⁶ J. Seele,¹¹
 R. Seidl,²³ V. Semenov,²² R. Seto,⁶ D. Sharma,⁶⁵ T. K. Shea,⁵ I. Shein,²² A. Shevel,^{50,57} T.-A. Shibata,^{51,61} K. Shigaki,²¹
 M. Shimomura,⁶² T. Shohjoh,⁶² K. Shoji,^{33,51} P. Shukla,³ A. Sickles,^{5,58} C. L. Silva,^{25,55} D. Silvermyr,⁴⁷ C. Silvestre,¹⁴
 K. S. Sim,³¹ B. K. Singh,² C. P. Singh,² V. Singh,² S. Skutnik,²⁵ M. Slune  ka,^{7,26} W. C. Smith,¹ A. Soldatov,²² R. A. Soltz,³⁵
 W. E. Sondheim,³⁶ S. P. Sorensen,⁶⁰ I. V. Sourikova,⁵ F. Staley,¹⁴ P. W. Stankus,⁴⁷ E. Stenlund,³⁸ M. Stepanov,⁴⁶ A. Ster,³⁰

S. P. Stoll,⁵ T. Sugitate,²¹ C. Suire,⁴⁸ A. Sukhanov,⁵ J. P. Sullivan,³⁶ J. Sziklai,³⁰ T. Tabaru,⁵² S. Takagi,⁶² E. M. Takagui,⁵⁵ A. Taketani,^{51,52} R. Tanabe,⁶² K. H. Tanaka,²⁹ Y. Tanaka,⁴⁴ S. Taneja,⁵⁸ K. Tanida,^{33,51,52} M. J. Tannenbaum,⁵ S. Tarafdar,² A. Taranenko,⁵⁷ P. Tarján,¹⁵ H. Themann,⁵⁸ D. Thomas,¹ T. L. Thomas,⁴⁵ M. Togawa,^{33,51,52} A. Toia,⁵⁸ J. Tojo,⁵¹ L. Tomášek,²⁴ H. Torii,^{21,51} R. S. Towell,¹ V.-N. Tram,³⁴ I. Tserruya,⁶⁵ Y. Tsuchimoto,^{21,51} S. K. Tuli,² H. Tydesjö,³⁸ N. Tyurin,²² C. Vale,^{5,25} H. Valle,⁶³ H. W. van Hecke,³⁶ E. Vazquez-Zambrano,¹² A. Veicht,²³ J. Velkovska,⁶³ R. Vértesi,^{15,30} A. A. Vinogradov,³² M. Virius,¹³ V. Vrba,²⁴ E. Vznuzdaev,⁵⁰ M. Wagner,^{33,51} D. Walker,⁵⁸ X. R. Wang,⁴⁶ D. Watanabe,²¹ K. Watanabe,⁶² Y. Watanabe,^{51,52} F. Wei,²⁵ J. Wessels,⁴¹ S. N. White,⁵ N. Willis,⁴⁸ D. Winter,¹² C. L. Woody,⁵ R. M. Wright,¹ M. Wysocki,¹¹ W. Xie,^{6,52} Y. L. Yamaguchi,^{10,64} K. Yamaura,²¹ R. Yang,²³ A. Yanovich,²² Z. Yasin,⁶ J. Ying,²⁰ S. Yokkaichi,^{51,52} G. R. Young,⁴⁷ I. Younus,⁴⁵ Z. You,⁴⁹ I. E. Yushmanov,³² W. A. Zajc,¹² O. Zaudtke,⁴¹ C. Zhang,^{12,47} S. Zhou,⁹ J. Zimányi,^{30,*} and L. Zolin²⁶

(PHENIX Collaboration)

¹Abilene Christian University, Abilene, Texas 79699, USA

²Department of Physics, Banaras Hindu University, Varanasi 221005, India

³Bhabha Atomic Research Centre, Bombay 400 085, India

⁴Collider-Accelerator Department, Brookhaven National Laboratory, Upton, New York 11973-5000, USA

⁵Physics Department, Brookhaven National Laboratory, Upton, New York 11973-5000, USA

⁶University of California-Riverside, Riverside, California 92521, USA

⁷Charles University, Ovocný trh 5, Praha 1, CZ-116 36, Prague, Czech Republic

⁸Chonbuk National University, Jeonju 561-756, Korea

⁹China Institute of Atomic Energy (CIAE), Beijing, People's Republic of China

¹⁰Center for Nuclear Study, Graduate School of Science, University of Tokyo, 7-3-1 Hongo, Bunkyo, Tokyo 113-0033, Japan

¹¹University of Colorado, Boulder, Colorado 80309, USA

¹²Columbia University, New York, New York 10027, USA and Nevis Laboratories, Irvington, New York 10533, USA

¹³Czech Technical University, Zikova 4, CZ-166 36 Prague 6, Czech Republic

¹⁴Dapnia, CEA Saclay, F-91191 Gif-sur-Yvette, France

¹⁵Debrecen University, H-4010 Debrecen, Egyetem tér 1, Hungary

¹⁶ELTE, Eötvös Loránd University, H-1117 Budapest, Pázmány Péter sétány 1/A, Hungary

¹⁷Ewha Womans University, Seoul 120-750, Korea

¹⁸Florida Institute of Technology, Melbourne, Florida 32901, USA

¹⁹Florida State University, Tallahassee, Florida 32306, USA

²⁰Georgia State University, Atlanta, Georgia 30303, USA

²¹Hiroshima University, Kagamiyama, Higashi-Hiroshima 739-8526, Japan

²²IHEP Protvino, State Research Center of Russian Federation, Institute for High Energy Physics, Protvino RU-142281, Russia

²³University of Illinois at Urbana-Champaign, Urbana, Illinois 61801, USA

²⁴Institute of Physics, Academy of Sciences of the Czech Republic, Na Slovance 2, CZ-182 21 Prague 8, Czech Republic

²⁵Iowa State University, Ames, Iowa 50011, USA

²⁶Joint Institute for Nuclear Research, RU-141980 Dubna, Moscow Region, Russia

²⁷Helsinki Institute of Physics, University of Jyväskylä, P. O. Box 35, FI-40014 Jyväskylä, Finland

²⁸KAERI, Cyclotron Application Laboratory, Seoul, Korea

²⁹KEK, High Energy Accelerator Research Organization, Tsukuba, Ibaraki 305-0801, Japan

³⁰KFKI Research Institute for Particle and Nuclear Physics of the Hungarian Academy of Sciences (MTA KFKI RMKI), P. O. Box 49,

H-1525 Budapest 114, Budapest, Hungary

³¹Korea University, Seoul 136-701, Korea

³²Russian Research Center "Kurchatov Institute," Moscow 123098, Russia

³³Kyoto University, Kyoto 606-8502, Japan

³⁴Laboratoire Leprince-Ringuet, Ecole Polytechnique, CNRS-IN2P3, Route de Saclay, F-91128 Palaiseau, France

³⁵Lawrence Livermore National Laboratory, Livermore, California 94550, USA

³⁶Los Alamos National Laboratory, Los Alamos, New Mexico 87545, USA

³⁷LPC, Université Blaise Pascal, CNRS-IN2P3, Clermont-Fd, F-63177 Aubiere Cedex, France

³⁸Department of Physics, Lund University, Box 118, SE-221 00 Lund, Sweden

³⁹University of Maryland, College Park, Maryland 20742, USA

⁴⁰Department of Physics, University of Massachusetts, Amherst, Massachusetts 01003-9337, USA

⁴¹Institut für Kernphysik, University of Muenster, D-48149 Muenster, Germany

⁴²Muhlenberg College, Allentown, Pennsylvania 18104-5586, USA

⁴³Myongji University, Yongin, Kyonggido 449-728, Korea

⁴⁴Nagasaki Institute of Applied Science, Nagasaki-shi, Nagasaki 851-0193, Japan

⁴⁵University of New Mexico, Albuquerque, New Mexico 87131, USA

⁴⁶New Mexico State University, Las Cruces, New Mexico 88003, USA

⁴⁷Oak Ridge National Laboratory, Oak Ridge, Tennessee 37831, USA⁴⁸IPN-Orsay, Université Paris Sud, CNRS-IN2P3, Boîte Postale 1, F-91406 Orsay, France⁴⁹Peking University, Beijing, People's Republic of China⁵⁰PNPI, Petersburg Nuclear Physics Institute, Gatchina, Leningrad region RU-188300, Russia⁵¹RIKEN Nishina Center for Accelerator-Based Science, Wako, Saitama 351-0198, Japan⁵²RIKEN BNL Research Center, Brookhaven National Laboratory, Upton, New York 11973-5000, USA⁵³Department of Physics, Rikkyo University, 3-34-1 Nishi-Ikebukuro, Toshima, Tokyo 171-8501, Japan⁵⁴Saint Petersburg State Polytechnic University, St. Petersburg 195251, Russia⁵⁵Universidade de São Paulo, Instituto de Física, Caixa Postal 66318, São Paulo CEP05315-970, Brazil⁵⁶System Electronics Laboratory, Seoul National University, Seoul, Korea⁵⁷Department of Chemistry, Stony Brook University, Stony Brook, SUNY, New York 11794-3400, USA⁵⁸Department of Physics and Astronomy, Stony Brook University, SUNY, Stony Brook, New York 11794, USA⁵⁹SUBATECH (Ecole des Mines de Nantes, CNRS-IN2P3, Université de Nantes) Boîte Postale, F-44307 Nantes, France⁶⁰University of Tennessee, Knoxville, Tennessee 37996, USA⁶¹Department of Physics, Tokyo Institute of Technology, Oh-okayama, Meguro, Tokyo 152-8551, Japan⁶²Institute of Physics, University of Tsukuba, Tsukuba, Ibaraki 305, Japan⁶³Vanderbilt University, Nashville, Tennessee 37235, USA⁶⁴Advanced Research Institute for Science and Engineering, Waseda University, 17 Kikui-cho, Shinjuku-ku, Tokyo 162-0044, Japan⁶⁵Weizmann Institute, Rehovot 76100, Israel⁶⁶Yonsei University, IPAP, Seoul 120-749, Korea

(Received 20 April 2010; published 18 February 2011)

The PHENIX experiment at the Relativistic Heavy Ion Collider has performed systematic measurements of ϕ meson production in the K^+K^- decay channel at midrapidity in $p + p$, $d + \text{Au}$, $\text{Cu} + \text{Cu}$, and $\text{Au} + \text{Au}$ collisions at $\sqrt{s_{NN}} = 200$ GeV. Results are presented on the ϕ invariant yield and the nuclear modification factor R_{AA} for $\text{Au} + \text{Au}$ and $\text{Cu} + \text{Cu}$, and R_{dA} for $d + \text{Au}$ collisions, studied as a function of transverse momentum ($1 < p_T < 7$ GeV/c) and centrality. In central and midcentral $\text{Au} + \text{Au}$ collisions, the R_{AA} of ϕ exhibits a suppression relative to expectations from binary scaled $p + p$ results. The amount of suppression is smaller than that of the π^0 and the η in the intermediate p_T range (2–5 GeV/c), whereas, at higher p_T , the ϕ , π^0 , and η show similar suppression. The baryon (proton and antiproton) excess observed in central $\text{Au} + \text{Au}$ collisions at intermediate p_T is not observed for the ϕ meson despite the similar masses of the proton and the ϕ . This suggests that the excess is linked to the number of valence quarks in the hadron rather than its mass. The difference gradually disappears with decreasing centrality, and, for peripheral collisions, the R_{AA} values for both particle species are consistent with binary scaling. $\text{Cu} + \text{Cu}$ collisions show the same yield and suppression as $\text{Au} + \text{Au}$ collisions for the same number of N_{part} . The R_{dA} of ϕ shows no evidence for cold nuclear effects within uncertainties.

DOI: 10.1103/PhysRevC.83.024909

PACS number(s): 21.65.Jk, 25.75.Dw

I. INTRODUCTION

Measurements of hadron spectra from $p + p$ and nucleus-nucleus collisions at the Relativistic Heavy Ion Collider (RHIC) provide a means to study the mechanisms of particle production and the properties of the medium formed in relativistic heavy ion collisions. At low transverse momentum $p_T < 2$ GeV/c, where the bulk of particles are produced, hadron production is governed by soft processes characterized by low-momentum transfer. The particle yields and the evolution of the interacting system are successfully described within the framework of thermal and hydrodynamical models [1–5].

At high transverse momentum $p_T > 5$ GeV/c, hard scattering processes become the dominant contribution. Because

of the large momentum transfer involved, the parton-parton scattering cross sections are amenable to perturbative QCD (pQCD) description, and hadron production can be calculated by using initial-state parton distribution functions and final-state fragmentation functions. Modifications to the hadron yields are expected in nucleus-nucleus collisions because of the interaction of the scattered parton with the hot and dense medium formed [6–8]. In the absence of interaction with the medium, the hard scatterings and the resulting hadron yields should scale with the number of binary nucleon-nucleon collisions (N_{coll}), whereas, in the medium, the yields are suppressed (jet quenching [9]) because of parton energy loss through gluon bremsstrahlung. High- p_T hadron suppression consistent with this scenario has been discovered in $\text{Au} + \text{Au}$ collisions at RHIC [10–12]. The same suppression by a factor of ~ 5 is observed for π^0 and η production, whereas, direct photons that do not interact with the medium, follow the expected binary scaling [13]. Single electrons that originate from the semileptonic decays of mesons that contain heavy quarks

^{*}Deceased.

[†]PHENIX spokesperson: jacak@skipper.physics.sunysb.edu

(charm and bottom) exhibit a large suppression at high p_T , similar within the experimental uncertainties to that of π^0 and η , which present a challenge for the bremsstrahlung explanation [14].

At intermediate transverse momentum $2 < p_T$ (GeV/c) < 5 , suppression of binary scaled production is observed for light π^0 and η mesons but not for protons and antiprotons in mid-central and central Au + Au collisions [15]. The p/π and \bar{p}/π ratios increase with centrality and exceed the values measured in $p + p$ by a factor of 3–5 in the most central collisions. A different suppression pattern between baryons and mesons is also observed for strange hadrons Λ and K_S^0 [16,17]. These baryon-meson differences in suppression are inconsistent with the picture of hadron production through hard scattering followed by partonic energy loss in medium and hadronization in vacuum according to the universal fragmentation functions. This poses the question whether hard scattering is the dominant source of baryon production at intermediate p_T . Studies of jet-like dihadron correlations in Au + Au collisions [18,19] imply nearly equal importance of the jet fragmentation as a production mechanism for mesons and baryons, except for the most central collisions. Therefore, the interpretation of the baryon nonsuppression results requires another particle production mechanism in addition to jet fragmentation at intermediate p_T .

There have been attempts to describe the different behavior of baryons and mesons through the strong radial flow that boosts particles with larger mass to higher p_T [20,21], through the recombination of soft and hard massive partons [22–24], through the interplay of the jet-quenched hard component and phenomenological soft-to-moderate p_T baryon junction component [25], or through the QCD color transparency of higher-twist contributions to inclusive hadroproduction cross sections, where baryons are produced directly in a short-distance subprocess [26]. Although several models reproduce p_T spectra, particle ratios, and elliptic flow for different hadrons reasonably well, the relative contributions from the different processes are difficult to infer.

The ϕ meson is a very rich probe of the medium formed in heavy ion collisions because it is sensitive to several aspects of the collision, which include strangeness enhancement and chiral-symmetry restoration as well as energy loss and the nuclear modification factor [27–31], which is the focus of this paper. Due to its small inelastic cross section for interaction with nonstrange hadrons [27,32], the ϕ meson is less affected by late hadronic rescattering and better reflects the initial evolution of the system. By being a meson with a mass comparable to that of the proton, it is interesting to see how the ϕ meson fits within the meson-baryon pattern described previously; by being a pure $s\bar{s}$ state, it puts additional constraints on the energy-loss and recombination models.

This paper presents systematic PHENIX measurements of ϕ meson production via the K^+K^- decay channel at $\sqrt{s_{NN}} = 200$ GeV, which includes the first PHENIX results in $p + p$, $d + \text{Au}$, and $\text{Cu} + \text{Cu}$ collisions and new results in Au + Au collisions. The latter have much higher statistics and a finer centrality binning in comparison to the previously published PHENIX results [28]. The results benefit from three different techniques, which involve different levels of kaon identification in the analyses. These, combined with the high

statistics of the analyzed data samples, allow for the extension of the p_T range of the measurements up to $p_T = 7.0$ GeV/c in all collision systems. The higher p_T reach and the higher precision of the data allow for sharper conclusions with respect to earlier results [28,30]. The Cu + Cu measurements are complementary to those on Au + Au and allow the study of nuclear effects with different nuclear overlap geometry for the same N_{part} and with smaller N_{part} uncertainties for $N_{\text{part}} < 100$.

The measurement of the ϕ meson production in $d + \text{Au}$ collisions is important for understanding cold nuclear matter effects that are of interest by themselves and are also essential for the interpretation of heavy ion collisions. As shown in Ref. [33], in the intermediate p_T range, charged pions practically are not enhanced in comparison to the binary scaled $p + p$ yield, whereas, protons and antiprotons exhibit some enhancement of $\sim 30\%$ in the most central collisions. The mechanism of multiple soft rescattering of partons in the initial state, which is usually invoked as the origin of the Cronin effect, does not explain this meson-baryon difference. One possible explanation comes from recombination models [34] in which baryons gain higher transverse momentum from recombination of three quarks in the final state in comparison to mesons consisting of only two quarks. Measurement of the Cronin effect for the ϕ mesons can provide additional constraints for the models that try to explain these cold nuclear effects.

II. EXPERIMENTAL SETUP AND DATA ANALYSIS

We report on the measurements of ϕ mesons at midrapidity in the K^+K^- decay channel in $p + p$, $d + \text{Au}$, $\text{Cu} + \text{Cu}$, and Au + Au collisions at $\sqrt{s_{NN}} = 200$ GeV by using data collected by the PHENIX experiment during the 2004, 2005, and 2008 physics runs. A detailed description of the PHENIX detector can be found elsewhere [35]. The measurements were performed by using the two PHENIX central arms, each covering 90° in azimuth at midrapidity ($|\eta| < 0.35$). The tracking of charged particles and the measurement of their momentum with typical resolution of $\delta p/p = 0.7 \oplus 1.1\% p$ [GeV/c] are performed by using the drift chambers and the first layer of the pad chambers (PCs). To reduce the background at high p_T , tracks are required to have a matching confirmation in the third layer of the PC or the electromagnetic calorimeter. Kaons are identified by using the time-of-flight (TOF) detector, which covers approximately 1/3 of the acceptance in one of the central arms. With a time resolution of ~ 115 ps, the TOF allows for clear π/K separation in the range of transverse momentum from 0.3 GeV/c to 2.2 GeV/c by using a 2σ p_T -dependent mass-squared selection cut as described in Ref. [28].

The beam-beam counters (BBCs) and zero-degree calorimeters (ZDCs) are dedicated subsystems that determine the collision vertex along the beam axis (z_{vtx}) and the event centrality and also provide the minimum bias interaction trigger. Events are categorized into centrality classes by using two-dimensional cuts in the space of BBC charge versus ZDC energy [36] for Au + Au collisions or only by the amount of charge deposited in the BBC [12,37] for $d + \text{Au}$ and $\text{Cu} + \text{Cu}$ collisions.

In any particular event, one cannot distinguish between kaons from ϕ decays and other kaons, so the ϕ meson yields are

TABLE I. Collision species, number of analyzed minimum bias events, accessible p_T range, and typical range of the SB ratio for the different $\phi \rightarrow K^+K^-$ analyses.

Species	$N [10^9]$	$p_T [\text{GeV}/c]$	SB	Technique
$p + p$	1.50	0.9–4.5	1/9–1/2	One kaon PID
	1.44	1.3–7.0	1/76–1/3	No PID
$d + \text{Au}$	1.69	1.1–7.0	1/245–1/12	No PID
$\text{Cu} + \text{Cu}$	0.77	1.1–2.95	1/91–1/9	One kaon PID
	0.78	1.9–7.0	1/205–1/24	No PID
$\text{Au} + \text{Au}$	0.72	1.1–3.95	1/19–1/2	Two kaons PID
	0.82	2.45–7.0	1/385–1/32	No PID

measured on a statistical basis. In each event, all tracks of opposite charge that pass the selection criteria are paired to form the invariant-mass distribution. This distribution contains both the signal (S) and an inherent combinatorial background (B). To maximize the statistical significance and the reach of the measurements, we use three different track selection techniques: no particle identification (PID) in which all tracks are assigned the kaon mass, but no TOF information is used, and one kaon PID or two kaons PID in which one or both tracks are identified as kaons in the TOF.

Table I lists, for each collision system and for each analysis technique, the number of analyzed minimum bias events in the vertex range $|z_{\text{vtx}}| < 30$ cm, the accessible p_T range, and the range of the signal-to-background (SB) ratio.

The raw yields of the ϕ are obtained by integrating the invariant-mass distributions in a window of ± 9 MeV/c^2 around the ϕ mass after subtracting the combinatorial background. In the analysis of $\text{Au} + \text{Au}$, $\text{Cu} + \text{Cu}$, and $d + \text{Au}$ data, the combinatorial background is estimated by using an event-mixing technique. The details of the method are given elsewhere [28]. In the no PID analysis, a significant residual background remains in the subtracted mass spectra because the mixed-event technique does not account for the abundant correlated pairs from other particle decays ($K_s^0 \rightarrow \pi^+\pi^-$, $\Lambda \rightarrow p\pi^-$, $\rho \rightarrow \pi^+\pi^-$, $\omega \rightarrow \pi^0\pi^+\pi^-$, etc.). In the one kaon PID analysis, the residual background is considerably smaller [38], while in the two kaon PID method, the background is negligible. Examples of subtracted mass spectra obtained in $\text{Au} + \text{Au}$ collisions with the two kaon PID and no PID techniques are shown in Fig. 1. The SB ratio depends on the collision system, the analysis technique, the ϕ transverse momentum, and the centrality. The typical ranges of the SB values for each collision system and each analysis technique are summarized in Table I.

The total combinatorial background in $p + p$ [38] as well as the residual background in $d + \text{Au}$, $\text{Cu} + \text{Cu}$, and $\text{Au} + \text{Au}$ analyses were estimated by fitting the mass spectra with the sum of a Breit-Wigner mass distribution function convolved with a Gaussian experimental mass resolution function to account for the ϕ signal and a polynomial function to account for the background. The typical experimental mass resolution for the ϕ meson was estimated to be ~ 1 MeV/c^2 by using Monte Carlo studies based on the known momentum resolution of the tracking system and time resolution of the TOF. To

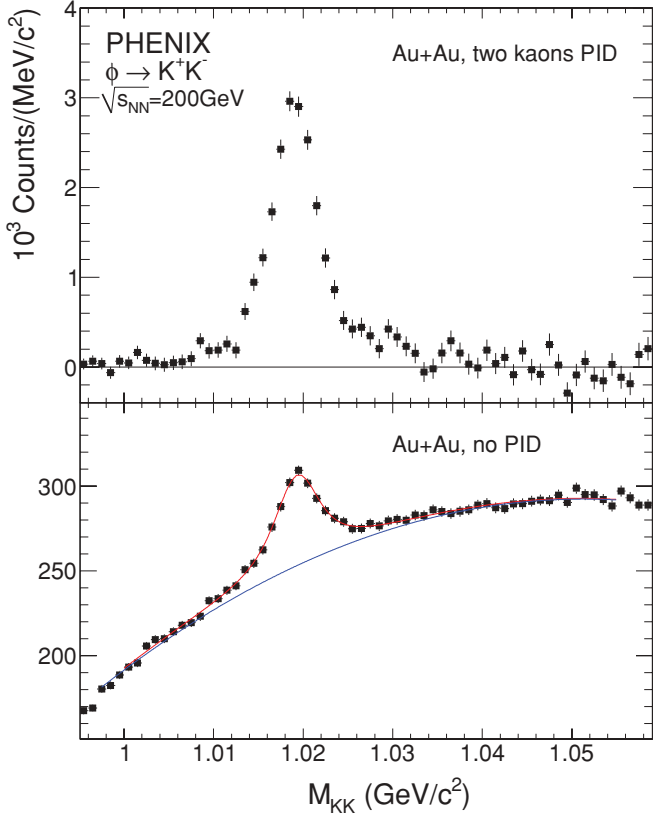


FIG. 1. (Color online) Invariant-mass distributions obtained with the two kaons PID and no PID methods in $\text{Au} + \text{Au}$ collisions after subtraction of the combinatorial background estimated by using the event-mixing technique. The plot on the top corresponds to integrated p_T range, whereas, the plot on the bottom is for the range $2 < p_T (\text{GeV}/c) < 3$. The no PID spectrum is fit to the sum of a Breit-Wigner function convolved with a Gaussian function to account for the ϕ signal and a polynomial function to account for the residual background.

describe the background, a second-order polynomial was used in most analyses, except for the $\text{Au} + \text{Au}$ no PID case where a third-order polynomial was used. Figure 1 shows an example of the fits.

The ϕ meson invariant yield in a given centrality and p_T bin is obtained by

$$\frac{1}{2\pi p_T} \frac{d^2 N}{dp_T dy} = \frac{N_\phi C_{\text{bias}}}{2\pi p_T N_{\text{evt}} \epsilon_{\text{rec}} \epsilon_{\text{embed}} B_{KK} \Delta p_T \Delta y}, \quad (1)$$

where N_{evt} is the number of analyzed events in the centrality bin under consideration, ϵ_{rec} corrects for the limited acceptance of the detector and for the ϕ meson reconstruction efficiency, ϵ_{embed} accounts for the losses in reconstruction efficiency caused by detector occupancy in heavy ion collisions, B_{KK} is the branching ratio for $\phi \rightarrow K^+K^-$ in vacuum, N_ϕ is the raw ϕ yield measured in the given bin, $C_{\text{bias}} = \epsilon_{\text{MB}}^{\text{BBC}} / \epsilon_\phi^{\text{BBC}}$, where $\epsilon_{\text{MB}}^{\text{BBC}}$ and $\epsilon_\phi^{\text{BBC}}$ are the BBC-trigger efficiencies for minimum bias and ϕ events, respectively. This C_{bias} correction is equal to 0.69 for $p + p$ [39] and varies from 0.92 to 0.85 as we go from peripheral to central $d + \text{Au}$ collisions [40]. In $\text{Au} + \text{Au}$ and $\text{Cu} + \text{Cu}$ collisions, the minimum bias trigger

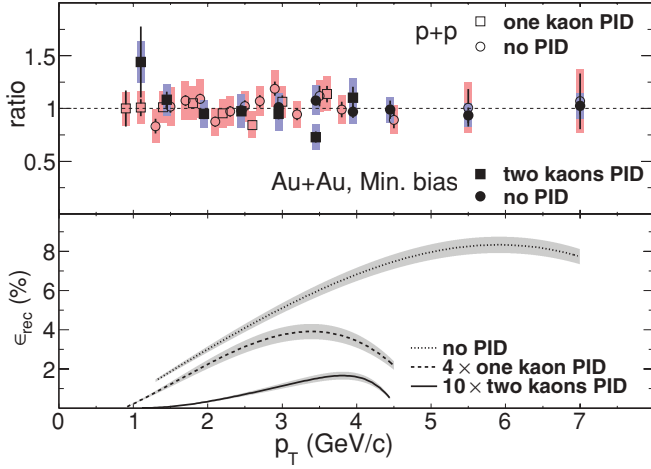


FIG. 2. (Color online) (Top) Ratios of yields obtained with no PID and one kaon PID (in $p + p$ collisions) or no PID and two kaons PID (in Au + Au collisions) to fits to the combined spectra. (Bottom) Comparison of the acceptance and reconstruction efficiencies for the three different analysis techniques.

is inefficient only for very peripheral collisions (centrality > 92.2% for Au + Au and > 94% for Cu + Cu). For all other centralities, 0–92.2% (0–94%) for Au + Au (Cu + Cu), there is no trigger bias, and $C_{bias} = 1$. In $p + p$, the invariant differential cross section at midrapidity is related to invariant yield as $E \frac{d^3\sigma}{dp^3} = \sigma_{pp}^{inel} \times \frac{1}{2\pi p_T} \frac{d^2N}{dp_T dy}$, where $\sigma_{pp}^{inel} = 42.2$ mb.

The bottom panel of Fig. 2 shows the acceptance and reconstruction efficiencies (ϵ_{rec}) of single ϕ mesons, determined by using a full GEANT simulation of the PHENIX detector, which uses different analysis techniques. There are very large differences that reach more than an order of magnitude between the three cases. Despite that, the invariant yield spectra obtained from the different techniques are in good agreement as demonstrated in the top panel of Fig. 2, which shows the ratios of yields obtained with no PID or with one kaon PID (no PID or two kaons PID) techniques in $p + p$ (Au + Au) to a fit performed for the combined data sets. This agreement implies good control over the systematic uncertainties that are quite different in the three cases and provide confidence on the robustness of the experimental results.

The detector occupancy related loss ($1 - \epsilon_{embed}$), which is calculated by embedding simulated K^+K^- pairs into real events, varies from 1% in peripheral to 29% (7%) in the most central Au + Au (Cu + Cu) collisions. No significant p_T dependence of occupancy-induced losses is observed. Consequently, occupancy cannot produce any p_T -dependent uncertainties in R_{AA} . A similar level of detector occupancy related losses in the number of reconstructed ϕ mesons was reported by the STAR experiment [41].

The results from measurements at low p_T , which use two kaons PID (in Au + Au collisions) and one kaon PID (in $p + p$ and Cu + Cu) are combined with the independent no PID measurements at intermediate and high p_T to form the final p_T spectra. The measurement in $d + Au$ is performed by using the no PID technique only. The invariant mass spectra

obtained with one kaon PID or two kaons PID methods are subsamples of the no PID distribution. Therefore, results obtained with different methods cannot be averaged directly. In the final spectra, the transition between different techniques occurs at $p_T = 1.3$ GeV/c in $p + p$, $p_T = 2.2$ GeV/c in Au + Au, and at $p_T = 3.2$ GeV/c in Cu + Cu collisions to obtain the smallest combined statistical and systematical uncertainties for the points.

Systematic uncertainties on the ϕ invariant yield are grouped into three categories: type A (point-to-point uncorrelated), which can move each point independently; type B (point-to-point p_T correlated), which can move points coherently, but not necessarily by the same relative amount; type C (global), which move all points by the same relative amount. The main contribution to the systematic errors of type A is the uncertainty in the raw yield extraction N_ϕ of 6%–25%. The error of type B is dominated by uncertainties in reconstruction efficiency ϵ_{rec} of 5%–9%, embedding corrections ϵ_{embed} of 1%–7%, and momentum scale of 1%–5%. The main contributions to the type C errors are the uncertainties in normalization for the $p + p$ ($d + Au$) cross section equal to 9.7% (7.8%) and in branching ratio B_{KK} of 1.2%.

III. RESULTS AND DISCUSSION

Figure 3 shows the fully corrected ϕ invariant yield as a function of p_T measured in $p + p$, $d + Au$, Cu + Cu, and Au + Au collisions at $\sqrt{s_{NN}} = 200$ GeV. The spectra are scaled by arbitrary factors for clarity and are fitted to exponential and Tsallis [42–44] functions shown by the dashed and solid lines, respectively. We used the Tsallis function adapted to the form [38]

$$\frac{1}{2\pi} \frac{d^2N}{dy dp_T} = \frac{1}{2\pi} \frac{dN}{dy} \frac{(n-1)(n-2)}{[nT + m_\phi(n-1)](nT + m_\phi)} \times \left(\frac{nT + m_T}{nT + m_\phi} \right)^{-n}, \quad (2)$$

where $\frac{dN}{dy}$, n , and T are free parameters, $m_T = \sqrt{p_T^2 + m_\phi^2}$, and m_ϕ is the mass of the ϕ meson. The spectral shapes for all collision systems and centralities are well described by the Tsallis function, while the exponential fits underestimate the ϕ meson yields at high p_T where the spectra begin to exhibit the power-law behavior expected for particles produced in hard scattering processes. For $p + p$ collisions, the departure from exponential shape occurs at ≈ 4 GeV/c. For all centralities in Au + Au collisions, the departure occurs at somewhat larger p_T , which suggests a larger contribution of soft processes to the ϕ meson production up to 4 to 5 GeV/c. Such behavior of the spectral shapes is in agreement with recombination models [22–24,45–47] predicting p_T spectra for different hadronic species based on the number and flavor of their valence quarks. At low transverse momentum, we do not observe a large change in the slopes of the spectra from central to peripheral collisions, supporting the expectation for smaller radial flow of ϕ mesons compared to other hadrons.

The large p_T reach of the results presented here allows for the study of medium-induced effects on ϕ meson production

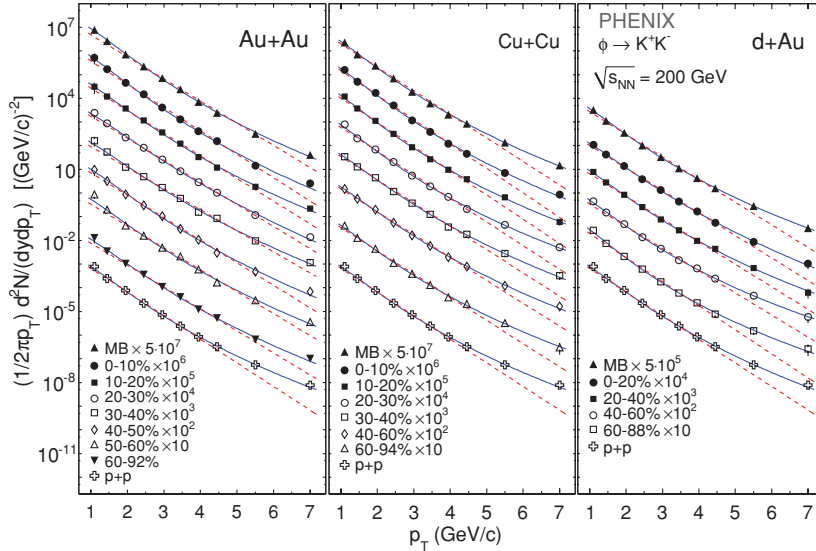


FIG. 3. (Color online) Invariant p_T spectra of the ϕ meson for different centrality bins in Au + Au, Cu + Cu, d + Au, and p + p collisions at $\sqrt{s_{NN}} = 200$ GeV. The statistical and systematic uncertainties are smaller than the size of the symbols. The spectra are fitted to exponential and Tsallis [42–44] functions shown by the dashed and solid lines, respectively.

at intermediate and high p_T by using the nuclear modification factor:

$$R_{AB}(\cdot) = dN_{AB}/(\langle N_{\text{coll}} \rangle \times dN_{pp}), \quad (3)$$

where dN_{AB} (dN_{pp}) is the differential ϕ yield in nucleus-nucleus (p + p) collisions and $\langle N_{\text{coll}} \rangle$ is the average number of nuclear collisions in the centrality bin under consideration [11,12,33]. The latter is determined solely by the density distribution of the nucleons in the nuclei A and B and by the impact parameter and is calculated using the Glauber formalism [48]. Deviation of R_{AB} from unity quantifies the degree of departure of the A + B yields from a superposition of incoherent nucleon-nucleon collisions.

Figure 4 shows a comparison of the R_{AA} for ϕ and π^0 from Ref. [50], proton and kaon from Ref. [33], and η from Ref. [51], all measured in Au + Au collisions at $\sqrt{s_{NN}} = 200$ GeV. The ϕ meson exhibits a different suppression pattern than that of lighter nonstrange mesons and baryons. For central collisions (top panel), the ϕ 's R_{AA} shows less suppression than π^0 and η in the intermediate p_T range of $2 < p_T (\text{GeV}/c) < 5$. At higher p_T values, $p_T > 5 \text{ GeV}/c$, the ϕ 's R_{AA} approaches and becomes comparable to the π^0 and η R_{AA} . These two features remain true for all centralities up to the most peripheral collisions as displayed in the bottom panel of Fig. 4 (see also Fig. 5). The panel shows that the π^0 is slightly suppressed (at the level of $\sim 20\%$) in peripheral Au + Au collisions, whereas, the ϕ is not suppressed. The kaon data cover only a very limited range at low p_T , but in this range, they seem to follow the R_{AA} trend of the ϕ better than that of the π^0 and η for central Au + Au collisions. The comparison with baryons, represented in Fig. 4 by the protons and antiprotons, shows a different pattern. For central collisions, the protons show no suppression but rather an enhancement at $p_T > 1.5 \text{ GeV}/c$, whereas, the ϕ mesons are suppressed. This difference between ϕ mesons and protons gradually disappears with decreasing centrality, and for the most peripheral collisions, the R_{AA} of ϕ and (anti)protons are very similar as demonstrated in the bottom panel.

The results presented here are in agreement with the previous PHENIX results [28], which were based on the

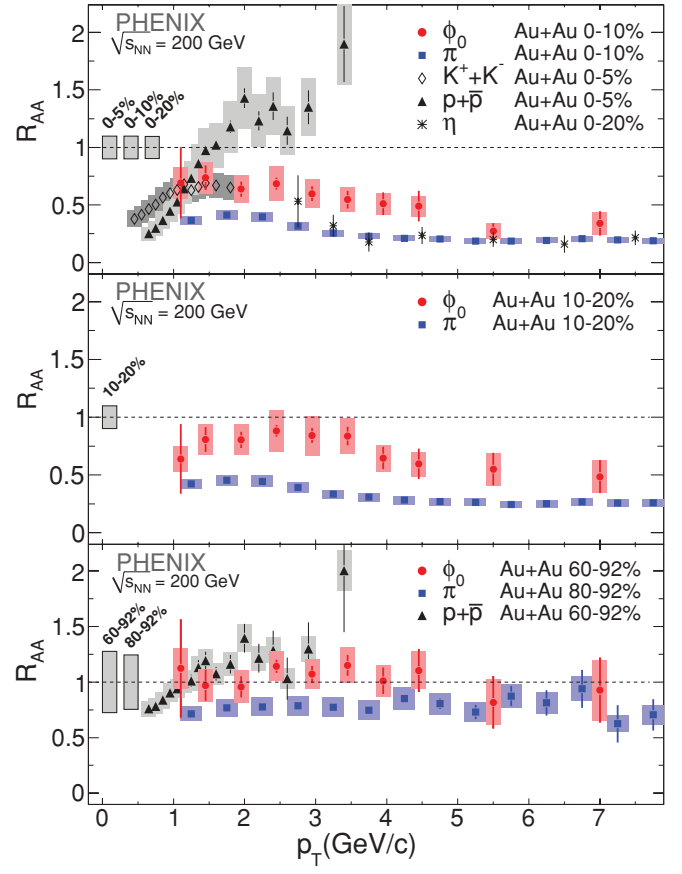


FIG. 4. (Color online) (Top) R_{AA} versus p_T for ϕ , π^0 , η , $(K^+ + K^-)$, and $(p + \bar{p})$ in central Au + Au collisions. (Middle) R_{AA} versus p_T for ϕ and π^0 in 10%-20% midcentral Au + Au collisions. (Bottom) R_{AA} versus p_T for ϕ , and $p + \bar{p}$ in 60%-92% and for π^0 in 80%-92% peripheral Au + Au collisions. Values for $(K^+ + K^-)$, $(p + \bar{p})$, π^0 , and η are from Refs. [12,33,49–51]. The uncertainty in the determination of $\langle N_{\text{coll}} \rangle$ is shown as a box on the left. The global uncertainty of $\sim 10\%$ related to the p + p reference normalization is not shown.

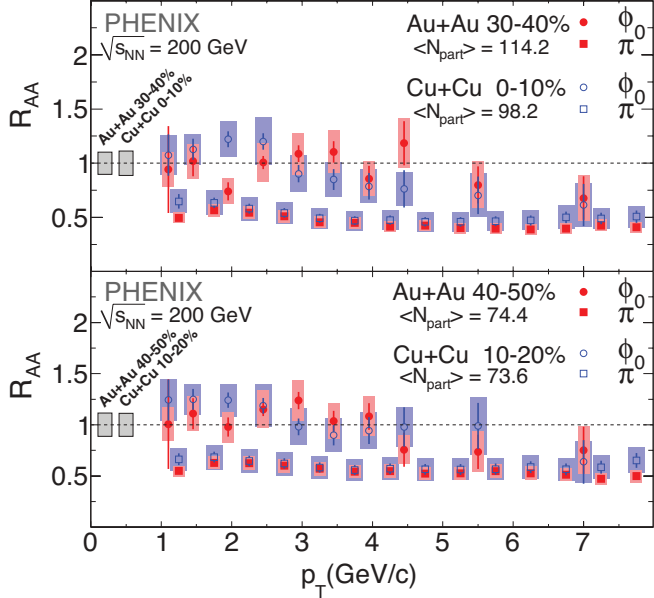


FIG. 5. (Color online) (Top) R_{AA} versus p_T for ϕ and π^0 for 30%–40% centrality Au + Au and 0%–10% centrality Cu + Cu collisions. (Bottom) R_{AA} versus p_T for ϕ and π^0 for 40%–50% centrality Au + Au and 10%–20% centrality Cu + Cu collisions. Values for π^0 are from Refs. [12,50]. The uncertainty in the determination of $\langle N_{coll} \rangle$ is shown as a box on the left. The global uncertainty of $\sim 10\%$ related to the $p + p$ reference normalization is not shown.

2002 RHIC run within the relatively larger uncertainties of the latter. The use of different analysis techniques and the larger Au + Au data sample of the 2004 run resulted in a higher precision and a larger p_T reach of R_{AA} that allowed for unveiling the different behavior of the ϕ meson (i.e., less suppression than π^0 but more suppression than baryons) in the intermediate p_T range. Our results differ from the ones recently published by the STAR Collaboration [29,30], which show that, in Au + Au collisions, R_{AA} is consistent with binary scaling in the intermediate p_T region, whereas, R_{CP} shows considerable suppression. This difference is traced down to the almost factor of 2 higher invariant p_T yield in the STAR experiment [29,30] in Au + Au collisions, compared to our results presented in Fig. 3, whereas, in $p + p$, both experiments are in reasonably good agreement.

Figure 5 compares the R_{AA} of ϕ in Au + Au and Cu + Cu in two centrality bins, which approximately correspond to the same number of participants in the two systems. Figure 6 shows the R_{AA} of the ϕ integrated for $p_T > 2.2 \text{ GeV}/c$ in Cu + Cu and Au + Au collisions versus N_{part} . Under these conditions, there is no difference in the R_{AA} of ϕ between the two systems, which indicates that the level of the suppression, when averaged over the azimuthal angle, scales with the average size of the nuclear overlap, regardless of the details of its shape. This behavior has been observed in other measurements, such as the R_{AA} of the π^0 . The π^0 suppression data in Au + Au and Cu + Cu taken from Refs. [12,50] are also shown in Fig. 5 for comparison. The similarity of the R_{AA} of ϕ in the two colliding systems implies that the features discussed previously for Au + Au in the context of Fig. 4, namely, that

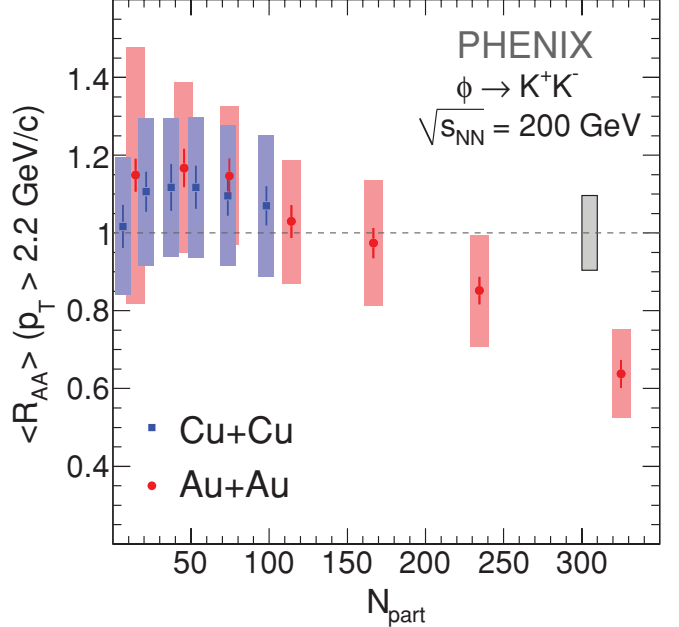


FIG. 6. (Color online) R_{AA} for ϕ integrated at $p_T > 2.2 \text{ GeV}/c$ in Cu + Cu and Au + Au collisions versus N_{part} . The global uncertainty related to the $p + p$ reference normalization is shown as a box on the right.

the ϕ exhibits an intermediate suppression between pions and baryons, also remain valid in the Cu + Cu system.

Our data disfavor radial flow as the dominant source for the particle species dependence of the suppression factors at intermediate p_T because the proton and ϕ R_{AA} factors differ by a factor of ~ 2 , despite their similar mass ($m_p \simeq m_\phi$), whereas, the kaon and ϕ show similar R_{AA} factors, although their masses differ by almost a factor of 2 ($m_\phi \simeq 2m_K$).

Recombination models [22–24,45–47] qualitatively explain the larger yield of baryons compared to mesons at intermediate p_T by the higher gain in p_T that comes from recombination of three quarks for baryons rather than two quarks for mesons. The same framework can be used to interpret the difference in suppression factors for π^0 and ϕ mesons. For π^0 production in the Hwa and Yang model [47], the contribution from the recombination of thermal (T) and shower (S) partons becomes comparable to that of the recombination of $T T$ partons already at $p_T \approx 3 \text{ GeV}/c$. For the ϕ , however, the strangeness enhancement preferentially feeds the thermal partons. Soft processes dominate over hard processes in a wider p_T range, and consequently, the $T T$ component remains dominant up to $p_T \approx 6 \text{ GeV}/c$ for the ϕ production [46]. The R_{AA} of ϕ becomes similar to that for π^0 at $p_T > 5$ to $6 \text{ GeV}/c$ where the contribution from fragmentation partons becomes significant for both particles. It is interesting to note that the η closely follows the π^0 despite its sizable ($\sim 50\%$) strangeness content [52].

Cold nuclear matter effects can also contribute to the differences in hadron suppression factors in A + A collisions. Figure 7 compares the R_{dA} for ϕ and π^0 from Ref. [49] and protons from Ref. [33] for central (top panel) and peripheral (bottom panel) $d + Au$ collisions. For both centralities, the

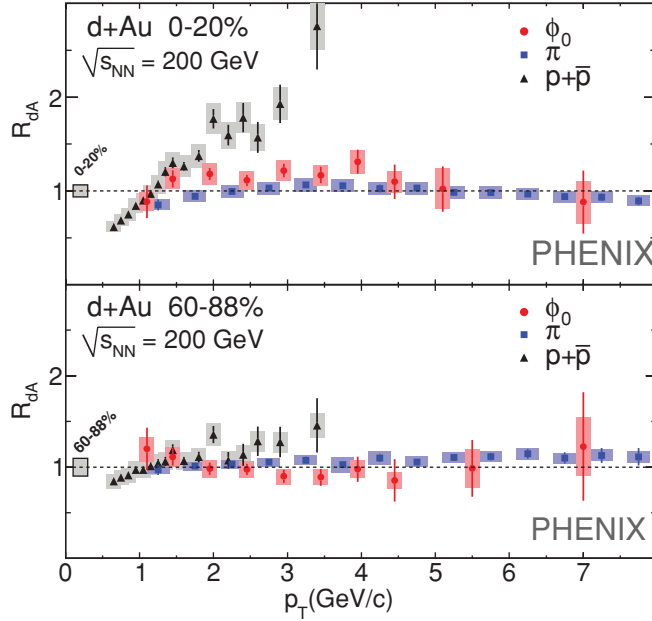


FIG. 7. (Color online) (Top) R_{dA} versus p_T for ϕ , π^0 and $(p + \bar{p})$ for 0%–20% centrality $d + \text{Au}$ collisions. (Bottom) R_{dA} versus p_T for ϕ , π^0 and $(p + \bar{p})$ for 60%–88% peripheral $d + \text{Au}$ collisions. Values for $(K^+ + K^-)$ and $(p + \bar{p})$ and π^0 are from Refs. [33,49]. The uncertainty in the determination of $\langle N_{\text{coll}} \rangle$ is shown as a box on the left. The global uncertainty of $\sim 10\%$ related to the $p + p$ reference normalization is not shown.

R_{dA} for ϕ and π^0 are similar, which indicates that cold nuclear effects are not responsible for the differences between ϕ and π^0 seen in $\text{Au} + \text{Au}$ and $\text{Cu} + \text{Cu}$ collisions. The proton's R_{dA} exhibits an enhancement for $p_T = 2$ –4 GeV/c , usually associated with the Cronin effect [53–58], whereas, the R_{dA} for ϕ indicates little or no enhancement. The lack of Cronin enhancement is also seen in the π^0 data [49] shown in Fig. 7 and has also been observed for other mesons in central and midcentral $d + \text{Au}$ collisions at $\sqrt{s_{NN}} = 200 \text{ GeV}$ [33,59,60].

IV. SUMMARY AND CONCLUSIONS

We have measured ϕ meson production at midrapidity via the K^+K^- decay channel in $p + p$, $d + \text{Au}$, $\text{Cu} + \text{Cu}$, and $\text{Au} + \text{Au}$ collisions at $\sqrt{s_{NN}} = 200 \text{ GeV}$. Invariant p_T spectra and nuclear modification factors have been presented over the p_T range of $1 < p_T < 7 \text{ GeV}/c$ for different centralities.

The ϕ meson exhibits a different suppression pattern compared to lighter mesons (π^0 and η) and baryons (protons and antiprotons) in heavy ion collisions. For all centralities, the ϕ meson is less suppressed than π^0 and η in the intermediate p_T range (2–5 GeV/c), whereas, at higher p_T , ϕ , π^0 , and η show similar suppression values. The available kaon R_{AA} data seem to follow the R_{AA} trend of the ϕ . The comparison with baryons shows that, in central $\text{Au} + \text{Au}$ collisions, the latter are enhanced with respect to binary scaling, whereas, the ϕ meson is suppressed, but this difference gradually disappears with decreasing centrality, and for peripheral collisions, the

baryons and the ϕ meson have very similar R_{AA} values consistent with binary scaling.

The same features are observed in $\text{Cu} + \text{Cu}$ collisions between the ϕ and π^0 . The ϕ meson invariant p_T spectra in $\text{Au} + \text{Au}$ and $\text{Cu} + \text{Cu}$ collisions for similar N_{part} values exhibit similar shape and yield over the entire p_T range of the measurement within the statistical and systematic uncertainties. This indicates that the production and suppression of the ϕ meson, when averaged over the azimuthal angle, scales with the average size of the nuclear overlap region, regardless of the details of its shape.

Cold nuclear effects cannot account for the observed differences. For all centralities, the ϕ 's R_{dA} in $d + \text{Au}$ collisions is consistent with binary scaling in agreement with other mesons. No meson species dependence is observed in R_{dA} within uncertainties.

The observed features at intermediate p_T in $\text{Au} + \text{Au}$ and $\text{Cu} + \text{Cu}$ collisions are qualitatively consistent with quark recombination models [22–24,45–47], which are also supported by ϕ elliptic flow measurements [29,31]. The systematic set of measurements presented here provides further constraints for these models. The similarity between the suppression patterns of different mesons at high p_T favors the production of these mesons via jet fragmentation outside the hot and dense medium created in the collision. Complementary jet correlation measurements, which involve ϕ mesons as a trigger as well as extension of the kaon data to higher p_T would be desirable to provide further insight into the ϕ meson production mechanism.

ACKNOWLEDGMENTS

We thank the staff of the Collider-Accelerator and Physics Departments at Brookhaven National Laboratory and the staff of the other PHENIX participating institutions for their vital contributions. We acknowledge support from the Office of Nuclear Physics in the Office of Science of the Department of Energy, the National Science Foundation, Abilene Christian University Research Council, Research Foundation of SUNY, and Dean of the College of Arts and Sciences, Vanderbilt University (USA), Ministry of Education, Culture, Sports, Science, and Technology and the Japan Society for the Promotion of Science (Japan), Conselho Nacional de Desenvolvimento Científico e Tecnológico and Fundação de Amparo à Pesquisa do Estado de São Paulo (Brazil), Natural Science Foundation of China (People's Republic of China), Ministry of Education, Youth and Sports (Czech Republic), Centre National de la Recherche Scientifique, Commissariat à l'Énergie Atomique, and Institut National de Physique Nucléaire et de Physique des Particules (France), Ministry of Industry, Science and Tekhnologies, Bundesministerium für Bildung und Forschung, Deutscher Akademischer Austausch Dienst, and Alexander von Humboldt Stiftung (Germany), Hungarian National Science Fund, OTKA (Hungary), Department of Atomic Energy and Department of Science and Technology (India), Israel Science Foundation (Israel), National Research Foundation (Korea), Ministry of Education and Science,

Russia Academy of Sciences, Federal Agency of Atomic Energy (Russia), VR and the Wallenberg Foundation (Sweden), the US Civilian Research and Development Foundation for

the Independent States of the Former Soviet Union, the US-Hungarian Fulbright Foundation for Educational Exchange, and the US-Israel Binational Science Foundation.

-
- [1] P. Braun-Munzinger *et al.*, Invited review for *Quark-Gluon Plasma*, edited by R. C. Hwa and X.-N. Wang (World Scientific, Singapore, 2003), Vol. 3, p. 491.
- [2] K. Adcox *et al.* (PHENIX Collaboration), *Nucl. Phys. A* **757**, 184 (2005).
- [3] P. F. Kolb and U. W. Heinz, Invited review for *Quark-Gluon Plasma*, edited by R. C. Hwa and X.-N. Wang (World Scientific, Singapore, 2003), Vol. 3, p. 634.
- [4] B. Muller and J. L. Nagle, *Ann. Rev. Nucl. Part. Sci.* **56**, 93 (2006).
- [5] P. Huovinen and P. Ruuskanen, *Ann. Rev. Nucl. Part. Sci.* **56**, 163 (2006).
- [6] M. Gyulassy *et al.*, *Phys. Lett. B* **243**, 432 (1990).
- [7] R. Baier *et al.*, *Nucl. Phys. B* **484**, 265 (1997).
- [8] M. Gyulassy *et al.*, *Nucl. Phys. B* **420**, 583 (1994).
- [9] D. d'Enterria (2009), arXiv:0902.2011 [nucl-ex].
- [10] K. Adcox *et al.* (PHENIX Collaboration), *Phys. Rev. Lett.* **88**, 022301 (2001).
- [11] S. S. Adler *et al.* (PHENIX Collaboration), *Phys. Rev. Lett.* **91**, 072301 (2003).
- [12] A. Adare *et al.* (PHENIX Collaboration), *Phys. Rev. Lett.* **101**, 162301 (2008).
- [13] S. S. Adler *et al.* (PHENIX Collaboration), *Phys. Rev. Lett.* **94**, 232301 (2005).
- [14] A. Adare *et al.* (PHENIX Collaboration), *Phys. Rev. Lett.* **98**, 172301 (2007).
- [15] S. S. Adler *et al.* (PHENIX Collaboration), *Phys. Rev. Lett.* **91**, 172301 (2003).
- [16] J. Adams *et al.* (STAR Collaboration), *Phys. Rev. Lett.* **92**, 052302 (2004).
- [17] J. Adams *et al.* (STAR Collaboration), *Phys. Rev. C* **71**, 064902 (2005).
- [18] S. S. Adler *et al.* (PHENIX Collaboration), *Phys. Rev. C* **71**, 051902 (2005).
- [19] A. Adare *et al.* (PHENIX Collaboration), *Phys. Lett. B* **649**, 359 (2007).
- [20] T. Hirano and Y. Nara, *Phys. Rev. C* **69**, 034908 (2004).
- [21] U. W. Heinz *et al.*, *Nucl. Phys. A* **702**, 269 (2002).
- [22] V. Greco, C. M. Ko, and P. Levai, *Phys. Rev. Lett.* **90**, 202302 (2003).
- [23] R. C. Hwa and C. B. Yang, *Phys. Rev. C* **67**, 034902 (2003).
- [24] R. J. Fries, B. Muller, C. Nonaka, and S. A. Bass, *Phys. Rev. Lett.* **90**, 202303 (2003).
- [25] I. Vitev and M. Gyulassy, *Phys. Rev. C* **65**, 041902 (2002).
- [26] S. J. Brodsky and A. Sickles, *Phys. Lett. B* **668**, 111 (2008).
- [27] A. Shor, *Phys. Rev. Lett.* **54**, 1122 (1985).
- [28] S. S. Adler *et al.* (PHENIX Collaboration), *Phys. Rev. C* **72**, 014903 (2005).
- [29] B. Abelev *et al.* (STAR Collaboration), *Phys. Rev. Lett.* **99**, 112301 (2007).
- [30] B. Abelev *et al.* (STAR Collaboration), *Phys. Lett. B* **673**, 183 (2009).
- [31] S. Afanasiev *et al.* (PHENIX Collaboration), *Phys. Rev. Lett.* **99**, 052301 (2007).
- [32] C. M. Ko and D. Seibert, *Phys. Rev. C* **49**, 2198 (1994).
- [33] S. S. Adler *et al.* (PHENIX Collaboration), *Phys. Rev. C* **74**, 024904 (2006).
- [34] R. C. Hwa and C. B. Yang, *Phys. Rev. Lett.* **93**, 082302 (2004).
- [35] K. Adcox *et al.* (PHENIX Collaboration), *Nucl. Instrum. Methods Phys. Res. A* **499**, 469 (2003).
- [36] K. Adcox *et al.* (PHENIX Collaboration), *Phys. Rev. C* **69**, 024904 (2004).
- [37] S. S. Adler *et al.* (PHENIX Collaboration), *Phys. Rev. Lett.* **94**, 082302 (2005).
- [38] S. S. Adler *et al.* (PHENIX Collaboration), arXiv:1005.3674 [hep-ex].
- [39] S. S. Adler *et al.* (PHENIX Collaboration), *Phys. Rev. Lett.* **98**, 172302 (2007).
- [40] S. S. Adler *et al.* (PHENIX Collaboration), *Phys. Rev. Lett.* **96**, 012304 (2006).
- [41] B. I. Abelev *et al.* (STAR Collaboration), *Phys. Rev. C* **79**, 064903 (2009).
- [42] C. Tsallis, *J. Stat. Phys.* **52**, 479 (1988).
- [43] C. Tsallis, *Braz. J. Phys.* **29**, 1 (1999).
- [44] G. Wilk and Z. Włodarczyk, *Phys. Rev. Lett.* **84**, 2770 (2000).
- [45] R. J. Fries, B. Muller, C. Nonaka, and S. A. Bass, *Phys. Rev. C* **68**, 044902 (2003).
- [46] R. C. Hwa and C. Yang, arXiv:nucl-th/0602024.
- [47] R. C. Hwa and C. B. Yang, *Phys. Rev. C* **70**, 024905 (2004).
- [48] M. L. Miller *et al.*, *Ann. Rev. Nucl. Part. Sci.* **57**, 205 (2007).
- [49] S. S. Adler *et al.* (PHENIX Collaboration), *Phys. Rev. Lett.* **98**, 172302 (2007).
- [50] A. Adare *et al.* (PHENIX Collaboration), *Phys. Rev. Lett.* **101**, 232301 (2008).
- [51] S. S. Adler *et al.* (PHENIX Collaboration), *Phys. Rev. Lett.* **96**, 202301 (2006).
- [52] V. Uvarov, *Phys. Lett. B* **511**, 136 (2001); arXiv:hep-ph/0105185.
- [53] J. W. Cronin *et al.*, *Phys. Rev. Lett.* **31**, 1426 (1973).
- [54] J. W. Cronin *et al.*, *Phys. Rev. D* **11**, 3105 (1975).
- [55] D. Antreasyan, J. W. Cronin, H. J. Frisch, M. J. Shochet, L. Kluberg, P. A. Piroué, and R. L. Sumner, *Phys. Rev. D* **19**, 764 (1979).
- [56] P. B. Straub *et al.*, *Phys. Rev. Lett.* **68**, 452 (1992).
- [57] P. B. Straub *et al.*, *Phys. Rev. D* **45**, 3030 (1992).
- [58] A. Accardi *et al.*, *Phys. Lett. B* **586**, 244 (2004).
- [59] J. Adams *et al.* (STAR Collaboration), *Phys. Lett. B* **616**, 8 (2005).
- [60] J. Adams *et al.* (STAR Collaboration), *Phys. Lett. B* **637**, 161 (2006).

Identified charged hadron production in $p + p$ collisions at $\sqrt{s} = 200$ and 62.4 GeV

- A. Adare,¹¹ S. Afanasiev,²⁶ C. Aidala,^{12,37} N. N. Ajitanand,⁵⁴ Y. Akiba,^{48,49} H. Al-Bataineh,⁴³ J. Alexander,⁵⁴ K. Aoki,^{31,48} L. Aphecetche,⁵⁶ R. Armendariz,⁴³ S. H. Aronson,⁶ J. Asai,^{48,49} E. T. Atomssa,³² R. Averbeck,⁵⁵ T. C. Awes,⁴⁴ B. Azmoun,⁶ V. Babintsev,²¹ M. Bai,⁵ G. Baksay,¹⁷ L. Baksay,¹⁷ A. Baldissari,¹⁴ K. N. Barish,⁷ P. D. Barnes,^{34,*} B. Bassalleck,⁴² A. T. Basye,¹ S. Bathe,⁷ S. Batsouli,⁴⁴ V. Baublis,⁴⁷ C. Baumann,³⁸ A. Bazilevsky,⁶ S. Belikov,^{6,*} R. Bennett,⁵⁵ A. Berdnikov,⁵¹ Y. Berdnikov,⁵¹ A. A. Bickley,¹¹ J. G. Boissevain,³⁴ H. Borel,¹⁴ K. Boyle,⁵⁵ M. L. Brooks,³² H. Buesching,⁶ V. Bumazhnov,²¹ G. Bunce,^{6,49} S. Butsyk,^{34,55} C. M. Camacho,³⁴ S. Campbell,⁵⁵ B. S. Chang,⁶³ W. C. Chang,² J.-L. Charvet,¹⁴ S. Chernichenko,²¹ J. Chiba,²⁷ C. Y. Chi,¹² M. Chiu,²² I. J. Choi,⁶³ R. K. Choudhury,⁴ T. Chujo,^{59,60} P. Chung,⁵⁴ A. Churyn,²¹ V. Cianciolo,⁴⁴ Z. Citron,⁵⁵ C. R. Cleven,¹⁹ B. A. Cole,¹² M. P. Comets,⁴⁵ P. Constantin,³⁴ M. Csand,¹⁶ T. Csorgo,²⁸ T. Dahms,⁵⁵ S. Dairaku,^{31,48} K. Das,¹⁸ G. David,⁶ M. B. Deaton,¹ K. Dehmelt,¹⁷ H. Delagrange,⁵⁶ A. Denisov,²¹ D. d'Enterria,^{12,32} A. Deshpande,^{49,55} E. J. Desmond,⁶ O. Dietzsch,⁵² A. Dion,⁵⁵ M. Donadelli,⁵² O. Drapier,³² A. Drees,⁵⁵ K. A. Drees,⁵ A. K. Dubey,⁶² A. Durum,²¹ D. Dutta,⁴ V. Dzhordzhadze,⁷ Y. V. Efremenko,⁴⁴ J. Egdemir,⁵⁵ F. Ellinghaus,¹¹ W. S. Emam,⁷ T. Engelmore,¹² A. Enokizono,³³ H. En'yo,^{48,49} S. Esumi,⁵⁹ K. O. Eyser,⁷ B. Fadem,³⁹ D. E. Fields,^{42,49} M. Finger Jr.,^{8,26} M. Finger,^{8,26} F. Fleuret,³² S. L. Fokin,³⁰ Z. Fraenkel,^{62,*} J. E. Frantz,⁵⁵ A. Franz,⁶ A. D. Frawley,¹⁸ K. Fujiwara,⁴⁸ Y. Fukao,^{31,47} T. Fusayasu,⁴¹ S. Gadrat,³³ I. Garishvili,⁵⁷ A. Glenn,¹¹ H. Gong,⁵⁵ M. Gonin,³² J. Gosset,¹⁴ Y. Goto,^{48,49} R. Granier de Cassagnac,³² N. Grau,^{12,25} S. V. Greene,⁶⁰ M. Grosse Perdekamp,^{22,49} T. Gunji,¹⁰ H.-A. Gustafsson,^{36,*} T. Hachiya,²⁰ A. Hadj Henni,⁵⁶ C. Haegemann,⁴² J. S. Haggerty,⁶ H. Hamagaki,¹⁰ R. Han,⁴⁶ H. Harada,²⁰ E. P. Hartouni,³³ K. Haruna,²⁰ E. Haslum,³⁶ R. Hayano,¹⁰ M. Heffner,³³ T. K. Hemmick,⁵⁵ T. Hester,⁷ X. He,¹⁹ H. Hiejima,²² J. C. Hill,²⁵ R. Hobbs,⁴¹ M. Hohlmann,¹⁷ W. Holzmann,⁵⁴ K. Homma,²⁰ B. Hong,²⁹ T. Horaguchi,^{10,48,58} D. Hornback,⁵⁷ S. Huang,⁶⁰ T. Ichihara,^{48,49} R. Ichimiya,⁴⁸ H. Iinuma,^{31,48} Y. Ikeda,⁵⁹ K. Imai,^{31,48} J. Imrek,¹⁵ M. Inaba,⁵⁹ Y. Inoue,^{50,48} D. Isenhower,¹ L. Isenhower,¹ M. Ishihara,⁴⁸ T. Isobe,¹⁰ M. Issah,⁵⁴ A. Isupov,²⁶ D. Ivanischev,⁴⁷ B. V. Jacak,^{55,†} J. Jia,¹² J. Jin,¹² O. Jinnouchi,⁴⁹ B. M. Johnson,⁶ K. S. Joo,⁴⁰ D. Jouan,⁴⁵ F. Kajihara,¹⁰ S. Kometani,^{10,48,61} N. Kamihara,^{48,49} J. Kamin,⁵⁵ M. Kaneta,⁴⁹ J. H. Kang,⁶³ H. Kanou,^{48,58} J. Kapustinsky,³⁴ D. Kawall,^{37,49} A. V. Kazantsev,³⁰ T. Kempel,²⁵ A. Khanzadeev,⁴⁷ K. M. Kijima,²⁰ J. Kikuchi,⁶¹ B. I. Kim,²⁹ D. H. Kim,⁴⁰ D. J. Kim,⁶³ E. Kim,⁵³ S. H. Kim,⁶³ E. Kinney,¹¹ K. Kiriluk,¹¹ Á. Kiss,¹⁶ E. Kistenev,⁶ A. Kiyomichi,⁴⁸ J. Klay,³³ C. Klein-Boesing,³⁸ L. Kochenda,⁴⁷ V. Kochetkov,²¹ B. Komkov,⁴⁷ M. Konno,⁵⁹ J. Koster,²² D. Kotchetkov,⁷ A. Kozlov,⁶² A. Kral,¹³ A. Kravitz,¹² J. Kubart,^{8,24} G. J. Kunde,³⁴ N. Kurihara,¹⁰ K. Kurita,^{50,48} M. Kurosawa,⁴⁸ M. J. Kweon,²⁹ Y. Kwon,^{57,63} G. S. Kyle,⁴³ R. Lacey,⁵⁴ Y. S. Lai,¹² J. G. Lajoie,²⁵ D. Layton,²² A. Lebedev,²⁵ D. M. Lee,³⁴ K. B. Lee,²⁹ M. K. Lee,⁶³ T. Lee,⁵³ M. J. Leitch,³⁴ M. A. L. Leite,⁵² B. Lenzi,⁵² P. Liebing,⁴⁹ T. Liška,¹³ A. Litvinenko,²⁶ H. Liu,⁴³ M. X. Liu,³⁴ X. Li,⁹ B. Love,⁶⁰ D. Lynch,⁶ C. F. Maguire,⁶⁰ Y. I. Makdisi,⁵ A. Malakhov,²⁶ M. D. Malik,⁴² V. I. Manko,³⁰ E. Mannel,¹² Y. Mao,^{46,48} L. Maek,^{8,24} H. Masui,⁵⁹ F. Matathias,¹² M. McCumber,⁵⁵ P. L. McGaughey,³⁴ N. Means,⁵⁵ B. Meredith,²² Y. Miake,⁵⁹ P. Mike,^{8,24} K. Miki,⁵⁹ T. E. Miller,⁶⁰ A. Milov,^{6,55} S. Mioduszewski,⁶ M. Mishra,³ J. T. Mitchell,⁶ M. Mitrovski,⁵⁴ A. K. Mohanty,⁴ Y. Morino,¹⁰ A. Morreale,⁷ D. P. Morrison,⁶ T. V. Moukhanova,³⁰ D. Mukhopadhyay,⁶⁰ J. Murata,^{50,48} S. Nagamiya,²⁷ Y. Nagata,⁵⁹ J. L. Nagle,¹¹ M. Naglis,⁶² M. I. Nagy,¹⁶ I. Nakagawa,^{48,49} Y. Nakamiya,²⁰ T. Nakamura,²⁰ K. Nakano,^{48,58} J. Newby,³³ M. Nguyen,⁵⁵ T. Niita,⁵⁹ B. E. Norman,³⁴ R. Nouicer,⁶ A. S. Nyanin,³⁰ E. O'Brien,⁶ S. X. Oda,¹⁰ C. A. Ogilvie,²⁵ H. Ohnishi,⁴⁸ K. Okada,⁴⁹ M. Oka,⁵⁹ O. O. Omiwade,¹ Y. Onuki,⁴⁸ A. Oskarsson,³⁶ M. Ouchida,²⁰ K. Ozawa,¹⁰ R. Pak,⁶ D. Pal,⁶⁰ A. P. T. Palounek,³⁴ V. Pantuev,^{23,55} V. Papavassiliou,⁴³ J. Park,⁵³ W. J. Park,²⁹ S. F. Pate,⁴³ H. Pei,²⁵ J.-C. Peng,²² H. Pereira,¹⁴ V. Peresedov,²⁶ D. Yu. Peressounko,³⁰ C. Pinkenburg,⁶ M. L. Purschke,⁶ A. K. Purwar,³⁴ H. Qu,¹⁹ J. Rak,⁴² A. Rakotozafindrabe,³² I. Ravinovich,⁶² K. F. Read,^{44,57} S. Rembeczki,¹⁷ M. Reuter,⁵⁵ K. Reygers,³⁸ V. Riabov,⁴⁷ Y. Riabov,⁴⁷ D. Roach,⁶⁰ G. Roche,³⁵ S. D. Rolnick,⁷ A. Romana,^{32,*} M. Rosati,²⁵ S. S. E. Rosendahl,³⁶ P. Rosnet,³⁵ P. Rukoyatkin,²⁶ P. Ruika,²⁴ V. L. Rykov,⁴⁸ B. Sahlmueller,³⁸ N. Saito,^{31,48,49} T. Sakaguchi,⁶ S. Sakai,⁵⁹ K. Sakashita,^{48,58} H. Sakata,²⁰ V. Samsonov,⁴⁷ S. Sato,²⁷ T. Sato,⁵⁹ S. Sawada,²⁷ K. Sedgwick,⁷ J. Seele,¹¹ R. Seidl,²² A. Yu. Semenov,²⁵ V. Semenov,²¹ R. Seto,⁷ D. Sharma,⁶² I. Shein,²¹ A. Shevel,^{47,54} T.-A. Shibata,^{48,58} K. Shigaki,²⁰ M. Shimomura,⁵⁹ K. Shoji,^{31,48} P. Shukla,⁴ A. Sickles,^{6,55} C. L. Silva,⁵² D. Silvermyr,⁴⁴ C. Silvestre,¹⁴ K. S. Sim,²⁹ B. K. Singh,³ C. P. Singh,³ V. Singh,³ S. Skutnik,²⁵ M. Sluneka,^{8,26} A. Soldatov,²¹ R. A. Soltz,³³ W. E. Sondheim,³⁴ S. P. Sorenson,⁵⁷ I. V. Sourikova,⁶ F. Staley,¹⁴ P. W. Stankus,⁴⁴ E. Stenlund,³⁶ M. Stepanov,⁴³ A. Ster,²⁸ S. P. Stoll,⁶ T. Sugitate,²⁰ C. Suire,⁴⁵ A. Sukhanov,⁶ J. Szklai,²⁸ T. Tabaru,⁴⁹ S. Takagi,⁵⁹ E. M. Takagui,⁵² A. Taketani,^{48,49} R. Tanabe,⁵⁹ Y. Tanaka,⁴¹ K. Tanida,^{48,49,53} M. J. Tannenbaum,⁶ A. Tarantenko,⁵⁴ P. Tarjan,¹⁵ H. Themann,⁵⁵ T. L. Thomas,⁴² M. Togawa,^{31,48} A. Toia,⁵⁵ J. Tojo,⁴⁸ L. Tomasek,²⁴ Y. Tomita,⁵⁹ H. Torii,^{20,48} R. S. Towell,¹ V.-N. Tram,³² I. Tserruya,⁶² Y. Tsuchimoto,²⁰ C. Vale,²⁵ H. Valle,⁶⁰ H. W. van Hecke,³⁴ A. Veicht,²² J. Velkovska,⁶⁰ R. Vertesi,¹⁵ A. A. Vinogradov,³⁰ M. Virius,¹³ V. Vrba,²⁴ E. Vznuzdaev,⁴⁷ M. Wagner,^{31,48} D. Walker,⁵⁵ X. R. Wang,⁴³ Y. Watanabe,^{48,49} F. Wei,²⁵ J. Wessels,³⁸ S. N. White,⁶ D. Winter,¹² C. L. Woody,⁶ M. Wysocki,¹¹ W. Xie,⁴⁹ Y. L. Yamaguchi,⁶¹ K. Yamaura,²⁰ R. Yang,²² A. Yanovich,²¹ Z. Yasin,⁷ J. Ying,¹⁹ S. Yokkaichi,^{48,49} G. R. Young,⁴⁴ I. Younus,⁴² I. E. Yushmanov,³⁰ W. A. Zajc,¹² O. Zaudtke,³⁸ C. Zhang,⁴⁴ S. Zhou,⁹ J. Zimanyi,^{28,*} and L. Zolin²⁶
(PHENIX Collaboration)

¹Abilene Christian University, Abilene, Texas 79699, USA²Institute of Physics, Academia Sinica, Taipei 11529, Taiwan³Department of Physics, Banaras Hindu University, Varanasi 221005, India

- ⁴Bhabha Atomic Research Centre, Bombay 400 085, India
⁵Collider Accelerator Department, Brookhaven National Laboratory, Upton, New York 11973-5000, USA
⁶Physics Department, Brookhaven National Laboratory, Upton, New York 11973-5000, USA
⁷University of California-Riverside, Riverside, California 92521, USA
⁸Charles University, Ovocný trh 5, Praha 1, 116 36, Prague, Czech Republic
⁹Science and Technology on Nuclear Data Laboratory, China Institute of Atomic Energy, Beijing 102413, P. R. China
¹⁰Center for Nuclear Study, Graduate School of Science, University of Tokyo, 7-3-1 Hongo, Bunkyo, Tokyo 113-0033, Japan
¹¹University of Colorado, Boulder, Colorado 80309, USA
¹²Columbia University, New York, New York 10027 and Nevis Laboratories, Irvington, New York 10533, USA
¹³Czech Technical University, Zikova 4, 166 36 Prague 6, Czech Republic
¹⁴Dapnia, CEA Saclay, F-91191, Gif-sur-Yvette, France
¹⁵Debrecen University, H-4010 Debrecen, Egyetem tér 1, Hungary
¹⁶ELTE, Eötvös Loránd University, H-1117 Budapest, Pázmány P. s. 1/A, Hungary
¹⁷Florida Institute of Technology, Melbourne, Florida 32901, USA
¹⁸Florida State University, Tallahassee, Florida 32306, USA
¹⁹Georgia State University, Atlanta, Georgia 30303, USA
²⁰Hiroshima University, Kagamiyama, Higashi-Hiroshima 739-8526, Japan
²¹IHEP Protvino, State Research Center of Russian Federation, Institute for High Energy Physics, Protvino, 142281, Russia
²²University of Illinois at Urbana-Champaign, Urbana, Illinois 61801, USA
²³Institute for Nuclear Research of the Russian Academy of Sciences, prospekt 60-letiya Oktyabrya 7a, Moscow 117312, Russia
²⁴Institute of Physics, Academy of Sciences of the Czech Republic, Na Slovance 2, 182 21 Prague 8, Czech Republic
²⁵Iowa State University, Ames, Iowa 50011, USA
²⁶Joint Institute for Nuclear Research, 141980 Dubna, Moscow Region, Russia
²⁷KEK, High Energy Accelerator Research Organization, Tsukuba, Ibaraki 305-0801, Japan
²⁸KFKI Research Institute for Particle and Nuclear Physics of the Hungarian Academy of Sciences (MTA KFKI RMKI), H-1525 Budapest 114, P.O. Box 49, Budapest, Hungary
²⁹Korea University, Seoul, 136-701, Korea
³⁰Russian Research Center "Kurchatov Institute," Moscow, 123098 Russia
³¹Kyoto University, Kyoto 606-8502, Japan
³²Laboratoire Leprince-Ringuet, Ecole Polytechnique, CNRS-IN2P3, Route de Saclay, F-91128, Palaiseau, France
³³Lawrence Livermore National Laboratory, Livermore, California 94550, USA
³⁴Los Alamos National Laboratory, Los Alamos, New Mexico 87545, USA
³⁵LPC, Université Blaise Pascal, CNRS-IN2P3, Clermont-Fd, 63177 Aubière Cedex, France
³⁶Department of Physics, Lund University, Box 118, SE-221 00 Lund, Sweden
³⁷Department of Physics, University of Massachusetts, Amherst, Massachusetts 01003-9337, USA
³⁸Institut für Kernphysik, University of Muenster, D-48149 Muenster, Germany
³⁹Muhlenberg College, Allentown, Pennsylvania 18104-5586, USA
⁴⁰Myongji University, Yongin, Kyonggi-do 449-728, Korea
⁴¹Nagasaki Institute of Applied Science, Nagasaki-shi, Nagasaki 851-0193, Japan
⁴²University of New Mexico, Albuquerque, New Mexico 87131, USA
⁴³New Mexico State University, Las Cruces, New Mexico 88003, USA
⁴⁴Oak Ridge National Laboratory, Oak Ridge, Tennessee 37831, USA
⁴⁵IPN-Orsay, Université Paris Sud, CNRS-IN2P3, Boîte Postale 1, F-91406, Orsay, France
⁴⁶Peking University, Beijing 100871, P. R. China
⁴⁷PNPI, Petersburg Nuclear Physics Institute, Gatchina, Leningrad region, 188300, Russia
⁴⁸RIKEN Nishina Center for Accelerator-Based Science, Wako, Saitama 351-0198, Japan
⁴⁹RIKEN BNL Research Center, Brookhaven National Laboratory, Upton, New York 11973-5000, USA
⁵⁰Physics Department, Rikkyo University, 3-34-1 Nishi-Ikebukuro, Toshima, Tokyo 171-8501, Japan
⁵¹Saint Petersburg State Polytechnic University, Saint Petersburg, 195251 Russia
⁵²Instituto de Física, Universidade de São Paulo, Caixa Postal 66318, São Paulo CEP 05315-970, Brazil
⁵³Seoul National University, Seoul, Korea
⁵⁴Chemistry Department, Stony Brook University, SUNY, Stony Brook, New York 11794-3400, USA
⁵⁵Department of Physics and Astronomy, Stony Brook University, SUNY, Stony Brook, New York 11794-3400, USA
⁵⁶SUBATECH (Ecole des Mines de Nantes, CNRS-IN2P3, Université de Nantes) Boîte Postale 20722-44307, Nantes, France
⁵⁷University of Tennessee, Knoxville, Tennessee 37996, USA
⁵⁸Department of Physics, Tokyo Institute of Technology, Oh-okayama, Meguro, Tokyo 152-8551, Japan
⁵⁹Institute of Physics, University of Tsukuba, Tsukuba, Ibaraki 305, Japan
⁶⁰Vanderbilt University, Nashville, Tennessee 37235, USA

⁶¹Waseda University, Advanced Research Institute for Science and Engineering, 17 Kikui-cho, Shinjuku-ku, Tokyo 162-0044, Japan
⁶²Weizmann Institute, Rehovot 76100, Israel
⁶³Yonsei University, IPAP, Seoul 120-749, Korea
(Received 3 February 2011; published 23 June 2011)

Transverse momentum distributions and yields for π^\pm , K^\pm , p , and \bar{p} in $p + p$ collisions at $\sqrt{s} = 200$ and 62.4 GeV at midrapidity are measured by the PHENIX experiment at the Relativistic Heavy Ion Collider (RHIC). These data provide important baseline spectra for comparisons with identified particle spectra in heavy ion collisions at RHIC. We present the inverse slope parameter T_{inv} , mean transverse momentum $\langle p_T \rangle$, and yield per unit rapidity dN/dy at each energy, and compare them to other measurements at different \sqrt{s} in $p + p$ and $p + \bar{p}$ collisions. We also present the scaling properties such as m_T scaling and x_T scaling on the p_T spectra between different energies. To discuss the mechanism of the particle production in $p + p$ collisions, the measured spectra are compared to next-to-leading-order or next-to-leading-logarithmic perturbative quantum chromodynamics calculations.

DOI: 10.1103/PhysRevC.83.064903

PACS number(s): 25.75.Dw, 25.40.Ve

I. INTRODUCTION

Single-particle spectra of identified hadrons in high-energy elementary collisions have interested physicists for many decades because of their fundamental nature and simplicity. Particle production, in general, can be categorized into two different regimes depending on the transverse momentum of the hadrons. One is soft multiparticle production, dominant at low transverse momentum ($p_T \leq 2 \text{ GeV}/c$), which corresponds to the $\sim 1 \text{ fm}$ scale of the nucleon radius described by constituent quarks. Another regime is hard-scattering particle production, evident at high transverse momentum ($p_T \geq 2 \text{ GeV}/c$) owing to the hard scattering of pointlike current quarks, which corresponds to a very short distance scale $\sim 0.1 \text{ fm}$ [1] and contributes less than a few percent of the cross section for $\sqrt{s} \leq 200 \text{ GeV}$. These two different regimes of particle production in $p + p$ collisions indicate that “elementary” $p + p$ collisions are actually rather complicated processes. It is interesting to know where the “soft-hard transition” happens, and its beam energy and particle species dependences, since they have not yet been fully understood.

In soft particle production, cosmic ray physicists observed in the 1950s that the average transverse momentum of secondary particles is limited to $\sim 0.5 \text{ GeV}/c$, independent of the primary energy [2,3]. Cocconi, Koester, and Perkins [4] then proposed the prescient empirical formula for the transverse momentum spectrum of meson production:

$$\frac{d\sigma}{p_T dp_T} = Ae^{-6p_T}, \quad (1)$$

where p_T is the transverse momentum in GeV/c and $\langle p_T \rangle = 2/6 = 0.333 \text{ GeV}/c$. The observation by Orear [5] that large-angle $p + p$ elastic scattering measurements at BNL Alternating Gradient Synchrotron (AGS) energies (10 to 30 GeV in incident energy) “can be fit by a single

exponential in transverse momentum, and that this exponential is the very same exponential that describes the transverse momentum distribution of pions produced in nucleon-nucleon collisions” led to the interpretation [6] that particle production is “statistical” with Eq. (1) as a thermal Boltzmann spectrum, with $1/6 = 0.167 \text{ GeV}/c$ representing the “temperature” T at which the mesons or protons are emitted [7].

It was natural in a thermal scenario [8,9] to represent the invariant cross section as a function of the rapidity (y) and the transverse mass ($m_T = \sqrt{p_T^2 + m^2}$) with a universal temperature parameter T . This description explained well the observed successively increasing $\langle p_T \rangle$ of π , K , p , and Λ with increasing rest mass [10–12], and had the added advantage of explaining, by the simple factor $e^{-6(m_K - m_\pi)} \sim 12\%$, the low value of $\sim 10\%$ observed for the K/π ratio at low p_T at CERN Intersecting Storage Rings (ISR) energies ($\sqrt{s} \sim 20\text{--}60 \text{ GeV}$) [13].

In 1964, the constituent quark model with SU(3) symmetry was introduced to explain the hadron flavor spectrum and the static properties of hadrons [14,15]. Later on, a dynamical model was developed to calculate the flavor dependence of identified hadrons in soft multiparticle production [16], together with the inclusive reaction formalism [17–19]. These theoretical studies on the particle production mechanism showed that there was much to be learned by simply measuring a single-particle spectrum, and it brought the study of identified inclusive single-particle production into the mainstream of $p + p$ physics.

One of the controversial issues in understanding soft multiparticle production in the 1950s was whether more than one meson could be produced in a single nucleon-nucleon collision (“multiple production”), or whether the multiple meson production observed in nucleon-nucleus ($p + A$) interactions was the result of several successive nucleon-nucleon collisions with each collision producing only a single meson (“plural production”) [20]. The issue was decided when multiple meson production was first observed in 1954 at the Brookhaven Cosmotron in collisions between neutrons with energies up to 2.2 GeV and protons in a hydrogen-filled cloud chamber [6,21].

Then the observation of multiparticle production occurring not only in nucleon-nucleus ($p + A$) but also in nucleon-

*Deceased.

†PHENIX spokesperson; jacak@skipper.physics.sunysb.edu

nucleon ($p + p$) collisions motivated Fermi and Landau to develop the statistical [22] and hydrodynamical [23] approach to multiparticle production. Belenkij and Landau observed that although the statistical model of Fermi is sufficient to describe the particle numbers in terms of only a temperature and a chemical potential, this model has to be extended to hydrodynamics, when particle spectra are considered. They also noted that the domain of the applicability of ideal relativistic hydrodynamics coincides with the domain of the applicability of thermodynamical models in high-energy $p + p$ collisions [23].

Understanding of the particle production by hard scattering partons has also been advanced by the appearance of a rich body of data in $p + p$ collisions at the CERN ISR [13,24,25] in the 1970s, followed by measurements at the Relativistic Heavy Ion Collider (RHIC) at $\sqrt{s} = 200$ [26–33] and 62.4 GeV [34] over the last decade. The hard scattering in $p + p$ collisions was discovered by the observation of an unexpectedly large yield of particles with large transverse momentum and the phenomena of dijets at the ISR [35]. These observations indicate that the hard scattering process occurs between the quark and gluon constituents (or partons) inside the nucleons. This scattering process can be described by perturbative quantum chromodynamics (pQCD) because the strong-coupling constant α_s of QCD becomes small (asymptotically free) for large-momentum-transfer (Q^2) parton-parton scatterings. After the initial high- Q^2 parton-parton scatterings, these partons fragment into high- p_T hadrons or jets. In fact, at RHIC energies, single-particle spectra of high- p_T hadrons are well described by pQCD [30,33,34]. Furthermore, x_T ($= 2p_T/\sqrt{s}$), which is also inspired by pQCD, is known to be a good scaling variable of the particle production at high p_T at both ISR [36] and RHIC [34] energies, so that x_T scaling can be used to distinguish between the soft and hard particle productions.

Another important point of measurements in $p + p$ collisions is as a baseline for the heavy ion ($A + A$) data. The nuclear modification factor R_{AA} , for example, uses p_T spectra in $p + p$ collisions as a denominator and those in $A + A$ collisions (with the appropriate scaling of number of binary nucleon-nucleon collisions) as a numerator. In addition, p_T spectra in $p + p$ provide a reference for bulk properties of $A + A$ collisions, such as the inverse slope parameter T_{inv} , mean transverse momentum $\langle p_T \rangle$, and yield per unit rapidity dN/dy . These data in $p + p$ collisions can be treated as baseline values for the smallest $A + A$ collisions.

In this paper, we present measurements of identified charged hadron p_T spectra for π^\pm, K^\pm, p , and \bar{p} at midrapidity in $p + p$ collisions at $\sqrt{s} = 200$ and 62.4 GeV from the PHENIX experiment. First, we compare the results of particle spectra at 200 GeV with those at 62.4 GeV as a function of p_T , m_T , and $m_T - m$ (where m is the rest mass). Second, the extracted values from p_T spectra, i.e., T_{inv} , $\langle p_T \rangle$, and dN/dy , are compared between the two beam energies. For the systematic study of particle production as a function of \sqrt{s} , the data are further compared to measurements in $p + p$ and $p + \bar{p}$ collisions at the CERN ISR and Fermi National Accelerator Laboratory (FNAL) Tevatron colliders.

From these measurements, we discuss the following key issues:

- (i) Hard scattering particle production: The data are compared with the results of perturbative quantum chromodynamics calculations.
- (ii) Transition from soft to hard physics: Since the p_T regions presented in this paper can cover the region where the soft-hard transition occurs, the scaling properties in m_T and x_T with their beam energy and particle species dependences are shown.
- (iii) Comparisons with heavy ion data as a baseline measurement: Some of the data in $p + p$ are compared with the existing data in Au + Au [37].

The paper is organized as follows. Section II describes the PHENIX detector as it was used in this measurement. Section III discusses the analysis details, including data sets, event selection, track selection, particle identification, corrections applied to the data, and systematic uncertainties. Section IV gives the experimental results for p_T spectra for identified charged particles, particle ratios, m_T scaling, the excitation function of observables (such as T_{inv} , $\langle p_T \rangle$, and dN/dy), and R_{AA} . Section V compares the results with next-to-leading-order (NLO) [38,39] and next-to-leading-logarithm (NLL) [40,41] pQCD calculations, and discusses soft and hard particle production and the transition between them. Section VI gives the summary and conclusions.

II. EXPERIMENTAL SETUP

The PHENIX experiment is designed to perform a broad study of $A + A$, $d + A$, and $p + p$ collisions to investigate nuclear matter under extreme conditions, as well as to measure the spin structure of the nucleon. It is composed of two central arms (called the east and west arm, respectively), two forward muon arms, and global detectors, as shown in Fig. 1. The central arms are designed to detect electrons, photons, and charged hadrons in the pseudorapidity range $|\eta| < 0.35$. The global detectors measure the start time, collision vertex, and charged hadron multiplicity of the interactions in the forward pseudorapidity region. The following sections describe those parts of the detector that are used in the present analysis. A detailed description of the complete set of detectors can be found elsewhere [42–46].

The beam-beam counters (BBCs) [45] determine the start time information for time-of-flight measurements and the collision vertex point, as well as providing the main collision trigger. The two BBCs are located at 1.44 m from the nominal interaction point along the beamline on each side. Each BBC comprises 64 Čerenkov telescopes, arranged radially around the beamline. The BBCs measure the number of charged particles in the pseudorapidity region $3.0 < |\eta| < 3.9$.

Charged particle tracks are reconstructed using the central arm spectrometers [46]. The east arm spectrometer of the PHENIX detector contains the following subsystems used in this analysis: drift chamber (DC), pad chamber (PC), and time-of-flight (TOF) detector. The magnetic field for the central arm spectrometers is supplied by the central magnet

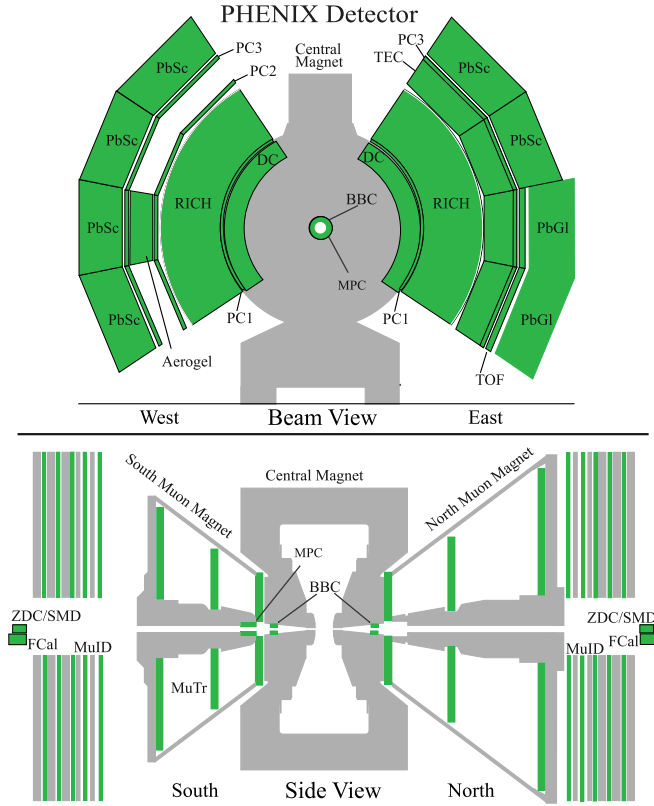


FIG. 1. (Color online) The PHENIX detector configuration for RHIC Run-6 data-taking period.

[43] that provides an axial field parallel to the beam around the collision vertex.

The drift chambers are the closest tracking detectors to the beamline, located at a radial distance of 2.2 m (geometric center; the same for the other detectors). They measure charged particle trajectories in the azimuthal direction to determine the transverse momentum of each particle. By combining the polar angle information from the first layer of PCs, as described below, with the transverse momentum, the total momentum p is determined. The momentum resolution in $p + p$ collisions is $\delta p/p \simeq 0.7\% \oplus 1.0\% \times p$ (GeV/c), where the first term is due to the multiple scattering before the DC and the second term is the angular resolution of the DC. The absolute momentum scale is known as $\pm 0.7\%$ rms from the reconstructed proton mass using TOF data.

The pad chambers are multiwire proportional chambers that form three separate layers of the central tracking system. The first layer (PC1) is located at the radial outer edge of each drift chamber at a distance of 2.49 m, while the third layer is at 4.98 m from the interaction point. The second layer is located at a radial distance of 4.19 m in the west arm only. The PC1 and DC, along with the vertex position measured by the BBC, are used in the global track reconstruction to determine the polar angle of each charged track.

The time-of-flight detector serves as the primary particle identification device for charged hadrons by measuring the stop time. The start time is given by the BBC. The TOF detector is located at a radial distance of 5.06 m from the interaction point in the east central arm. This contains 960 scintillator slats

oriented along the azimuthal direction. It is designed to cover $|\eta| < 0.35$ and $\Delta\phi = 45^\circ$ in azimuthal angle. The intrinsic timing resolution is $\sigma \simeq 115$ ps, which in combination with the BBC timing resolution of 60 ps allows for a 2.6σ π/K separation at $p_T \simeq 2.5$ GeV/ c , and K/p separation out to $p_T = 4.5$ GeV/ c , using an asymmetric particle-identification (PID) cut, as described below.

III. DATA ANALYSIS

The two RHIC data sets analyzed are 2005 data for $p + p$ collisions at $\sqrt{s} = 200$ GeV and 2006 data for $p + p$ collisions at $\sqrt{s} = 62.4$ GeV. Each data set was analyzed separately by taking into account the different run conditions and accelerator performance. In this section, we explain the event selection, track reconstruction, particle identification, and corrections to obtain the p_T spectra. The event normalization and systematic uncertainties are also presented.

A. Event selection

We use the PHENIX minimum bias trigger events, which are determined by a coincidence between north and south BBC signals, requiring at least one hit on both sides of the BBCs. Owing to the limited acceptance, approximately only half of $p + p$ inelastic events result in a BBC trigger. The PHENIX minimum bias data, triggered by BBC in $p + p$ collisions within a vertex cut of ± 30 cm, include $\sigma_{\text{BBC}} = 23.0 \pm 2.2$ mb at $\sqrt{s} = 200$ GeV and $\sigma_{\text{BBC}} = 13.7 \pm 1.5$ mb at $\sqrt{s} = 62.4$ GeV (see Sec. III E). We analyze 9.2×10^8 minimum bias events for the 2005 $p + p$ data at $\sqrt{s} = 200$ GeV, which is more than 30 times larger than the 2003 data set [26], and 2.14×10^8 minimum bias events for the 2006 data at $\sqrt{s} = 62.4$ GeV.

B. Track reconstruction and particle identification

As in previous publications [37,47], charged particle tracks are reconstructed by the DC based on a combinatorial Hough transform, which gives the angle of the track in the main bend plane. PC1 is used to measure the position of the hit in the longitudinal direction along the beam axis. When combined with the location of the collision vertex along the beam axis, the PC1 hit gives the polar angle of the track. Only tracks with valid information from both DC and PC1 are used in the analysis. To associate a track with a hit on the TOF detector, the track is projected to its expected hit location on the TOF detector. We require tracks to have a hit on the TOF detector within $\pm 2\sigma$ of the expected hit location in both the azimuthal and beam directions. The track reconstruction efficiency is approximately 98% in $p + p$ collisions. Finally, a cut on the energy loss in the TOF scintillator is applied to each track. This β -dependent energy loss cut is based on a parametrization of the Bethe-Bloch formula. The flight path length is calculated from a fit to the reconstructed track trajectory in the magnetic field. The background due to random association of DC and PC1 tracks with TOF hits is reduced to a negligible level when the mass cut used for particle identification is applied.

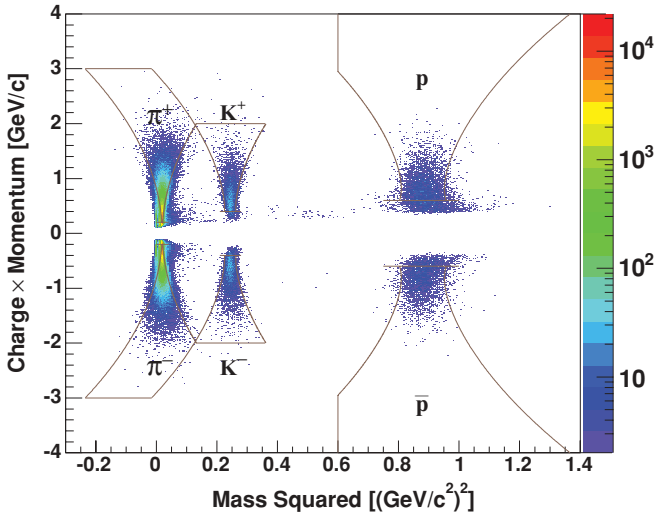


FIG. 2. (Color online) Momentum multiplied by charge versus mass squared distribution in $p + p$ collisions at $\sqrt{s} = 62.4$ GeV. The lines indicate the PID cut boundaries (2σ) for pions, kaons, and protons (antiprotons) from left to right, respectively.

Charged particles are identified using the combination of three measurements: time-of-flight data from the BBC and TOF detector, momentum from the DC, and flight path length from the collision vertex point to the TOF detector hit position. The mass squared is derived from

$$m^2 = \frac{p^2}{c^2} \left[\left(\frac{t_{\text{TOF}}}{L/c} \right)^2 - 1 \right], \quad (2)$$

where p is the momentum, t_{TOF} is the time of flight, L is the flight path length, and c is the speed of light. The charged particle identification is performed using cuts in m^2 and momentum space. In Fig. 2, a plot of momentum multiplied by charge versus m^2 is shown together with applied PID cuts as solid curves. We use 2σ standard deviation PID cuts in m^2 and momentum space for each particle species. The PID cut is based on a parametrization of the measured m^2 width as a function of momentum,

$$\begin{aligned} \sigma_{m^2}^2 &= \frac{\sigma_\alpha^2}{K_1^2} (4m^4 p^2) + \frac{\sigma_{\text{MS}}^2}{K_1^2} \left[4m^4 \left(1 + \frac{m^2}{p^2} \right) \right] \\ &\quad + \frac{\sigma_t^2 c^2}{L^2} [4p^2(m^2 + p^2)], \end{aligned} \quad (3)$$

where σ_α is the angular resolution, σ_{MS} is the multiple-scattering term, σ_t is the overall time-of-flight resolution, m is the centroid of the m^2 distribution for each particle species, and K_1 is the magnetic field integral constant term of 101 mrad GeV. The parameters for PID are $\sigma_\alpha = 0.99$ mrad, $\sigma_{\text{MS}} = 1.02$ mrad GeV, and $\sigma_t = 130$ ps. For pion identification above $2 \text{ GeV}/c$, we apply an asymmetric PID cut to reduce kaon contamination of pions. As shown by the lines in Fig. 2, the overlap regions that are within the 2σ cuts for both pions and kaons are excluded. The lower momentum cutoffs are $0.3 \text{ GeV}/c$ for pions, $0.4 \text{ GeV}/c$ for kaons, and $0.5 \text{ GeV}/c$ for protons and antiprotons. The lower momentum cutoff value

for p and \bar{p} is larger than for pions and kaons due to the larger energy loss effect.

For kaons, the upper momentum cutoff is $2 \text{ GeV}/c$ since the $\pi + p$ contamination level for kaons is $\approx 8\%$ at that momentum. The upper momentum cutoff for pions is $p_T = 3 \text{ GeV}/c$ where the $K + p$ contamination reaches $\approx 3\%$. Electron (positron) and decay muon background at very low p_T ($< 0.3 \text{ GeV}/c$) are well separated from the pion mass-squared peak. For protons the upper momentum cutoff is set at $4.5 \text{ GeV}/c$. For protons and antiprotons an additional cut, $m^2 > 0.6(\text{GeV}/c^2)^2$, is introduced to reduce the contamination. The contamination background on each particle species is subtracted statistically after applying these PID cuts.

C. Efficiency corrections

We use a GEANT [48] based Monte Carlo simulation program of the PHENIX detector, to correct for geometrical acceptance, reconstruction efficiency, in-flight decay for π and K , multiple-scattering effect, and nuclear interactions with materials in the detector (including \bar{p} absorption). Single-particle tracks are passed from GEANT to the PHENIX event reconstruction software [47]. In this simulation, the BBC, DC, and TOF detector responses are tuned to match the real data. For example, dead areas of the DC and TOF detector are included, and momentum and time-of-flight resolutions are tuned. The track association to the TOF detector both in azimuth and along the beam axis as a function of momentum and the PID cut boundaries are parametrized to match the real data. A fiducial cut is applied to choose identical active areas on the TOF detector in both the simulation and data.

We generate 1×10^7 single-particle events for each particle species (π^\pm , K^\pm , p , and \bar{p}) with flat p_T distributions for high p_T ($2\text{--}4 \text{ GeV}/c$ for pions and kaons, $2\text{--}8 \text{ GeV}/c$ for p and \bar{p}) with enhancement at low p_T ($< 2 \text{ GeV}/c$). Weighting functions to the p_T distributions are also used to check the effect of steepness, which is less than $\sim 1\%$ level on the final yields in the measured p_T range. The rapidity range is set to be wider than the PHENIX acceptance, i.e., flat in $-0.6 < y < 0.6$ ($\Delta y = 1.2$) to deal with particles coming from outside [the denominator of Eq. (4) is weighted with a factor $1/\Delta y = 1/1.2$ in order to normalize the yield for unit rapidity]. The efficiencies are determined in each p_T bin by dividing the reconstructed output by the generated input as expressed as follows:

$$\epsilon(p_T) = \frac{\text{no. of reconstructed MC tracks}}{\text{no. of generated MC tracks}}. \quad (4)$$

The resulting correction factors $C_{\text{eff}}(p_T)$ [$= 1/\epsilon(p_T)$] are multiplied by the raw p_T spectra for each p_T bin and for each individual particle species (see Sec. III G).

D. Feed-down corrections

The proton and antiproton p_T spectra are corrected for feed-down from weak decays of hyperons. The detailed procedure for the feed-down correction can be found in [26]. We include the following decay modes: $\Lambda \rightarrow p\pi^-$, $\Sigma^+ \rightarrow p\pi^0$, and Λ

production from Σ^0, Ξ^0, Ξ^- . The feed-down contributions for antiproton yields are also estimated using the above decay modes for antiparticles.

In order to estimate the fractions of protons and antiprotons from weak decays of hyperons in the measured proton and antiproton p_T spectra, we use three input Λ and $\bar{\Lambda}$ p_T spectra:

- (i) measured Λ and $\bar{\Lambda}$ p_T spectra in PHENIX in $p + p$ collisions at $\sqrt{s} = 200$ and 62.4 GeV,
- (ii) measured p (\bar{p}) distributions scaled with measured Λ ($\bar{\Lambda}$) distributions [31], and
- (iii) measured p (\bar{p}) distributions scaled with ISR Λ ($\bar{\Lambda}$) distributions [25].

Using each input above, proton and antiproton spectra from weak decays are calculated by using Monte Carlo simulation to take into account decay kinematics, the PHENIX track reconstruction efficiency, and experimental acceptance. Then systematic uncertainties are evaluated from different Λ and $\bar{\Lambda}$ spectra inputs. The resulting uncertainties on the final proton and antiproton spectra are of the order of 20%–30% at $p_T = 0.6$ GeV/c and 2%–5% at $p_T = 4$ GeV/c. The fractional contribution of the feed-down protons (antiprotons) to the total measured proton (antiproton) spectra, $\delta_{\text{feed}}(p_T)$, is approximately 10%–20% (5%–15%) at $p_T = 4$ GeV/c for 200 GeV $p + p$ (62.4 GeV $p + p$) and it shows an increase at lower p_T as shown in Fig. 3. The correction factor for the feed-down correction can be expressed as $C_{\text{feed}}(p_T) = 1 - \delta_{\text{feed}}(p_T)$, by which the raw p_T spectra are multiplied (see Sec. III G).

The feed-down correction for protons is different from that for antiprotons at 62.4 GeV, because of the difference in Λ/p and $\bar{\Lambda}/\bar{p}$ ratio at this beam energy. At 62.4 GeV the Λ/p ratio is 0.2, while the $\bar{\Lambda}/\bar{p}$ ratio is ≈ 0.4 [25], so that the feed-down contribution for antiprotons is bigger than that for protons. At 200 GeV, these two ratios are almost the same [31]; therefore the feed-down corrections for p and \bar{p} become identical.

E. Cross-section normalization

The BBC serves a dual function as both the minimum bias trigger and the calibrated luminosity monitor. The luminosity \mathcal{L} is defined as the interaction rate for a given cross section, $dN/dt = \mathcal{L}\sigma$, and the total number of events for a given cross section is

$$N = \sigma \times \int \mathcal{L} dt, \quad (5)$$

where $\int \mathcal{L} dt$ is the integrated luminosity. To connect the number of minimum bias triggered events and the integrated luminosity, σ_{BBC} is introduced, where $1/\sigma_{\text{BBC}}$ corresponds to the integrated luminosity per minimum bias triggered event [Eq. (6)]:

$$N_{\text{BBC}} = \sigma_{\text{BBC}} \times \int \mathcal{L} dt, \quad (6)$$

where N_{BBC} is the number of minimum bias events and $\int \mathcal{L} dt$ is the corresponding integrated luminosity. σ_{BBC} is measured

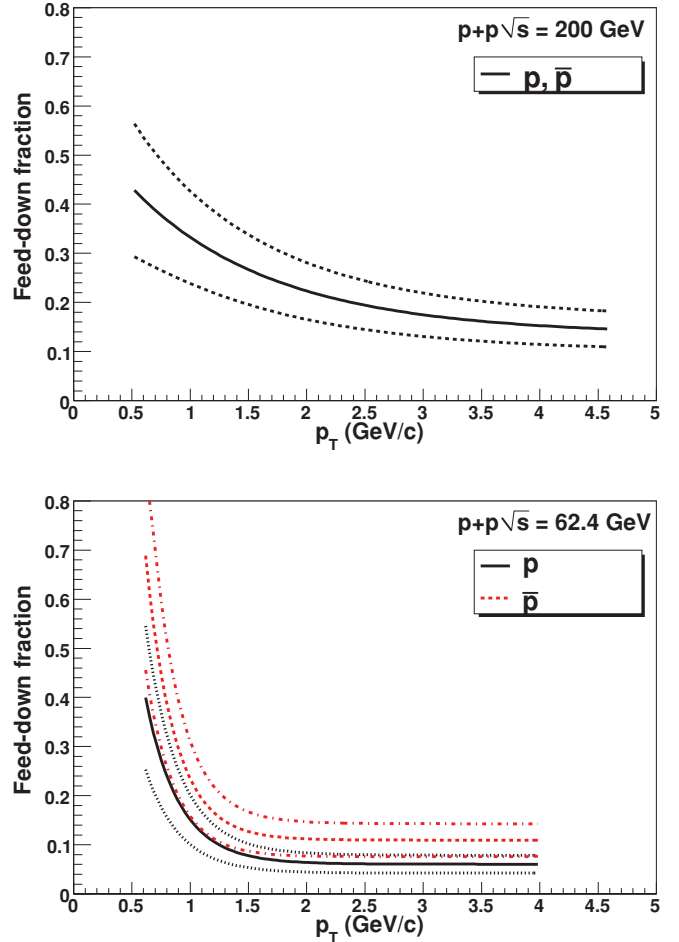


FIG. 3. (Color online) Fraction of feed-down protons and antiprotons as a function of p_T with systematic uncertainties. Top: 200 GeV $p + p$ (positive and negative functions are common). Bottom: 62.4 GeV $p + p$.

by a Van der Meer scan method (Vernier scan) in PHENIX [34,49].

Vernier scans were performed for $\sqrt{s} = 200$ and 62.4 GeV data sets. The σ_{BBC} obtained are 23.0 ± 2.2 and 13.7 ± 1.5 mb for $\sqrt{s} = 200$ and 62.4 GeV, respectively. The quoted uncertainty is a systematic uncertainty. These values were reported in our measurements of π^0 production [30,34].

Since the minimum bias trigger registers only half of the $p + p$ inelastic cross section, it is expected that there is a trigger bias against particles in the central spectrometers. This was checked with π^0 's in the electromagnetic calorimeter with high- p_T photon triggered events, and with charged tracks in the accelerator's beam crossing (clock) triggered events. The trigger bias ϵ_{bias} determined from the ratio (f_{π^0}) of the number of π^0 in the high- p_T photon triggered sample with and without the BBC trigger requirement [34]. We assume that ϵ_{bias} is process dependent and so that it is measured as $\epsilon_{\text{bias}} = f_{\pi^0}$. This ratio, f_{π^0} , is 0.79 ± 0.02 independent of the transverse momentum for $\sqrt{s} = 200$ GeV. At 62.4 GeV, the trigger bias was found to be transverse momentum dependent [34]. Figure 4 shows that the trigger bias f_{π^0} is $\approx 40\%$ up to $p_T \approx 3$ GeV/c, and monotonically decreases to 25% at $p_T \approx$

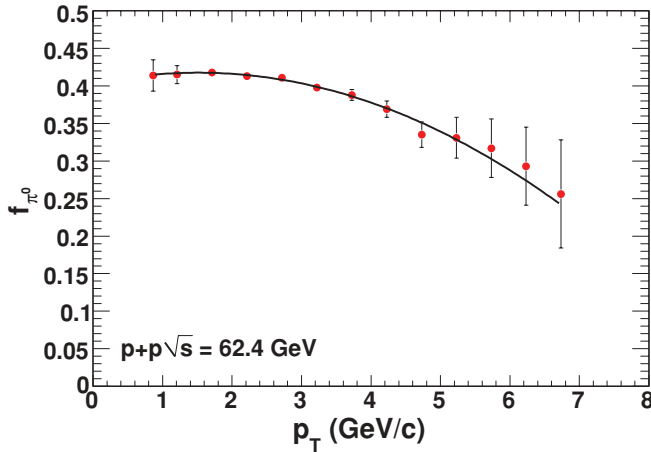


FIG. 4. (Color online) Fraction of the inclusive π^0 yield that satisfied the BBC trigger condition in 62.4 GeV $p + p$. Data points are from Fig. 1 of [34].

7 GeV/c. As described in the previous PHENIX publication [34], this decrease can be understood by the fact that most of the energy is used for the production of high-energy jets which contain the measured high- $p_T \pi^0$ and charged hadrons, and there is not enough energy left to produce particles for $\sqrt{s} = 62.4$ GeV $p + p$ collisions at the forward rapidity ($3.0 < |\eta| < 3.9$) where the BBC is located. This drop can be seen only for 62.4 GeV data. Also, we assume no particle species dependence for this trigger bias. We use this p_T -dependent trigger bias correction for charged hadrons by using fitted coefficients of a second-order polynomial, as shown in Fig. 4.

With those values, the invariant yield per BBC trigger count (Y/N_{BBC}) is related to the invariant cross section (σ) using

$$\sigma = (Y/N_{\text{BBC}}) \times (\sigma_{\text{BBC}}/\epsilon_{\text{bias}}). \quad (7)$$

F. Systematic uncertainties

In order to estimate the systematic uncertainties, p_T spectra with slightly different analysis cuts from those we use for the final results are prepared, and these spectra are compared to those with the standard analysis cuts. We checked the following analysis cuts: (1) fiducial, (2) track association windows, and (3) PID.

For each spectrum with modified cuts, the same changes in the cuts are made in the Monte Carlo simulation. The fully corrected spectra with different cut conditions are divided by the spectra with the baseline cut condition, resulting in uncertainties associated with each cut condition as a function of p_T . The obtained uncertainties are added in quadrature. Tables I and II show the systematic uncertainties on p_T spectra for each data set. There are three categories of systematic uncertainty: Type A is a point-to-point error uncorrelated between p_T bins, type B is p_T correlated, where all points move in the same direction but not by the same factor, while in type C all points move by the same factor independent of p_T [50]. In this study, the systematic uncertainties on feed-down correction and PID contamination correction are type B; other systematic uncertainties on applied analysis cuts

TABLE I. Systematic uncertainties on the p_T spectra for $\sqrt{s} = 200$ GeV $p + p$ given in percent. The number in parentheses includes the p_T dependence of the uncertainties for PID cut, feed-down correction, and PID contamination correction.

Source	π^+	π^-	K^+	K^-	p	\bar{p}
Fiducial cut	5	5	4	5	4	5
Track matching	4	4	5	4	4	4
PID cut	3	3	2	2	2–8	2–10
Efficiency correction	2	2	2	2	2	2
Feed-down correction	—	—	—	—	4–25	4–25
PID contamination	—	—	—	—	0–2	0–2
Total	7	7	7	7	6 (8–25)	7 (9–25)

are type C. There are two types of PID-related uncertainties. One is the systematic uncertainty of the yield extraction, which is evaluated by changing the PID boundary in the m^2 vs momentum plane. The other is the systematic uncertainty of the particle contamination, which is evaluated by using the contamination fraction. The fraction is estimated by fitting m^2 distributions on each p_T slice under the conditions of (1) fixed parameters for p and \bar{p} mass centroid and width, (2) p and \bar{p} mass centroid free with fixed mass width, and (3) p and \bar{p} mass width free with fixed mass centroid.

The systematic uncertainty on the BBC cross section is 9.7% and 11% for $\sqrt{s} = 200$ and 62.4 GeV, respectively. The systematic uncertainty on the trigger bias is 3% and 1%–5% for $\sqrt{s} = 200$ and 62.4 GeV, respectively (see Sec. III E). These uncertainties on normalization (type C) are not included in Tables I and II. All the figures and tables, including the tables in the Appendix, do not include the normalization uncertainties, unless explicitly noted.

G. Invariant cross section

The differential invariant cross section is determined as

$$E \frac{d^3\sigma}{dp^3} = \frac{1}{2\pi p_T} \frac{\sigma_{\text{BBC}}}{N_{\text{BBC}} C_{\text{bias}}^{\text{BBC}}(p_T)} \times C_{\text{eff}}(p_T) C_{\text{feed}}(p_T) \frac{d^2N}{dp_T dy}, \quad (8)$$

TABLE II. Systematic uncertainties on the p_T spectra for $\sqrt{s} = 62.4$ GeV $p + p$ given in percent. The number in parentheses includes the p_T dependence of the uncertainties for feed-down correction and PID contamination correction.

Source	π^+	π^-	K^+	K^-	p	\bar{p}
Fiducial cut	6	5	6	5	7	5
Track matching	2	2	3	3	3	3
PID cut	2	2	3	3	4	4
Efficiency correction	2	2	2	2	2	2
Feed-down correction	—	—	—	—	1–16	3–50
PID contamination	—	—	0–5	0–5	—	—
Total	7	6	7	7	9 (9–18)	7 (8–50)

where σ is the cross section, p_T is the transverse momentum, y is the rapidity, N_{BBC} is the number of minimum bias events, σ_{BBC} is the minimum bias cross section measured by the BBC, $C_{\text{eff}}(p_T)$ is the acceptance correction factor including detector efficiency, $C_{\text{bias}}^{\text{BBC}}(p_T)$ is the trigger bias, $C_{\text{feed}}(p_T)$ is the feed-down correction factor only for protons and antiprotons, and N is the number of measured tracks.

IV. RESULTS

In this section, we show the transverse momentum distributions and yields for π^\pm , K^\pm , p , and \bar{p} in $p + p$ collisions at $\sqrt{s} = 200$ and 62.4 GeV at midrapidity measured by the PHENIX experiment. We also present the transverse mass (m_T) spectra, the inverse slope parameter T_{inv} , mean transverse momentum $\langle p_T \rangle$, yield per unit rapidity dN/dy , and particle ratios at each energy, and compare them to other measurements at different \sqrt{s} in $p + p$ and $p + \bar{p}$ collisions. The measured T_{inv} , $\langle p_T \rangle$, and dN/dy in $p + p$ 200 GeV are also compared with those in published results for Au + Au at 200 GeV. The nuclear modification factor R_{AA} for 200 GeV Au + Au obtained using the present study in $p + p$ 200 GeV is also presented.

A. p_T spectra

Figure 5 shows transverse momentum spectra for π^\pm , K^\pm , p , and \bar{p} in 200 and 62.4 GeV $p + p$ collisions. Feed-down correction for weak decays is applied for p and \bar{p} , and the same correction factors are consistently used for all figures throughout Sec. IV unless otherwise specified. Each of the p_T spectra is fitted with an exponential functional form:

$$\frac{1}{2\pi p_T} \frac{d^2\sigma}{dy dp_T} = A \exp\left(-\frac{p_T}{T}\right), \quad (9)$$

where A is a normalization factor and T is an inverse slope parameter for p_T . The fitting parameters and χ^2/NDF (where NDF is the number of degrees of freedom) obtained by using Eq. (9) for π^\pm , K^\pm , p , and \bar{p} in 200 and 62.4 GeV $p + p$ collisions are tabulated in Table III. The fitting range is fixed as $p_T = 0.5\text{--}1.5 \text{ GeV}/c$ for π^\pm , $0.6\text{--}2.0 \text{ GeV}/c$ for K^\pm , and $0.8\text{--}2.5 \text{ GeV}/c$ for p , \bar{p} at both collision energies.

Figure 5 shows that pions, protons, and antiprotons exhibit an exponential spectral shape at low p_T and a power-law shape at high p_T , while kaons are exponential in the measured p_T range. The transition from exponential to power law can be better seen at $p_T \sim 2 \text{ GeV}/c$ for pions and at $p_T \sim 3 \text{ GeV}/c$ for protons and antiprotons at both energies. The fractions of soft and hard components gradually change in the transition region.

Ratios of the p_T spectra at 200 GeV to those at 62.4 GeV are shown in the bottom plot of Fig. 5. The left panel shows the ratios for positively charged particles and the right panel those for the negatively charged particles. The data for neutral pions [30,34] are also shown on both panels. The ratios show a clear increase as a function of p_T for all the ratios. Since hard scattering is expected to be the dominant particle production process at high p_T , this strong p_T dependence indicates two features: (1) the spectral shape is harder for

200 GeV compared to that for 62.4 GeV, and (2) there is a universal shape for all particle species up to $p_T = 2\text{--}3 \text{ GeV}/c$. In the same figure, the results from NLO pQCD calculations with the de Florian–Sassot–Stratmann (DSS) fragmentation function [38,39] for pions with different factorization, fragmentation, and renormalization scales (which are equal) are also shown. The agreement is relatively poor, due to the disagreement between the NLO pQCD calculation [38,39] with DSS fragmentation function and measurement for pions at $\sqrt{s} = 62.4 \text{ GeV}$. As we will discuss in detail in Sec. V C, it is found that NLL pQCD [40,41] gives a better description of the data for $p + p$ at 62.4 GeV.

Please note that each line in pQCD is calculated for each μ ($= p_T/2, p_T, 2p_T$) value. The hard scale resides in the hard scattering, which is expected to be the same regardless of hadron species. The theoretical uncertainty in the ratio of NLO [38,39] (200 GeV)/(62.4 GeV) significantly cancels. The same comparison of ratio for NLL results cannot be made due to the unreliability of resummation in NLL pQCD at 200 GeV in the low- p_T region [51].

B. m_T spectra

In $p + p$ (\bar{p}) collisions at high energies, the transverse mass (m_T) spectra of identified hadrons show a universal scaling behavior, and this fact is known as m_T scaling. In order to check the m_T scaling and to gain a further insight into the particle production mechanism especially at high p_T at RHIC energies, transverse mass spectra in 200 and 62.4 GeV $p + p$ collisions are shown in Fig. 6. The data for π^\pm , K^\pm , p , and \bar{p} in 200 and 62.4 GeV are from this study. The π^0 spectra are taken from the PHENIX measurements [30,34]. From the STAR experiment, π^\pm , p , and \bar{p} spectra in 200 GeV $p + p$ are taken from [33]; and K_s^0 , Λ , and $\bar{\Lambda}$ spectra in 200 GeV $p + p$ are taken from [31]. The π^\pm , K^\pm , p , and \bar{p} spectra in 63 GeV $p + p$ are from [13], and Λ and $\bar{\Lambda}$ spectra in 63 GeV $p + p$ are from the ISR experiment [25]. For both energies one can see similar spectral shapes that differ in normalization. To see the similarities or differences of spectral shapes in m_T more clearly, we normalize the yield of each particle species to that of charged pions in the range $m_T = 1.0\text{--}1.5 \text{ GeV}/c^2$. The scaling factors are given in Table IV.

Figure 7 shows the m_T spectra with such scaling factors implemented. These normalization scaling factors are determined to match the yield of each particle species to that of charged pions in the range of $m_T = 1.0\text{--}1.5 \text{ GeV}/c^2$. The bottom panels on the plots in Fig. 7 are the ratio of data to the fitting result using a Tsallis function [52] for π^0 data at 200 GeV [30] and 62.4 GeV [34]. Above $m_T > 1.5 \text{ GeV}/c^2$, these figures indicate a clear separation between meson and baryon spectra. The meson spectra are apparently harder than the baryon spectra in this representation. This effect can be seen more clearly on the $\sqrt{s} = 200 \text{ GeV}$ data set than on data measured at 62.4 GeV. Such a baryon-meson splitting in m_T spectra have been reported by the STAR experiment in $p + p$ collisions at $\sqrt{s} = 200 \text{ GeV}$ [31]. The authors of [31] argued that, for a given jet energy, mesons might be produced with higher transverse momentum than baryons, because meson production in jet fragmentation requires only

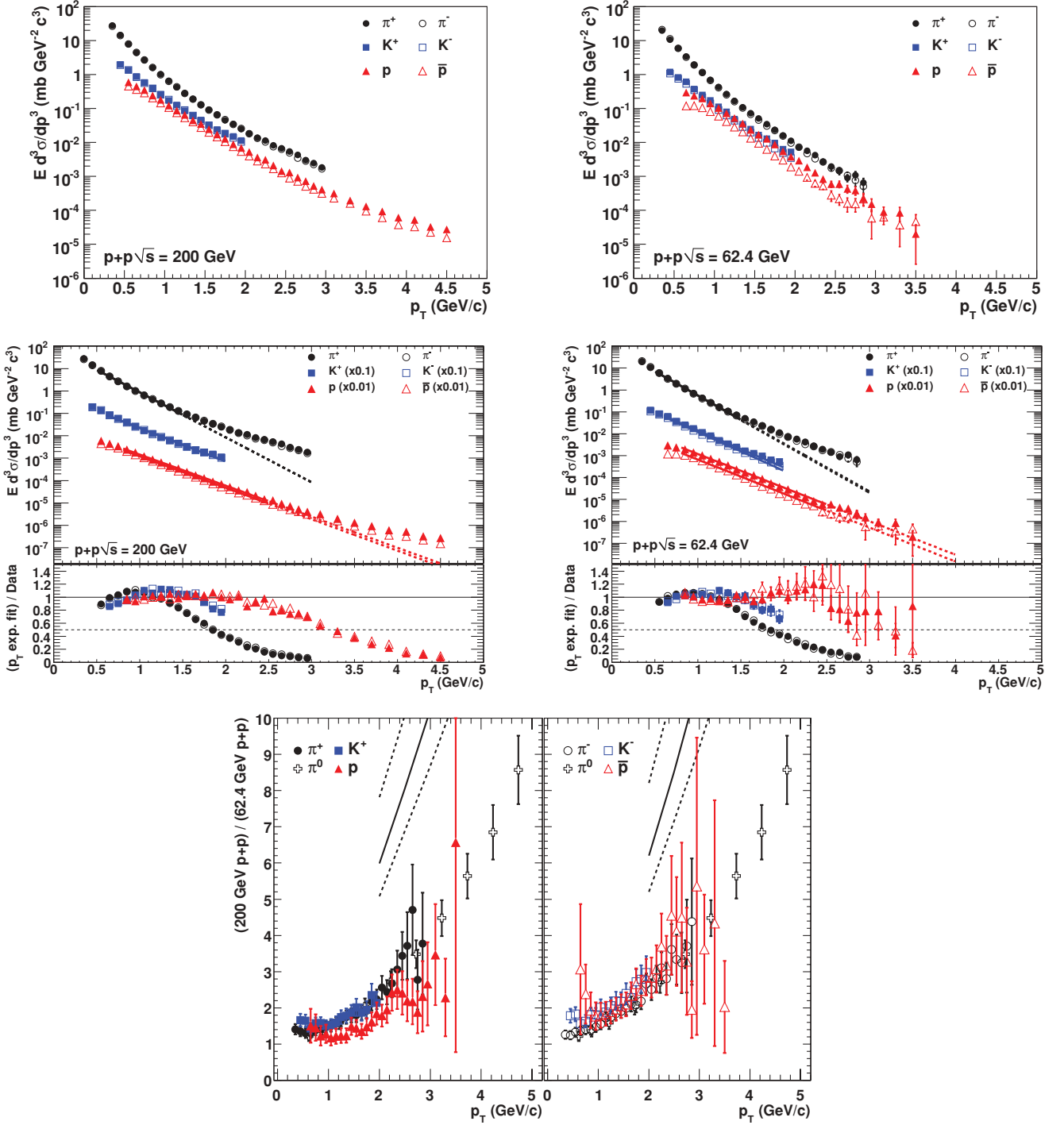


FIG. 5. (Color online) (Top, middle) Transverse momentum distributions for π^\pm , K^\pm , p , and \bar{p} in $p + p$ collisions at $\sqrt{s} =$ (left) 200 and (right) 62.4 GeV at midrapidity. Only statistical uncertainties are shown. (Middle plots) Each spectrum is fitted with an exponential function. (Lower panels of middle plots) Ratio of the exponential fit to data for each particle species. (Bottom) Ratios of p_T spectra for π^\pm , π^0 [30,34], K^\pm , p , and \bar{p} in 200 GeV $p + p$ collisions to those in 62.4 GeV $p + p$ collisions. Statistical and systematic uncertainties are combined in quadrature. The trigger cross section uncertainty is not included. The lines represent the NLO pQCD calculations [38,39] (DSS fragmentation function) for pions with different factorization, fragmentation, and renormalization scales (which are equal).

a (quark, antiquark) pair, while baryon production requires a (diquark, antidiquark) pair.

Instead of using the scaling factors obtained from the low- m_T region as listed in Table IV, one can introduce another set

of scaling factors to match m_T spectra at higher m_T , because the spectral shapes for different particle species in the high- p_T region in the 200 GeV data are also very similar [28]. In this case, m_T spectra for baryons overshoot those for mesons at low

TABLE III. Fitting results for A, T of Eq. (9) for p_T spectra for π^\pm, K^\pm, p , and \bar{p} in 200 and 62.4 GeV $p + p$ collisions. The fitting range is fixed as $p_T = 0.5\text{--}1.5 \text{ GeV}/c$ for π^\pm , $0.6\text{--}2.0 \text{ GeV}/c$ for K^\pm , and $0.8\text{--}2.5 \text{ GeV}/c$ for p, \bar{p} at both collision energies.

\sqrt{s} (GeV)	Hadron	A	T (GeV/c)	χ^2/NDF
200	π^+	80.1 ± 7.2	0.220 ± 0.004	11.5/8
	π^-	80.7 ± 7.5	0.220 ± 0.004	13.5/8
	K^+	6.45 ± 0.50	0.296 ± 0.005	29.4/12
	K^-	6.62 ± 0.51	0.293 ± 0.004	18.8/12
	p	3.24 ± 0.38	0.318 ± 0.006	3.3/15
	\bar{p}	2.83 ± 0.35	0.318 ± 0.006	2.8/15
	π^+	78.0 ± 7.0	0.203 ± 0.003	9.0/8
	π^-	81.0 ± 6.2	0.200 ± 0.003	11.1/8
	K^+	6.17 ± 0.52	0.264 ± 0.004	15.6/12
	K^-	6.01 ± 0.49	0.254 ± 0.004	10.0/12
	p	4.61 ± 0.48	0.275 ± 0.005	2.8/15
	\bar{p}	2.95 ± 0.36	0.267 ± 0.005	2.9/15

m_T [28]. In Sec. IV C, we discuss the spectral shape at low m_T in detail, by taking into account the hadron mass effect.

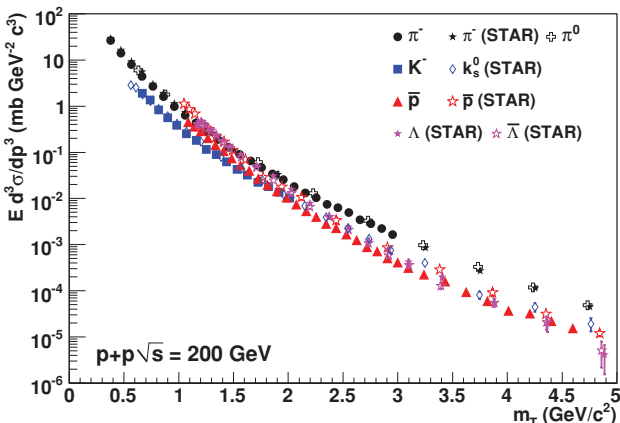
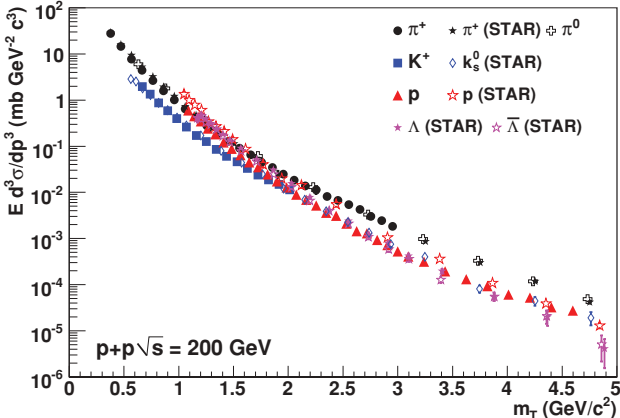


TABLE IV. Normalization scaling factors for m_T spectra for Fig. 7. The scaling factors for the STAR experiment are determined from [31,33] and those for the ISR results are determined from [25].

\sqrt{s} (GeV)	Expt.	π^+	π^-	π^0	K^+	K^-	K_s^0	p	\bar{p}	Λ	$\bar{\Lambda}$
200	PHENIX	1.0	1.0	0.9	2.4	2.4	—	1.15	1.4	—	—
200	STAR	1.0	1.0	—	—	—	2.4	0.75	0.75	0.8	0.9
62.4	PHENIX	1.0	1.0	0.9	2.32	2.88	—	0.9	1.5	—	—
63	ISR	—	—	—	—	—	—	—	—	0.4	0.5

C. $m_T - m$ spectra

Figure 8 shows the $m_T - m$ spectra for π^\pm, K^\pm, p , and \bar{p} in 200 and 62.4 GeV $p + p$ collisions, respectively. When analyzing these $m_T - m$ spectra of various identified hadrons, one discusses the spectral shape mainly in the low- $(m_T - m)$ region. Each of these spectra is fitted with an exponential functional form:

$$\frac{1}{2\pi m_T} \frac{d^2\sigma}{dy dm_T} = A \exp\left(-\frac{m_T - m}{T_{\text{inv}}}\right), \quad (10)$$

where A is a normalization factor and T_{inv} is called the inverse slope parameter. The fitting parameters and χ^2/NDF

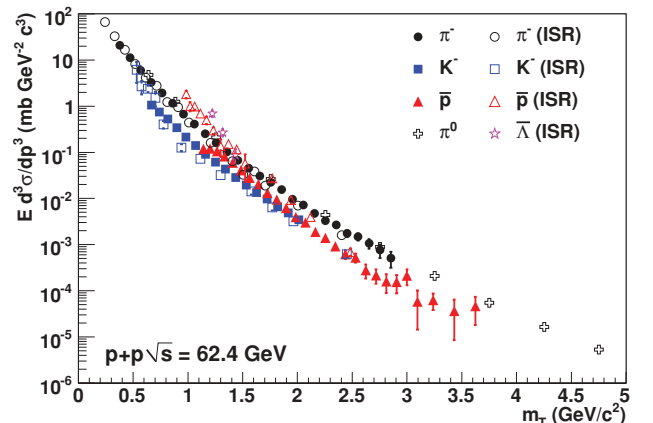
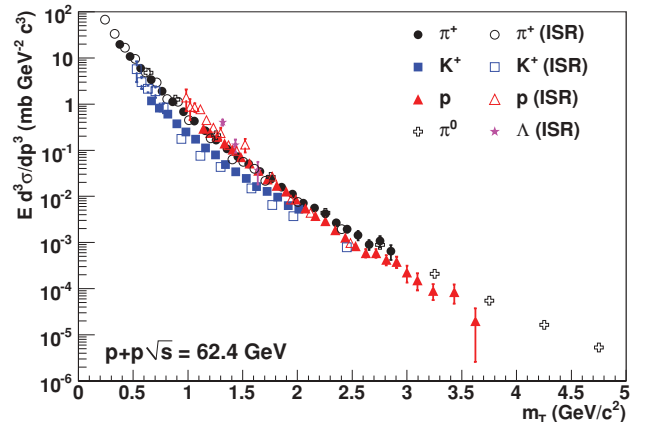


FIG. 6. (Color online) Transverse mass distributions for π^\pm, π^0, K^\pm, p , and \bar{p} in $p + p$ collisions at $\sqrt{s} =$ (left) 200 and (right) 62.4 GeV at midrapidity for (upper) positive and (lower) negative hadrons. Only statistical uncertainties are shown. The references for STAR data are π^\pm, p , and \bar{p} [33] and K_s^0, Λ , and $\bar{\Lambda}$ [31]. The references for ISR data are π^\pm, K^\pm, p , and \bar{p} [13] and Λ and $\bar{\Lambda}$ [25].

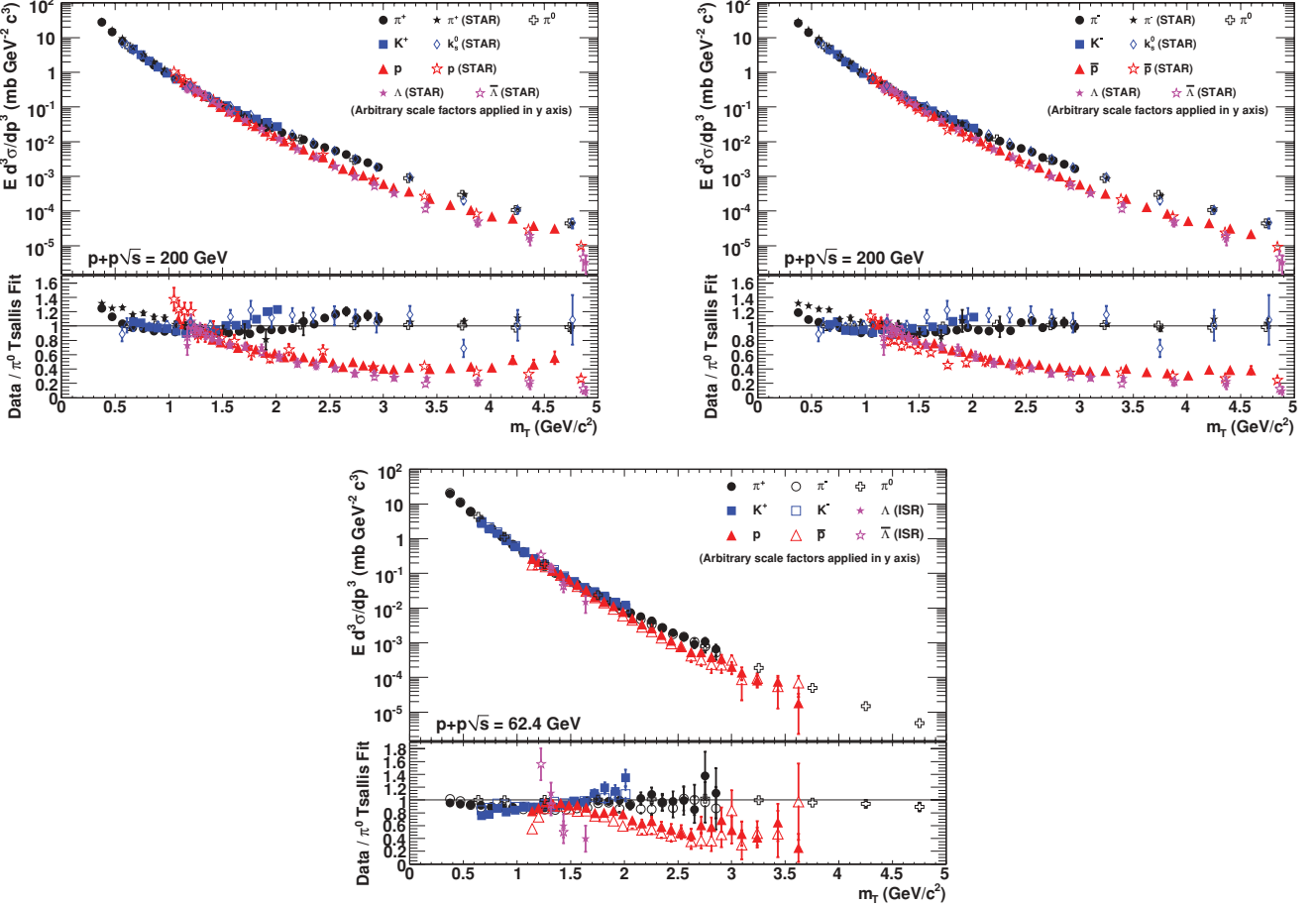


FIG. 7. (Color online) Scaled transverse mass distributions for π^\pm , π^0 , K^\pm , p , and \bar{p} in $p + p$ collisions at $\sqrt{s} =$ (upper) 200 and (lower) 62.4 GeV at midrapidity for (upper left) positive, (upper right) negative, and (lower) \pm hadrons. Only statistical uncertainties are shown. (Upper) The STAR spectra for K_s^0 , Λ , $\bar{\Lambda}$ are from [31]. (Lower) The ISR spectra for Λ , $\bar{\Lambda}$ are from [25]. Arbitrary scaling factors are applied to match the yield of other particles to that of charged pions in the range of $m_T = 1.0\text{--}1.5 \text{ GeV}/c^2$. The lower panels of each plot show the ratio to the π^0 Tsallis fit [52].

obtained by using Eq. (10) for π^\pm , K^\pm , p , and \bar{p} in 200 and 62.4 GeV $p + p$ collisions, are tabulated in Table V. The fitting range is fixed as $m_T - m = 0.3\text{--}1.0 \text{ GeV}/c^2$ for all particle species at both collision energies. We obtain smaller χ^2/NDF for protons and antiprotons than those for pions and kaons, because of the larger systematic uncertainties for p and \bar{p} at low p_T due to the uncertainties of weak decay feed-down corrections. As seen in Fig. 8 the spectra are exponential in the low- $(m_T - m)$ range. At higher transverse mass, the spectra become less steep, corresponding to an emerging power law behavior. The transition from exponential to power law can be seen at $m_T - m = 1\text{--}2 \text{ GeV}/c^2$ for all particle species.

The dependence of T_{inv} on hadron mass is shown in Fig. 9. These slope parameters are almost independent of the energy of $\sqrt{s} = 62.4$ and 200 GeV. The inverse slope parameter of kaons is similar to that of protons while the slope parameter of pions has slightly smaller values. It may be possible that the lower T_{inv} values for pions are due to pions from resonance decays (e.g., ρ , Λ), although such an effect is reduced by the lower transverse momentum cut. An alternative explanation is that hydrodynamical collective behavior may develop even in the small $p + p$ system, which we explore in Sec. V A.

In Fig. 10, the collision energy dependence of T_{inv} is shown by compiling results from past experiments [24,33,53–56]. The values of T_{inv} reported here are obtained by fitting all the p_T spectra in the same way. The fitting range is $m_T - m = 0.3\text{--}1.0 \text{ GeV}/c^2$ for all particle species in all collision systems. The T_{inv} values for RHIC energies are consistent with earlier experimental results at other energies [24,53–56]. For both pions and kaons, the inverse slope parameters increase with collision energy from $T_{\text{inv}} = 120 \text{ MeV}/c^2$ to $170 \text{ MeV}/c^2$ ($240 \text{ MeV}/c^2$) for pions (kaons) up to $\sqrt{s} = 200 \text{ GeV}$. According to Tevatron data, T_{inv} seems to be saturated at \sqrt{s} above 200 GeV. The inverse slope parameters of protons and antiprotons indicate an increase at lower \sqrt{s} which keeps on increasing even at Tevatron energies. We look forward to data from the Large Hadron Collider to further clarify these issues.

D. Particle ratios

Figures 11 and 12 show particle ratios such as antiparticle-to-particle, K/π , and p/π as a function of p_T . The STAR data are from [57] and the ISR data are from [24]. The π^-/π^+ and K^-/K^+ ratios show a flat p_T dependence at both 200

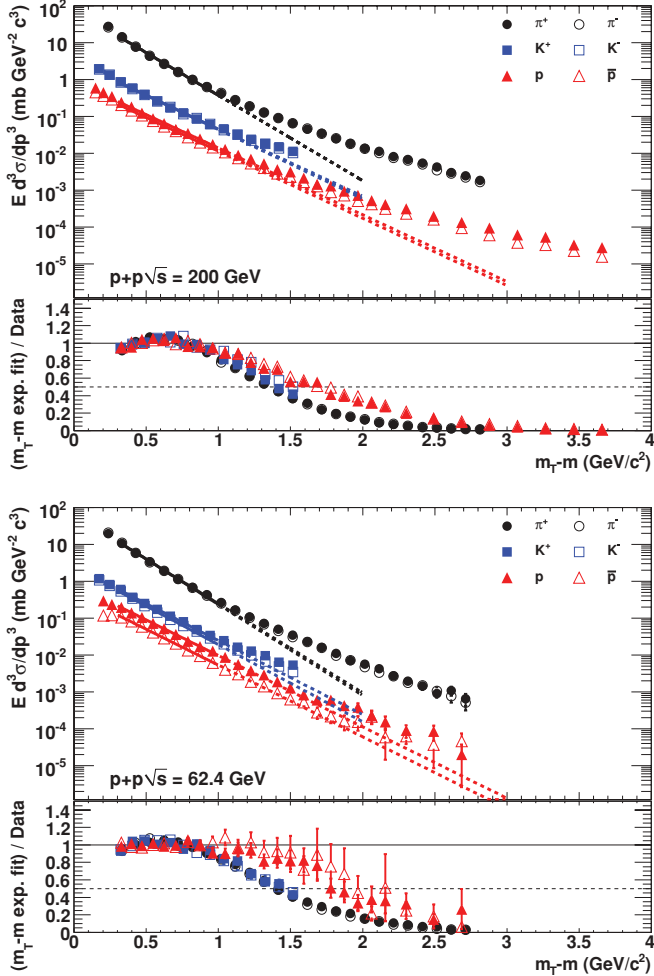


FIG. 8. (Color online) $m_T - m$ spectra for π^\pm , K^\pm , p , and \bar{p} in $p + p$ collisions at $\sqrt{s} =$ (upper) 200 and (lower) 62.4 GeV at midrapidity. Only statistical uncertainties are shown. Each spectrum is fitted with the exponential form of Eq. (10) in the range of $m_T - m = 0.3\text{--}1.0 \text{ GeV}/c^2$. Solid lines represent the functions in the fitted range; dashed lines show the extrapolation of these functions beyond this range. (Lower panels) Ratio of the exponential fit to data for each particle species.

and 62.4 GeV energies. The π^-/π^+ ratio is almost unity at both energies. The K^-/K^+ ratio is consistent with unity at $\sqrt{s} = 200 \text{ GeV}$, while it decreases to 0.8–0.9 in the measured p_T range at 62.4 GeV. On the other hand, the \bar{p}/p ratio seems to be a decreasing function of p_T at 200 GeV, from the value of ≈ 0.8 at $p_T = 1.0 \text{ GeV}/c$ to 0.6 at $p_T = 4.5 \text{ GeV}/c$. Note that we fitted the \bar{p}/p ratio for 200 GeV $p + p$ from $p_T = 1\text{--}4.5 \text{ GeV}/c$ to a linear function, $a + b p_T$, which gives $a = 0.93 \pm 0.02$ and $b = -0.07 \pm 0.01$. This decrease, also seen at lower \sqrt{s} [24], might be the result of a difference of fragmentation between quark jet and gluon jet in the high- p_T region as suggested by the DSS fragmentation functions [51]. However, the NLO pQCD calculation [38,39] using the DSS fragmentation functions (lines on the panels for \bar{p}/p ratios) shows that this effect is in disagreement with the measured \bar{p}/p ratios. At 62.4 GeV, we cannot draw conclusions about the significance of the decrease of the \bar{p}/p ratios as a function

TABLE V. Fitting results for A, T_{inv} of Eq. (10) for π^\pm , K^\pm , p , and \bar{p} in 200 and 62.4 GeV $p + p$ collisions. The fitting range is fixed as $m_T - m = 0.3\text{--}1.0 \text{ GeV}/c^2$ for all particle species at both collision energies.

\sqrt{s} (GeV)	Hadron	A	T_{inv} (GeV/ c^2)	χ^2/NDF
200	π^+	73.4 ± 7.1	0.190 ± 0.005	5.6/5
	π^-	74.8 ± 7.2	0.189 ± 0.005	3.1/5
	K^+	3.25 ± 0.29	0.232 ± 0.007	3.6/6
	K^-	2.99 ± 0.27	0.239 ± 0.008	3.6/6
	p	0.85 ± 0.14	0.245 ± 0.014	1.0/7
	\bar{p}	0.74 ± 0.13	0.241 ± 0.014	0.5/7
62.4	π^+	61.7 ± 5.9	0.182 ± 0.005	3.1/5
	π^-	65.2 ± 5.3	0.179 ± 0.004	4.7/5
	K^+	2.44 ± 0.22	0.219 ± 0.007	2.6/6
	K^-	2.21 ± 0.20	0.213 ± 0.006	4.6/6
	p	0.81 ± 0.10	0.227 ± 0.010	1.1/7
	\bar{p}	0.49 ± 0.07	0.221 ± 0.010	0.3/7

of p_T due to large statistical fluctuations. It is important to note the agreement of the ISR measurements of the antiparticle-to-particle ratios as a function of p_T at $\sqrt{s} = 62.4 \text{ GeV}$ (Fig. 11) with the present measurements except for the \bar{p}/p ratio, where there is a large discrepancy. The \bar{p}/p ratio integrated over all p_T decreases from 0.8 at 200 GeV to 0.5 at 62.4 GeV (see further discussion in Sec. IV E). At low p_T , the large systematic uncertainties of the \bar{p}/p ratio are due to the uncertainties of the weak decay feed-down corrections.

Figure 12 presents the ratios of K^+/π^+ , K^-/π^- , p/π^+ , p/π^0 , \bar{p}/π^- , and \bar{p}/π^0 as a function of p_T . Both the K^+/π^+ and the K^-/π^- ratios increase with increasing p_T up to the $p_T = 2 \text{ GeV}/c$ limit of the measurement. Both the p/π^0 and the \bar{p}/π^0 ratios seem to increase with p_T for $p_T > 2 \text{ GeV}/c$, although the \bar{p}/π^0 ratio is relatively flat at $\sqrt{s} = 200 \text{ GeV}$ in the same transverse momentum region. Clearly, better statistics are required to reach a firm conclusion. As a function of \sqrt{s} the K^+/π^+ , \bar{p}/π^- , and \bar{p}/π^0 ratios do not change significantly, while the K^-/π^- ratio increases and the p/π^+ and p/π^0 ratios decrease significantly for $p_T > 1 \text{ GeV}/c$ as the collision energy is increased from $\sqrt{s} = 62.4$ to 200 GeV.

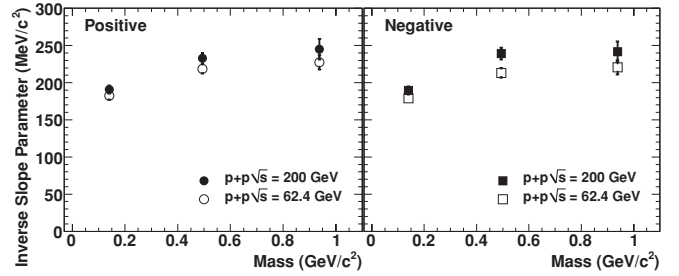


FIG. 9. Inverse slope parameter T_{inv} for π^\pm , K^\pm , p , and \bar{p} in $p + p$ collisions at $\sqrt{s} = 200$ and 62.4 GeV. The fitting range is $m_T - m = 0.3\text{--}1.0 \text{ GeV}/c^2$ for all particle species at both collision energies. The errors are statistical and systematic combined. The statistical errors are negligible.

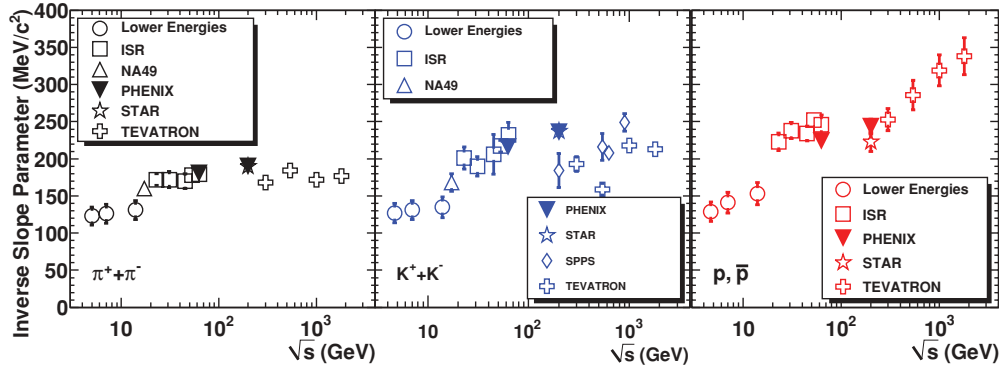


FIG. 10. (Color online) Inverse slope parameter T_{inv} for $\pi^+ + \pi^-$, $K^+ + K^-$, p , and \bar{p} in $p + p$ and $p + \bar{p}$ collisions versus collision energy \sqrt{s} . The fitting range is $m_T - m = 0.3\text{--}1.0 \text{ GeV}/c^2$ for all particle species for all collision systems. The errors are statistical and systematic combined. The statistical errors are negligible. The other experimental data are taken from [24,33,53–56].

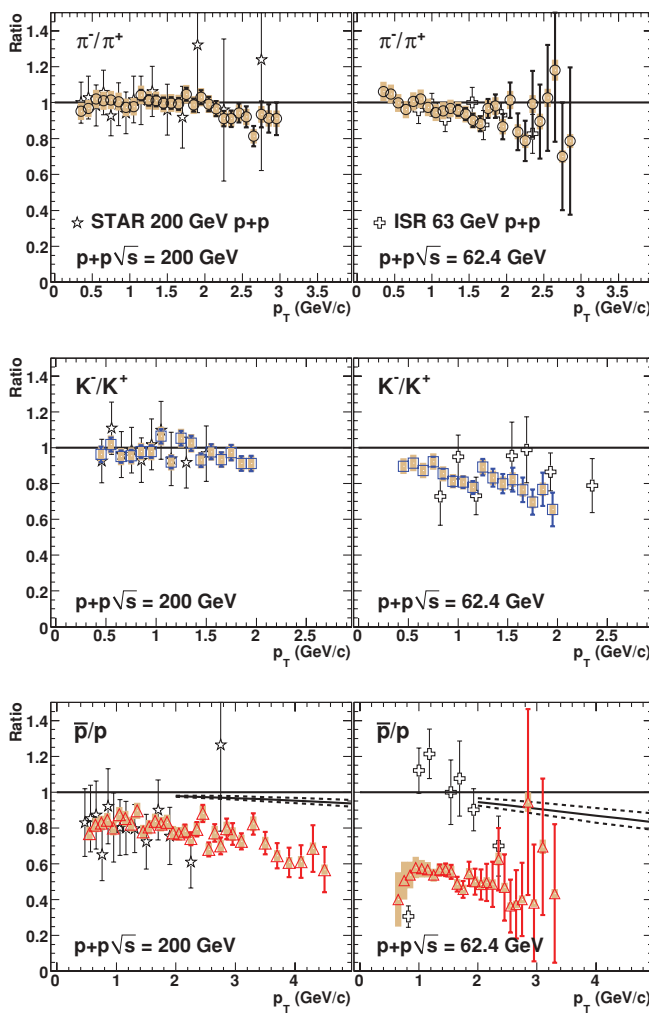


FIG. 11. (Color online) π^-/π^+ , K^-/K^+ , and \bar{p}/p ratios as a function of p_T in $p + p$ collisions at $\sqrt{s} =$ (left) 200 and (right) 62.4 GeV. Systematic uncertainties are shown as vertical shaded band. The STAR data are from [57] and the ISR data are from [24]. For \bar{p}/p ratios, the NLO pQCD calculations using the DSS fragmentation functions [38,39] are also shown as (solid lines) $\mu = p_T$ and (dashed lines) $\mu = 2p_T, p_T/2$.

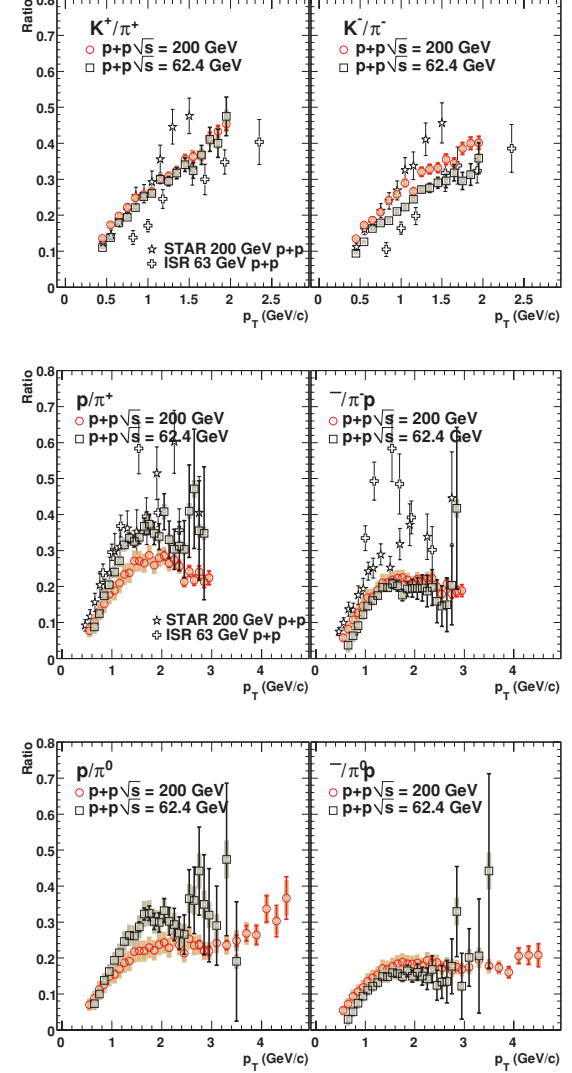


FIG. 12. (Color online) (Top) K^+/π^+ and K^-/π^- ratios, (middle) p/π^+ , and (bottom) \bar{p}/π^- ratios, and (bottom) p/π^0 and \bar{p}/π^0 ratios as a function of p_T in $p + p$ collisions at $\sqrt{s} =$ (left) 200 and (right) 62.4 GeV. Systematic uncertainties are shown as vertical shaded bands.

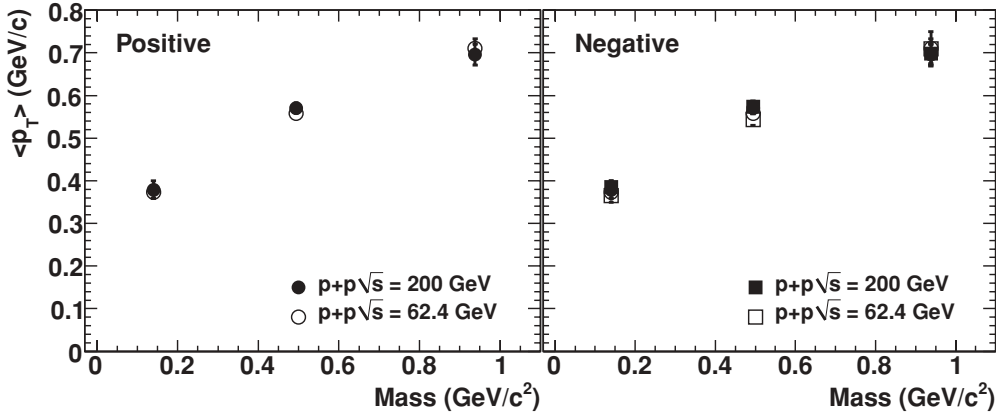


FIG. 13. Mean transverse momentum $\langle p_T \rangle$ as a function of mass in $p + p$ collisions at $\sqrt{s} = 200$ and 62.4 GeV. The errors are statistical and systematic combined. The statistical errors are negligible.

E. $\langle p_T \rangle$ and dN/dy

The mean transverse momentum $\langle p_T \rangle$ and particle yield per unit rapidity dN/dy are determined by integrating the measured p_T spectrum for each particle species. For the unmeasured p_T region, we fit the measured p_T spectrum with a Tsallis function [52] given below, as in a related publication [28], and also with an m_T exponential function, and then extrapolate the function obtained to the unmeasured p_T region. The p_T ranges for fitting are 0.4–3.0 GeV/c for pions, 0.4–2.0 GeV/c for kaons, and 0.5–4.0 GeV/c for protons and antiprotons.

The final yield dN/dy is calculated by taking the sum of the yield from the data and the yield from the functional form in the unmeasured p_T region. The total inelastic cross sections are assumed to be 42.0 and 35.6 mb for 200 and 62.4 GeV, respectively. For $\langle p_T \rangle$, we integrate the measured p_T spectrum with p_T weighting, and then divide it by the obtained dN/dy . The final values are obtained by averaging the results of the two fits. The systematic uncertainties are evaluated as half of the difference between these fitting values.

(a) The Tsallis distribution is given by Eq. (11) below. In this fitting form, the free parameters are dN/dy , q , and C ,

while the mass m is fixed to the hadron mass. The fitting results are given in Table VI.

$$\frac{1}{2\pi p_T} \frac{d^2N}{dy dp_T} = \frac{dN}{dy} \frac{(q-1)(q-2)}{2\pi qC [qC + m(q-2)]} \times \left[1 + \frac{m_T - m}{qC} \right]^{-q}. \quad (11)$$

(b) The exponential distribution in m_T is given by Eq. (12) below. The free fit parameters are the normalization constant A and the inverse slope parameter T_{inv} .

$$\frac{1}{2\pi p_T} \frac{d^2N}{dy dp_T} = A \exp\left(-\frac{m_T}{T_{\text{inv}}}\right), \quad (12)$$

$$\frac{dN}{dy} = 2\pi A(mT_{\text{inv}} + T_{\text{inv}}^2). \quad (13)$$

The $\langle p_T \rangle$ values obtained are summarized in Table VII. They are plotted in Fig. 13, which indicates a clear increase of $\langle p_T \rangle$ with hadron mass. The values at 200 GeV are almost the same as those for the 62.4 GeV data. If the spectral shape is a pure exponential, $\langle p_T \rangle$ should be equal to $2T_{\text{inv}}$ analytically.

TABLE VI. Fitting results from using the Tsallis distribution [Eq. (11)] for π^\pm , K^\pm , p , and \bar{p} in $p + p$ collisions at $\sqrt{s} = 200$ and 62.4 GeV.

\sqrt{s} (GeV)	Hadron	dN/dy	q	C	χ^2/NDF
200	π^+	0.963 ± 0.071	8.24 ± 0.33	0.115 ± 0.006	4.3/23
	π^-	0.900 ± 0.063	8.95 ± 0.39	0.123 ± 0.006	3.2/23
	K^+	0.108 ± 0.006	6.25 ± 0.64	0.137 ± 0.011	1.6/13
	K^-	0.103 ± 0.005	7.00 ± 0.78	0.147 ± 0.011	2.9/13
	p	0.044 ± 0.004	11.1 ± 1.6	0.184 ± 0.014	4.1/22
	\bar{p}	0.037 ± 0.003	12.0 ± 1.8	0.186 ± 0.014	1.3/22
62.4	π^+	0.782 ± 0.056	12.1 ± 0.9	0.133 ± 0.007	4.6/22
	π^-	0.824 ± 0.053	11.9 ± 0.7	0.128 ± 0.006	4.8/22
	K^+	0.076 ± 0.003	10.2 ± 1.8	0.165 ± 0.012	4.9/13
	K^-	0.067 ± 0.003	11.6 ± 2.1	0.164 ± 0.011	2.2/13
	p	0.040 ± 0.003	24.5 ± 9.9	0.201 ± 0.015	7.1/21
	\bar{p}	0.022 ± 0.002	32.5 ± 21.0	0.202 ± 0.018	7.9/21

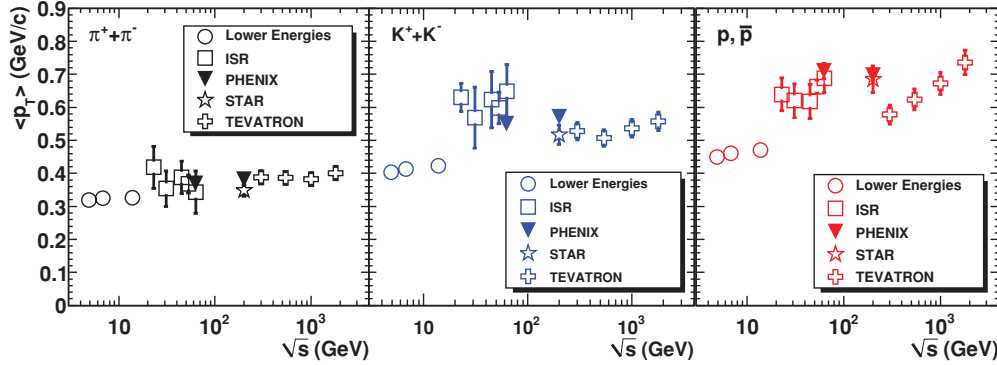


FIG. 14. (Color online) Mean transverse momentum $\langle p_T \rangle$ for $\pi^+ + \pi^-$, $K^+ + K^-$, p , and \bar{p} as a function of \sqrt{s} in $p + p$ and $p + \bar{p}$ collisions [24,33,53,54,58]. The errors are statistical and systematic combined. The statistical errors are negligible.

By comparing Tables V and VII, we see that the measured $\langle p_T \rangle$ is almost $2T_{\text{inv}}$ for pions. But for kaons and (anti)protons, the measured $\langle p_T \rangle$ is systematically larger than $2T_{\text{inv}}$. This demonstrates that the spectral shape at low p_T is not a pure exponential especially for kaons and (anti)protons.

The collision energy dependence of $\langle p_T \rangle$ for each particle type is shown in Fig. 14. Data shown here are as follows: lower-energy data [53], ISR data [24], Tevatron data [54,58], and RHIC data from STAR [33] and PHENIX (present study). The $\langle p_T \rangle$ values for all the other experiments have been determined by fitting the p_T spectra. For pions, the $\langle p_T \rangle$ shows a linear increase in $\ln(\sqrt{s})$. For kaons and (anti)protons the increase is much faster than that for pions. However, systematic issues at both lower- and higher-center-of-mass energies remain to be resolved.

Figure 15 shows the dependence of $\langle p_T \rangle$ on the centrality of the collisions (given by the number of participating nucleons, N_{part}) for π^\pm , K^\pm , p , and \bar{p} in Au + Au collisions at $\sqrt{s_{\text{NN}}} = 200$ GeV [37] as compared to minimum bias $p + p$ collisions at $\sqrt{s} = 200$ GeV (present analysis). The error bars in the figure represent the statistical errors. The systematic errors from cut conditions are shown as shaded boxes on the

right for each particle species. The systematic errors from extrapolations, which are scaled by a factor of 2 for clarity, are shown at the bottom for each particle species. It is found that $\langle p_T \rangle$ for all particle species increases from the most peripheral to midcentral collisions, and appears to saturate from the midcentral to central collisions. The $\langle p_T \rangle$ in $p + p$ are consistent with the expectation from the N_{part} dependence in Au + Au, and are similar to the values in peripheral Au + Au.

The dN/dy values at midrapidity are summarized in Table VII. They are plotted in Fig. 16 as a function of hadron mass for both 200 and 62.4 GeV collision energies. There are differences in the yield between 200 and 62.4 GeV especially for kaons and antiprotons, continuing the trend observed at lower \sqrt{s} [24]. It is interesting to note that even in the situation

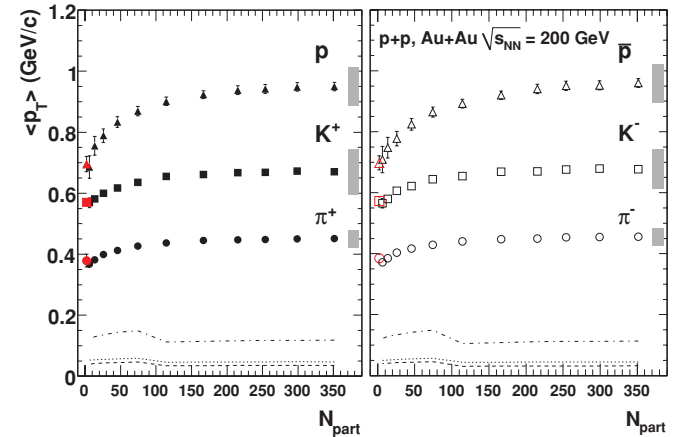


FIG. 15. (Color online) Mean transverse momentum as a function of centrality (N_{part}) for pions, kaons, protons, and antiprotons at $\sqrt{s_{\text{NN}}} = 200$ GeV in the present $p + p$ analysis (lowest N_{part} points, red) and previous Au + Au [37] analysis (all higher N_{part} points, black). The left (right) panel shows the $\langle p_T \rangle$ for positive (negative) particles. The error bars are statistical errors. The systematic errors from cut conditions are shown as shaded boxes on the right for each particle species. The systematic errors from extrapolations, which are scaled by a factor of 2 for clarity, are shown in the bottom for protons and antiprotons (dash-dotted lines), kaons (dotted lines), and pions (dashed lines).

\sqrt{s} (GeV)	Hadron	$\langle p_T \rangle$ (GeV/c)	dN/dy
200	π^+	0.379 ± 0.021	0.842 ± 0.127
	π^-	0.385 ± 0.014	0.810 ± 0.096
	K^+	0.570 ± 0.012	0.099 ± 0.010
	K^-	0.573 ± 0.014	0.096 ± 0.009
	p	0.696 ± 0.025	0.043 ± 0.003
	\bar{p}	0.698 ± 0.023	0.035 ± 0.002
62.4	π^+	0.373 ± 0.013	0.722 ± 0.066
	π^-	0.366 ± 0.016	0.750 ± 0.079
	K^+	0.558 ± 0.012	0.072 ± 0.004
	K^-	0.544 ± 0.013	0.064 ± 0.004
	p	0.710 ± 0.023	0.034 ± 0.002
	\bar{p}	0.709 ± 0.040	0.018 ± 0.001

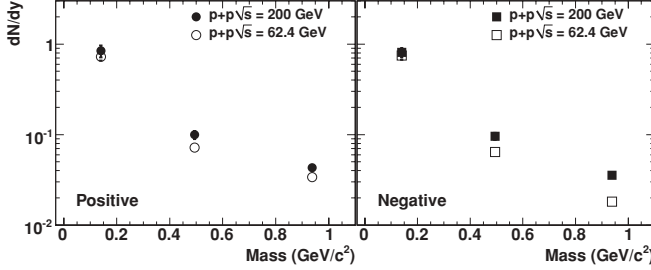


FIG. 16. Particle yield dN/dy as a function of mass in $p + p$ collisions at $\sqrt{s} = 200$ and 62.4 GeV. The errors are statistical and systematic combined. The statistical errors are negligible.

that dN/dy is different between $\sqrt{s} = 200$ and 62.4 GeV, $\langle p_T \rangle$ is quite similar for both energies.

Figure 17 shows dN/dy as a function of collision energy for each particle species. Our results on dN/dy are consistent with those at ISR energies [24]. It should be noted that STAR quotes the nonsingle diffractive (NSD) multiplicity while our measurement quotes the inelastic multiplicity, normalizing the integrated measured inclusive cross section by the total inelastic cross section [59]. At $\sqrt{s} = 200$ GeV, the inelastic cross section (σ_{inel}) is 42 mb [60], and the single diffractive (SD) cross section is almost equal to the double diffractive (DD) cross section, $\sigma_{NN}^{\text{SD}} \approx \sigma_{NN}^{\text{DD}} \approx 4$ mb [61]. As the single diffractive cross section refers only to the projectile proton in a $p + p$ fixed target measurement, one has to subtract the SD cross section for each proton from the inelastic cross section to

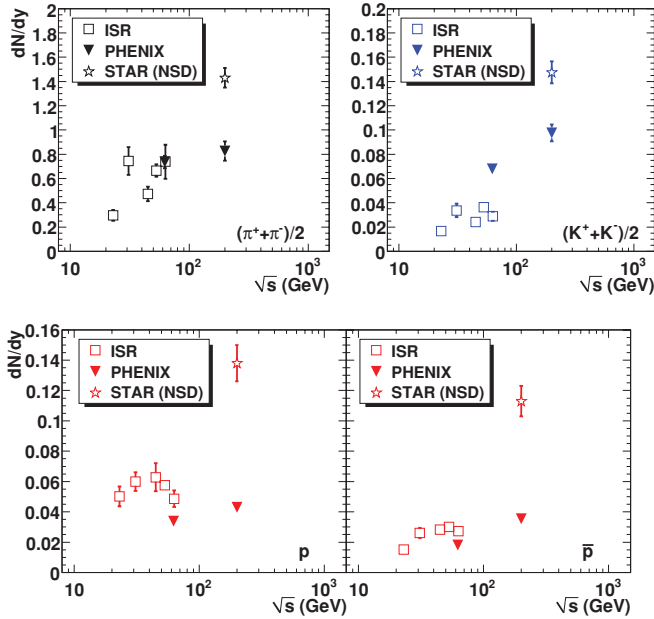


FIG. 17. (Color online) (Upper) Particle yield dN/dy at midrapidity for $(\pi^+ + \pi^-)/2$ and $(K^+ + K^-)/2$ as a function of \sqrt{s} in $p + p$ collisions [24,29]. The errors are statistical and systematic combined, but the statistical errors are negligible. The dN/dy from STAR is determined for NSD $p + p$ events. (Lower) Similar plots for p and \bar{p} with feed-down correction applied to our data. The dN/dy from STAR is determined for NSD $p + p$ events, and is not corrected for weak decay feed-down.

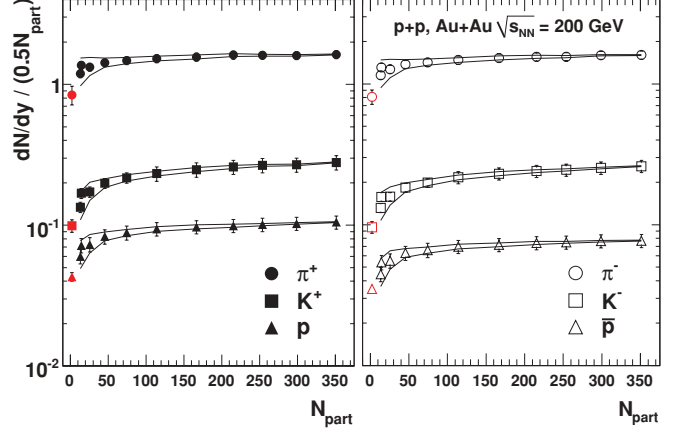


FIG. 18. (Color online) Particle yield per unit rapidity (dN/dy) per participant pair ($0.5N_{\text{part}}$) at $\sqrt{s_{NN}} = 200$ GeV as a function of N_{part} for pions, kaons, protons, and antiprotons in the present $p + p$ analysis (lowest N_{part} points, red) and previous $Au + Au$ [37] analysis (all higher N_{part} points, black). The left (right) panel shows the dN/dy for positive (negative) particles. The error bars represent the quadratic sum of statistical errors and systematic errors from cut conditions. The lines represent the effect of the systematic error on N_{part} , which affects all curves in the same way.

determine the NSD cross section [62]. The resulting NSD cross section (σ^{NSD}) should be $42 - 2 \times 4$ mb = 34 mb. The ratio of the NSD multiplicity to the inelastic multiplicity is $\sigma_{\text{inel}}/\sigma^{\text{NSD}} = 42/34 = 1.24$, i.e., the NSD multiplicity is 24% higher than the inelastic multiplicity, and this effect can actually be seen in the experimental data [63].

We would like to point out also that the NSD charged particle multiplicity at $\sqrt{s} = 200$ GeV by STAR is $\approx 20\%$ larger than other NSD results [63]. By taking this fact and the difference between NSD and inelastic cross sections into account, one can understand the $\approx 50\%$ difference in yields between STAR and the present analysis, for pions and kaons, as shown in Fig. 17. For protons and antiprotons the difference between STAR and the present analysis is larger than those in pions and kaons. In addition to the effects we have mentioned above, the weak decay feed-down correction can contribute to it, since we remove p and \bar{p} from the weak decay (see Sec. III D), while STAR does not.

Figure 18 shows the collision centrality dependence of dN/dy per participant pair ($0.5N_{\text{part}}$) in $p + p$ (present analysis) and $Au + Au$ [37] collisions at $\sqrt{s_{NN}} = 200$ GeV. The error bars on each point represent the quadratic sum of the statistical errors and systematic errors from cut conditions. The statistical errors are negligible. The lines represent the effect of the systematic error on N_{part} , which affects all curves in the same way. The data indicate that dN/dy per participant pair increases for all particle species with N_{part} up to ≈ 100 , and saturates from the midcentral to the most central collisions. As seen in Fig. 15 for $\langle p_T \rangle$, the dN/dy values in $p + p$ are consistent with the expectation from the N_{part} dependence in $Au + Au$.

TABLE VIII. Inverse slope parameter T_{inv} for π^\pm , K^\pm , p , and \bar{p} for $p + p$ collisions at $\sqrt{s} = 200$ and 62.4 GeV. The fit ranges are 0.2–1.0 GeV/c^2 for pions and 0.1–1.0 GeV/c^2 for kaons, protons, and antiprotons in $m_T - m$. These fit ranges are chosen in order to perform a comparison with T_{inv} in Au + Au collisions at RHIC [37]. The errors are statistical and systematic combined, but the statistical errors are negligible.

\sqrt{s} (GeV)	Hadron	T_{inv} (MeV/c^2)	χ^2/NDF
200	π^+	183 ± 4	12.9/6
	π^-	184 ± 4	7.5/6
	K^+	221 ± 5	10.0/8
	K^-	225 ± 6	12.4/8
	p	236 ± 10	2.3/10
	\bar{p}	235 ± 10	1.2/10
	π^+	178 ± 4	5.7/6
62.4	π^-	174 ± 3	9.8/6
	K^+	216 ± 5	3.0/8
	K^-	209 ± 5	5.3/8
	p	230 ± 8	1.4/9
	\bar{p}	225 ± 9	2.0/9

F. Nuclear modification factor R_{AA}

In order to quantify the modification effect in nucleus-nucleus ($A + A$) collisions with respect to nucleon-nucleon collisions, the nuclear modification factor R_{AA} is used. R_{AA} is the ratio between the yield in $A + A$ scaled by the average number of binary nucleon-nucleon collisions ($\langle N_{\text{coll}} \rangle$) and the yield in $p + p$, as defined by the following equation:

$$R_{AA}(p_T) = \frac{(1/N_{AA}^{\text{evt}}) d^2N_{AA}/dp_T dy}{\langle T_{AA} \rangle \times d^2\sigma_{pp}/dp_T dy} \quad (14)$$

where $\langle T_{AA} \rangle$ is the nuclear thickness function, defined as follows: $\langle T_{AA} \rangle = \langle N_{\text{coll}} \rangle / \sigma_{pp}^{\text{inel}}$. For the total $A + A$ interaction cross section σ_{AA}^{int} (minimum bias $A + A$ collisions), $\langle T_{AA} \rangle = A^2 / \sigma_{AA}^{\text{int}}$.

In general, R_{AA} is expressed as a function of p_T and collision centrality for $A + A$ collisions. Due to the dominance of hard scatterings of partons at high p_T , R_{AA} is expected to be around unity above $p_T \approx 2 \text{ GeV}/c$, if there is no yield modification by the nucleus in $A + A$. If there is a suppression (enhancement), R_{AA} is less than (greater than) unity. For the total $A + A$ interaction cross section at a given p_T integrated over centrality (minimum bias $A + A$ collisions) $\sigma_{AA}(p_T) = A^2 \sigma_{pp}(p_T)$ and $R_{AA}(p_T) \equiv 1.0$.

Figure 19 shows the R_{AA} of π^\pm , π^0 , K^\pm , p , and \bar{p} in Au + Au collisions at $\sqrt{s_{NN}} = 200 \text{ GeV}$ at 0%–5% collision centrality. The data for identified charged hadrons in Au + Au at $\sqrt{s_{NN}} = 200 \text{ GeV}$ are taken from [37] measured by the PHENIX experiment, and those for $p + p$ are taken from the present analysis at $\sqrt{s} = 200 \text{ GeV}$. The R_{AA} for neutral pions is taken from [64]. The overall normalization uncertainty on R_{AA} (13.8%) is shown as a shaded box around unity (at $p_T = 0.1 \text{ GeV}/c$); it is the quadratic sum of (1) the uncertainty of the $p + p$ inelastic cross section (9.7%) and (2) the uncertainty $\langle N_{\text{coll}} \rangle$ (9.9%).

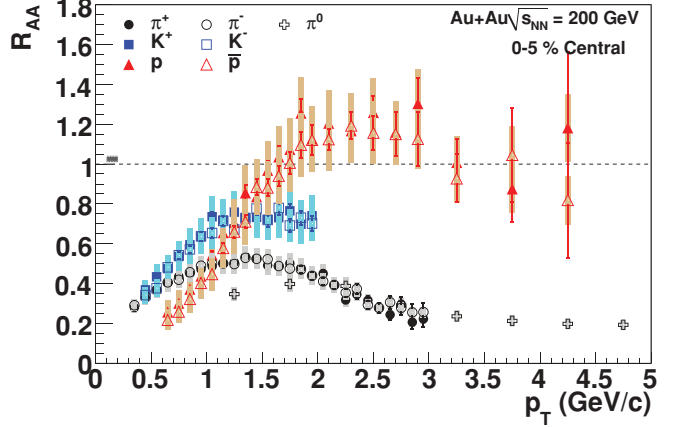


FIG. 19. (Color online) R_{AA} of π^\pm , π^0 , K^\pm , p , and \bar{p} in Au + Au collisions at $\sqrt{s_{NN}} = 200 \text{ GeV}$ at 0%–5% collision centrality. The data for identified charged hadrons in Au + Au at $\sqrt{s_{NN}} = 200 \text{ GeV}$ are taken from [37] and those for $p + p$ from the present analysis at $\sqrt{s} = 200 \text{ GeV}$. The neutral pion data (PHENIX) are taken from [64]. The statistical uncertainties are shown as bars and the systematic uncertainties are shown as shaded boxes on each data point. The overall normalization uncertainty on R_{AA} (13.8%) is shown in the shaded box around unity (at $p_T = 0.1 \text{ GeV}/c$), which is the quadratic sum of (1) the uncertainty of $p + p$ inelastic cross sections (9.7%) and (2) the uncertainty $\langle N_{\text{coll}} \rangle$ (9.9%).

For pions R_{AA} is greatly suppressed by a factor of ≈ 5 , compared to $p + p$. This suppression effect is understood to be due to jet quenching or energy loss of partons in the hot and dense medium created in Au + Au central collisions at RHIC energies [65,66]. For kaons there is a similar trend as for pions over a more limited p_T range. For protons and antiprotons there is an enhancement in $p_T = 2$ –4 GeV/c . As reported in [26,37,67], possible explanations of the observed enhancements include the quark recombination model [68–70] and/or strong partonic and hadronic radial flow [71].

V. DISCUSSION

In this section, we discuss (1) soft particle production at low p_T , including the possibility of radial flow in $p + p$ collisions, and (2) the transition from the soft to the hard process, and hadron fragmentation at high p_T , where we show the x_T scaling of measured spectra, and make a comparison with NLO [38,39] and NLL [40,41] pQCD calculations.

A. Radial flow

In heavy ion collisions at RHIC energies, it is found that the inverse slope parameter (T_{inv}) of $m_T - m$ spectra has a clear dependence on the hadron mass, i.e., heavier particles have larger inverse slope parameters [37,72]. T_{inv} increases almost linearly as a function of particle mass; T_{inv} is largest when the nucleus-nucleus collision has a small impact parameter (central collisions). Also, T_{inv} is smallest for the collisions with a large impact parameter (peripheral collisions), as shown in

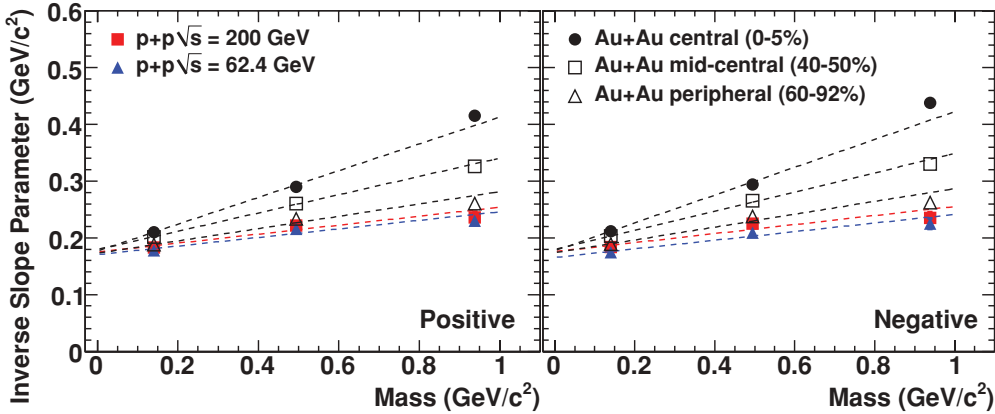


FIG. 20. (Color online) Mass dependence of inverse slope parameter T_{inv} in $m_T - m$ spectra for (left) positive and (right) negative hadrons in $p + p$ collisions at $\sqrt{s} = 200$ and 62.4 GeV, as well as for peripheral, midcentral, and central $\text{Au} + \text{Au}$ collisions at $\sqrt{s_{NN}} = 200$ GeV [37]. The errors are statistical and systematic combined, smaller than the symbols. The statistical errors are negligible. The fit ranges are 0.2 – 1.0 GeV/c^2 for pions and 0.1 – 1.0 GeV/c^2 for kaons, protons, and antiprotons in $m_T - m$ [37]. The dotted lines represent a linear fit of the results for each data set as a function of mass using Eq. (15).

Fig. 20. This experimental observation can be interpreted as the existence of a radial flow generated by violent nucleon-nucleon collisions in two colliding nuclei and developed both in the quark-gluon plasma phase and in hadronic rescatterings [71]. The radial flow velocity increases the transverse momentum of particles proportional to their mass; thus T_{inv} increases linearly as a function of particle mass. It is interesting to determine whether or not such an expansion is observed in high-energy $p + p$ collisions [58].

Figure 20 shows the mass dependence of the inverse slope parameter T_{inv} in $m_T - m$ spectra for positive (left) and negative (right) particles in $p + p$ collisions at $\sqrt{s} = 200$ and 62.4 GeV (also shown in Fig. 9) as well as for peripheral, midcentral, and central $\text{Au} + \text{Au}$ collisions at $\sqrt{s_{NN}} = 200$ GeV [37]. The fit ranges are $m_T - m = 0.2$ – 1.0 GeV/c^2 for pions, and $m_T - m = 0.1$ – 1.0 GeV/c^2 for kaons, protons, and antiprotons, which are chosen in order to perform a fair comparison with T_{inv} in $\text{Au} + \text{Au}$ collisions at RHIC [37]. The values of T_{inv} in $p + p$ for these fit ranges (see Table VIII) are all lower by roughly one standard deviation than the values in Table V for the common fit range of $m_T - m = 0.3$ – 1.0 GeV/c^2 .

In general, the inverse slope parameters increase with increasing particle mass in both $\text{Au} + \text{Au}$ and $p + p$ collisions at 200 GeV. However, this increase is only modest in $p + p$ collisions and slightly weaker than in $60\%-92\%$ central $\text{Au} + \text{Au}$ collisions at 200 GeV.

Also note that there is a mean multiplicity dependence of the transverse momentum spectra in $p + p$ collisions [54] that is not discussed in the present paper.

We use a radial flow picture [73,74] with the fitting function

$$T = T_0 + m\langle u_t \rangle^2, \quad (15)$$

where T_0 is a hadron freeze-out temperature and $\langle u_t \rangle$ is a measure of the strength of the (average radial) transverse flow. The relationship between the averaged transverse velocity

$\langle \beta_t \rangle$ and $\langle u_t \rangle$ is given by

$$\langle \beta_t \rangle = \langle u_t \rangle / \sqrt{1 + \langle u_t \rangle^2}. \quad (16)$$

The dotted lines in Fig. 20 represent the linear fit to the $p + p$ collisions at $\sqrt{s} = 200$ and 62.4 GeV which are compared to those in $\text{Au} + \text{Au}$ collisions at $\sqrt{s_{NN}} = 200$ GeV in three different collision centrality classes. The fit results in $p + p$ are also given in Table IX. For the $\text{Au} + \text{Au}$ most central data ($0\%-5\%$), $\langle u_t \rangle \approx 0.49 \pm 0.07$, while in $p + p$, $\langle u_t \rangle \approx 0.28$ at both 62.4 and 200 GeV. While this radial flow model is consistent with the data in central and midcentral $\text{Au} + \text{Au}$, i.e., the $\pi/K/p$ points are on a straight line, it does not give a good description of either peripheral $\text{Au} + \text{Au}$ or $p + p$ collisions (poor χ^2 in Table IX). Also the data from the STAR experiment [29] show that the transverse flow velocity $\langle \beta \rangle$ extracted by the blast wave model fitting [73] in $p + p$ collisions at $\sqrt{s} = 200$ GeV (0.244 ± 0.081) is smaller than those in central and midcentral $\text{Au} + \text{Au}$ collisions at the same energy [≈ 0.6 in $\text{Au} + \text{Au}$ at $\sqrt{s} = 200$ GeV ($0\%-5\%$)]. These observations provide evidence for the absence of radial flow in $p + p$ collisions, where the $\pi/K/p$ points are obviously not on a straight line (Fig. 9), and that the radial flow develops only for a larger system.

TABLE IX. The extracted fit parameters of the freeze-out temperature (T_0) and the measure of the strength of the average radial transverse flow ($\langle u_t \rangle$) using Eq. (15). The fit results shown here are for positive and negative particles, and for the two different energies.

\sqrt{s} (GeV)	\pm	T_0 (MeV/ c^2)	$\langle u_t \rangle$	χ^2/NDF
200	Positive	175 ± 5	0.28 ± 0.02	4.1/1
	Negative	176 ± 5	0.28 ± 0.02	6.0/1
62.4	Positive	170 ± 5	0.27 ± 0.02	5.4/1
	Negative	165 ± 4	0.28 ± 0.02	3.8/1

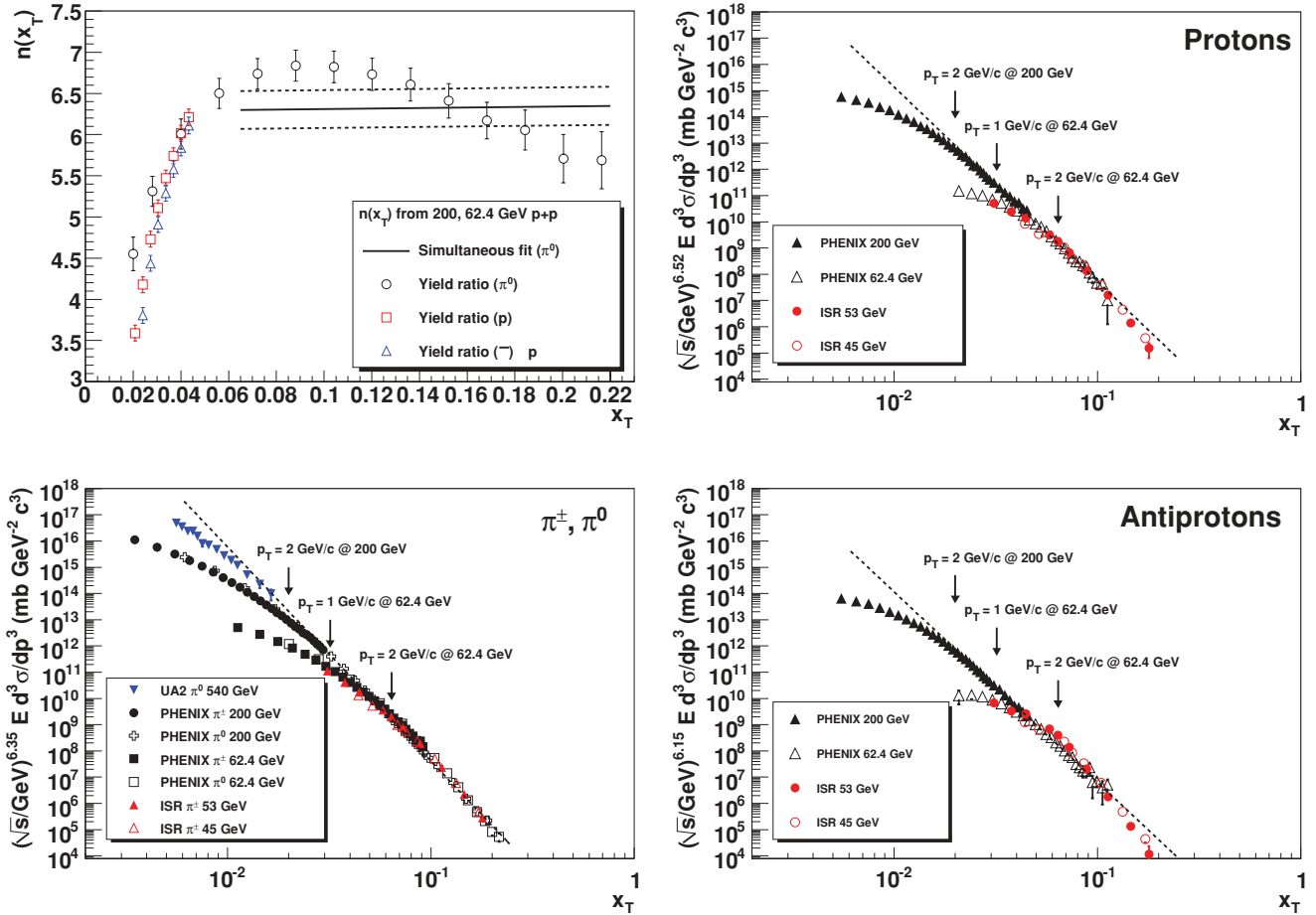


FIG. 21. (Color online) (Upper left) x_T scaling power n_{eff} as determined from the ratios of yields as a function of x_T , for (open circles) neutral pions, (open squares) protons, and (open triangles) antiprotons using $p + p$ data at $\sqrt{s} = 200$ and 62.4 GeV energies. The error of each data point is from the systematic and statistical errors of p_T spectra. The other plots show x_T spectra for (lower left) pions (π^\pm, π^0), (upper right) protons, and (lower right) antiprotons in $p + p$ collisions at different \sqrt{s} at midrapidity. Only statistical uncertainties are shown. The dashed curves are the fitting results.

B. x_T scaling

From the measurements of p_T spectra of hadrons in $p + p$ collisions, it is known that fragmentation of hard scattered partons is the dominant production mechanism of high- p_T hadrons. It has been predicted theoretically from general principles that such a production mechanism leads to a data scaling behavior called “ x_T scaling” [36], where the scaling variable is defined as $x_T = 2p_T/\sqrt{s}$. Such a data scaling behavior was seen first on preliminary ISR data at CERN as reported in [36].

In the kinematic range corresponding to the x_T scaling limit, the invariant cross section near midrapidity can be written as

$$E \frac{d^3\sigma}{dp^3} = \frac{1}{p_T^{n_{\text{eff}}}} F(x_T) = \frac{1}{\sqrt{s}^{n_{\text{eff}}}} G(x_T), \quad (17)$$

where $F(x_T)$ and $G(x_T)$ are universal scaling functions. The parameter n_{eff} is characteristic for the type of interaction between constituent partons. For example, for single-photon or vector gluon exchange, $n_{\text{eff}} = 4$ [1]. Because of higher-order effects, the running of the strong coupling constant $\alpha_s = \alpha_s(Q^2)$, the evolution of the parton distribution functions

and fragmentation functions, and nonvanishing transverse momentum k_T of the initial state, n_{eff} in general is not a constant but a function of x_T and \sqrt{s} , i.e., $n_{\text{eff}} = n_{\text{eff}}(x_T, \sqrt{s})$. This n_{eff} corresponds to the logarithmic variation of yield ratios at the same x_T for different \sqrt{s} [75]. Note that the x_T scaling power n_{eff} is different from the exponent n that characterizes the power-law behavior of the single-particle invariant spectrum at high p_T .

The value of n_{eff} depends on both the value of \sqrt{s} and the range of x_T and, depending on the reaction, tends to settle at an asymptotic value between 6 and 4.5 where hard scattering dominates and higher-twist effects are small. This fact can also be used to determine the transition between soft and hard particle production mechanisms.

Earlier measurements of $n_{\text{eff}}(x_T, \sqrt{s})$ in $p + p$ collisions found values in the range of 5–8 [35,36,76–79]. Here we present the PHENIX results for the x_T scaling of pions, protons, and antiprotons and compare them with earlier data measured at various different values of \sqrt{s} . Due to the limited p_T range of our kaon measurements, kaons are not included in these comparisons.

TABLE X. Summary of x_T scaling power n_{eff} in $p + p$ collisions. The errors are systematic error from the fitting.

Hadron	A	n_{eff}	m	χ^2/NDF
π	0.82 ± 0.08	6.35 ± 0.23	8.16 ± 0.22	156/31
p	1.12 ± 0.17	6.52 ± 0.59	7.41 ± 0.29	40/38
\bar{p}	0.84 ± 0.04	6.15 ± 0.05	7.26 ± 0.07	30/38

We have evaluated the x_T scaling power n_{eff} using two different methods that are both based on Eq. (17):

Method 1 is based on the linear variation of the logarithm of the ratio of the yields at different \sqrt{s} :

$$n_{\text{eff}}(x_T) = \frac{\log[\text{yield}(x_T, 62.4)/\text{yield}(x_T, 200)]}{\log(200/62.4)}. \quad (18)$$

The $n_{\text{eff}}(x_T)$ is shown in Fig. 21 as a function of x_T for neutral pions, protons, and antiprotons for $p + p$ collisions at RHIC.

Method 2 is based on fitting the x_T distributions for a given type of particle measured at different energies. A common fitting function is defined as follows:

$$E \frac{d^3\sigma}{dp^3} = \left(\frac{A}{\sqrt{s}} \right)^{n_{\text{eff}}} x_T^{-m}, \quad (19)$$

limiting the fitting region to the high-transverse-momentum region ($p_T > 2 \text{ GeV}/c$).

The x_T distributions for pions, protons, and antiprotons are shown in Fig. 21. PHENIX data are presented together with earlier data of [24,30,34,80]. Dashed curves show the fitting results. The obtained n_{eff} values are summarized in Table X.

The exponent n_{eff} of the x_T scaling is found to have similar values for different particles, in the range of 6.3–6.5 for pions, protons, and antiprotons. The data points deviate from the x_T scaling in the transverse momentum region of $p_T < 2 \text{ GeV}/c$. This scaling violation may be interpreted as a transition from hard to soft multiparticle production. For the highest x_T points for protons and antiprotons (but not for pions) the asymptotic x_T curve gets steeper. Further measurements at larger x_T , possibly at lower center-of-mass energies, are needed to clarify this point.

C. Comparison to NLO and NLL pQCD calculations

In Figs. 22 and 23, our results for pion, proton, and antiproton p_T spectra at $\sqrt{s} = 200$ and 62.4 GeV in $p + p$ collisions are compared to the NLO pQCD calculations [38,39]. Because of the limited p_T reach in the measurements, the results for charged kaons are not compared to the NLO pQCD calculations. In these NLO pQCD calculations for $\eta < 1$ from Vogelsang [51], the cross section is factorized into initial parton distribution functions (PDFs) in the colliding protons, short-distance partonic hard scattering cross sections which can be evaluated using perturbative QCD, and parton-to-hadron fragmentation functions (FFs).

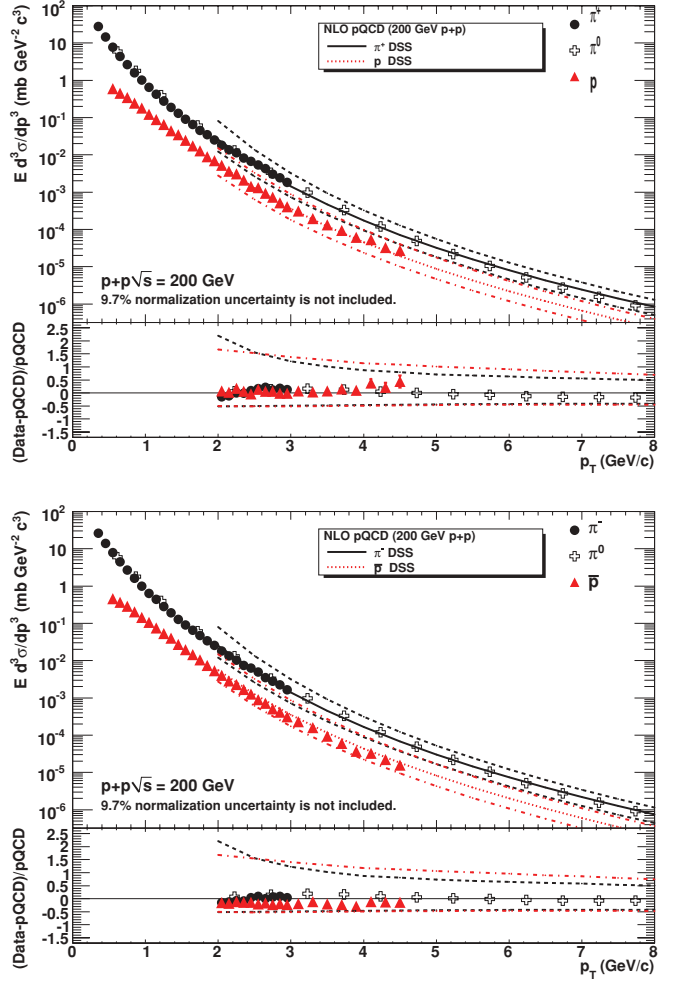


FIG. 22. (Color online) Transverse momentum distributions for (upper) positive and (lower) negative particles at $\sqrt{s} = 200 \text{ GeV}$ in $p + p$ collisions. Only statistical uncertainties are shown. The normalization uncertainty (9.7%) is not included. NLO pQCD calculations [38,39] (DSS fragmentation functions) are also shown. Solid lines are for $\mu = p_T$, and dashed lines are for $\mu = p_T/2, 2p_T$. The lower panel in each plot shows the ratio of (data – pQCD result)/pQCD result for each particle species.

For the description of the initial parton distributions, the Coordinated Theoretical-Experimental Project on QCD (CTEQ6M5) [81] PDFs are used. Different scales $\mu = p_T/2, p_T, 2p_T$ are utilized, which represent factorization, renormalization, and fragmentation scales. These provide initial conditions for the pQCD cross section calculations. Partons are then fragmented to hadrons with the help of the de Florian–Sassot–Stratmann (DSS) set of fragmentation functions which have charge separation [82]. There are several other FFs, such as the Albino–Kniehl–Kramer (AKK) [83] and the Kniehl–Kramer–Potter (KKP) [84]. Only the results for DSS FFs are shown in this paper, because they give better agreement with our measurements than other FFs. For example, in $p + p$ collisions at $\sqrt{s} = 200 \text{ GeV}$ the yields for $(p + \bar{p})/2$ in AKK (KKP) FFs are a factor of 2 smaller (larger) than the present measurement.

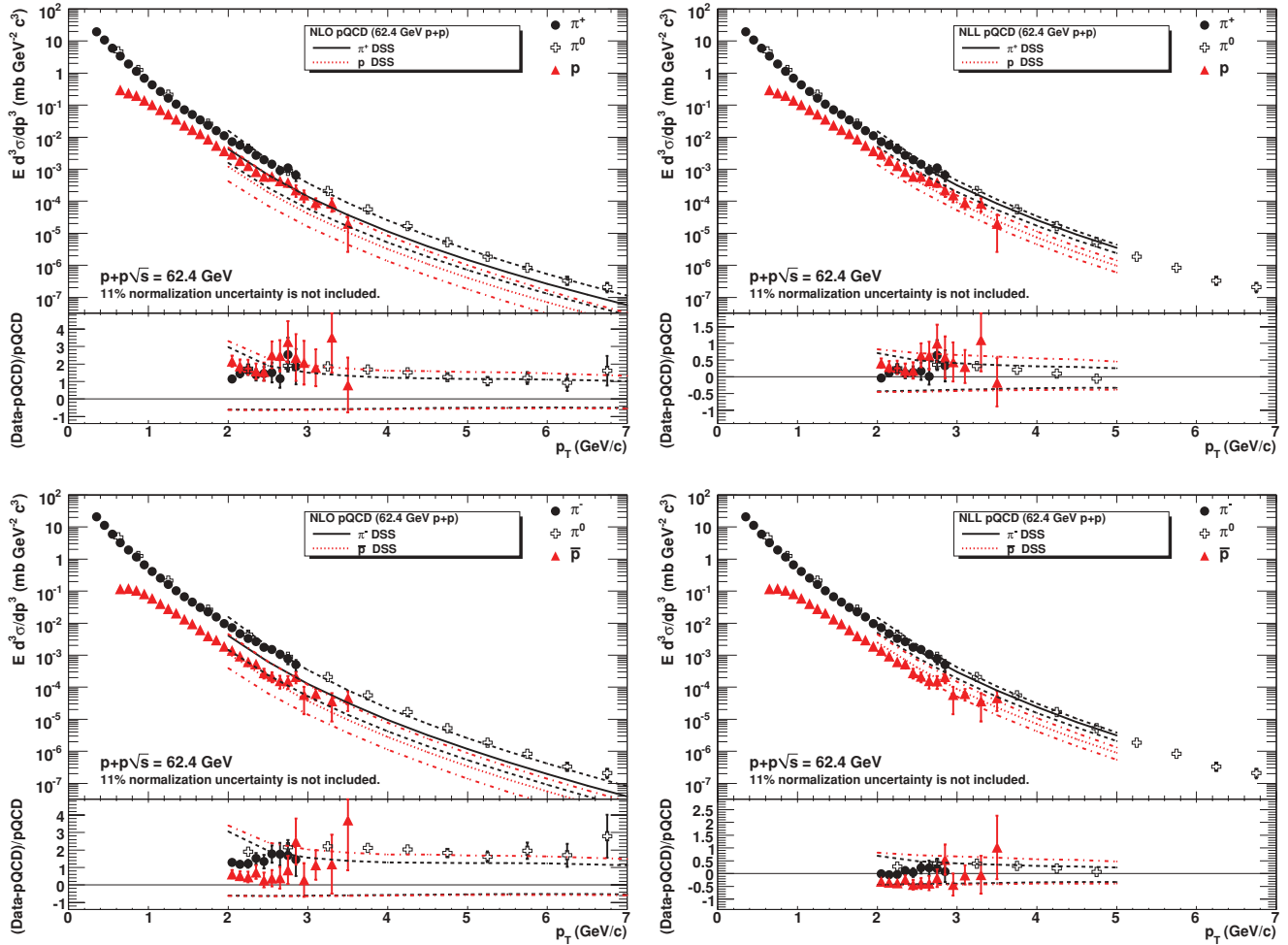


FIG. 23. (Color online) Transverse momentum distributions for (upper) positive and (lower) negative particles at $\sqrt{s} = 62.4$ GeV in $p + p$ collisions. Only statistical uncertainties are shown. The normalization uncertainty (11%) is not included. (Left) NLO [38,39] and (right) NLL pQCD calculations [40,41] (DSS fragmentation functions) are also shown. Solid lines are for $\mu = p_T$, and dashed lines are for $\mu = p_T/2, 2p_T$. The lower panel in each plot shows the ratio of (data – pQCD result)/pQCD result for each particle species.

It is known that pion production in $\sqrt{s} = 200$ GeV $p + p$ collisions is reasonably well described by pQCD down to $p_T \sim 2$ GeV/ c and up to $p_T \sim 20$ GeV/ c [30,33]. However, there are large variations in the p and \bar{p} yields among various fragmentation functions [33], as we mentioned above. From the comparisons between baryon data and pQCD calculations at both $\sqrt{s} = 200$ and 62.4 GeV, it is potentially interesting to obtain a constraint on the fragmentation function, particularly the gluon fragmentation function for p and \bar{p} .

For the DSS fragmentation function, there is good agreement between the data and NLO pQCD calculations for pions and protons at 200 GeV, but not so good agreement with \bar{p} . It is more clearly shown in Fig. 11 that the \bar{p}/p ratio at 200 GeV is not correctly described with the NLO + DSS framework, which indicates that there is still room to improve the DSS fragmentation functions. The left-side plots of Fig. 23 show that for 62.4 GeV NLO + DSS pQCD calculations underestimate yields by a factor of 2 or 3 for all species. However, as it is still on the edge of the scale

uncertainty of the NLO calculation, NLO pQCD agrees with the data within the large uncertainties.

As shown in [34], the NLL calculations [40,41] give much better agreement with the data for π^0 in $p + p$ collisions at $\sqrt{s} = 62.4$ GeV. This means the resummed calculation is necessary to describe the cross section at 62.4 GeV. On the other hand, the resummation for $\sqrt{s} = 200$ GeV is not reliable, since the resummation can be done for a larger $x_T = 2p_T/\sqrt{s}$, which is not accessible for $\sqrt{s} = 200$ GeV data due to the p_T limitation of particle identifications for charged hadrons in PHENIX. The right-side plots of Fig. 23 show the p_T distributions for π^\pm , p , and \bar{p} in $p + p$ collisions at 62.4 GeV, together with the results of NLL pQCD calculations [40,41]. The DSS FFs are used. It is found that the agreement between NLL pQCD and data is better than that for NLO pQCD.

The presented p_T spectra extend to the semihard 3–4 GeV/ c region for pions and (anti)protons, which make them useful as a baseline to study in further detail the nuclear modification factor in $A + A$ collisions. More detailed measurements at larger p_T are necessary for the further understanding of

FFs and their particle species dependence at each beam energy.

VI. SUMMARY AND CONCLUSION

We have presented transverse momentum distributions and yields for π^\pm , K^\pm , p , and \bar{p} in $p + p$ collisions at $\sqrt{s} = 200$ and 62.4 GeV at midrapidity, which provide an important baseline for heavy-ion-collision measurements at RHIC. The inverse slope parameter T_{inv} , mean transverse momentum $\langle p_T \rangle$, and yield per unit rapidity dN/dy are compared to the measurements at different \sqrt{s} in $p + p$ and $p + \bar{p}$ collisions. While T_{inv} and $\langle p_T \rangle$ show a similar value for all particle species between 200 and 62.4 GeV, dN/dy shows a relatively large difference, especially for kaons and antiprotons, between 200 and 62.4 GeV. The \bar{p}/p ratio is ~ 0.8 at 200 GeV and ~ 0.5 at 62.4 GeV and the p_T dependence of the p/π^+ (p/π^0) ratio varies between 62.4 and 200 GeV. Together with the measured dN/dy , this gives insight into baryon transport and production at midrapidity.

We also analyzed the scaling properties of identified particle spectra, such as the m_T scaling and x_T scaling. Baryons and mesons are split in the m_T spectral shape at both 200 and 62.4 GeV. This splitting can be understood as the difference of hard production yields between baryons and mesons. The x_T scaling power n_{eff} shows similar values for pions, protons, and antiprotons.

We also compared the results in $p + p$ collisions at 200 GeV with those in Au + Au collisions at 200 GeV in the same experiment. It is found that T_{inv} , $\langle p_T \rangle$, and dN/dy change smoothly from $p + p$ to Au + Au, and all the values in $p + p$ are consistent with expectations from the N_{part} dependence in Au + Au. For the nuclear modification factor R_{AA} , there is a large suppression for pions, while there is an enhancement for protons and antiprotons at $p_T = 2\text{--}4$ GeV/ c . The observed suppression can be understood by the energy loss of partons in the hot and dense medium created in Au + Au central collisions at RHIC energies [65,66]. Possible explanations of the observed enhancements for protons and antiprotons include quark recombination [68–70] and/or strong partonic and hadronic radial flow [71].

Identified particle spectra are extended to the semihard 3–4 GeV/ c region for pions and (anti)protons, which makes it possible to study in further detail the nuclear modification factor of identified particles in $A + A$ collisions. NLO pQCD calculations [38,39] with DSS fragmentation functions show good agreement for pions and protons at 200 GeV, while there is less good agreement for \bar{p} . This indicates that fragmentation functions should be further improved.

For 62.4 GeV, NLO pQCD calculations underestimate by a factor of 2 or 3 the yields for all particle species. In contrast, NLL pQCD calculations [40,41] give a better agreement with the data. This suggests that resummed calculations are necessary to describe the cross section at 62.4 GeV.

From comparisons to some calculations such as those in the NLO or NLL pQCD framework, one can discuss the mechanism of soft and hard particle production in $p + p$ collisions. There is a transition between these two regions (“soft-hard transition”) at $p_T \sim 2$ GeV/ c for pions, and at

$p_T \sim 3$ GeV/ c for (anti)protons, or equivalently, $m_T - m = 1\text{--}2$ GeV/ c^2 for all particle species at both energies. The fractions of soft and hard components gradually change in the transition region. The new measurements presented in this work indicate that understanding the behavior of T_{inv} and $\langle p_T \rangle$ of identified particles in $p + p$ collisions requires clarifying the \sqrt{s} dependence through further measurements both at higher \sqrt{s} at the Large Hadron Collider and with lower-energy scans at RHIC.

ACKNOWLEDGMENTS

We thank the staff of the Collider-Accelerator and Physics Departments at Brookhaven National Laboratory and the staff of the other PHENIX participating institutions for their vital contributions. We thank Werner Vogelsang for providing the results of pQCD calculations. We acknowledge support from the Office of Nuclear Physics in the Office of Science of the Department of Energy, the National Science Foundation, a sponsored research grant from Renaissance Technologies LLC, Abilene Christian University Research Council, Research Foundation of SUNY, and Dean of the College of Arts and Sciences, Vanderbilt University (USA), Ministry of Education, Culture, Sports, Science, and Technology and the Japan Society for the Promotion of Science (Japan), Conselho Nacional de Desenvolvimento Científico e Tecnológico and Fundação de Amparo à Pesquisa do Estado de São Paulo (Brazil), Natural Science Foundation of China (People’s Republic of China), Ministry of Education, Youth and Sports (Czech Republic), Centre National de la Recherche Scientifique, Commissariat à l’Énergie Atomique, and Institut National de Physique Nucléaire et de Physique des Particules (France), Ministry of Industry, Science and Technologies, Bundesministerium für Bildung und Forschung, Deutscher Akademischer Austausch Dienst, and Alexander von Humboldt Stiftung (Germany), Hungarian National Science Fund, OTKA (Hungary), Department of Atomic Energy and Department of Science and Technology (India), Israel Science Foundation (Israel), National Research Foundation and WCU program of the Ministry Education Science and Technology (Korea), Ministry of Education and Science, Russia Academy of Sciences, Federal Agency of Atomic Energy (Russia), VR and the Wallenberg Foundation (Sweden), the U.S. Civilian Research and Development Foundation for the Independent States of the Former Soviet Union, the U.S.-Hungarian Fulbright Foundation for Educational Exchange, and the U.S.-Israel Binational Science Foundation

APPENDIX: TABLE OF CROSS SECTIONS

The cross sections for π^\pm , K^\pm , p , and \bar{p} in $p + p$ collisions at $\sqrt{s} = 200$ and 62.4 GeV at midrapidity are tabulated in Tables XI–XVIII. Statistical and systematic uncertainties are also shown. The normalization uncertainty (9.7% for 200 GeV, 11% for 62.4 GeV) is not included. For protons and antiprotons, there are two kinds of table, i.e., with and without the feed-down weak decay corrections.

TABLE XI. π^+ and π^- cross sections [$E d^3\sigma/dp^3$ (mb GeV $^{-2}$ c 3)] in $p + p$ collisions at $\sqrt{s} = 200$ GeV. Statistical (second column) and systematic (third column) uncertainties are shown for each particle species. The normalization uncertainty (9.7%) is not included.

p_T (GeV/c)	π^+	π^-
0.35	$2.77 \times 10^1 \pm 3.0 \times 10^{-1} \pm 1.9$	$2.63 \times 10^1 \pm 3.7 \times 10^{-1} \pm 1.8$
0.45	$1.45 \times 10^1 \pm 1.5 \times 10^{-1} \pm 1.0$	$1.40 \times 10^1 \pm 2.0 \times 10^{-1} \pm 9.8 \times 10^{-1}$
0.55	$7.76 \pm 8.6 \times 10^{-2} \pm 5.4 \times 10^{-1}$	$7.91 \pm 1.2 \times 10^{-1} \pm 5.5 \times 10^{-1}$
0.65	$4.39 \pm 5.3 \times 10^{-2} \pm 3.1 \times 10^{-1}$	$4.44 \pm 7.0 \times 10^{-2} \pm 3.1 \times 10^{-1}$
0.75	$2.65 \pm 3.5 \times 10^{-2} \pm 1.9 \times 10^{-1}$	$2.69 \pm 4.6 \times 10^{-2} \pm 1.9 \times 10^{-1}$
0.85	$1.59 \pm 2.2 \times 10^{-2} \pm 1.1 \times 10^{-1}$	$1.60 \pm 2.9 \times 10^{-2} \pm 1.1 \times 10^{-1}$
0.35	$2.77 \times 10^1 \pm 3.0 \times 10^{-1} \pm 1.9$	$2.63 \times 10^1 \pm 3.7 \times 10^{-1} \pm 1.8$
0.45	$1.45 \times 10^1 \pm 1.5 \times 10^{-1} \pm 1.0$	$1.40 \times 10^1 \pm 2.0 \times 10^{-1} \pm 9.8 \times 10^{-1}$
0.55	$7.76 \pm 8.6 \times 10^{-2} \pm 5.4 \times 10^{-1}$	$7.91 \pm 1.2 \times 10^{-1} \pm 5.5 \times 10^{-1}$
0.65	$4.39 \pm 5.3 \times 10^{-2} \pm 3.1 \times 10^{-1}$	$4.44 \pm 7.0 \times 10^{-2} \pm 3.1 \times 10^{-1}$
0.75	$2.65 \pm 3.5 \times 10^{-2} \pm 1.9 \times 10^{-1}$	$2.69 \pm 4.6 \times 10^{-2} \pm 1.9 \times 10^{-1}$
0.85	$1.59 \pm 2.2 \times 10^{-2} \pm 1.1 \times 10^{-1}$	$1.60 \pm 2.9 \times 10^{-2} \pm 1.1 \times 10^{-1}$
0.95	$1.01 \pm 1.5 \times 10^{-2} \pm 7.1 \times 10^{-2}$	$9.83 \times 10^{-1} \pm 1.9 \times 10^{-2} \pm 6.9 \times 10^{-2}$
1.05	$6.45 \times 10^{-1} \pm 1.1 \times 10^{-2} \pm 4.5 \times 10^{-2}$	$6.30 \times 10^{-1} \pm 1.3 \times 10^{-2} \pm 4.4 \times 10^{-2}$
1.15	$4.18 \times 10^{-1} \pm 7.2 \times 10^{-3} \pm 2.9 \times 10^{-2}$	$4.36 \times 10^{-1} \pm 9.5 \times 10^{-3} \pm 3.1 \times 10^{-2}$
1.25	$2.76 \times 10^{-1} \pm 5.0 \times 10^{-3} \pm 1.9 \times 10^{-2}$	$2.79 \times 10^{-1} \pm 6.3 \times 10^{-3} \pm 2.0 \times 10^{-2}$
1.35	$1.88 \times 10^{-1} \pm 3.6 \times 10^{-3} \pm 1.3 \times 10^{-2}$	$1.90 \times 10^{-1} \pm 4.4 \times 10^{-3} \pm 1.3 \times 10^{-2}$
1.45	$1.29 \times 10^{-1} \pm 2.6 \times 10^{-3} \pm 9.0 \times 10^{-3}$	$1.29 \times 10^{-1} \pm 3.1 \times 10^{-3} \pm 9.0 \times 10^{-3}$
1.55	$9.07 \times 10^{-2} \pm 1.9 \times 10^{-3} \pm 6.4 \times 10^{-3}$	$9.05 \times 10^{-2} \pm 2.3 \times 10^{-3} \pm 6.3 \times 10^{-3}$
1.65	$6.52 \times 10^{-2} \pm 1.4 \times 10^{-3} \pm 4.6 \times 10^{-3}$	$6.47 \times 10^{-2} \pm 1.7 \times 10^{-3} \pm 4.5 \times 10^{-3}$
1.75	$4.48 \times 10^{-2} \pm 9.9 \times 10^{-4} \pm 3.1 \times 10^{-3}$	$4.69 \times 10^{-2} \pm 1.2 \times 10^{-3} \pm 3.3 \times 10^{-3}$
1.85	$3.45 \times 10^{-2} \pm 8.1 \times 10^{-4} \pm 2.4 \times 10^{-3}$	$3.40 \times 10^{-2} \pm 9.3 \times 10^{-4} \pm 2.4 \times 10^{-3}$
1.95	$2.49 \times 10^{-2} \pm 6.1 \times 10^{-4} \pm 1.7 \times 10^{-3}$	$2.56 \times 10^{-2} \pm 7.4 \times 10^{-4} \pm 1.8 \times 10^{-3}$
2.05	$1.83 \times 10^{-2} \pm 4.7 \times 10^{-4} \pm 1.3 \times 10^{-3}$	$1.81 \times 10^{-2} \pm 5.5 \times 10^{-4} \pm 1.3 \times 10^{-3}$
2.15	$1.37 \times 10^{-2} \pm 3.8 \times 10^{-4} \pm 9.6 \times 10^{-4}$	$1.33 \times 10^{-2} \pm 4.3 \times 10^{-4} \pm 9.3 \times 10^{-4}$
2.25	$1.13 \times 10^{-2} \pm 3.5 \times 10^{-4} \pm 7.9 \times 10^{-4}$	$1.03 \times 10^{-2} \pm 3.6 \times 10^{-4} \pm 7.2 \times 10^{-4}$
2.35	$8.21 \times 10^{-3} \pm 2.8 \times 10^{-4} \pm 5.7 \times 10^{-4}$	$7.48 \times 10^{-3} \pm 2.8 \times 10^{-4} \pm 5.2 \times 10^{-4}$
2.45	$6.73 \times 10^{-3} \pm 2.5 \times 10^{-4} \pm 4.7 \times 10^{-4}$	$6.34 \times 10^{-3} \pm 2.7 \times 10^{-4} \pm 4.4 \times 10^{-4}$
2.55	$5.39 \times 10^{-3} \pm 2.3 \times 10^{-4} \pm 3.8 \times 10^{-4}$	$4.96 \times 10^{-3} \pm 2.3 \times 10^{-4} \pm 3.5 \times 10^{-4}$
2.65	$4.27 \times 10^{-3} \pm 2.0 \times 10^{-4} \pm 3.0 \times 10^{-4}$	$3.47 \times 10^{-3} \pm 1.8 \times 10^{-4} \pm 2.4 \times 10^{-4}$
2.75	$3.02 \times 10^{-3} \pm 1.6 \times 10^{-4} \pm 2.1 \times 10^{-4}$	$2.82 \times 10^{-3} \pm 1.6 \times 10^{-4} \pm 2.0 \times 10^{-4}$
2.85	$2.45 \times 10^{-3} \pm 1.4 \times 10^{-4} \pm 1.7 \times 10^{-4}$	$2.23 \times 10^{-3} \pm 1.5 \times 10^{-4} \pm 1.6 \times 10^{-4}$
2.95	$1.82 \times 10^{-3} \pm 1.2 \times 10^{-4} \pm 1.3 \times 10^{-4}$	$1.66 \times 10^{-3} \pm 1.2 \times 10^{-4} \pm 1.2 \times 10^{-4}$

TABLE XII. K^+ and K^- cross sections [$E d^3\sigma/dp^3$ (mb GeV $^{-2}$ c 3)] in $p + p$ collisions at $\sqrt{s} = 200$ GeV. Statistical (second column) and systematic (third column) uncertainties are shown for each particle species. The normalization uncertainty (9.7%) is not included.

p_T (GeV/c)	K^+	K^-
0.45	$1.96 \pm 5.0 \times 10^{-2} \pm 1.4 \times 10^{-1}$	$1.89 \pm 7.0 \times 10^{-2} \pm 1.3 \times 10^{-1}$
0.55	$1.35 \pm 3.0 \times 10^{-2} \pm 9.4 \times 10^{-2}$	$1.37 \pm 4.3 \times 10^{-2} \pm 9.6 \times 10^{-2}$
0.65	$8.71 \times 10^{-1} \pm 1.9 \times 10^{-2} \pm 6.1 \times 10^{-2}$	$8.28 \times 10^{-1} \pm 2.3 \times 10^{-2} \pm 5.8 \times 10^{-2}$
0.75	$5.86 \times 10^{-1} \pm 1.3 \times 10^{-2} \pm 4.1 \times 10^{-2}$	$5.60 \times 10^{-1} \pm 1.6 \times 10^{-2} \pm 3.9 \times 10^{-2}$
0.85	$3.95 \times 10^{-1} \pm 8.7 \times 10^{-3} \pm 2.8 \times 10^{-2}$	$3.87 \times 10^{-1} \pm 1.1 \times 10^{-2} \pm 2.7 \times 10^{-2}$
0.95	$2.60 \times 10^{-1} \pm 5.8 \times 10^{-3} \pm 1.8 \times 10^{-2}$	$2.54 \times 10^{-1} \pm 7.3 \times 10^{-3} \pm 1.8 \times 10^{-2}$
1.05	$1.72 \times 10^{-1} \pm 3.9 \times 10^{-3} \pm 1.2 \times 10^{-2}$	$1.83 \times 10^{-1} \pm 5.5 \times 10^{-3} \pm 1.3 \times 10^{-2}$
1.15	$1.26 \times 10^{-1} \pm 3.0 \times 10^{-3} \pm 8.9 \times 10^{-3}$	$1.16 \times 10^{-1} \pm 3.5 \times 10^{-3} \pm 8.1 \times 10^{-3}$
1.25	$8.52 \times 10^{-2} \pm 2.1 \times 10^{-3} \pm 6.0 \times 10^{-3}$	$8.97 \times 10^{-2} \pm 2.8 \times 10^{-3} \pm 6.3 \times 10^{-3}$
1.35	$6.08 \times 10^{-2} \pm 1.5 \times 10^{-3} \pm 4.3 \times 10^{-3}$	$6.23 \times 10^{-2} \pm 2.0 \times 10^{-3} \pm 4.4 \times 10^{-3}$
1.45	$4.59 \times 10^{-2} \pm 1.2 \times 10^{-3} \pm 3.2 \times 10^{-3}$	$4.27 \times 10^{-2} \pm 1.4 \times 10^{-3} \pm 3.0 \times 10^{-3}$
1.55	$3.29 \times 10^{-2} \pm 9.0 \times 10^{-4} \pm 2.3 \times 10^{-3}$	$3.21 \times 10^{-2} \pm 1.1 \times 10^{-3} \pm 2.2 \times 10^{-3}$
1.65	$2.39 \times 10^{-2} \pm 6.6 \times 10^{-4} \pm 1.7 \times 10^{-3}$	$2.23 \times 10^{-2} \pm 7.4 \times 10^{-4} \pm 1.6 \times 10^{-3}$
1.75	$1.86 \times 10^{-2} \pm 5.3 \times 10^{-4} \pm 1.3 \times 10^{-3}$	$1.81 \times 10^{-2} \pm 6.2 \times 10^{-4} \pm 1.3 \times 10^{-3}$
1.85	$1.49 \times 10^{-2} \pm 4.4 \times 10^{-4} \pm 1.0 \times 10^{-3}$	$1.36 \times 10^{-2} \pm 4.7 \times 10^{-4} \pm 9.5 \times 10^{-4}$
1.95	$1.13 \times 10^{-2} \pm 3.5 \times 10^{-4} \pm 7.9 \times 10^{-4}$	$1.03 \times 10^{-2} \pm 3.7 \times 10^{-4} \pm 7.2 \times 10^{-4}$

TABLE XIII. p and \bar{p} cross sections [$Ed^3\sigma/dp^3$ (mb GeV $^{-2}$ c 3)] in $p + p$ collisions at $\sqrt{s} = 200$ GeV. Statistical (second column) and systematic (third column) uncertainties are shown for each particle species. The normalization uncertainty (9.7%) is not included. Feed-down weak decay corrections are not applied.

p_T (GeV/c)	p	\bar{p}
0.55	$1.02 \pm 2.0 \times 10^{-2} \pm 6.2 \times 10^{-2}$	$7.88 \times 10^{-1} \pm 1.6 \times 10^{-2} \pm 5.5 \times 10^{-2}$
0.65	$7.40 \times 10^{-1} \pm 1.4 \times 10^{-2} \pm 4.5 \times 10^{-2}$	$6.04 \times 10^{-1} \pm 1.2 \times 10^{-2} \pm 4.2 \times 10^{-2}$
0.75	$5.58 \times 10^{-1} \pm 1.1 \times 10^{-2} \pm 3.4 \times 10^{-2}$	$4.62 \times 10^{-1} \pm 9.1 \times 10^{-3} \pm 3.2 \times 10^{-2}$
0.85	$3.77 \times 10^{-1} \pm 7.7 \times 10^{-3} \pm 2.3 \times 10^{-2}$	$3.18 \times 10^{-1} \pm 6.3 \times 10^{-3} \pm 2.2 \times 10^{-2}$
0.95	$2.73 \times 10^{-1} \pm 5.9 \times 10^{-3} \pm 1.6 \times 10^{-2}$	$2.18 \times 10^{-1} \pm 4.4 \times 10^{-3} \pm 1.5 \times 10^{-2}$
1.05	$1.80 \times 10^{-1} \pm 4.0 \times 10^{-3} \pm 1.1 \times 10^{-2}$	$1.58 \times 10^{-1} \pm 3.3 \times 10^{-3} \pm 1.1 \times 10^{-2}$
1.15	$1.27 \times 10^{-1} \pm 2.9 \times 10^{-3} \pm 7.6 \times 10^{-3}$	$1.08 \times 10^{-1} \pm 2.4 \times 10^{-3} \pm 7.6 \times 10^{-3}$
1.25	$9.18 \times 10^{-2} \pm 2.2 \times 10^{-3} \pm 5.5 \times 10^{-3}$	$7.54 \times 10^{-2} \pm 1.7 \times 10^{-3} \pm 5.3 \times 10^{-3}$
1.35	$6.24 \times 10^{-2} \pm 1.6 \times 10^{-3} \pm 3.7 \times 10^{-3}$	$5.58 \times 10^{-2} \pm 1.3 \times 10^{-3} \pm 3.9 \times 10^{-3}$
1.45	$4.80 \times 10^{-2} \pm 1.3 \times 10^{-3} \pm 2.9 \times 10^{-3}$	$3.73 \times 10^{-2} \pm 8.9 \times 10^{-4} \pm 2.6 \times 10^{-3}$
1.55	$3.32 \times 10^{-2} \pm 9.1 \times 10^{-4} \pm 2.0 \times 10^{-3}$	$2.68 \times 10^{-2} \pm 6.6 \times 10^{-4} \pm 1.9 \times 10^{-3}$
1.65	$2.31 \times 10^{-2} \pm 6.5 \times 10^{-4} \pm 1.4 \times 10^{-3}$	$1.93 \times 10^{-2} \pm 4.9 \times 10^{-4} \pm 1.4 \times 10^{-3}$
1.75	$1.70 \times 10^{-2} \pm 5.0 \times 10^{-4} \pm 1.0 \times 10^{-3}$	$1.39 \times 10^{-2} \pm 3.7 \times 10^{-4} \pm 9.8 \times 10^{-4}$
1.85	$1.17 \times 10^{-2} \pm 3.6 \times 10^{-4} \pm 7.0 \times 10^{-4}$	$9.69 \times 10^{-3} \pm 2.6 \times 10^{-4} \pm 6.8 \times 10^{-4}$
1.95	$8.98 \times 10^{-3} \pm 2.9 \times 10^{-4} \pm 5.4 \times 10^{-4}$	$6.94 \times 10^{-3} \pm 1.9 \times 10^{-4} \pm 4.9 \times 10^{-4}$
2.05	$6.68 \times 10^{-3} \pm 2.3 \times 10^{-4} \pm 4.0 \times 10^{-4}$	$5.12 \times 10^{-3} \pm 1.5 \times 10^{-4} \pm 3.6 \times 10^{-4}$
2.15	$4.62 \times 10^{-3} \pm 1.6 \times 10^{-4} \pm 2.8 \times 10^{-4}$	$3.61 \times 10^{-3} \pm 1.1 \times 10^{-4} \pm 2.5 \times 10^{-4}$
2.25	$3.91 \times 10^{-3} \pm 1.5 \times 10^{-4} \pm 2.4 \times 10^{-4}$	$2.90 \times 10^{-3} \pm 9.2 \times 10^{-5} \pm 2.0 \times 10^{-4}$
2.35	$2.63 \times 10^{-3} \pm 1.0 \times 10^{-4} \pm 1.6 \times 10^{-4}$	$2.09 \times 10^{-3} \pm 7.0 \times 10^{-5} \pm 1.5 \times 10^{-4}$
2.45	$1.79 \times 10^{-3} \pm 7.4 \times 10^{-5} \pm 1.1 \times 10^{-4}$	$1.58 \times 10^{-3} \pm 5.5 \times 10^{-5} \pm 1.1 \times 10^{-4}$
2.55	$1.62 \times 10^{-3} \pm 7.0 \times 10^{-5} \pm 1.0 \times 10^{-4}$	$1.10 \times 10^{-3} \pm 4.2 \times 10^{-5} \pm 7.8 \times 10^{-5}$
2.65	$1.15 \times 10^{-3} \pm 5.4 \times 10^{-5} \pm 7.2 \times 10^{-5}$	$8.85 \times 10^{-4} \pm 3.7 \times 10^{-5} \pm 6.3 \times 10^{-5}$
2.75	$8.89 \times 10^{-4} \pm 4.4 \times 10^{-5} \pm 5.6 \times 10^{-5}$	$6.22 \times 10^{-4} \pm 2.8 \times 10^{-5} \pm 4.4 \times 10^{-5}$
2.85	$6.38 \times 10^{-4} \pm 3.5 \times 10^{-5} \pm 4.1 \times 10^{-5}$	$5.07 \times 10^{-4} \pm 2.4 \times 10^{-5} \pm 3.6 \times 10^{-5}$
2.95	$4.97 \times 10^{-4} \pm 3.0 \times 10^{-5} \pm 3.2 \times 10^{-5}$	$3.80 \times 10^{-4} \pm 2.0 \times 10^{-5} \pm 2.7 \times 10^{-5}$
3.05	$4.13 \times 10^{-4} \pm 2.6 \times 10^{-5} \pm 2.7 \times 10^{-5}$	$3.13 \times 10^{-4} \pm 1.7 \times 10^{-5} \pm 2.3 \times 10^{-5}$
3.10	$3.80 \times 10^{-4} \pm 1.8 \times 10^{-5} \pm 2.5 \times 10^{-5}$	$2.75 \times 10^{-4} \pm 1.1 \times 10^{-5} \pm 2.0 \times 10^{-5}$
3.30	$2.33 \times 10^{-4} \pm 1.3 \times 10^{-5} \pm 1.6 \times 10^{-5}$	$1.92 \times 10^{-4} \pm 9.0 \times 10^{-6} \pm 1.4 \times 10^{-5}$
3.50	$1.57 \times 10^{-4} \pm 1.0 \times 10^{-5} \pm 1.1 \times 10^{-5}$	$1.12 \times 10^{-4} \pm 6.5 \times 10^{-6} \pm 8.6 \times 10^{-6}$
3.70	$1.11 \times 10^{-4} \pm 8.9 \times 10^{-6} \pm 8.3 \times 10^{-6}$	$7.16 \times 10^{-5} \pm 5.2 \times 10^{-6} \pm 5.8 \times 10^{-6}$
3.90	$7.25 \times 10^{-5} \pm 7.2 \times 10^{-6} \pm 5.8 \times 10^{-6}$	$4.40 \times 10^{-5} \pm 4.0 \times 10^{-6} \pm 3.8 \times 10^{-6}$
4.10	$6.23 \times 10^{-5} \pm 6.7 \times 10^{-6} \pm 5.3 \times 10^{-6}$	$3.81 \times 10^{-5} \pm 3.9 \times 10^{-6} \pm 3.6 \times 10^{-6}$
4.30	$3.83 \times 10^{-5} \pm 5.5 \times 10^{-6} \pm 3.6 \times 10^{-6}$	$2.63 \times 10^{-5} \pm 3.3 \times 10^{-6} \pm 2.8 \times 10^{-6}$
4.50	$3.22 \times 10^{-5} \pm 5.2 \times 10^{-6} \pm 3.3 \times 10^{-6}$	$1.82 \times 10^{-5} \pm 2.8 \times 10^{-6} \pm 2.2 \times 10^{-6}$

TABLE XIV. p and \bar{p} cross sections [$Ed^3\sigma/dp^3$ (mb GeV $^{-2}$ c 3)] in $p + p$ collisions at $\sqrt{s} = 200$ GeV. Statistical (second column) and systematic (third column) uncertainties are shown for each particle species. The normalization uncertainty (9.7%) is not included. Feed-down weak decay corrections are applied.

p_T (GeV/c)	p	\bar{p}
0.55	$5.93 \times 10^{-1} \pm 1.1 \times 10^{-2} \pm 1.4 \times 10^{-1}$	$4.56 \times 10^{-1} \pm 9.2 \times 10^{-3} \pm 1.1 \times 10^{-1}$
0.65	$4.45 \times 10^{-1} \pm 8.4 \times 10^{-3} \pm 9.4 \times 10^{-2}$	$3.63 \times 10^{-1} \pm 7.0 \times 10^{-3} \pm 7.8 \times 10^{-2}$
0.75	$3.47 \times 10^{-1} \pm 6.9 \times 10^{-3} \pm 6.6 \times 10^{-2}$	$2.87 \times 10^{-1} \pm 5.6 \times 10^{-3} \pm 5.6 \times 10^{-2}$
0.85	$2.42 \times 10^{-1} \pm 4.9 \times 10^{-3} \pm 4.2 \times 10^{-2}$	$2.04 \times 10^{-1} \pm 4.0 \times 10^{-3} \pm 3.6 \times 10^{-2}$
0.95	$1.80 \times 10^{-1} \pm 3.9 \times 10^{-3} \pm 2.9 \times 10^{-2}$	$1.44 \times 10^{-1} \pm 2.9 \times 10^{-3} \pm 2.4 \times 10^{-2}$
1.05	$1.22 \times 10^{-1} \pm 2.7 \times 10^{-3} \pm 1.8 \times 10^{-2}$	$1.06 \times 10^{-1} \pm 2.2 \times 10^{-3} \pm 1.6 \times 10^{-2}$
1.15	$8.77 \times 10^{-2} \pm 2.0 \times 10^{-3} \pm 1.2 \times 10^{-2}$	$7.48 \times 10^{-2} \pm 1.6 \times 10^{-3} \pm 1.1 \times 10^{-2}$
1.25	$6.46 \times 10^{-2} \pm 1.6 \times 10^{-3} \pm 8.4 \times 10^{-3}$	$5.31 \times 10^{-2} \pm 1.2 \times 10^{-3} \pm 7.1 \times 10^{-3}$
1.35	$4.47 \times 10^{-2} \pm 1.1 \times 10^{-3} \pm 5.5 \times 10^{-3}$	$4.00 \times 10^{-2} \pm 9.4 \times 10^{-4} \pm 5.1 \times 10^{-3}$
1.45	$3.49 \times 10^{-2} \pm 9.4 \times 10^{-4} \pm 4.1 \times 10^{-3}$	$2.72 \times 10^{-2} \pm 6.5 \times 10^{-4} \pm 3.3 \times 10^{-3}$
1.55	$2.45 \times 10^{-2} \pm 6.8 \times 10^{-4} \pm 2.7 \times 10^{-3}$	$1.98 \times 10^{-2} \pm 4.9 \times 10^{-4} \pm 2.3 \times 10^{-3}$

TABLE XIV. (*Continued.*)

p_T (GeV/c)	p	\bar{p}
1.65	$1.73 \times 10^{-2} \pm 4.9 \times 10^{-4} \pm 1.9 \times 10^{-3}$	$1.45 \times 10^{-2} \pm 3.7 \times 10^{-4} \pm 1.6 \times 10^{-3}$
1.75	$1.28 \times 10^{-2} \pm 3.8 \times 10^{-4} \pm 1.3 \times 10^{-3}$	$1.06 \times 10^{-2} \pm 2.8 \times 10^{-4} \pm 1.2 \times 10^{-3}$
1.85	$8.92 \times 10^{-3} \pm 2.7 \times 10^{-4} \pm 8.9 \times 10^{-4}$	$7.42 \times 10^{-3} \pm 2.0 \times 10^{-4} \pm 7.9 \times 10^{-4}$
1.95	$6.95 \times 10^{-3} \pm 2.2 \times 10^{-4} \pm 6.8 \times 10^{-4}$	$5.37 \times 10^{-3} \pm 1.5 \times 10^{-4} \pm 5.6 \times 10^{-4}$
2.05	$5.21 \times 10^{-3} \pm 1.8 \times 10^{-4} \pm 4.9 \times 10^{-4}$	$4.00 \times 10^{-3} \pm 1.2 \times 10^{-4} \pm 4.0 \times 10^{-4}$
2.15	$3.63 \times 10^{-3} \pm 1.3 \times 10^{-4} \pm 3.4 \times 10^{-4}$	$2.84 \times 10^{-3} \pm 8.7 \times 10^{-5} \pm 2.8 \times 10^{-4}$
2.25	$3.10 \times 10^{-3} \pm 1.2 \times 10^{-4} \pm 2.8 \times 10^{-4}$	$2.30 \times 10^{-3} \pm 7.3 \times 10^{-5} \pm 2.2 \times 10^{-4}$
2.35	$2.10 \times 10^{-3} \pm 8.2 \times 10^{-5} \pm 1.9 \times 10^{-4}$	$1.67 \times 10^{-3} \pm 5.6 \times 10^{-5} \pm 1.6 \times 10^{-4}$
2.45	$1.44 \times 10^{-3} \pm 6.0 \times 10^{-5} \pm 1.3 \times 10^{-4}$	$1.27 \times 10^{-3} \pm 4.4 \times 10^{-5} \pm 1.2 \times 10^{-4}$
2.55	$1.31 \times 10^{-3} \pm 5.7 \times 10^{-5} \pm 1.1 \times 10^{-4}$	$8.89 \times 10^{-4} \pm 3.4 \times 10^{-5} \pm 8.3 \times 10^{-5}$
2.65	$9.31 \times 10^{-4} \pm 4.4 \times 10^{-5} \pm 8.0 \times 10^{-5}$	$7.19 \times 10^{-4} \pm 3.0 \times 10^{-5} \pm 6.6 \times 10^{-5}$
2.75	$7.26 \times 10^{-4} \pm 3.6 \times 10^{-5} \pm 6.2 \times 10^{-5}$	$5.08 \times 10^{-4} \pm 2.3 \times 10^{-5} \pm 4.6 \times 10^{-5}$
2.85	$5.23 \times 10^{-4} \pm 2.9 \times 10^{-5} \pm 4.4 \times 10^{-5}$	$4.16 \times 10^{-4} \pm 2.0 \times 10^{-5} \pm 3.8 \times 10^{-5}$
2.95	$4.09 \times 10^{-4} \pm 2.4 \times 10^{-5} \pm 3.4 \times 10^{-5}$	$3.13 \times 10^{-4} \pm 1.6 \times 10^{-5} \pm 2.8 \times 10^{-5}$
3.05	$3.41 \times 10^{-4} \pm 2.2 \times 10^{-5} \pm 2.9 \times 10^{-5}$	$2.58 \times 10^{-4} \pm 1.4 \times 10^{-5} \pm 2.3 \times 10^{-5}$
3.10	$3.14 \times 10^{-4} \pm 1.5 \times 10^{-5} \pm 2.6 \times 10^{-5}$	$2.28 \times 10^{-4} \pm 9.3 \times 10^{-6} \pm 2.0 \times 10^{-5}$
3.30	$1.94 \times 10^{-4} \pm 1.1 \times 10^{-5} \pm 1.6 \times 10^{-5}$	$1.60 \times 10^{-4} \pm 7.5 \times 10^{-6} \pm 1.4 \times 10^{-5}$
3.50	$1.32 \times 10^{-4} \pm 8.6 \times 10^{-6} \pm 1.1 \times 10^{-5}$	$9.42 \times 10^{-5} \pm 5.4 \times 10^{-6} \pm 8.6 \times 10^{-6}$
3.70	$9.35 \times 10^{-5} \pm 7.5 \times 10^{-6} \pm 8.2 \times 10^{-6}$	$6.03 \times 10^{-5} \pm 4.4 \times 10^{-6} \pm 5.6 \times 10^{-6}$
3.90	$6.13 \times 10^{-5} \pm 6.1 \times 10^{-6} \pm 5.6 \times 10^{-6}$	$3.72 \times 10^{-5} \pm 3.4 \times 10^{-6} \pm 3.6 \times 10^{-6}$
4.10	$5.28 \times 10^{-5} \pm 5.7 \times 10^{-6} \pm 5.1 \times 10^{-6}$	$3.24 \times 10^{-5} \pm 3.3 \times 10^{-6} \pm 3.4 \times 10^{-6}$
4.30	$3.26 \times 10^{-5} \pm 4.7 \times 10^{-6} \pm 3.3 \times 10^{-6}$	$2.23 \times 10^{-5} \pm 2.8 \times 10^{-6} \pm 2.6 \times 10^{-6}$
4.50	$2.75 \times 10^{-5} \pm 4.4 \times 10^{-6} \pm 3.0 \times 10^{-6}$	$1.56 \times 10^{-5} \pm 2.4 \times 10^{-6} \pm 2.0 \times 10^{-6}$

TABLE XV. π^+ and π^- cross sections [$Ed^3\sigma/dp^3$ (mb GeV $^{-2}c^3$)] in $p + p$ collisions at $\sqrt{s} = 62.4$ GeV. Statistical (second column) and systematic (third column) uncertainties are shown for each particle species. The normalization uncertainty (11%) is not included.

p_T (GeV/c)	π^+	π^-
0.35	$1.96 \times 10^1 \pm 1.8 \times 10^{-1} \pm 1.4$	$2.08 \times 10^1 \pm 1.5 \times 10^{-1} \pm 1.3$
0.45	$1.07 \times 10^1 \pm 1.1 \times 10^{-1} \pm 7.5 \times 10^{-1}$	$1.12 \times 10^1 \pm 8.6 \times 10^{-2} \pm 6.7 \times 10^{-1}$
0.55	$5.95 \pm 6.3 \times 10^{-2} \pm 4.2 \times 10^{-1}$	$5.94 \pm 4.9 \times 10^{-2} \pm 3.6 \times 10^{-1}$
0.65	$3.38 \pm 3.9 \times 10^{-2} \pm 2.4 \times 10^{-1}$	$3.25 \pm 3.0 \times 10^{-2} \pm 1.9 \times 10^{-1}$
0.75	$1.91 \pm 2.4 \times 10^{-2} \pm 1.3 \times 10^{-1}$	$1.92 \pm 2.0 \times 10^{-2} \pm 1.2 \times 10^{-1}$
0.85	$1.13 \pm 1.6 \times 10^{-2} \pm 7.9 \times 10^{-2}$	$1.15 \pm 1.3 \times 10^{-2} \pm 6.9 \times 10^{-2}$
0.95	$6.86 \times 10^{-1} \pm 1.0 \times 10^{-2} \pm 4.8 \times 10^{-2}$	$6.68 \times 10^{-1} \pm 8.4 \times 10^{-3} \pm 4.0 \times 10^{-2}$
1.05	$4.30 \times 10^{-1} \pm 7.2 \times 10^{-3} \pm 3.0 \times 10^{-2}$	$4.06 \times 10^{-1} \pm 5.7 \times 10^{-3} \pm 2.4 \times 10^{-2}$
1.15	$2.65 \times 10^{-1} \pm 4.9 \times 10^{-3} \pm 1.9 \times 10^{-2}$	$2.53 \times 10^{-1} \pm 4.0 \times 10^{-3} \pm 1.5 \times 10^{-2}$
1.25	$1.66 \times 10^{-1} \pm 3.5 \times 10^{-3} \pm 1.2 \times 10^{-2}$	$1.60 \times 10^{-1} \pm 2.9 \times 10^{-3} \pm 9.6 \times 10^{-3}$
1.35	$1.08 \times 10^{-1} \pm 2.6 \times 10^{-3} \pm 7.5 \times 10^{-3}$	$1.03 \times 10^{-1} \pm 2.1 \times 10^{-3} \pm 6.2 \times 10^{-3}$
1.45	$7.20 \times 10^{-2} \pm 1.9 \times 10^{-3} \pm 5.0 \times 10^{-3}$	$6.74 \times 10^{-2} \pm 1.6 \times 10^{-3} \pm 4.0 \times 10^{-3}$
1.55	$5.04 \times 10^{-2} \pm 1.5 \times 10^{-3} \pm 3.5 \times 10^{-3}$	$4.54 \times 10^{-2} \pm 1.2 \times 10^{-3} \pm 2.7 \times 10^{-3}$
1.65	$3.48 \times 10^{-2} \pm 1.2 \times 10^{-3} \pm 2.4 \times 10^{-3}$	$3.07 \times 10^{-2} \pm 9.7 \times 10^{-4} \pm 1.8 \times 10^{-3}$
1.75	$2.33 \times 10^{-2} \pm 9.5 \times 10^{-4} \pm 1.6 \times 10^{-3}$	$2.25 \times 10^{-2} \pm 8.3 \times 10^{-4} \pm 1.4 \times 10^{-3}$
1.85	$1.58 \times 10^{-2} \pm 7.8 \times 10^{-4} \pm 1.1 \times 10^{-3}$	$1.55 \times 10^{-2} \pm 6.8 \times 10^{-4} \pm 9.3 \times 10^{-4}$
1.95	$1.11 \times 10^{-2} \pm 6.7 \times 10^{-4} \pm 7.8 \times 10^{-4}$	$9.63 \times 10^{-3} \pm 5.2 \times 10^{-4} \pm 5.8 \times 10^{-4}$
2.05	$7.13 \times 10^{-3} \pm 5.2 \times 10^{-4} \pm 5.0 \times 10^{-4}$	$7.23 \times 10^{-3} \pm 4.7 \times 10^{-4} \pm 4.3 \times 10^{-4}$
2.15	$5.63 \times 10^{-3} \pm 5.0 \times 10^{-4} \pm 4.0 \times 10^{-4}$	$4.72 \times 10^{-3} \pm 3.9 \times 10^{-4} \pm 2.9 \times 10^{-4}$
2.25	$4.22 \times 10^{-3} \pm 4.3 \times 10^{-4} \pm 3.0 \times 10^{-4}$	$3.32 \times 10^{-3} \pm 3.4 \times 10^{-4} \pm 2.0 \times 10^{-4}$
2.35	$2.69 \times 10^{-3} \pm 3.7 \times 10^{-4} \pm 1.9 \times 10^{-4}$	$2.67 \times 10^{-3} \pm 3.3 \times 10^{-4} \pm 1.7 \times 10^{-4}$
2.45	$1.96 \times 10^{-3} \pm 3.1 \times 10^{-4} \pm 1.4 \times 10^{-4}$	$1.75 \times 10^{-3} \pm 2.9 \times 10^{-4} \pm 1.1 \times 10^{-4}$
2.55	$1.45 \times 10^{-3} \pm 3.3 \times 10^{-4} \pm 1.1 \times 10^{-4}$	$1.49 \times 10^{-3} \pm 2.7 \times 10^{-4} \pm 9.8 \times 10^{-5}$
2.65	$9.07 \times 10^{-4} \pm 2.2 \times 10^{-4} \pm 7.0 \times 10^{-5}$	$1.07 \times 10^{-3} \pm 2.5 \times 10^{-4} \pm 7.3 \times 10^{-5}$
2.75	$1.09 \times 10^{-3} \pm 3.0 \times 10^{-4} \pm 8.6 \times 10^{-5}$	$7.62 \times 10^{-4} \pm 2.5 \times 10^{-4} \pm 5.4 \times 10^{-5}$
2.85	$6.48 \times 10^{-4} \pm 2.3 \times 10^{-4} \pm 5.3 \times 10^{-5}$	$5.10 \times 10^{-4} \pm 2.0 \times 10^{-4} \pm 3.7 \times 10^{-5}$

TABLE XVI. K^+ and K^- cross sections [$E d^3\sigma/dp^3$ (mb GeV $^{-2}$ c 3)] in $p + p$ collisions at $\sqrt{s} = 62.4$ GeV. Statistical (second column) and systematic (third column) uncertainties are shown for each particle species. The normalization uncertainty (11%) is not included.

p_T (GeV/c)	K^+	K^-
0.45	$1.18 \pm 2.7 \times 10^{-2} \pm 8.2 \times 10^{-2}$	$1.06 \pm 1.9 \times 10^{-2} \pm 7.4 \times 10^{-2}$
0.55	$8.18 \times 10^{-1} \pm 1.8 \times 10^{-2} \pm 5.7 \times 10^{-2}$	$7.48 \times 10^{-1} \pm 1.3 \times 10^{-2} \pm 5.2 \times 10^{-2}$
0.65	$6.07 \times 10^{-1} \pm 1.3 \times 10^{-2} \pm 4.3 \times 10^{-2}$	$5.30 \times 10^{-1} \pm 9.6 \times 10^{-3} \pm 3.7 \times 10^{-2}$
0.75	$3.72 \times 10^{-1} \pm 8.4 \times 10^{-3} \pm 2.6 \times 10^{-2}$	$3.43 \times 10^{-1} \pm 6.7 \times 10^{-3} \pm 2.4 \times 10^{-2}$
0.85	$2.50 \times 10^{-1} \pm 6.1 \times 10^{-3} \pm 1.8 \times 10^{-2}$	$2.14 \times 10^{-1} \pm 4.6 \times 10^{-3} \pm 1.5 \times 10^{-2}$
0.95	$1.73 \times 10^{-1} \pm 4.7 \times 10^{-3} \pm 1.2 \times 10^{-2}$	$1.40 \times 10^{-1} \pm 3.4 \times 10^{-3} \pm 9.8 \times 10^{-3}$
1.05	$1.12 \times 10^{-1} \pm 3.3 \times 10^{-3} \pm 7.8 \times 10^{-3}$	$9.05 \times 10^{-2} \pm 2.5 \times 10^{-3} \pm 6.3 \times 10^{-3}$
1.15	$7.94 \times 10^{-2} \pm 2.7 \times 10^{-3} \pm 5.6 \times 10^{-3}$	$6.17 \times 10^{-2} \pm 1.9 \times 10^{-3} \pm 4.3 \times 10^{-3}$
1.25	$4.88 \times 10^{-2} \pm 1.9 \times 10^{-3} \pm 3.4 \times 10^{-3}$	$4.35 \times 10^{-2} \pm 1.5 \times 10^{-3} \pm 3.0 \times 10^{-3}$
1.35	$3.41 \times 10^{-2} \pm 1.5 \times 10^{-3} \pm 2.4 \times 10^{-3}$	$2.84 \times 10^{-2} \pm 1.2 \times 10^{-3} \pm 2.0 \times 10^{-3}$
1.45	$2.45 \times 10^{-2} \pm 1.2 \times 10^{-3} \pm 1.7 \times 10^{-3}$	$1.96 \times 10^{-2} \pm 9.2 \times 10^{-4} \pm 1.4 \times 10^{-3}$
1.55	$1.63 \times 10^{-2} \pm 9.5 \times 10^{-4} \pm 1.1 \times 10^{-3}$	$1.34 \times 10^{-2} \pm 7.6 \times 10^{-4} \pm 9.4 \times 10^{-4}$
1.65	$1.28 \times 10^{-2} \pm 8.0 \times 10^{-4} \pm 9.1 \times 10^{-4}$	$9.77 \times 10^{-3} \pm 6.2 \times 10^{-4} \pm 7.0 \times 10^{-4}$
1.75	$9.56 \times 10^{-3} \pm 6.8 \times 10^{-4} \pm 7.1 \times 10^{-4}$	$6.65 \times 10^{-3} \pm 4.8 \times 10^{-4} \pm 4.9 \times 10^{-4}$
1.85	$6.34 \times 10^{-3} \pm 5.4 \times 10^{-4} \pm 5.0 \times 10^{-4}$	$4.87 \times 10^{-3} \pm 4.2 \times 10^{-4} \pm 3.8 \times 10^{-4}$
1.95	$5.28 \times 10^{-3} \pm 5.1 \times 10^{-4} \pm 4.4 \times 10^{-4}$	$3.45 \times 10^{-3} \pm 3.7 \times 10^{-4} \pm 2.9 \times 10^{-4}$

TABLE XVII. p and \bar{p} cross sections [$E d^3\sigma/dp^3$ (mb GeV $^{-2}$ c 3)] in $p + p$ collisions at $\sqrt{s} = 62.4$ GeV. Statistical (second column) and systematic (third column) uncertainties are shown for each particle species. The normalization uncertainty (11%) is not included. Feed-down weak decay corrections are not applied.

p_T (GeV/c)	p	\bar{p}
0.65	$4.63 \times 10^{-1} \pm 7.1 \times 10^{-3} \pm 4.2 \times 10^{-2}$	$3.09 \times 10^{-1} \pm 4.6 \times 10^{-3} \pm 2.2 \times 10^{-2}$
0.75	$3.28 \times 10^{-1} \pm 5.4 \times 10^{-3} \pm 3.0 \times 10^{-2}$	$2.19 \times 10^{-1} \pm 3.6 \times 10^{-3} \pm 1.5 \times 10^{-2}$
0.85	$2.49 \times 10^{-1} \pm 4.5 \times 10^{-3} \pm 2.2 \times 10^{-2}$	$1.59 \times 10^{-1} \pm 2.9 \times 10^{-3} \pm 1.1 \times 10^{-2}$
0.95	$1.69 \times 10^{-1} \pm 3.4 \times 10^{-3} \pm 1.5 \times 10^{-2}$	$1.10 \times 10^{-1} \pm 2.3 \times 10^{-3} \pm 7.7 \times 10^{-3}$
1.05	$1.20 \times 10^{-1} \pm 2.7 \times 10^{-3} \pm 1.1 \times 10^{-2}$	$7.50 \times 10^{-2} \pm 1.8 \times 10^{-3} \pm 5.3 \times 10^{-3}$
1.15	$8.12 \times 10^{-2} \pm 2.1 \times 10^{-3} \pm 7.3 \times 10^{-3}$	$4.95 \times 10^{-2} \pm 1.4 \times 10^{-3} \pm 3.5 \times 10^{-3}$
1.25	$5.81 \times 10^{-2} \pm 1.7 \times 10^{-3} \pm 5.2 \times 10^{-3}$	$3.32 \times 10^{-2} \pm 1.1 \times 10^{-3} \pm 2.3 \times 10^{-3}$
1.35	$3.95 \times 10^{-2} \pm 1.4 \times 10^{-3} \pm 3.6 \times 10^{-3}$	$2.37 \times 10^{-2} \pm 9.4 \times 10^{-4} \pm 1.7 \times 10^{-3}$
1.45	$2.55 \times 10^{-2} \pm 9.9 \times 10^{-4} \pm 2.3 \times 10^{-3}$	$1.53 \times 10^{-2} \pm 7.1 \times 10^{-4} \pm 1.1 \times 10^{-3}$
1.55	$1.84 \times 10^{-2} \pm 8.4 \times 10^{-4} \pm 1.7 \times 10^{-3}$	$1.07 \times 10^{-2} \pm 6.0 \times 10^{-4} \pm 7.5 \times 10^{-4}$
1.65	$1.37 \times 10^{-2} \pm 7.2 \times 10^{-4} \pm 1.2 \times 10^{-3}$	$7.03 \times 10^{-3} \pm 4.7 \times 10^{-4} \pm 4.9 \times 10^{-4}$
1.75	$9.31 \times 10^{-3} \pm 5.8 \times 10^{-4} \pm 8.4 \times 10^{-4}$	$4.49 \times 10^{-3} \pm 3.7 \times 10^{-4} \pm 3.1 \times 10^{-4}$
1.85	$5.90 \times 10^{-3} \pm 4.4 \times 10^{-4} \pm 5.3 \times 10^{-4}$	$3.39 \times 10^{-3} \pm 3.4 \times 10^{-4} \pm 2.4 \times 10^{-4}$
1.95	$4.02 \times 10^{-3} \pm 3.6 \times 10^{-4} \pm 3.6 \times 10^{-4}$	$2.12 \times 10^{-3} \pm 2.4 \times 10^{-4} \pm 1.5 \times 10^{-4}$
2.05	$3.11 \times 10^{-3} \pm 3.1 \times 10^{-4} \pm 2.8 \times 10^{-4}$	$1.58 \times 10^{-3} \pm 2.2 \times 10^{-4} \pm 1.1 \times 10^{-4}$
2.15	$1.99 \times 10^{-3} \pm 2.5 \times 10^{-4} \pm 1.8 \times 10^{-4}$	$1.04 \times 10^{-3} \pm 1.7 \times 10^{-4} \pm 7.3 \times 10^{-5}$
2.25	$1.37 \times 10^{-3} \pm 2.1 \times 10^{-4} \pm 1.2 \times 10^{-4}$	$6.99 \times 10^{-4} \pm 1.5 \times 10^{-4} \pm 4.9 \times 10^{-5}$
2.35	$8.94 \times 10^{-4} \pm 1.5 \times 10^{-4} \pm 8.0 \times 10^{-5}$	$5.90 \times 10^{-4} \pm 1.3 \times 10^{-4} \pm 4.1 \times 10^{-5}$
2.45	$6.34 \times 10^{-4} \pm 1.3 \times 10^{-4} \pm 5.7 \times 10^{-5}$	$3.13 \times 10^{-4} \pm 1.1 \times 10^{-4} \pm 2.2 \times 10^{-5}$
2.55	$6.33 \times 10^{-4} \pm 1.4 \times 10^{-4} \pm 5.7 \times 10^{-5}$	$2.43 \times 10^{-4} \pm 8.3 \times 10^{-5} \pm 1.7 \times 10^{-5}$
2.65	$4.56 \times 10^{-4} \pm 1.2 \times 10^{-4} \pm 4.1 \times 10^{-5}$	$1.80 \times 10^{-4} \pm 7.9 \times 10^{-5} \pm 1.3 \times 10^{-5}$
2.75	$4.11 \times 10^{-4} \pm 1.1 \times 10^{-4} \pm 3.7 \times 10^{-5}$	$1.74 \times 10^{-4} \pm 7.5 \times 10^{-5} \pm 1.2 \times 10^{-5}$
2.85	$2.40 \times 10^{-4} \pm 9.5 \times 10^{-5} \pm 2.2 \times 10^{-5}$	$2.39 \times 10^{-4} \pm 9.1 \times 10^{-5} \pm 1.7 \times 10^{-5}$
2.95	$1.63 \times 10^{-4} \pm 6.6 \times 10^{-5} \pm 1.5 \times 10^{-5}$	$6.57 \times 10^{-5} \pm 5.0 \times 10^{-5} \pm 4.7 \times 10^{-6}$
3.10	$9.65 \times 10^{-5} \pm 3.7 \times 10^{-5} \pm 8.9 \times 10^{-6}$	$7.07 \times 10^{-5} \pm 2.8 \times 10^{-5} \pm 5.1 \times 10^{-6}$
3.30	$9.05 \times 10^{-5} \pm 4.1 \times 10^{-5} \pm 8.5 \times 10^{-6}$	$4.14 \times 10^{-5} \pm 3.2 \times 10^{-5} \pm 3.1 \times 10^{-6}$
3.50	$2.13 \times 10^{-5} \pm 1.9 \times 10^{-5} \pm 2.0 \times 10^{-6}$	$5.21 \times 10^{-5} \pm 3.2 \times 10^{-5} \pm 4.0 \times 10^{-6}$

TABLE XVIII. p and \bar{p} cross sections [$E d^3\sigma/dp^3$ (mb GeV $^{-2}$ c 3)] in $p + p$ collisions at $\sqrt{s} = 62.4$ GeV. Statistical (second column) and systematic (third column) uncertainties are shown for each particle species. The normalization uncertainty (11%) is not included. Feed-down weak decay corrections are applied.

p_T (GeV/c)	p	\bar{p}
0.65	$2.95 \times 10^{-1} \pm 4.5 \times 10^{-3} \pm 6.6 \times 10^{-2}$	$1.18 \times 10^{-1} \pm 1.8 \times 10^{-3} \pm 6.5 \times 10^{-2}$
0.75	$2.38 \times 10^{-1} \pm 3.9 \times 10^{-3} \pm 3.8 \times 10^{-2}$	$1.20 \times 10^{-1} \pm 2.0 \times 10^{-3} \pm 3.4 \times 10^{-2}$
0.85	$1.96 \times 10^{-1} \pm 3.5 \times 10^{-3} \pm 2.5 \times 10^{-2}$	$1.05 \times 10^{-1} \pm 1.9 \times 10^{-3} \pm 1.9 \times 10^{-2}$
0.95	$1.40 \times 10^{-1} \pm 2.8 \times 10^{-3} \pm 1.6 \times 10^{-2}$	$8.12 \times 10^{-2} \pm 1.7 \times 10^{-3} \pm 1.1 \times 10^{-2}$
1.05	$1.03 \times 10^{-1} \pm 2.3 \times 10^{-3} \pm 1.1 \times 10^{-2}$	$5.91 \times 10^{-2} \pm 1.4 \times 10^{-3} \pm 6.6 \times 10^{-3}$
1.15	$7.18 \times 10^{-2} \pm 1.9 \times 10^{-3} \pm 7.1 \times 10^{-3}$	$4.07 \times 10^{-2} \pm 1.1 \times 10^{-3} \pm 4.0 \times 10^{-3}$
1.25	$5.23 \times 10^{-2} \pm 1.5 \times 10^{-3} \pm 5.1 \times 10^{-3}$	$2.81 \times 10^{-2} \pm 9.4 \times 10^{-4} \pm 2.6 \times 10^{-3}$
1.35	$3.60 \times 10^{-2} \pm 1.2 \times 10^{-3} \pm 3.4 \times 10^{-3}$	$2.04 \times 10^{-2} \pm 8.1 \times 10^{-4} \pm 1.8 \times 10^{-3}$
1.45	$2.34 \times 10^{-2} \pm 9.1 \times 10^{-4} \pm 2.2 \times 10^{-3}$	$1.33 \times 10^{-2} \pm 6.2 \times 10^{-4} \pm 1.1 \times 10^{-3}$
1.55	$1.70 \times 10^{-2} \pm 7.7 \times 10^{-4} \pm 1.6 \times 10^{-3}$	$9.42 \times 10^{-3} \pm 5.2 \times 10^{-4} \pm 7.8 \times 10^{-4}$
1.65	$1.27 \times 10^{-2} \pm 6.7 \times 10^{-4} \pm 1.2 \times 10^{-3}$	$6.19 \times 10^{-3} \pm 4.1 \times 10^{-4} \pm 5.1 \times 10^{-4}$
1.75	$8.67 \times 10^{-3} \pm 5.4 \times 10^{-4} \pm 8.1 \times 10^{-4}$	$3.97 \times 10^{-3} \pm 3.3 \times 10^{-4} \pm 3.2 \times 10^{-4}$
1.85	$5.51 \times 10^{-3} \pm 4.1 \times 10^{-4} \pm 5.1 \times 10^{-4}$	$3.00 \times 10^{-3} \pm 3.0 \times 10^{-4} \pm 2.4 \times 10^{-4}$
1.95	$3.76 \times 10^{-3} \pm 3.3 \times 10^{-4} \pm 3.5 \times 10^{-4}$	$1.88 \times 10^{-3} \pm 2.2 \times 10^{-4} \pm 1.5 \times 10^{-4}$
2.05	$2.91 \times 10^{-3} \pm 2.9 \times 10^{-4} \pm 2.7 \times 10^{-4}$	$1.41 \times 10^{-3} \pm 2.0 \times 10^{-4} \pm 1.1 \times 10^{-4}$
2.15	$1.86 \times 10^{-3} \pm 2.4 \times 10^{-4} \pm 1.7 \times 10^{-4}$	$9.24 \times 10^{-4} \pm 1.5 \times 10^{-4} \pm 7.4 \times 10^{-5}$
2.25	$1.28 \times 10^{-3} \pm 2.0 \times 10^{-4} \pm 1.2 \times 10^{-4}$	$6.21 \times 10^{-4} \pm 1.3 \times 10^{-4} \pm 5.0 \times 10^{-5}$
2.35	$8.39 \times 10^{-4} \pm 1.4 \times 10^{-4} \pm 7.7 \times 10^{-5}$	$5.25 \times 10^{-4} \pm 1.2 \times 10^{-4} \pm 4.2 \times 10^{-5}$
2.45	$5.95 \times 10^{-4} \pm 1.2 \times 10^{-4} \pm 5.5 \times 10^{-5}$	$2.78 \times 10^{-4} \pm 9.4 \times 10^{-5} \pm 2.2 \times 10^{-5}$
2.55	$5.94 \times 10^{-4} \pm 1.3 \times 10^{-4} \pm 5.5 \times 10^{-5}$	$2.16 \times 10^{-4} \pm 7.4 \times 10^{-5} \pm 1.7 \times 10^{-5}$
2.65	$4.28 \times 10^{-4} \pm 1.1 \times 10^{-4} \pm 3.9 \times 10^{-5}$	$1.60 \times 10^{-4} \pm 7.0 \times 10^{-5} \pm 1.3 \times 10^{-5}$
2.75	$3.86 \times 10^{-4} \pm 1.1 \times 10^{-4} \pm 3.6 \times 10^{-5}$	$1.55 \times 10^{-4} \pm 6.6 \times 10^{-5} \pm 1.2 \times 10^{-5}$
2.85	$2.25 \times 10^{-4} \pm 8.9 \times 10^{-5} \pm 2.1 \times 10^{-5}$	$2.13 \times 10^{-4} \pm 8.1 \times 10^{-5} \pm 1.7 \times 10^{-5}$
2.95	$1.54 \times 10^{-4} \pm 6.2 \times 10^{-5} \pm 1.4 \times 10^{-5}$	$5.85 \times 10^{-5} \pm 4.4 \times 10^{-5} \pm 4.7 \times 10^{-6}$
3.10	$9.06 \times 10^{-5} \pm 3.4 \times 10^{-5} \pm 8.5 \times 10^{-6}$	$6.30 \times 10^{-5} \pm 2.5 \times 10^{-5} \pm 5.2 \times 10^{-6}$
3.30	$8.50 \times 10^{-5} \pm 3.8 \times 10^{-5} \pm 8.1 \times 10^{-6}$	$3.69 \times 10^{-5} \pm 2.8 \times 10^{-5} \pm 3.1 \times 10^{-6}$
3.50	$2.00 \times 10^{-5} \pm 1.7 \times 10^{-5} \pm 2.0 \times 10^{-6}$	$4.64 \times 10^{-5} \pm 2.8 \times 10^{-5} \pm 4.0 \times 10^{-6}$

-
- [1] S. M. Berman, J. D. Bjorken, and J. B. Kogut, *Phys. Rev. D* **4**, 3388 (1971).
- [2] J. Nishimura, *Soryushiron Kenkyu* **12**, 24 (1956).
- [3] G. Cocconi, *Phys. Rev.* **111**, 1699 (1958).
- [4] G. Cocconi, L. J. Koester, and D. H. Perkins, LRL Report No. UCRL-10022, 1961 (unpublished), p. 167.
- [5] J. Orear, *Phys. Rev. Lett.* **12**, 112 (1964).
- [6] R. Hagedorn, *Proceedings of NATO Advanced Research Workshop on Hot Hadronic Matter: Theory and Experiment, Divonne-les-Bains, France, 1994*, edited by J. Letessier, H. H. Gutbrod, and J. Rafelski (Plenum Press, New York, 1995), p. 13.
- [7] J. Erwin, W. Ko, R. L. Lander, D. E. Pellett, and P. M. Yager, *Phys. Rev. Lett.* **27**, 1534 (1971).
- [8] R. Hagedorn, *Nucl. Phys. B* **24**, 93 (1970).
- [9] S. Barshay and Y. A. Chao, *Phys. Lett. B* **38**, 229 (1972).
- [10] H. Bøggild *et al.* (Scandinavian Bubble Chamber Collaboration), *Nucl. Phys. B* **57**, 77 (1973).
- [11] M. Deutschmann *et al.*, *Nucl. Phys. B* **70**, 189 (1974).
- [12] J. Bartke *et al.* (Aachen-Berlin-Bonn-CERN-Cracow-Heidelberg-Warsaw Collaboration), *Nucl. Phys. B* **120**, 14 (1977).
- [13] B. Alper *et al.* (British-Scandinavian Collaboration), *Nucl. Phys. B* **100**, 237 (1975).
- [14] M. Gell-Mann, *Phys. Lett.* **8**, 214 (1964).
- [15] G. Zweig, CERN Reports No. 8182/TH.401 and No. 8419/TH.412, 1964 (unpublished).
- [16] V. V. Anisovich and M. N. Kobrinsky, *Phys. Lett. B* **52**, 217 (1974), and references therein.
- [17] R. P. Feynman, *Phys. Rev. Lett.* **23**, 1415 (1969).
- [18] J. Benecke, T. T. Chou, C.-N. Yang, and E. Yen, *Phys. Rev.* **188**, 2159 (1969).
- [19] A. H. Mueller, *Phys. Rev. D* **2**, 2963 (1970).
- [20] U. Camerini, W. O. Lock, and D. H. Perkins, *Prog. Cosmic Ray Phys.* **1**, 1 (1952).
- [21] W. B. Fowler, R. P. Shutt, A. M. Thorndike, and W. L. Whittemore, *Phys. Rev.* **95**, 1026 (1954).
- [22] E. Fermi, *Phys. Rev.* **81**, 683 (1951).
- [23] S. Z. Belenkij and L. D. Landau, *Nuovo Cimento Suppl.* **3**, 15 (1956); *Usp. Fiz. Nauk* **56**, 309 (1955).
- [24] B. Alper *et al.* (British-Scandinavian Collaboration), *Nucl. Phys. B* **87**, 19 (1975).
- [25] D. Drijard *et al.* (CERN-Dortmund-Heidelberg-Warsaw Collaboration), *Z. Phys. C* **12**, 217 (1982).
- [26] S. S. Adler *et al.* (PHENIX Collaboration), *Phys. Rev. C* **74**, 024904 (2006).
- [27] S. S. Adler *et al.* (PHENIX Collaboration), *Phys. Rev. Lett.* **91**, 241803 (2003).

- [28] A. Adare *et al.* (PHENIX Collaboration), *Phys. Rev. D* **83**, 052004 (2011).
- [29] B. I. Abelev *et al.* (STAR Collaboration), *Phys. Rev. C* **79**, 034909 (2009).
- [30] A. Adare *et al.* (PHENIX Collaboration), *Phys. Rev. D* **76**, 051106 (2007).
- [31] B. I. Abelev *et al.* (STAR Collaboration), *Phys. Rev. C* **75**, 064901 (2007).
- [32] J. Adams *et al.* (STAR Collaboration), *Phys. Rev. D* **74**, 032006 (2006).
- [33] J. Adams *et al.* (STAR Collaboration), *Phys. Lett. B* **637**, 161 (2006).
- [34] A. Adare *et al.* (PHENIX Collaboration), *Phys. Rev. D* **79**, 012003 (2009).
- [35] P. Dariulat, *Annu. Rev. Nucl. Part. Sci.* **30**, 159 (1980).
- [36] R. Blankenbecler, S. Brodsky, and J. Gunion, *Phys. Lett. B* **42**, 461 (1972).
- [37] S. S. Adler *et al.* (PHENIX Collaboration), *Phys. Rev. C* **69**, 034909 (2004).
- [38] B. Jager, A. Schafer, M. Stratmann, and W. Vogelsang, *Phys. Rev. D* **67**, 054005 (2003).
- [39] D. de Florian, *Phys. Rev. D* **67**, 054004 (2003).
- [40] D. de Florian and W. Vogelsang, *Phys. Rev. D* **71**, 114004 (2005).
- [41] D. de Florian, W. Vogelsang, and F. Wagner, *Phys. Rev. D* **76**, 094021 (2007).
- [42] K. Adcox *et al.* (PHENIX Collaboration), *Nucl. Instrum. Methods Phys. Res., Sect. A* **499**, 469 (2003).
- [43] S. H. Aronson *et al.* (PHENIX Collaboration), *Nucl. Instrum. Methods Phys. Res., Sect. A* **499**, 480 (2003).
- [44] M. Aizawa *et al.* (PHENIX Collaboration), *Nucl. Instrum. Methods Phys. Res., Sect. A* **499**, 508 (2003).
- [45] M. Allen *et al.* (PHENIX Collaboration), *Nucl. Instrum. Methods Phys. Res., Sect. A* **499**, 549 (2003).
- [46] K. Adcox *et al.* (PHENIX Collaboration), *Nucl. Instrum. Methods Phys. Res., Sect. A* **499**, 489 (2003).
- [47] J. T. Mitchell *et al.* (PHENIX Collaboration), *Nucl. Instrum. Methods Phys. Res., Sect. A* **482**, 491 (2002).
- [48] Computer code GEANT 3.2.1, CERN Computing Library, 1993, [<http://wwwasdoc.web.cern.ch/wwwasdoc/pdfdir/geant.pdf>].
- [49] A. Drees and Z. Xu, *Proceedings of the 2001 Particle Accelerator Conference, Chicago, Illinois, USA, 2001* (IEEE Operations Center, Piscataway, NJ, USA), p. 3120.
- [50] A. Adare *et al.* (PHENIX Collaboration), *Phys. Rev. C* **77**, 064907 (2008).
- [51] W. Vogelsang (private communication).
- [52] C. Tsallis, *J. Stat. Phys.* **52**, 479 (1988).
- [53] A. M. Rossi *et al.*, *Nucl. Phys. B* **84**, 269 (1975).
- [54] T. Alexopoulos *et al.* (E735 Collaboration), *Phys. Rev. D* **48**, 984 (1993).
- [55] M. Kliemant, B. Lungwitz, and M. Gazdzicki, *Phys. Rev. C* **69**, 044903 (2004).
- [56] C. Alt *et al.* (NA49 Collaboration), *Eur. Phys. J. C* **45**, 343 (2006).
- [57] J. Adams *et al.* (STAR Collaboration), *Phys. Lett. B* **616**, 8 (2005).
- [58] T. Alexopoulos *et al.*, *Phys. Rev. Lett.* **64**, 991 (1990).
- [59] R. E. Ansorge *et al.* (UA5 Collaboration), *Nucl. Phys. B* **328**, 36 (1989).
- [60] M. L. Miller, K. Reygers, S. J. Sanders, and P. Steinberg, *Annu. Rev. Nucl. Part. Sci.* **57**, 205 (2007).
- [61] B. Z. Kopeliovich, *Phys. Rev. C* **68**, 044906 (2003).
- [62] B. Z. Kopeliovich (private communication).
- [63] K. Aamodt *et al.* (ALICE Collaboration), *Eur. Phys. J. C* **68**, 89 (2010).
- [64] A. Adare *et al.* (PHENIX Collaboration), *Phys. Rev. Lett.* **101**, 232301 (2008).
- [65] S. S. Adler *et al.* (PHENIX Collaboration), *Phys. Rev. Lett.* **91**, 072301 (2003).
- [66] K. Adcox *et al.* (PHENIX Collaboration), *Nucl. Phys. A* **757**, 184 (2005).
- [67] S. S. Adler *et al.* (PHENIX Collaboration), *Phys. Rev. Lett.* **91**, 172301 (2003).
- [68] R. J. Fries, B. Muller, C. Nonaka, and S. A. Bass, *Phys. Rev. Lett.* **90**, 202303 (2003).
- [69] R. C. Hwa and C. B. Yang, *Phys. Rev. C* **67**, 034902 (2003).
- [70] V. Greco, C. M. Ko, and P. Levai, *Phys. Rev. Lett.* **90**, 202302 (2003).
- [71] T. Hirano and Y. Nara, *Phys. Rev. C* **69**, 034908 (2004).
- [72] K. Adcox *et al.* (PHENIX Collaboration), *Phys. Rev. C* **69**, 024904 (2004).
- [73] E. Schnedermann, J. Sollfrank, and U. W. Heinz, *Phys. Rev. C* **48**, 2462 (1993).
- [74] T. Csörgő, S. V. Akkelin, Y. Hama, B. Lukács, and Y. M. Sinyukov, *Phys. Rev. C* **67**, 034904 (2003).
- [75] F. Arleo, S. J. Brodsky, D. S. Hwang, and A. M. Sickles, *Phys. Rev. Lett.* **105**, 062002 (2010).
- [76] R. F. Cahalan, K. A. Geer, J. Kogut, and L. Susskind, *Phys. Rev. D* **11**, 1199 (1975).
- [77] A. Clark *et al.*, *Phys. Lett. B* **74**, 267 (1978).
- [78] A. Angelis *et al.* (CCOR Collaboration), *Phys. Lett. B* **79**, 505 (1978).
- [79] C. Kourkoumelis *et al.*, *Phys. Lett. B* **84**, 271 (1979).
- [80] M. Banner *et al.* (UA2 Collaboration), *Phys. Lett.* **115B**, 1 (1982).
- [81] J. Pumplin *et al.*, *J. High Energy Phys.* **07** (2002) 012 .
- [82] D. de Florian, R. Sassot, and M. Stratmann, *Phys. Rev. D* **75**, 114010 (2007).
- [83] S. Albino, B. Kniehl, and G. Kramer, *Nucl. Phys. B* **725**, 181 (2005).
- [84] B. Kniehl, G. Kramer, and B. Potter, *Nucl. Phys. B* **597**, 337 (2001).